Title
Non-Photonic Electron at High Transverse Momentum in Au+Au Collisions and Bottom Quark Production in p+p Collisions at sqrt(sNN) = 200 GeV

Author
Xu, Wenqin

Publication Date
2012

Peer reviewed|Thesis/dissertation

University of California

Los Angeles

Non-Photonic Electron at High Transverse Momentum in Au+Au Collisions and Bottom Quark Production in p+p Collisions at $\sqrt{s_{\rm NN}}$ = 200 GeV

A dissertation submitted in partial satisfaction

of the requirements for the degree

Doctor of Philosophy in Physics

by

Wenqin Xu

2012

Abstract of the Dissertation

Non-Photonic Electron at High Transverse Momentum in Au+Au Collisions and Bottom Quark Production in p+p Collisions at $\sqrt{s_{\rm NN}}$ = 200 GeV

by

Wenqin Xu

Doctor of Philosophy in Physics

University of California, Los Angeles, 2012

Professor Huan Z. Huang, Chair

A new form of matter with de-confined quarks and gluons, named the "Quark Gluon Plasma" (QGP), is predicted by Lattice Qutantum Chromodynamics to exist at high temperatures and/or high baryon density regions in the QCD phase diagram. Experimental evidence indicates that the QCD matter created in high energy Au+Au collisions at the Relativistic Heavy Ion Collider (RHIC) in Brookhaven National Lab is a strongly-coupled Quark-Gluon Plasma. One of the central goals of heavy ion physics is to understand the QGP through quantitative comparisons between theoretical calculations and experimental measurements. Heavy flavor quarks are believed to be a unique probe for this task, because they are dominantly produced in the initial hard scatterings, where the production rate can be well calculated by perturbative-QCD(pQCD). When heavy favor quarks traverse the QGP medium, they bear the imprints of the medium via their interactions with the medium. Dynamical models have been developed to calculate the interactions between heavy quarks and the QGP medium to quantitatively extract the medium properties.

This dissertation presents a series of experimental studies with the electrons

produced in the semi-leptonic decays of heavy flavor quarks in Au+Au and p+p collisions, which serve as the proxies for heavy flavor quarks. These electrons are referred to as non-photonic electrons (NPE), to be differentiated from the main background of photonic electrons. The production of NPE at high p_T is found to be highly suppressed in central and semi-central Au+Au collisions, compared to binary-collision scaled production in p+p collisions. The azimuthal anisotropy of NPE is found to be finite at high p_T, and the azimuthal correlation between high p_T NPE and low p_T hadrons exhibits a broadening in the away-side, both of which strengthen the evidence for a strong coupling between heavy flavor quarks and the QGP medium. In addition, the bottom quark production cross-section in p+p collisions is obtained based on the measured spectrum of NPE and the ratio of bottom/charm decay electrons.

The dissertation of Wenqin Xu is approved.

George J. Igo

Gang Li

Graciela B. Gelmini

Huan Z. Huang, Committee Chair

University of California, Los Angeles

2012

To my parents and my wife,

who are always there for me

Table of Contents

1 Introduction to Relativistic Heavy Ion Collisions 1

1.1 Introduction to Quantum Chromodynamics 1

1.2 The Quark-Gluon-Plasma 3

1.3 The experimental probes of QGP 9

1.3.1 A little history 9

1.3.2 The stages of high energy heavy ion collisions at RHIC . . 9

1.3.3 Particle production 10

1.3.4 Elliptic flow 13

1.3.5 Jet quenching 20

1.3.6 heavy flavor 27

2 Experimental set-ups 32

2.1 Relativistic Heavy Ion Collider 32

2.2 STAR detector system 35

2.2.1 Overview 35

2.2.2 The Time Projection Chamber 37

2.2.3 Barrel ElectroMagnetic Calorimeter and Barrel Shower Maximum Detector 40

2.2.4 Heavy Flavor Tracker 41

3 Analysis of Non-Photonic Electron spectrum 45

3.1 Overview of analysis procedures 45

3.2 Data sets 46

3.2.1 Triggers 46
3.2.2 Run selection 47
3.2.3 Event selection and centrality determination 48
3.3 Track quality cuts 53
3.4 Electron identification 54
3.4.1 BEMC point reconstruction and track matching 55
3.4.2 E/P and Number of BSMD strips 60
3.4.3 TPC ionization energy loss $n\sigma_e$ 64
3.5 Photonic electron reconstruction 69
3.6 Heavy quarkonia decay and Drell-Yan 76
3.7 K_{e3} decay 80
3.8 Efficiency studies 80
3.8.1 Introduction to embedding 80
3.8.2 Single electron efficiency 81
3.8.3 Photonic electron reconstruction efficiency 86
3.9 High tower trigger efficiency 92
3.10 Systematic uncertainties 100
3.10.1 From photonic electron reconstruction efficiency 100
3.10.2 From single electron efficiency 100
3.10.3 From J/Ψ and other feed down 101
3.11 Additional ingredients for NPE R_{AA} 102
3.12 Results and discussion 106
3.12.1 NPE p_T spectrum and R_{AA} Results 106
3.12.2 Model comparison 107

4 NPE azimuthal anisotropy and correlation 118

4.1 NPE azimuthal anisotropy 118

4.1.1 Event Plane Reconstruction 120

4.1.2 Hadron flow 121

4.1.3 NPE elliptic flow 122

4.1.4 Model comparison 125

4.2 NPE-hadron azimuthal correlation 127

4.2.1 Measurements of the NPE-hadron azimuthal correlation . 127

4.2.2 Models of the NPE-hadron azimuthal correlation 131

5 Measurement of Charm/Bottom Ratios and Bottom quark production in p+p collisions 133

5.1 Bottom decay electrons 134

5.1.1 High p_T e_B/e_{npe} in p+p 134

5.1.2 Differential cross section of bottom decay electrons 137

5.1.3 FONLL calculations of NPE 142

5.1.4 Integrated cross section of bottom decay electrons 142

5.2 PYTHIA calculations 143

5.3 Bottom production cross section 154

6 Conclusion and Outlook 157

A List of Rejected Runs 159

B Error propagation in elliptic flow calculations 162

References 164

List of Figures

1.1 A NLO QCD fit of F_2 4

1.2 NLO pQCD jet spectra 5

1.3 Theoretical expectations of the QCD phase diagram 6

1.4 LQCD calculations of phase transition 8

1.5 A schematic view of the time evolution of the QGP 11

1.6 Yields of different hadrons 12

1.7 Hadrons p_T spectra and the mass ordering of mean p_T 14

1.8 The elliptic flow of various hadrons 16

1.9 Elliptic flow versus N_{part} and p_T 17

1.10 Constituent Quark Number Scaling 19

1.11 $R_{F_2}^A = \frac{F_2^A}{AF_2^N}$ 21

1.12 Dihadron correlations for different collision systems 22

1.13 Summary plot of R_{AA} 24

1.14 Path length dependence induced elliptic flow 27

1.15 The spectra and R_{AA} of heavy flavor decay electrons by STAR . . 29

1.16 The R_{AA} and v_2 of heavy flavor decay electrons by PHENIX . . . 30

2.1 A schematic drawing of RHIC complex 33

2.2 A schematic side view of STAR. 36

2.3 An illustration of the STAR TPC 38

2.4 The readout pads for STAR TPC 40

2.5 BEMC module 42

2.6 BSMD 43

2.7 HFT 44

3.1 Number of events in NPE11 trigger divided by that in MinBias . 49

3.2 Distributions of vertex positions 50

3.3 The efficiency of V_Z cuts 50

3.4 The efficiency of V_Z cuts in selected centrality 51

3.5 Distribution of $\Delta\phi$ 58

3.6 Distribution of ΔZ for positive η 58

3.7 Distribution of ΔZ for negative η 59

3.8 Two dimensional distribution of ΔZ and η 59

3.9 Distribution of E/p 61

3.10 Two dimensional distribution of number of BSMD strips 61

3.11 One dimensional distribution of number of BSMD strips 64

3.12 Distributions of $n\sigma_e$ 66

3.13 Distributions of $n\sigma_e$ for photonic electrons 68

3.14 The opening angle for photonic electrons 71

3.15 The opening angle for photonic electrons in ϕ plane and θ plane . 72

3.16 The DCA for photonic electrons 72

3.17 The mis-reconstructed DCA position for photonic electrons 73

3.18 The invariant mass distribution 75

3.19 The J/Ψ spectra at mid-rapidity 77

3.20 The J/Ψ decay electron spectra 79

3.21 η and ϕ distributions of tracks in embedding and in data. 83

3.22 TPC tracking efficiency in 0$\sim$60% centrality. 83

3.23 Number of BSMD strips: data-embedding comparison 85

3.24 The combined BEMC efficiency 86
3.25 The overall single electron efficiency 87
3.26 The simulated invariant mass of e^+ and e^- in Dalitz decays 88
3.27 The reconstructed invariant mass of e^+ and e^- in Dalitz decays . 89
3.28 The simulated opening angle of e^+ and e^- in Dalitz decays 89
3.29 The reconstructed DCA of e^+ and e^- in Dalitz decays 89
3.30 The overall photonic electron reconstruction efficiencies 90
3.31 Gamma conversion versus all photonic 91
3.32 The combined photonic electron reconstruction efficiency 91
3.33 NPE11 trigger efficiency based on inclusive electrons 93
3.34 NPE11 trigger efficiency based on inclusive electrons in each centrality 95
3.35 NPE11 trigger efficiency based on photonic electrons 96
3.36 NPE15 trigger efficiency based on inclusive electrons 97
3.37 NPE15 trigger efficiency based on inclusive electrons in each centrality 98
3.38 NPE15 trigger efficiency based on photonic electrons 99
3.39 J/Ψ decay electron divided by total NPE for different centrality. . 103
3.40 Non-photonic electron production in p+p collisions 104
3.41 The NPE spectrum and R_{AA} in 0 to 5% centrality. 108
3.42 The NPE spectrum and R_{AA} in 0 to 10% centrality. 109
3.43 The NPE spectrum and R_{AA} in 10 to 20% centrality. 110
3.44 The NPE spectrum and R_{AA} in 20 to 40% centrality. 111
3.45 The NPE spectrum and R_{AA} in 40 to 60% centrality. 112
3.46 Heavy meson R_{AA} from the GBA model 113
3.47 NPE R_{AA} from the HFR model 115

3.48 Charm versus bottom in model 115

3.49 NPE R_{AA} from the SVZ model 116

4.1 The angle difference between bottom and electron daughters. . . . 119

4.2 The event plane Ψ_{EP} distribution. 121

4.3 The charged hadrons elliptic flow 123

4.4 $\Delta\phi$ distribution for NPE 125

4.5 The elliptic flows of NPE 126

4.6 NPE v_2 in model 127

4.7 Artificial correlations due to detector non-uniformity 129

4.8 The NPE-hadron correlation 132

5.1 Relative bottom mesons contributions to NPE 135

5.2 Interpolation based on FONLL predictions 138

5.3 Separated spectra of electrons originating from bottom/charm . . 141

5.4 Spectra of electron originating from bottom quarks 145

5.5 PYTHIA calculation with parameters from e-h paper 151

5.6 PYTHIA with MSEL= 5 153

List of Tables

3.1 The electron identification cuts 63

3.2 The efficiency of $n\sigma_e$ and the electron purity 67

3.3 The partner electron identification cuts 70

3.4 The cuts applied to identify photonic electrons 76

3.5 Non-photonic electron production in p+p collisions 105

3.6 N_{binary} 105

3.7 NPE spectra shifts 107

5.1 Relative bottom meson contributions to NPE 136

5.2 The cross section of electrons from bottom hadron decays 139

5.3 The cross section of electrons from bottom hadron decays, syst. . 139

5.4 The cross section of electrons from charm hadron decays 140

5.5 The cross section of electrons from charm hadron decays, syst. . . 140

5.6 PYTHIA with MSEL= 1 147

5.7 PYTHIA calculations with various parameters 148

5.8 The parameters set in the NPE-hadron correlation study 149

5.9 PYTHIA calculation with parameters from the e-h paper 150

5.10 PYTHIA with MSEL= 5 152

5.11 Bottom hadron admixture 155

Acknowledgments

I give my most sincere gratitude to my advisor, Professor H. Huang, without whom this work could not be possible. I especially thank him for his physics insight and his guidance, which led me to enjoy the beauty and excitement of modern physics at a professional level and benefited me enormously. I also thank my co-advisor, Professor C. A. Whitten Jr., whose very warm-hearted support and encouragement always made me feel comfortable and motivated. We are deeply saddened by his unexpected death and he will always be remembered.

I would like to thank Professor G. Igo and S. Trentalange for our discussions on physics and beyond physics, which enlightened me in many aspects; I want to extend my thanks to G. Wang, O. Tsai and B. Biritz, who passed their vast knowledge to me and patiently helped me build my professional expertise. I feel thankful for daily help from all the former and current members of the research group, including V. Ghazikhanian, J. Ma, S. Guertin, X. Lin, D. Gangadharan, D. Staszak, P. Kurnadi, S. Sakai, R. Cendejas, F. Zhao, Y. Pan, X. Liu, B. Zhu, N. Shah, L. Dunkelberger, and K. Landry.

It has been wonderful to work with the STAR collaboration and my many thanks go to Dr. Nu Xu and other collaborators, who commit themselves to training the younger generation.

My special thanks go to my parents, who always encouraged me to pursue my dream and supported me unconditionally. I also deeply appreciate the sacrifices my beloved wife, Chenkun Wang, has been making for me. She is the sweetest thing in my life.

Vita

July, 2006	Bachelor of Science, University of Science and Technology of China
June, 2008	Master of Science, University of California, Los Angeles
2006-2011	Research Assistant, Experimental QCD and neutrino physics group University of California, Los Angeles
2011-2012	Dissertation Year Fellowship, University of California, Los Angeles

CHAPTER 1

Introduction to Relativistic Heavy Ion Collisions

1.1 Introduction to Quantum Chromodynamics

Nuclear and particle physics aims to understand nature in terms of the most fundamental ingredients and interactions. The most fundamental ingredients, so-called elementary particles, include spin 1/2 fermions, which are the constituents of matter, and spin 1 gauge bosons, which are the force carriers. Except gravity, the other three most fundamental interactions can be well understood by quantum field theories. Quantum Chromodynamics (QCD), based on the SU(3) group, is the theory of the strong interactions of colored quarks and gluons.

The triumph of the Standard Model of particle physics, especially in the language of quantum field theories, builds on its remarkable ability to predict and explain experimental observations. One of the most discussed examples is the spin g-factor g_s of the electron magnetic moment $\vec{\mu_s} = -g_s\mu_B(\vec{s}/\hbar)$, where $\vec{s}$ is electron spin, and $\mu_B(s/\hbar)$ is the Bohr magneton. In the Quantum Electrodynamics (QED), where electron-virtual photon interactions are treated perturbatively as higher order corrections, $(g_s - 2)/2$ is calculated to be between $1159.6520950 \times 10^{-6}$ and $1159.6523791 \times 10^{-6}$ [1]. The uncertainty arises from the limited knowledge of the fine-structure constant α, since g_s can be calculated to arbitrary precision in theory. The up-to-date experimental result $(g_s - 2)/2 = 1159.65218073(28) \times 10^{-6}$ [2] exhibits remarkable consistency with theoretical calculations.

With a much larger coupling constant, perturbative expansion in QCD is impossible at low energies. However, as a renormalizable quantum field theory, the QCD coupling constant depends on the renormalization scale. The β-function ($\beta(g) = -\frac{g^3}{(4\pi)^2}(\frac{11}{3}N - \frac{2}{3}n_f)$ at high energy), which describes the running of the coupling constant, is negative thanks to the non-Abelian nature of the strong interaction and the fact that there are less than seventeen different quark flavors at relevant energy scales [3]. As a result, the strong coupling constant decreases with increasing energy scale at high energy, an essential QCD property known as asymptotic freedom. On the other hand, when (anti)quarks are pulled away to a larger distance, which is equivalent to a lower momentum transfer, the coupling becomes larger. Eventually, the potential between (anti)quarks grows roughly linearly with distance until there is enough energy to make a new pair of quark and anti-quark, which combines with original (anti)quarks and forms hadrons again.

The strong interaction and the underlying QCD theory are complicated in many ways, yet extremely intriguing and important. For example, the chiral symmetry of u, d quarks is spontaneously broken in the strong interaction, due to the existence of a quark condensate in the vacuum, *i.e.*$< 0|\bar{Q}Q|0 >=< 0|\bar{Q}_L Q_R + \bar{Q}_R Q_L|0 >\neq 0$, with the corresponding Goldstone bosons being the pions [3, 4]. This is the reason why we don't see another copy of existing hadrons with the same quantum numbers but opposite parities. This mechanism, structurally similar to the Higgs mechanism, is responsible for the majority of the mass of light flavor hadrons. As a result, the mass of the visible matter in the universe is mostly due to QCD interactions.

The high precision experimental support for QCD and the quark model often come at relatively high momentum transfer square (Q^2), where the strong coupling constant is small enough for perturbative QCD (pQCD) to be applicable. For example, the dependence of the structure function F_2 (the integral of quark distribution functions) on Q^2, often measured in deeply inelastic electron-proton

scatterings (DIS), is of great importance in our understanding of the structure of hadrons. Firstly the structure function has a near flat feature, also known as the Bjorken scaling, and the feature is one of the most important pieces of evidence for point-like objects in hadrons, supporting the existence of quarks. Secondly, the evolution of the structure function at various fixed parton momentum fraction, *i.e.* Bjorken $x = \frac{Q^2}{2p \cdot q}$, can be well described by functionals from pQCD calculations involving the DGLAP (Dokshitzer-Gribov-Lipatov-Altarelli-Parisi) equation, which describe the parton evolution at large Q^2 and fixed x. An example is shown in Figure 1.1 [5].

Among many other successes of Perturbative QCD, its overwhelming power at describing the dynamics of hadronic jet production and heavy quark production is outstanding. The former (hadronic jets) is demonstrated in Figure 1.2 [6, 7], where the consistence between data and Next-Leading-Order (NLO) pQCD calculations spans many orders of magnitude and different collision energies. The latter (heavy quarks) is particularly important for this dissertation and will be discussed in later chapters.

1.2 The Quark-Gluon-Plasma

Thanks to the intriguing nature of the strong interaction, the QCD phase diagram is very rich in new physical phenomena. In particular, a new form of matter with de-confined quarks and gluons has been predicted as early as the 1970's (see *e.g.* [8] for a review), and it has been named the "Quark Gluon Plasma" (QGP). The QGP is expected at the high temperature and/or the high baryon density regions of the QCD phase diagram (Figure 1.3 [9]).

The study of the QGP, together with the general exploration of the QCD phase diagram, deepens our understanding of the thermal properties of strong interactions and QCD. For example, it is a rare example of a many-body system

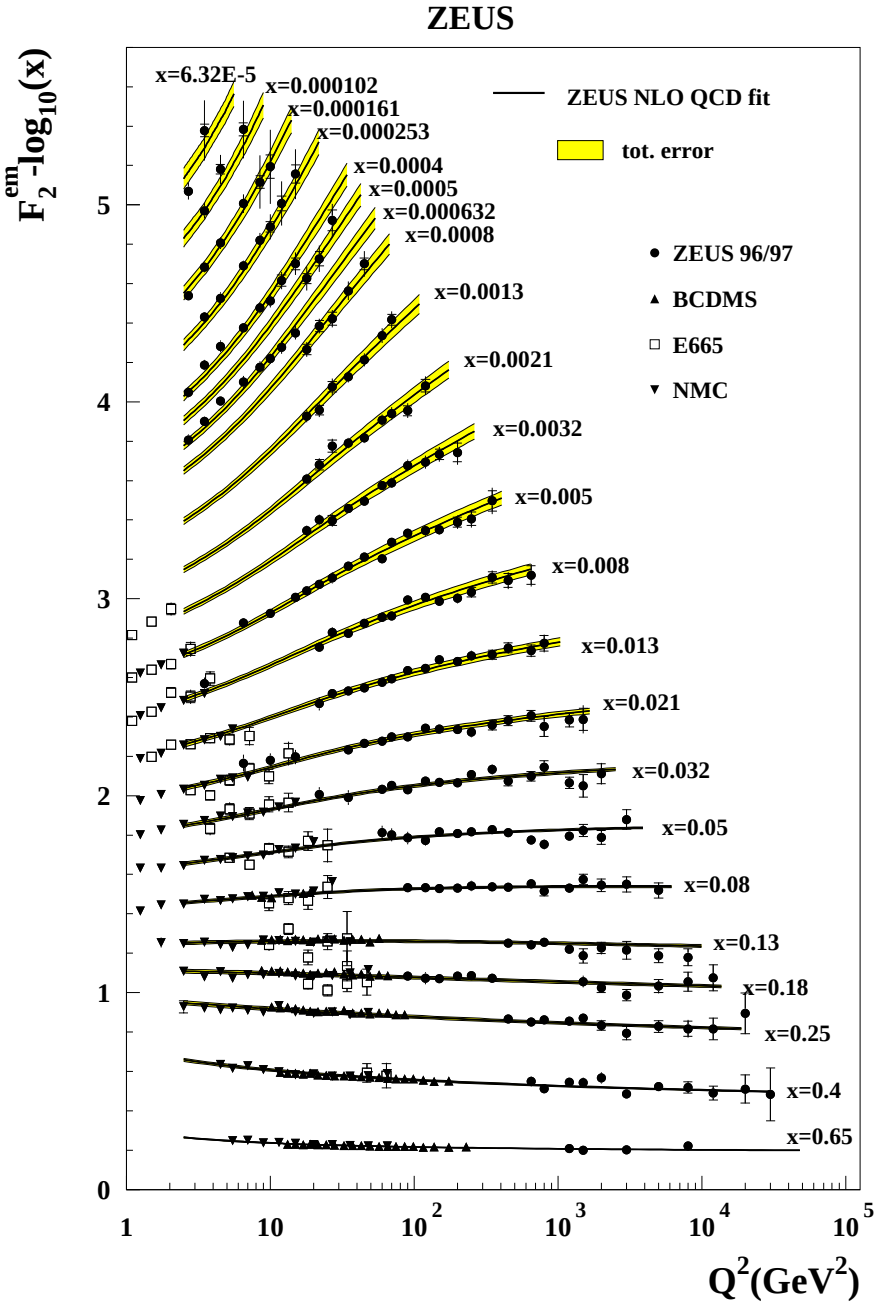

Figure 1.1: A Next-to-Leading-Order pQCD fit describes ZEUS and proton fixed–target F_2 data very well over a broad kinematic range. Figure taken from [5].

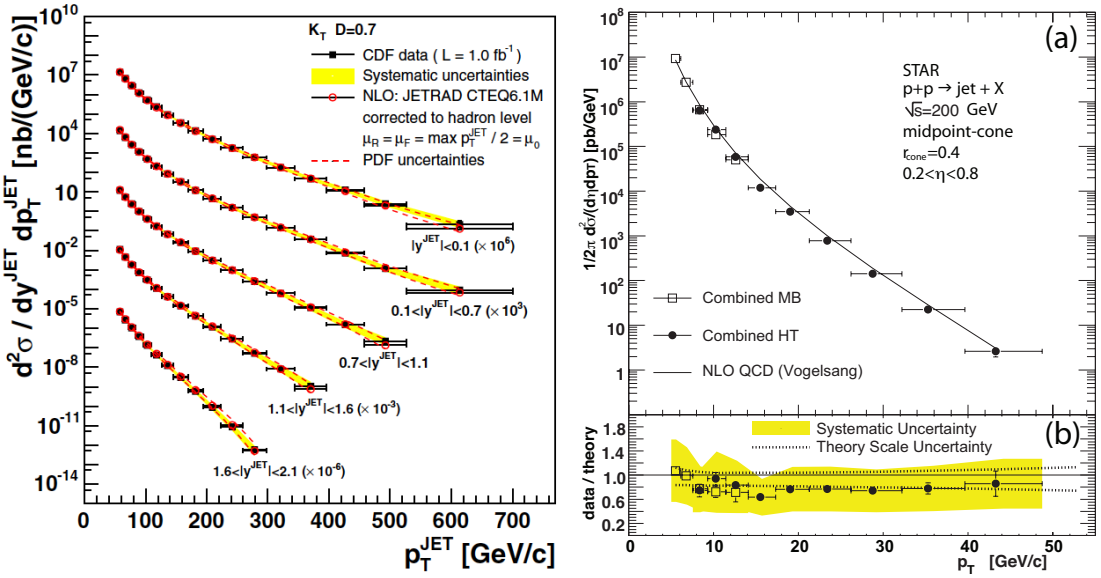

Figure 1.2: Next-to-Leading-Order pQCD calculations compared with jet spectra in p+$p$collisions at $\sqrt{s}$ = 1.96TeV (left plot, taken from [6]) and 200GeV (right plot, taken from [7])

of strong interactions where some quantitative calculations, including pQCD, are possible. Lattice QCD (LQCD), the principle tool for quantitative QCD calculations at non-perturbative regimes, has been extensively used to study hadron masses. QGP provides new dimensions for LQCD to develop further and build more benchmarks. In addition, it is possible to explore the basic properties and structures of the QCD vacuum, *e.g.* LQCD suggests that spontaneously broken chiral symmetry could be restored in the QGP phase transition [10].

As *the* state for matter at extremely high temperature and/or high baryon density, the importance of the QGP extends beyond particle and nuclear physics. A QGP phase with baryon density vastly above normal nuclear density, corresponding to the bottom right corner of Figure 1.3, may exist in neutron stars. A QGP phase with extremely high temperature, expected to be at the left top corner of Figure 1.3, may exist in the early universe one microsecond after the Big Bang [11, 12, 13, 14, 15]. The study of QGP also has a significant impact on our understanding of the universe.

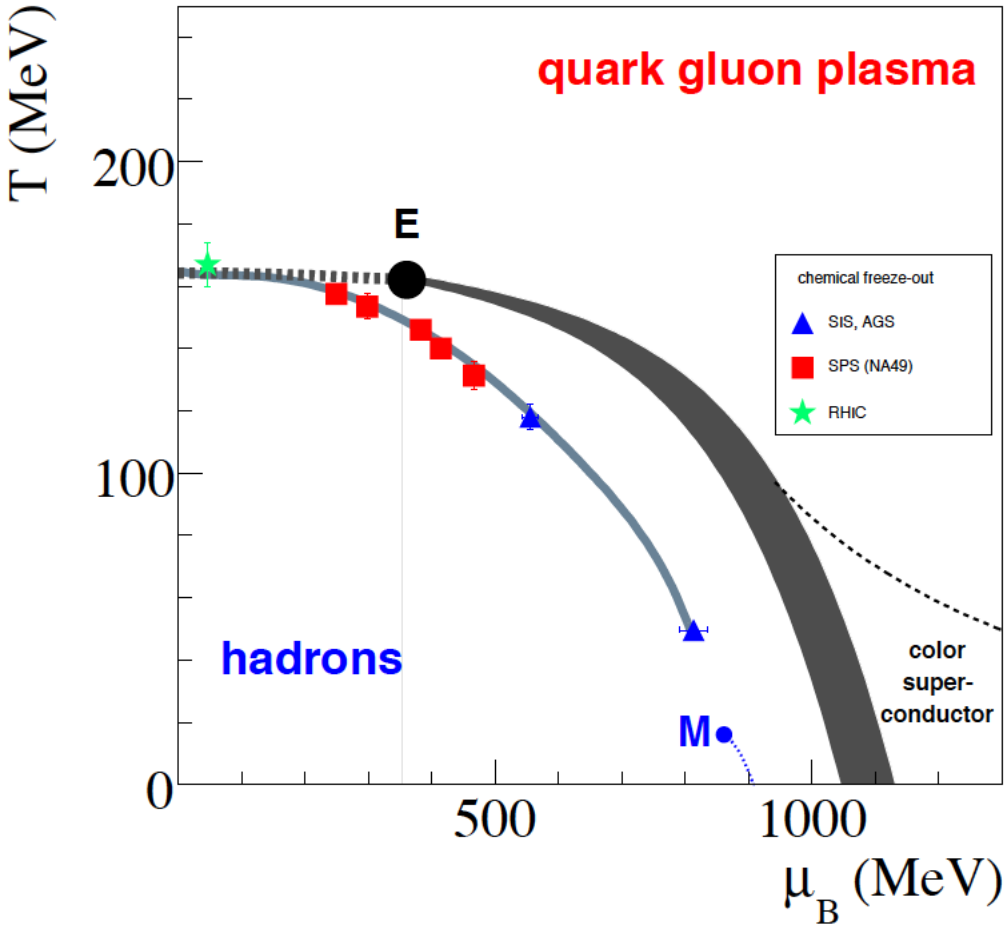

Figure 1.3: Theoretical expectations of the QCD phase diagram. The markers (blue triangles, red squares, and green stars) roughly indicate the range accessible via heavy ion colliders, including Heavy Ion Synchrotron(SIS) at Helmholtzzentrum für Schwerionenforschung(GSI), Alternating Gradient Synchrotron(AGS) at Brookhaven National Laboratory (BNL), the Super Proton Synchrotron(SPS) at European Organization for Nuclear Research (CERN) and Relativistic Heavy Ion Collider (RHIC) at BNL. Figure taken from [9].

A sufficiently high temperature is the key to creating this new form of matter in colliders. Following a more complete calculation in chapter one of [16], one can use a simplified picture to roughly obtain the magnitude of the temperature for the phase transition, if any, between QGP and hadronic matter. The MIT bag model of hadrons [17] says there is an external negative pressure present in a system with parton degrees of freedom, such as in QGP. The bag pressure B is determined to be around $(150MeV)^4$ [18]. As the QGP cooling down to lower temperature, a transition into hadronic matter takes places, which has smaller number of degrees of freedom but no bag pressure any more. In the approximation of non-interacting and massless particles, the (Stefan-Boltzmann) pressure is $P_{SB} \propto \ g\ T^4$, where g is number of degrees of freedom. In the transition stage, it is reasonable to assume the two systems have the same pressure, so $g_{QGP}\ \times T_c^4 - B = g_{had} \times T_c^4$, where T_c means the critical temperature at the phase transition. Thus, the transition temperature depends on the bag pressure and weakly on the relative change of number of degrees of freedom, as a result of it being related to T^4. Since the relative change of number of degrees of freedom is not orders of magnitude away from 1, the transition temperature is roughly on the order of $B^{1/4}$, *i.e.* on the order of 100 MeV. Indeed, recent LQCD calculation suggests that this transition temperature is around 160 MeV for zero chemical potential, as shown in Figure 1.4 [10, 14], where the active number of degrees of freedom, indicated by p/T^4, rapidly increases. The emerging new degrees of freedom indicate a new form of matter is created, and we know that it is with partonic level degrees of freedom in LQCD.

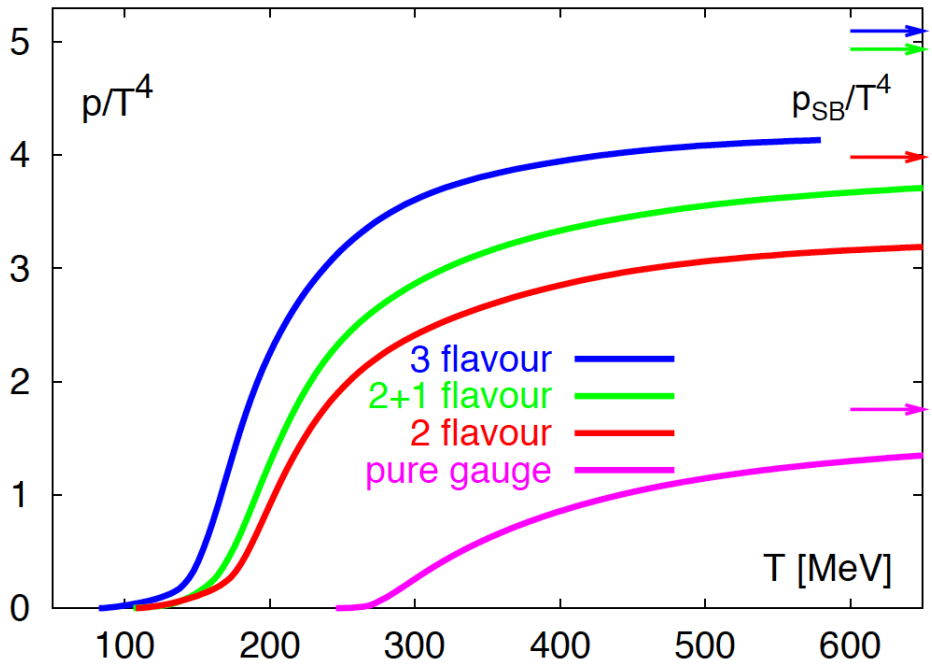

Figure 1.4: A LQCD calculations of pressure as a function of temperature for different treatments of partons. The rapid change in pressure is in response to the change in the active number of degrees of freedom. Figure taken from [10].

1.3 The experimental probes of QGP

1.3.1 A little history

The idea of creating the QGP in a laboratory by colliding heavy ions was discussed almost concurrently with the theories. For example, in 1974, T. D. Lee and G. C. Wick proposed that "one may produce the abnormal nuclear state by increasing the nuclear density through, say, high-energy collisions between very heavy nuclei." [19]. For more examples, see [20]. For decades, vast experimental efforts have been made to search and study the QGP with heavy ion collisions at a succession of facilities with increasing energy.

The most pioneering work began in the late 1970's and early 1980's on the Bevalac accelerator at Lawrence Berkeley National Laboratory(LBNL). With top bombarding energy of ≤ 2.1GeV, a milestone phenomenon called "collective flow" was discovered, indicating nuclear matter can indeed be compressed in nuclear collisions [21]. Experimental programs continue at the Heavy Ion Synchrotron(SIS) at Helmholtzzentrum für Schwerionenforschung(GSI), Alternating Gradient Synchrotron(AGS) at Brookhaven National Laboratory (BNL) and the Super Proton Synchrotron(SPS) at European Organization for Nuclear Research (CERN) at $\sqrt{s}$ around a few GeV. Nowadays, the Relativistic Heavy Ion Collider (RHIC) at BNL can provide heavy ion collisions at a broad range of $\sqrt{s}$ from several GeV up to 200 GeV and the Large Hadron Collider at CERN holds the highest energy record of 2.76 TeV.

1.3.2 The stages of high energy heavy ion collisions at RHIC

When approaching each other at an energy of 100 GeV per nucleon, the two colliding Au ions are Lorenz-contracted into two disks with high density and in the overlapping region a fireball is created in the collision. The dimension and the

energy density of the fireball vary with the impact parameter, directly related to the centrality of the collision. The centrality reflects the integrated percentile of geometrical cross section of heavy ion collisions, for example the $0 \sim 5\%$ centrality contains the most central collisions corresponding to the top 5% geometrical cross section with the smallest impact parameters. The most peripheral collisions are similar to an incoherent sum of a few p+p collisions, where no QGP is expected. In central and semi-central collisions, the energy density is high enough and the fireball soon reaches a (locally) thermalized equilibrium state with relevant parton-level degrees of freedom at very high temperature. This hot and dense medium at RHIC has features consistent with the state of QGP, as shown in Figure 1.5. This QGP medium expands rapidly with falling energy density until the temperature decreases to the critical temperature T_c when the medium evolves into a mixed phase where partonic and hadronic matter may coexist. At the chemical freeze-out boundary, hadronization takes place and the hadron species are fixed, with temperature T_{ch}. The final hadrons interact with each other kinematically in a non-equilibrium hadron gas state, and the interactions cease at the kinematic freeze-out boundary with temperature T_{ki} (or T_{fo} as in Figure 1.5).

1.3.3 Particle production

One important feature of particle production in Au+Au collisions at RHIC is that different transverse momentum (p_T) regions may come from different production mechanisms. The bulk of the particles falls into the so called soft sector, with approximately $p_T < 2\ GeV/c$, and they are dominated by thermal production from the QGP medium. The hard sector is the high p_T particles (approximately $p_T > 6\ GeV/c$) sitting in the perturbative domain, which are mainly produced in jet fragmentation. At p_T between 2 GeV/c and 6 GeV/c, coalescence comes into play.

In the soft sector, the particle production exhibits features of thermal statistics

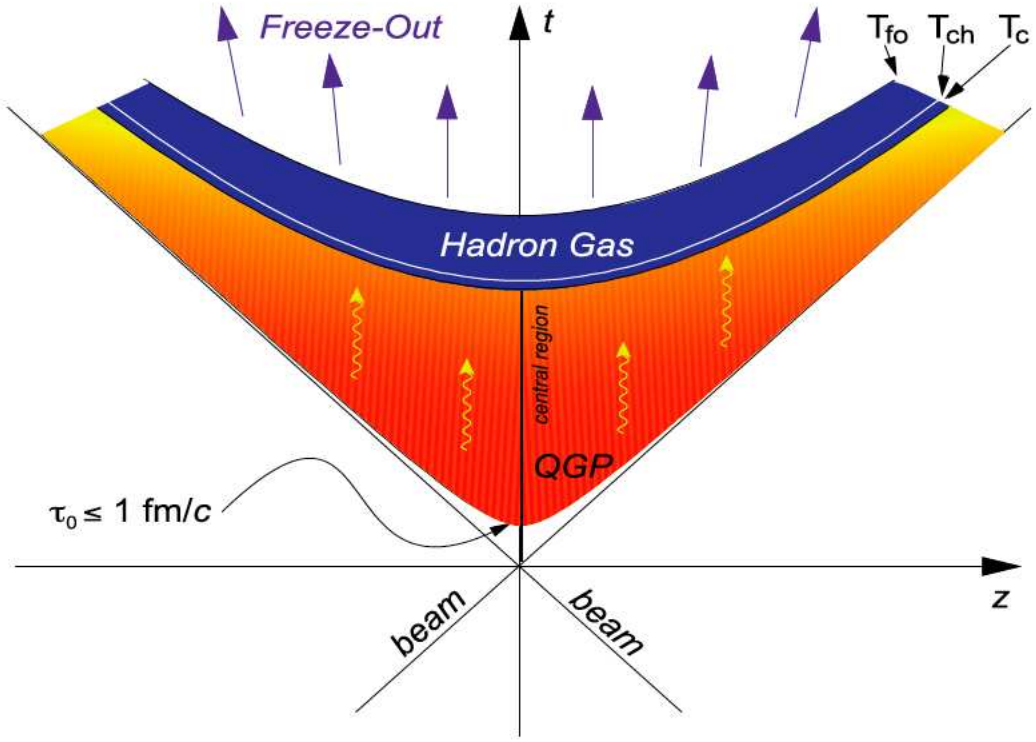

Figure 1.5: A schematic view of the time evolution of the QGP. Figure taken from [9].

and the differential particle spectra at middle rapidity can generally be described by hydrodynamics. Firstly, the production yield for different hadron species, especially the comparison between non-strange and strange hadrons, is consistent with thermal statistical production. Figure 1.6 shows a recent thermal statistical model being able to describe the production yield of various particles [22] in Au+Au collisions, including strange particles.

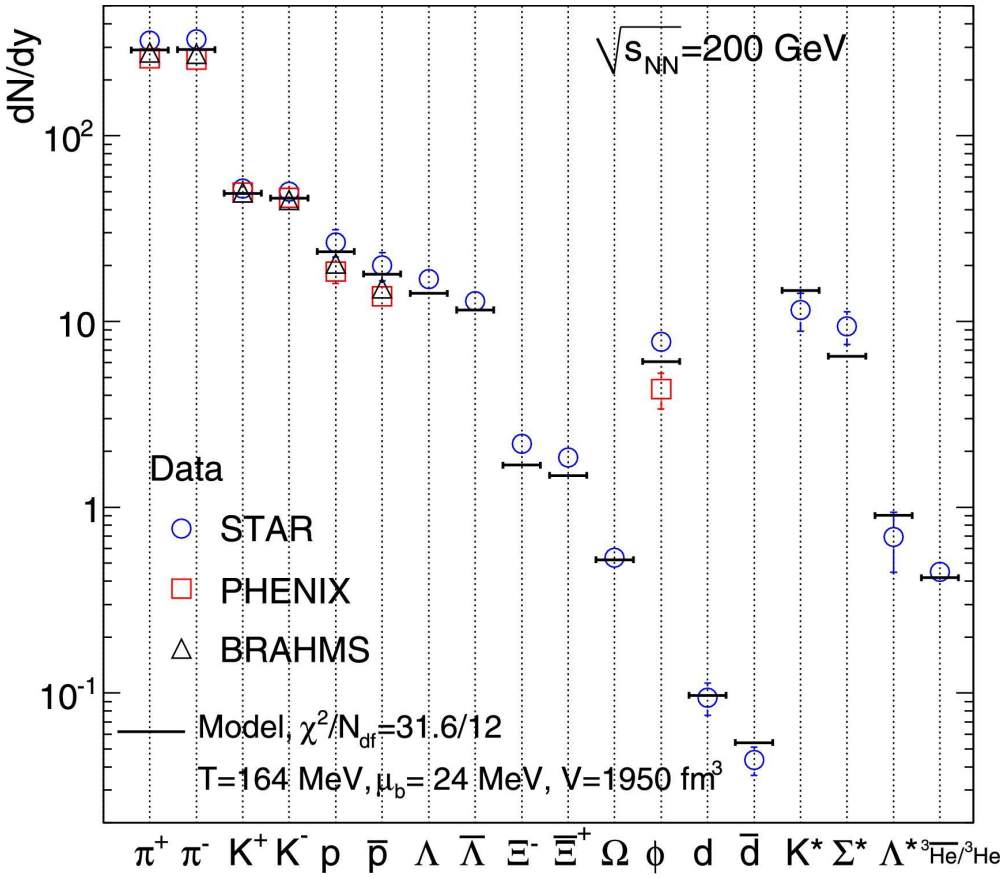

Figure 1.6: The yields of different hadrons, compared with a thermal statistical model fit of combined data. Figure taken from [22].

Secondly, the particle p_T spectra can be well reproduced by hydrodynamics calculations up to about 2GeV/c, shown in Figure 1.7 upper plot. The determination of the soft sector as $p_T < 2GeV/c$ is partially based on the spectra comparisons, and partially based on the elliptic flow measurements to be discussed later. A clear mass ordering of mean p_T, almost following a straight line, is also observed

in the lower plot, which is a characteristic result of hydrodynamic expansion. In a hydrodynamical system, particles behave collectively forming an universal velocity field for different particles, resulting that particles with higher mass obtain larger momentum. The hydrodynamic calculations shown in Figure 1.7 is a hybrid combining three-dimensional hydrodynamics for the equilibrium QGP stage of the medium and a transport approach for the non-equilibrium hadronic stage. Such a combination produces a better agreement with data over hydrodynamics alone [24].

1.3.4 Elliptic flow

In most heavy ion collisions, the overlapping area of two near-spherical ions is an ellipsoid shape with a finite eccentricity, like an almond. With a constant pressure at the boundary of this almond-shaped fireball, the pressure gradient along the minor axis of the fireball is higher than that along the major axis. This asymmetric pressure field boosts the particles flying outwards asymmetrically, exhibiting more push by the higher pressure gradient along the minor axis, leading to an azimuthal anisotropy in momentum space. At the same time, the original eccentricity of the fireball is diminishing due to the fact that the expansion is more rapid along the minor axis. In other words, this is a self-quenching process. Therefore, the final azimuthal anisotropy in the collective motion of the bulk particles is very sensitive to the early time evolution of the fireball and provides a valuable tool to probe the Equation of State (EoS) of the fireball. Fourier decomposition has often been applied to the differential particle spectra with respect to the azimuthal angle, as in Equation 1.3.1, and the second harmonic term is the most significant term representing the azimuthal anisotropy of hadrons in momentum space, and the coefficient v_2 is called the elliptic flow [25].

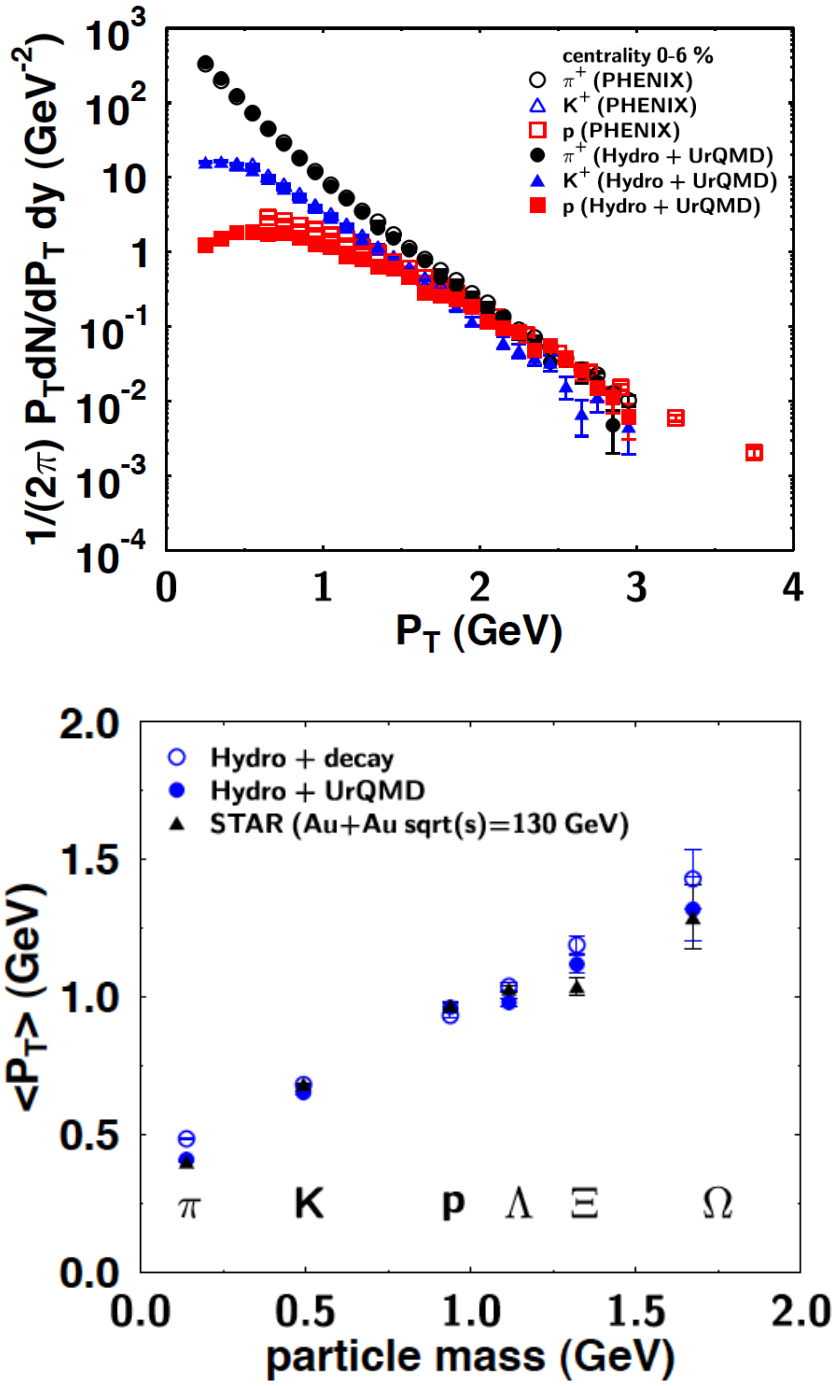

Figure 1.7: Upper Plot: The transverse momentum p_T spectra for π, K and p measured by PHENIX [23], compared with a hydrodynamics calculation [24]. Lower Plot: The mass ordering of mean p_T. Both figures are taken from [24].

$$E\frac{d^3N}{d\vec{p}^{\,3}} = \frac{1}{2\pi}\,\frac{d^2N}{p_t dp_t dy}\,\{1 + \sum_{n=1}^{\infty} 2v_n \cos[n(\phi - \Psi_r)]\} \tag{1.3.1}$$

In principle, the azimuthal angle should be written with respect to the true reaction plane Ψ_r in each collision, which is defined by the beam direction and the impact parameter [14]. However, this true reaction plane can not be definitively measured, but only approximately estimated. The estimator, usually based on the angular distribution of final state particles, is referred to as the event plane Ψ_{EP} and the effects due to the finite number of final state particles can be incorporated into the event plane resolution corrections [25].

Figure 1.8 shows the elliptic flow for various hadrons [26, 27, 28] in heavy ion collisions. The large magnitude of the elliptic flows can also be observed in hydrodynamic calculations with partonic degrees of freedom, which also suggest a system with hadronic level degrees of freedom does not have enough coupling to produce the large elliptic flows. Moreover, hydrodynamics captures two main features of the measured elliptic flow. Firstly, the mass ordering is clearly present. Because a common collectivity (such as the elliptic flow) pushes particles at a common velocity, more heavier hadrons get pushed to higher p_T. As a result, heavier hadrons at higher p_T can be found to have the same elliptic flow of lighter hadrons at lower p_T. Secondly, for any specific particle type, the elliptic flow increases with increasing p_T, because particles can be boosted to higher velocities along the direction with larger pressure gradient and larger elliptic flow [29].

Since near zero mean free path is required for a system to evolve hydrodynamically, the successful application of hydrodynamics at RHIC strongly support the conclusion that the hot and dense QCD medium created at RHIC is indeed in a state of thermal equilibrium, with microscopic ingredients strongly interacting with each other. This is a major finding at RHIC since the QGP was expected to be in a gas-like state with weak couplings. Recently, the hydrodynamical cal-

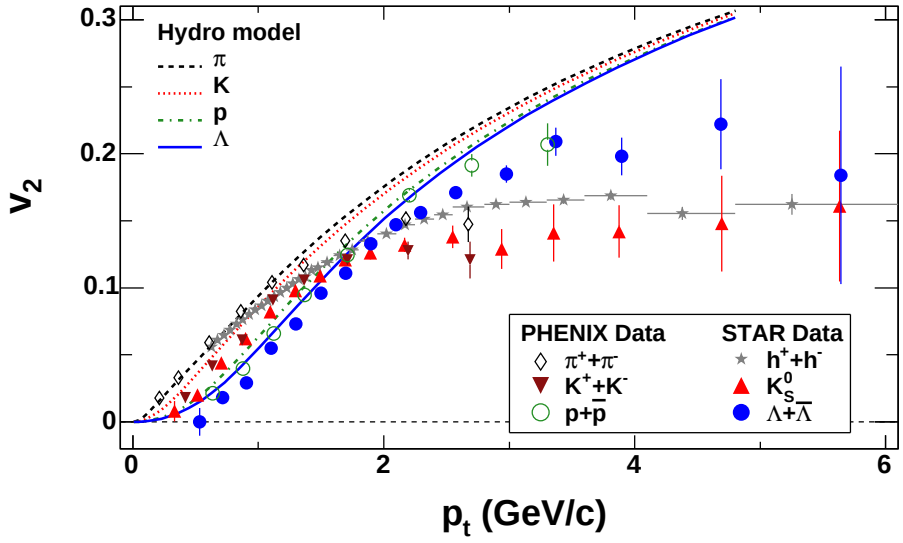

Figure 1.8: The elliptic flow of various hadrons as a function of p_T from STAR [26, 27] and PHENIX [28], compared with an early hydrodynamics calculation [30]. Figure taken from [26].

culations used at RHIC have many new developments, including 1) hybrid types with transport cascade modules implemented after hydro evolution to deal with hadronization and hadron interactions in the final state, 2) different implementations of the initial condition of the collisions, and 3) viscous hydro calculations with finite shear viscosity to entropy density ratio η/s. For a recent review, see *e.g.* [31]. One of the crucial information we learned with these recent developments is that the shear viscosity to entropy ratio η/s is so low in this hot and dense QCD medium created at RHIC that it is called a "perfect" liquid [32]. The η/s ratios that make hydro-data consistent, as shown in Figure 1.9, are always smaller than 0.16, and are in the vicinity of the KSS bound ($\frac{1}{4\pi}$) for any strongly coupled quantum liquid as predicted using the string theory [33].

At intermediate p_T approximately between $2 \sim 6$ GeV/c, experimental v_2 values deviate from hydro calculations, and they reach a saturation region, as shown in Figure 1.8. A novel phenomenal of Constituent Quark Number Scaling of v_2 was discovered experimentally. In Figure 1.10 upper plot, both v_2 and p_T of

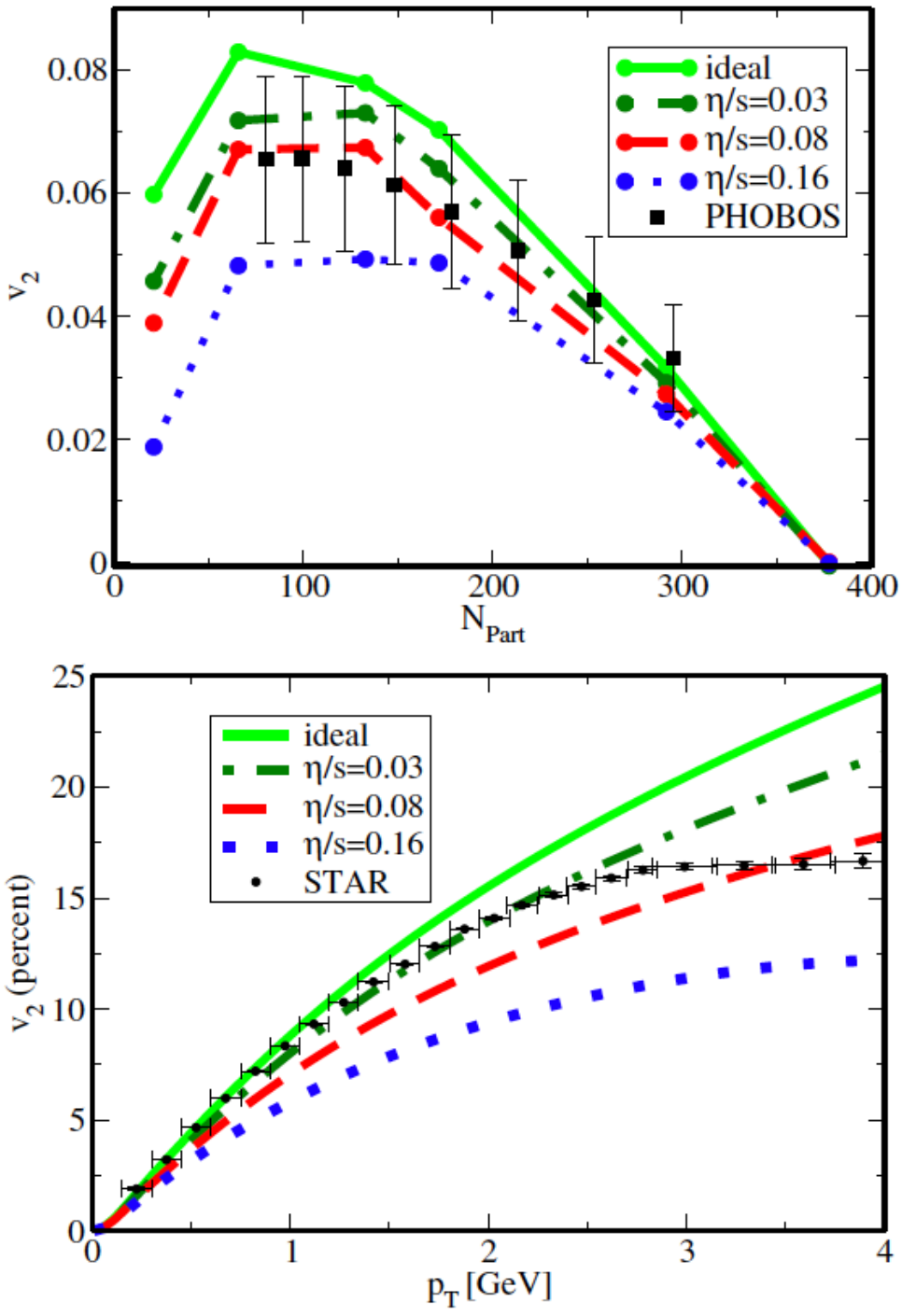

Figure 1.9: The elliptic flow at a function of Number of participant (N_{part}) and p_T measured by PHOBOS [34] and STAR [35], compared with viscous hydrodynamical calculations with various η/s ratios [36]. Figure taken from [36].

various hadron species are divided by the number of constituent quarks (n_q) in the hadrons, *i.e.* n_q=2 for mesons and 3 for baryons, and the number-of-quark scaled elliptic flows for different types of hadron converge together. The Constituent Quark Number Scaling can be readily understood as the elliptic flow of intermediate p_T hadrons come from the combination of an universal distribution for constituent quarks. This finding has become one of the most direct pieces of evidence for partonic degrees of freedom in the QCD medium. This also leads to the understanding that the main microscopic process of intermediate p_T hadron production is via quark recombination/coalescence. However, the quark recombination/coalescence is not necessarily simple $2 \rightarrow 1$ and $3 \rightarrow 1$ processes, and more realistic models are under development, for example, the Resonance Recombination Model [38]. The quark recombination/coalescence model is a microscopic view of hadronization and is compatible with thermal and hydro particle production. The Constituent Quark Number Scaling does not hold for low p_T , as shown in Figure 1.10 lower plot, where particle hadronization could still proceed through recombination processes, but the recombination could be complicated and the hadrons do not necessary follow the simple kinematic properties of the constituent quarks.

The properties of the bulk soft and intermediate particles, *i.e.* the hydrodynamic expansion and Constituent Quark Number Scaling, lead to the conclusion that the active degrees of freedom in the hot and dense medium created at RHIC is indeed partonic. Given the unexpected strong couplings among the ingredients, this new state of matter is properly named a sQGP (strongly coupled Quark Gluon Plasma) [14]. At high p_T most particles are clearly not from thermal statistical production from the medium any more, but rather from the high Q^2 scatterings at the initial stage of the collision. However, finite v_2 is still observed due to path-length dependence of energy loss in the QGP, which will be discussed in the next section.

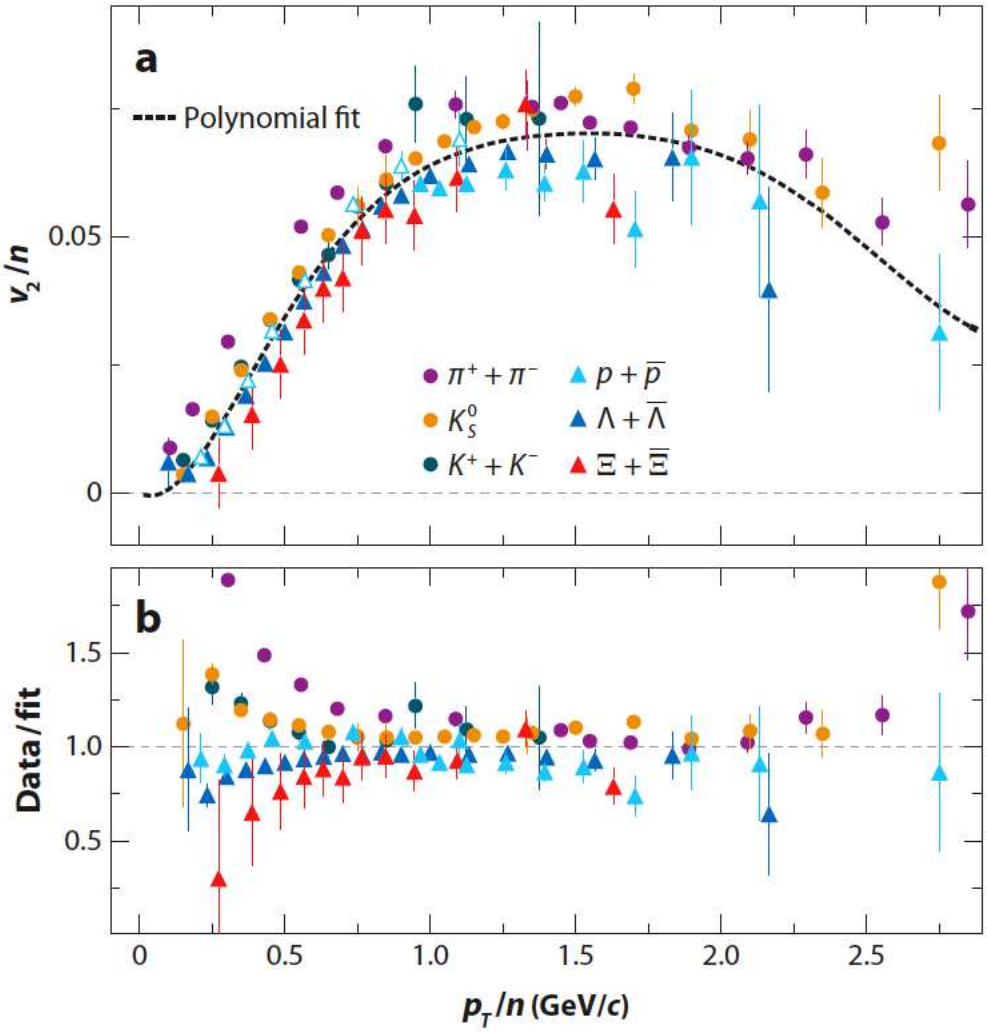

Figure 1.10: Upper Plot: The number-of-quark-scaled elliptic flow as a function of number-of-quark-scaled p_T measured at RHIC. The dotted curve is a universal fit to all hadron species. Lower Plot: The deviation of each hadron from the fitted universal distribution. Figure taken from [37].

1.3.5 Jet quenching

High energy partons traversing the hot and dense medium interact with the medium and lose energy due to QCD color charge interactions. The initial production of high energy partons per binary nucleon-nucleon collision is expected to be comparable in p+p collisions and heavy ion collisions, except for some initial state and/or other cold nuclear matter effects, which were estimated to be minor at RHIC for moderate Bjorken x, as we shall see later. If there are no interactions between high energy partons and the medium, then the final states of high p_T particles, either in terms of (the leading-particles of) jets or heavy flavor hadrons, should also be the same in p+p and in heavy ion collisions. In other words, the observed differences reflect the interactions between the high energy partons and the medium. Consequently, high energy partons are powerful hard probes to study the properties of the medium.

It is necessary to evaluate initial state effects before one separates the final state effects. First of all, the quark distribution in nuclei is known to be different from that in nucleons, and the ratio of the structure function in nuclei divided by the incoherent sum of that in nucleons $R_{F_2}^A = \frac{F_2^A}{AF_2^N}$ quantifies the difference, shown in Figure 1.11. Four regions of Bjorken x are identified separately:

- the large x region (approximately $x > 0.8$) is the Fermi motion region where the parton carries a large fraction of the nucleon momentum along with the fermi motion of the nucleons.

- approximately $0.3 < x < 0.8$ is named the EMC region where the $R_{F_2}^A$ becomes lower than unity, because it was discovered by the European Muon Collaboration [40]. For a review, see for example [41].

- approximately $0.1 < x < 0.3$ is the anti-shadowing region where $R_{F_2}^A > 1$ to compensate the suppressed $R_{F_2}^A$ elsewhere.

- the small x region (approximately $x < 0.1$) is the shadowing region where $R_{F_2}^A$ slowly decreases with diminishing x. Generally speaking, the shadowing is caused by large parton density in the region.

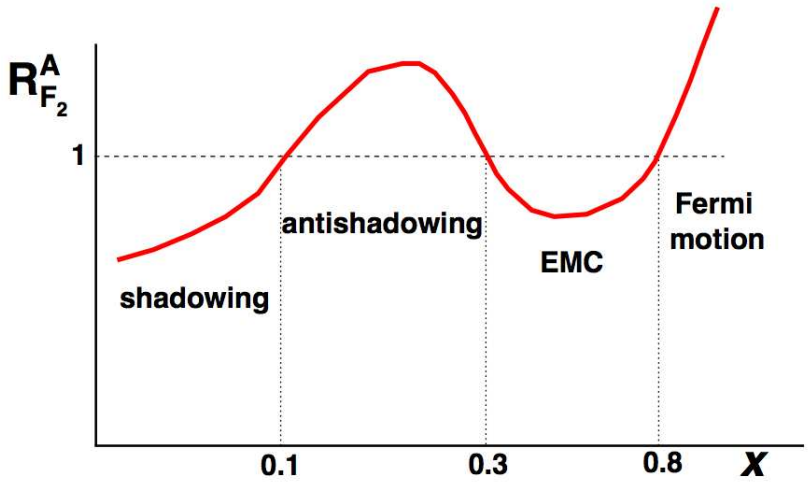

Figure 1.11: A sketch of the nuclear structure function divided by the incoherent sum up of nucleon structure functions ($R_{F_2}^A = \frac{F_2^A}{AF_2^N}$, F_2 is the structure function discussed in the previous section) as a function of Bjorken x. Figure taken from [39].

For most high p_T partons with p_T at a few to a dozen GeV in Au+Au collisions at 200 GeV, they correspond to $x \sim 0.1$, *i.e.* just entering the shadowing region, so the initial state effect can be very minor. In addition, there is another type of initial state effect, namely the Cronin effect, which can be understood dynamically as, after the initial hard parton-parton scattering, the outgoing partons have a certain chance to scatter with other parton(s) in the nuclei. The probability of such a process is very small in elementary collisions, but enhanced by the thickness of nuclei in heavy ion collisions. These effects are also known as cold nuclear effects (CNE), in contrast to the interactions with the hot dense QCD medium. Since the direct photons created in the initial scatterings do not interact with the QCD medium, they can be used to study the CNE. Also, particle production at

forward rapidity involving small x is another important tool. Nevertheless, one of the most convincing ways to understand the magnitude of the CNE is to use d+Au collisions as a reference experiment, where CNE is present in Au nuclei but the size of deuteron is too small to create a QCD medium. In Figure 1.12, high p_T hadron-hadron azimuthal correlation is measured for p+p, $d+A$ and Au+Au collisions. The hadrons are required to be at high p_T so that they are likely to be the leading particles of jets, whose parent partons are created in pairs in the initial hard scatterings. The created pair of partons move along opposite directions in the transverse plane, as a result of momentum conservation, and give rise to the correlated peak on the away side $\Delta\phi = \pi$, seen in both p+p and $d+Au$ collisions. However, in Au+Au collisions one of the partons is scattered in the QCD medium so it loses significant energy as well as the original direction, resulting in the quenching of the peak on the away side. This phenomenon is known as the jet quenching and the contrast between $d+Au$ and Au+Au indicates the final state effect dominates over any initial state effects in the measured kinematic region.

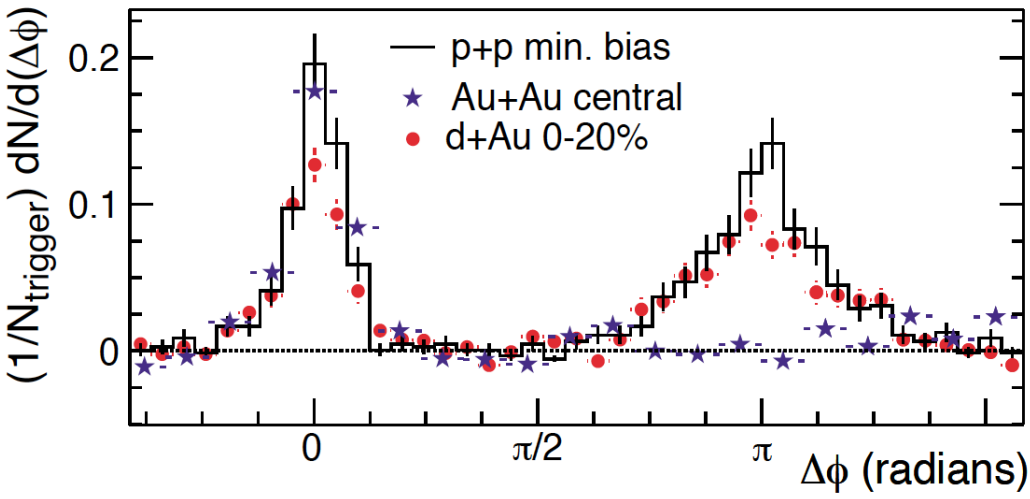

Figure 1.12: Dihadron correlations for different collision systems. The contrast between $d+Au$ and Au+Au indicates overwhelming final state effects. STAR data from [42]. Figure taken from the STAR Decadal plan.

We use the nuclear modification factor R_{AA} to quantitatively study jet quench-

ing, defined as

$$R_{AA}(p_T) = \frac{dN^2_{AA}/(dp_T dy)}{< N_{coll} > dN^2_{pp}/(dp_T dy)} \tag{1.3.2}$$

where the R_{AA} is essentially the ratio of scaled particle yields in different collisions. The p+p yield is scaled by N_{coll}, number of binary (nucleon) collisions, which is estimated via models. The most widely used model is the Glauber model [43], in which

$$N_{coll}(\vec{b}) = AB\hat{T}_{AB}(\vec{b})\sigma^{NN}_{inel} \tag{1.3.3a}$$

$$\hat{T}_{AB}(\vec{b}) = \int \hat{T}_A(\vec{s})\hat{T}_B(\vec{s}-\vec{b})d^2s \tag{1.3.3b}$$

where A and B are the mass numbers, T_A and T_B are the nuclear thickness function describing the nuclear profile and $\vec{b}$ is the impact parameter. The connection between the model calculation and experiment is can be obtained by matching the $d\sigma/db$ in the model with dN_{event}/dN_{ch} from experimental data.

As aforementioned, if heavy ion collisions are merely the incoherent sum of elementary nucleon collisions, *i.e.* if CNE and QGP are absent, R_{AA} should be unity. Experimentally R_{AA} values are found to be much smaller than one for high p_T light flavor hadrons, *i.e.* the jet quenching. Figure 1.13 summarizes the measured R_{AA} covering a very broad p_T range at various collision energies at 3 generations of accelerators. Theoretical model calculations are also presented for comparison.

Similar to the case of QED, the high energy partons lose energy in the QCD medium via i) medium induced gluon bremsstrahlung radiation and ii) elastic collisions with the constituents of the medium. The induced gluon radiation has been extensively studied in the language of pQCD by many formalisms and models. For

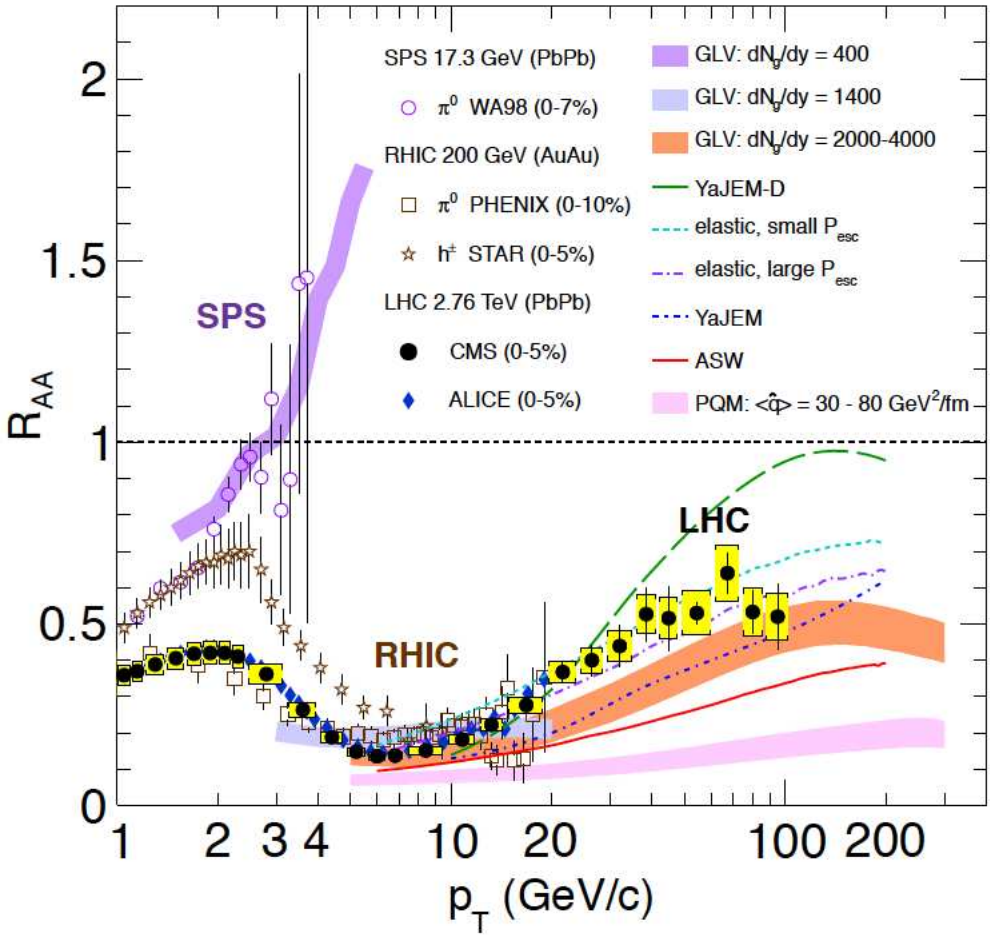

Figure 1.13: A recent summary plot of R_{AA} measured over the last decade at different facilities, compared with various theoretical calculations. See the text for more details on the theoretical calculations. Figure taken from [44].

example, Figure 1.13 shows calculations with Gyulassy-Levai-Vitev (GLV) [45, 46], Armesto-Salgado-Wiedeman (ASW) [47], YaJEM (Yet another Jet Energy-loss Model) [48] and Baier-Dokshitzer-Mueller-Peigné-Schiff (BDMPS) [49] formalisms. (BDMPS is used by the Parton-Quenching-Model [50] in the Figure). There is also the High-Twist (HT) [51] formalism, not shown here. All of them are based on pQCD calculations, sharing some common assumptions, including:

- Collinear factorization. Collinear factorization assumes that the whole process can indeed be separated into several sequential incoherent stages, such as the initial production of hard probes in the high momentum transfer scatterings, the hard probes traveling through the QCD medium and then hadronization. (Except the HT formalism, where hadronization is coupled with medium interaction and the fragmentation functions are modified by the medium.)

- The hadronization of high energy partons happens outside the medium. This is reasonable since the energetic partons are very relativistic and thus the formation time of hadrons is largely Lorenz elongated. (Except HT and certain model calculations [52] for heavy flavor quarks.)

- The medium itself is non-perturbative but the interaction between high energy partons and the medium is perturbative.

- The medium is modeled to evolve independently of the hard parton, if not entirely static.

At the core of these pQCD formalisms for gluon radiation is the quantum effect named after Landau, Pomeranchuk and Migdal (LPM) [53], which states that during the formation time of the bremsstrahlung photons/gluons, the interferences of the multiple scatterings over the path length (of the photons/gluons going through the medium) is usually destructive. This leads to a radiation rate

depending on parton path length L, and results in a characteristic quadratic path length dependence for the parton total energy loss $\Delta E \propto \hat{q}L^2$, albeit the exact dependence differs in different formalisms. The transport coefficient $\hat{q}$, defined as mean momentum transfer per path length, is a variable that quantitatively measures the property of the medium. For example, it relates to the density of scattering centers in the medium as well as the interaction mechanisms, and the extraction of the transport coefficient via model-data comparisons is one of the scientific goals of heavy ion physics.

These formalisms and models have different dynamical treatments of the QCD medium and the kinematics of the interactions. For example, while BDMPS regards the medium as multiple soft scattering centers, GLV considers few hard scatterings (current calculations consider only one hard scattering). In addition, although most models only focus on the leading partons, recent Monte Carlo simulations, such as YaJEM, study the whole shower evolution. For recent reviews and comparisons, see for example [54, 31].

These models all agree with data reasonably well, with a wide range of extracted (equivalent) $\hat{q}$ to be approximately 2$\sim$20 $(GeV)^2/fm$. The measurements of R_{AA} alone, not to mention the experimental precision on R_{AA}, do not have the necessary power to distinguish models. More differential and alternative probes are needed.

One of the promising probes to provide more constraints is the elliptic flow at high p_T. As demonstrated in Figure 1.14, the path length is different along the major and minor axes of the fireball, so the energy loss of partons traversing different axis could be different as well, resulting in different magnitude of quenching azimuthally and consequently an effective elliptic flow at high p_T. The present measurement of elliptic flow at high p_T seems to indicate the total energy loss may have a stronger than quadratic dependence on the path length, as $\Delta E \propto \hat{q}L^n, n \geq 3$ [55]. One of the explanations being put forward is that the jet

quenching is stronger in some regions of the medium with temperature near the critical temperature T_c [56].

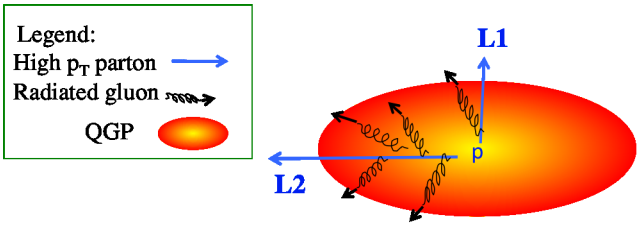

Figure 1.14: A cartoon of high energy parton traversing the QCD medium. The parton could experience different path lengths at different azimuthal angles (path length L1 is shorter than L2), demonstrating the generation of high p_T elliptic flow.

1.3.6 heavy flavor

At RHIC top energy, heavy quarks (charm and bottom) are dominantly created in initial gluon fusions and the production rates can be calculated by pQCD framework [57]. Unlike the hadronic jet production where p_T is the only relevant energy scale, two relevant energy scales, the heavy quark mass m_Q and transverse momentum p_T, are present in the heavy flavor production. Therefore, re-summation of the logarithmic terms $\log(p_T/m_Q)$ improves the calculation [58]. One calculation with such re-summation implemented is the Fixed-Order plus Next-to-Leading-Logarithm (FONLL) calculation in [59].

When heavy quarks traverse the QCD medium they also interact with medium. Theoretically we do expect the magnitudes, and even the mechanisms, to be different from that of light partons, at least in two aspects:

- Firstly, there is a hierarchy for radiation energy loss, *i.e.* $\Delta E(g) > \Delta E(q) > \Delta E(c) > \Delta E(b)$, where the first inequality is caused by the color-factor (Casimir) of gluons $C_A = 3$ being larger than that of quarks $C_F = 4/3$. The latter part of the inequality is due to the dead cone effect [60], in which the gluon radiation of heavy quarks is largely suppressed within the forward

direction as a result of reduced accelerations and decelerations of massive heavy quarks.

- Secondly, there could be a considerable contribution from the elastic collisions. This is similar to the scenario of an electron traversing through normal matter, where the rate of radiation (*i.e.* bremsstrahlung) energy loss will not surpass the collisional (*i.e.* ionization) energy loss unless the electron energy exceeds a critical energy. The collisional energy loss could be relatively large for heavy quarks at moderate to low energy.

Overall, dynamical models predicted, at most, a moderate suppression for heavy quarks, which contradicts the experimental discoveries shown in Figure 1.15 and Figure 1.16. Experimentally, we found the heavy flavor decay electrons, as proxies of heavy quarks, are suppressed as much as the light flavor hadrons, and a finite heavy flavor elliptic flow, if confirmed with more precise data, could also suggest a strong heavy flavor coupling to the medium. This unexpected contradiction is sometimes referred to as the "the heavy quark jet puzzle" and has been regarded as one of the outstanding problems in the field [64, 65].

Many theoretical attempts have been made to attack it from various aspects, *e.g.* [66, 67, 52], including efforts from the string theory via the gauge-string duality , the so called AdS/CFT correspondence(anti de Sitter/conformal field theory correspondence) [68, 69]. For a recent review, see for example [70, 71]. In a brief summary, the early model calculations can match data only if the heavy flavor electrons are exclusively from charm decays. However, according to both theoretical [59] and experimental studies [72], bottom quark could begin to contribute significantly at below 5GeV/c, albeit with considerable uncertainties. We will discuss the most recent theoretical developments in later chapters, after our analyses are presented.

To quantitatively understand the QGP state created at RHIC, our goal is

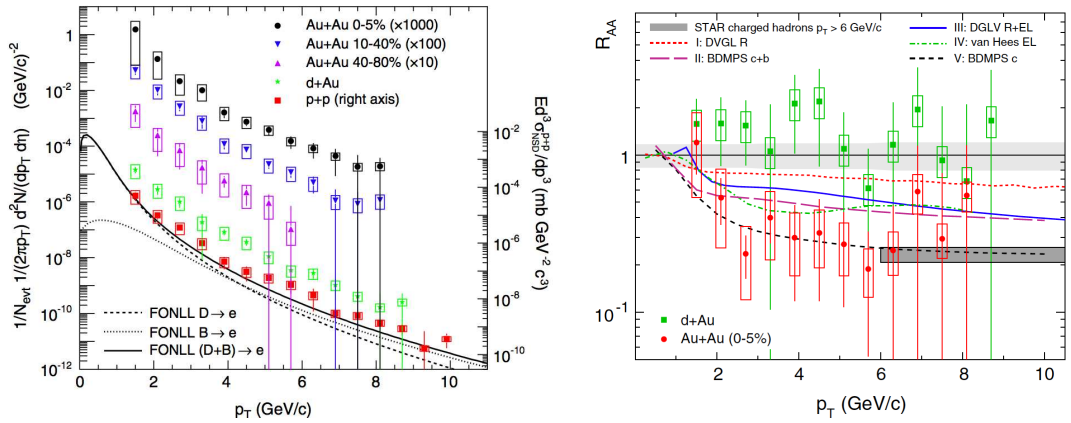

(a) Heavy flavor decay electrons spectra

(b) Heavy flavor decay electrons R_{AA}

Figure 1.15: The spectra and R_{AA} of heavy flavor decay electrons measured by STAR. Theoretical calculations are compared. DVGL is a generalization based on the GLV formalism. The van Hess calculation is an elastic collisional energy loss calculation. EL denotes additional elastic collisional energy losses are considered. See [61] and references therein. Figure taken from [61]

to improve the measurement of STAR R_{AA} and the elliptic flow of heavy flavor decay electrons from heavy ion collisions. The previous STAR data have very large uncertainties, as shown in Figure 1.15. Recently, we have improved the precision of the measurement of heavy flavor decay electron production in p+p collisions [73] with an uncertainty level of roughly 20%. The motivation of this dissertation is to make precision measurements in Au+Au collisions and initiate a comprehensive set of studies with heavy flavor decay electrons.

The heavy flavor decay electrons are also called Non-Photonic Electrons (NPE), since the biggest electron background in this analysis is photonic electrons, and we will use this name in this dissertation. For simplicity, both electrons and positrons are referred to as electrons, unless otherwise explicitly specified.

This dissertation is organized as follows. In chapter one, we will introduce the QGP and discuss the current experimental and theoretical understandings. In chapter two, we will discuss the apparatus used for this analysis, namely the RHIC accelerator and STAR detector. In chapter three, the common details

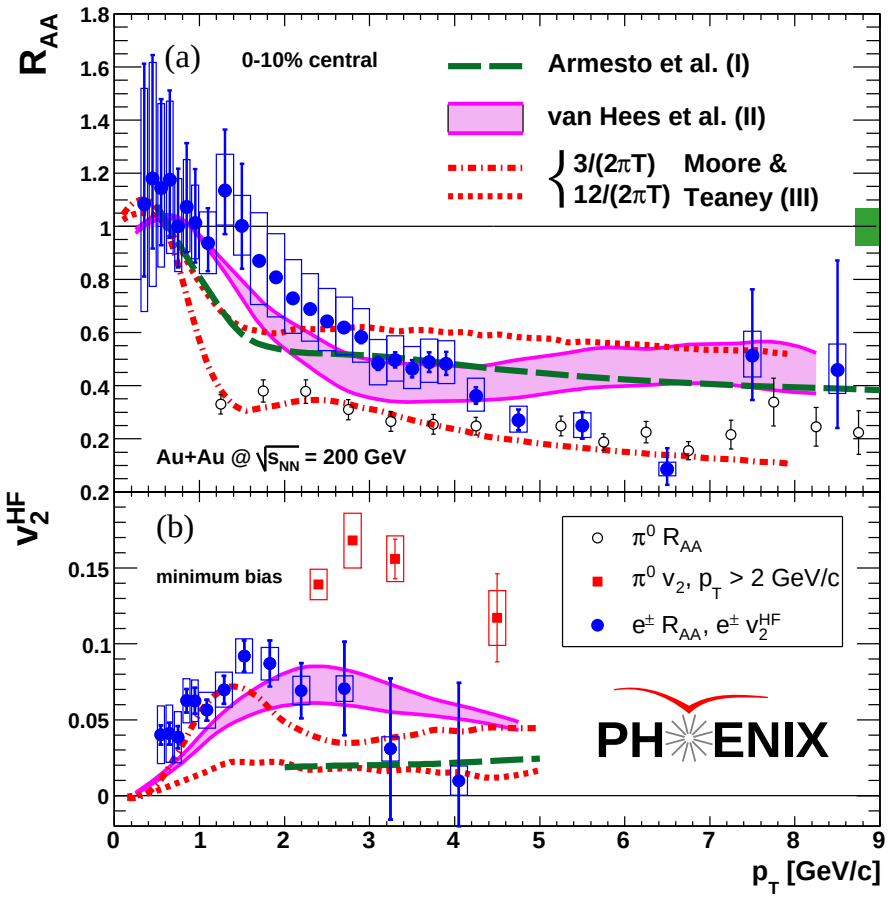

Figure 1.16: The R_{AA} and elliptic flow of heavy flavor decay electrons measured by PHENIX, figure taken from [62]. The theoretical calculation denoted as Moore & Teaney [63] considers the heavy quark energy loss as a diffusion problem. See [62] and references therein.

of all NPE analyses will be discussed and the results of NPE p_T spectrum will be presented. In chapter four, we will outline additional/specific steps for NPE azimuthal anisotropy and NPE-hadron azimuthal correlation analyses and the results will be shown. The comparisons to model calculations are discussed immediately after each measurement. In chapter five, we will discuss the measurement of the bottom quark production cross-section in $p+p$ collisions. Finally, in chapter six, well will conclude this dissertation and discuss the outlook.

CHAPTER 2

Experimental set-ups

2.1 Relativistic Heavy Ion Collider

The Relativistic Heavy Ion Collider (RHIC) complex at Brookhaven National Laboratory is a national QCD facility designed to accelerate heavy and light ions, *e.g.* gold ions and deuterons, as well as polarized protons to relativistic energies. The highest center-of-mass energy per nucleon-nucleon pair is 200 GeV for heavy ion collisions and 500 GeV for p+p collisions. It is, so far, the only collider that can collide polarized protons. It can also provide collisions at a wide range of energies, reaching as low as a several GeV, with any nucleus species from protons to uranium.

The RHIC complex is composed of several subsystems, including the main RHIC ring, the Alternating Gradient Synchrotron (AGS) and other components. A schematic drawing of this complex is shown in Figure 2.1. The main RHIC rings utilize super-conducting magnets to provide strong magnetic fields, and the focusing is stronger than needed for a proton collider in order to accommodate the stronger Coulomb repulsion among the heavy ions. The main RHIC rings are composed of two identical, quasi-circular, 2.4 mile rings, and they intersect at six locations [74]. The STAR experiment is located at 6 o'clock, and the PHENIX experiment is located at 8 o'clock. The PHOBOS and BRAHMS experiments used to be located at 10 and 2 o'clock, respectively.

The ions are accelerated step-by-step and we will mainly discuss gold ions

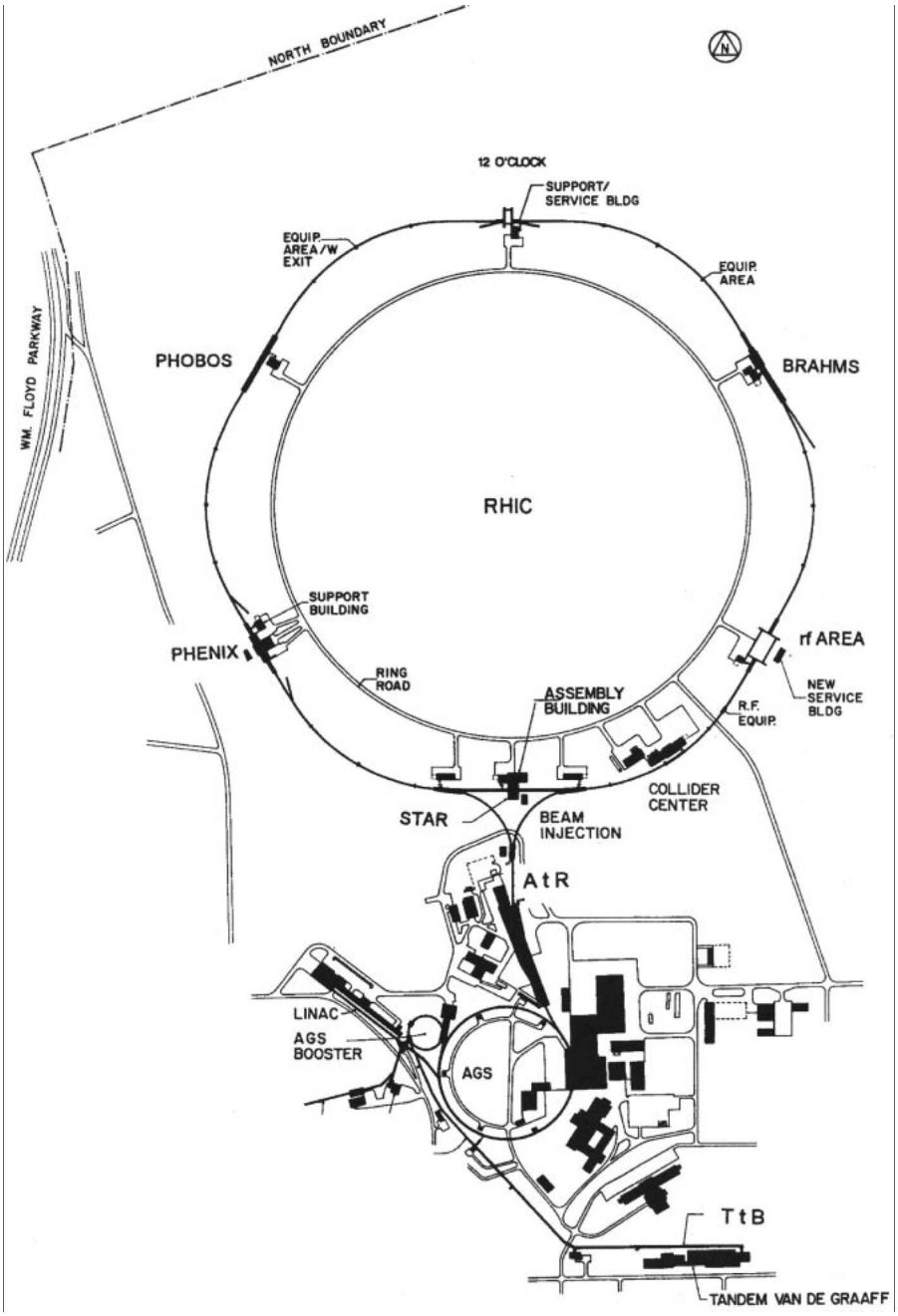

Figure 2.1: A schematic drawing of the RHIC complex. Figure taken from [74].

here. Step 1: After being produced by the ion sources, the heavy and light ions are sent into the Tandem Van De Graaff accelerator, whereas the protons are sent into the 200 MeV linear accelerator (LINAC). Both the Tandem Van De Graaff accelerator and the LINAC use an electric potential to accelerate charged particles. For example, in the Tandem Van De Graaff accelerator, 32 electrons are stripped off a gold atom, and the 32+ charged gold ions will be accelerated to about 1 MeV per nucleon. There are two Tandem Van De Graaff accelerators at RHIC, and they can both be used at the same time in order to achieve collisions between different nucleus species, such as deuterium + gold (d+Au) collisions. From year 2012, a new beam injector, the Electron Beam Ion Source(EBIS), along with two small linear accelerators, will replace the Tandem Van De Graaff accelerators. They will enable easier operation and maintenance, and the acceleration of more nucleus species, including uranium, will be achievable [32].

Step 2: After Step 1, the ions from the Tandem Van De Graaff accelerator enter the Booster Synchrotron (the AGS-Booster in Figure 2.1). A synchrotron is a circular accelerator with the accelerating voltage adjusted to synchronize with the circulation period of the particles being accelerated [32].

Step 3: The gold ions then enter the AGS, which is well known for its three Nobel-Prize-discoveries, the J/Ψ particle (1976), CP violation in kaon decay (1980) and the muon neutrino (1988). This synchrotron is named with "Alternating Gradient" since the field gradients of the focusing magnets are successively alternated in orthogonal directions [32]. While the effect for each magnet is focusing in one direction and defocusing in another direction at one time, the overall effect is focusing in both directions. The gold ions leave AGS with energy around 10 GeV per nucleon, and are stripped to a 77+ charge state [75].

Step 4: The gold ions then enter the AGS to RHIC transfer line (AtR), and a foil at the beginning of this line strips off the last two electrons from the gold ions. Then the ions begin their final acceleration and storage in the main RHIC

rings. The two beams can be accelerated, or even deaccelerated, to various final collision energies, and can be stored for up to 10 hours.

Since year 2010, the RHIC accelerator has been successfully increasing its luminosity. From year 2012, stochastic cooling will be fully applied in RHIC rings and a dramatic improvement on the luminosity is expected [32].

2.2 STAR detector system

2.2.1 Overview

The Solenoidal Tracker at RHIC (STAR) [76] is made of several sub-detectors covering a large solid angle. As the name suggests, at the heart of STAR is the cylindrical-shaped Time Projection Chamber (TPC), which provides particle tracking and particle identification (PID) via track ionization energy loss [77]. The beam crossing point is at the center of the TPC and we label the beam direction as the Z direction. Since Run08, the TPC has been the innermost tracking device at STAR. Between the TPC and the beam pipe, there used to be a Silicon Vertex Tracker (SVT) and a Silicon Strip Detector (SSD), which have been decommissioned for the ongoing Heavy Flavor Tracker (HFT) upgrade. Surrounding the TPC, the Time-of-Flight Detector (TOF) [78] was completed in 2010, extending STAR PID ability to above 1 GeV/c [79]. Outside the TOF is the STAR calorimeter system, made of the Barrel ElectroMagnetic Calorimeter (BEMC) and the Barrel Shower Maximum Detector (BSMD) [80]. There is an End-cap ElectroMagnetic Calorimeter (EEMC) in one side of STAR covering pseudo-rapidity range $1.086 \leq \eta \leq 2.00$ and 2π in azimuthal angle[81]. Outside the BEMC is the STAR magnet coils and Iron York, which provides a magnetic field along the beam line with ± 0.25 T and ± 0.5 T [82]. The outermost cylindrical layer is the Muon Telescope Detector (MTD) [83], to be completed in 2014.
STAR also has several other sub-detectors for various purposes, including beam

monitoring and triggering. A pair of scintillator detectors, called the Beam−Beam Counters (BBC), are located at high pseudo-rapidity positions at either side 3.5 meters away from the center of STAR, monitoring event rates in p+p collisions. A pair of Zero Degree Calorimeter Detectors (ZDC) are located along the beam pipe on both sides of the collision region [84], monitoring small-angle scattering of neutral particles such as spectator neutrons from the collisions. A pair of Vertex Position Detectors (VPD) are also located very close to the beam pipe at Z= ±5.6 meters at both sides [78]. The pair of VPDs provides the start time of collisions, which is essential for particle time-of-flight measurements. All of the three detectors are fast enough to serve as trigger detectors. The Forward Meson Spectrometer (FMS), replacing its predecessor Forward Pion Detector (FPD), is located at 7.5 meters West of STAR, and it mainly detects neutral mesons such as the π^0. The Forward Pion Detector (FPD) is moved to the east of STAR. A schematic side view of the STAR detector is shown in Figure 2.2.

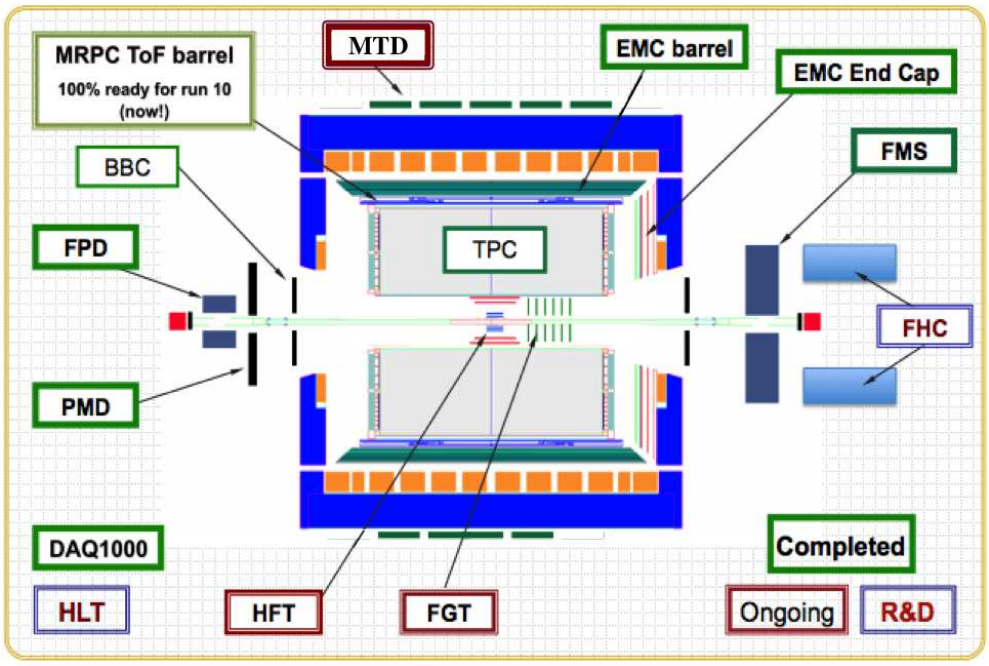

Figure 2.2: A schematic side view of STAR.

2.2.2 The Time Projection Chamber

The STAR TPC surrounds the beam pipe and the beam crossing regime, covering pseudo-rapidity range $-1.8 \leq \eta \leq 1.8$ and 2π in azimuthal angle. It has an Inner Field Cage (IFC) with a radius of 50 cm, and an Outer Field Cage (OFC) at radius 200 cm. The IFC, OFC and the end caps at both ends of the TPC seal the P10 gas (10% methane, 90% argon) inside [77]. There is a Central Membrane (CM) at the center of the TPC, dividing the TPC into two halves, each 210 cm long. See Figure 2.3 for an illustration.

The materials for the field cages were carefully selected to reduce the photonic conversions and multiple Coulomb scatterings. The material budget is 0.13% X_0 for the 40 cm insulating gas between IFC and beam pipe, 0.52% X_0 for the IFC, and 1.26% X_0 for the OFC. The P10 gas itself presents a considerable contribution of 1.17% X_0 [77].

An electric field is generated by the 28 kV negative potential applied on the CM, which serves as the Cathode. The Anode of this electric field is the end caps at ground. The field cages are segmented into a total of 182 conducting rings, biased by 2 MΩ resistors between the rings. The potentials on the rings gradually change from ground to negative 28 kV, the closer to the CM the more negative. Together, the field cages, the CM and the end caps provide a uniform electric field pointing to the center of the TPC (Z=0) from both ends of the TPC(Z=$\pm$210 cm), with a field strength of about 133 V/cm. The charged tracks ionize the P10 gas, and the electrons from ionization drift under the influence of the electric field towards both ends of the TPC. The drifting is a slow process, with a typical drifting velocity of 5.45 cm/μs, translating into a maximum of about 40 μs total drifting time.

At both ends of the TPC, there are readout systems based on Multi-Wire Proportional Chambers (MWPC) with readout pads. The system is composed of

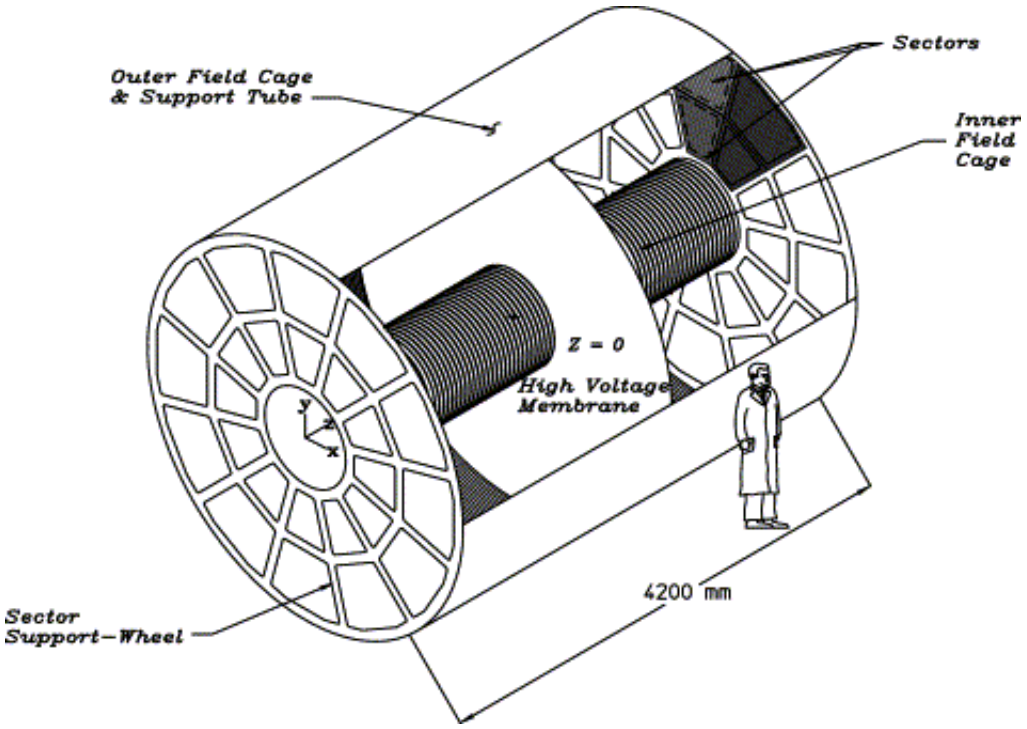

Figure 2.3: An illustration of the STAR TPC. Taken from [77]. The STAR TPC is 4.2 meters in length, along the beamline, and 4.0 meters in diameter, with IFC at radius=50 cm and OFC at radius=200 cm.

three layers of wires and one final (farthest from TPC center) layer of readout pads. The drifting electrons will first encounter the gate wire grid, which allows the drifting electrons to come through while an event is being recorded and blocks charged particles from entering the MWPC area at the rest of the time. This gate grid is also the boundary of the electric field in TPC. The next layer is a ground grid shielding the electric field inside the MWPC regime. The drifting electrons are accelerated near the third layer, the Anode grid of wires, and produce avalanches. The large amount of positive ions produced in the avalanche induce an image on the readout pads. The readout pads are arranged in concentrical rows in 12 super sectors along the ϕ direction, and each super sector is composed of one inner sector and one outer sector. The pad size is determined by the required two hit resolution for track separation. The size of induced charge distribution on the pad plane depends on electron diffusion in the gas and the separation distance between the anode and the pad plane. The inner readout pads are optimized to deal with the highest track density, so they are smaller in size and require a large amount of front end electronics. Therefore the rows of inner pads are separated from each other with space in between. The outer readout pads are optimized to measure the track energy loss by collecting more electrons, so they are bigger in size and the rows are contiguous, as shown in Figure 2.4.

The distance between the anode wire grid and the readouts are adjusted separately for the inner and outer sectors, 2 mm and 4 mm respectively, so that the induced image is always about 3-pads wide and the transverse position is measured especially by looking at the charge distributions on the two pads on the sides. The longitudinal position is measured by the drifting time (time difference between collision start and pad readout) times the drift velocity. The drift velocity is known to 0.1% due to two factors. Firstly, the operation voltage of P10 gas makes the drifting velocity stay in a stable and flat plateau of the drift velocity curve. Secondly, the STAR TPC has a laser calibration system to measure the

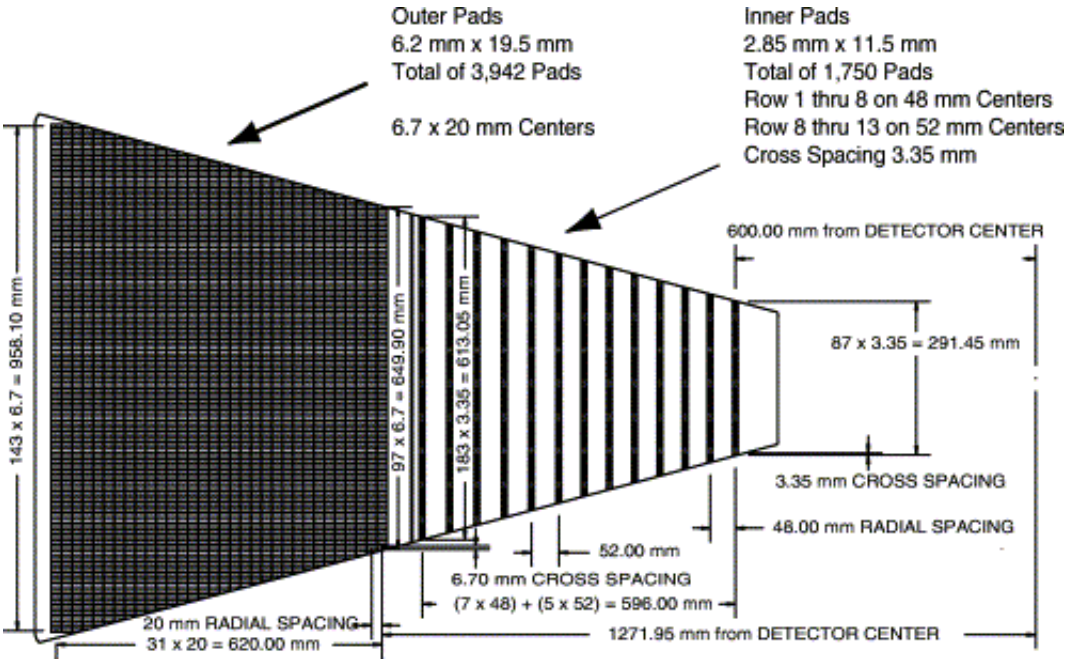

Figure 2.4: The readout pads for the MWPC for the STAR TPC. Figure taken from [77]. This is the final (farthest from the center) layer of the MWPC.

drift velocity [85]. The track hit position resolution in both direction can reach 1 mm or less. The primary vertex resolution in the transverse plane depends on the charged particle multiplicity and is found to be 350 μm for more than 1000 tracks [77].

2.2.3 Barrel ElectroMagnetic Calorimeter and Barrel Shower Maximum Detector

Covering pseudo-rapidity range $-1 \leq \eta \leq 1$ and 2π, the STAR Barrel ElectroMagnetic Calorimeter (BEMC) is in a cylindrical shape with an inner radius of 223.5 cm and an outer radius of 263 cm. It has 120 modules each covering $\Delta\eta = 1$ and $\Delta\phi = 6^\circ$ or $\sim 0.1rad$ (in other words, there are 60 BEMC modules surrounding each half of TPC, with their long sides parallel to each other and to the beam pipe). As shown in Figure 2.5, each BEMC module is a stack of 21 layers of plastic scintillators with 20 layers of lead sandwiched in between, forming

a total depth of approximately twenty radiation lengths ($20X_0$) at mid-rapidity. Each BEMC module is segmented into 40 towers each with size $\Delta\eta = 0.05$ and $\Delta\phi = 0.05$ rad, *i.e.* an array of 2(along ϕ direction)×20(along η direction) towers. For each tower, one PMT is used to read out the sum of light outputs from the 21 layers of plastic scintillators. The energy resolution is expected to be $\delta E/E \sim 14\%\sqrt{E/1\ GeV} \bigoplus 1.5\%$ [80].

The STAR Barrel Shower Maximum Detector (BSMD) is located inside the BEMC between the 5th layer of lead and 6th layer of scintillator, at a depth of approximately $5X_0$. Each BSMD module is a wire proportional counter sandwiched by two layers of strip readout, shown in Figure 2.6. Since each BSMD module is inside a BEMC module, there are also 120 BSMD modules. There are 150 strips on each of the two planes of one BSMD module. On the front plane of BSMD, *i.e.* the layer closer to the interaction region, these strips are arranged in a line along η, each with a size of $\Delta\eta = 0.0064$ ($1/150 = 0.0067$ and this translates to ~ 1.5 cm at low η) and $\Delta\phi = 0.1$ rad (~ 23 cm). The main purpose of this plane is to map out the shower profile along η with a very fine resolution, and thus it is referred to as BSMD-η. The other 150 strips on the back plane of BSMD are arranged as a $15(\phi)\times10(\eta)$ array. The granularity is $\Delta\phi = 0.1/15 = 0.00667$ rad and $\Delta\eta = 1/10 = 0.1$ rad. The very fine granularity along ϕ provides a fine measurement of shower profile along the ϕ direction and this is the BSMD-ϕ plane. High spatial resolution ($\sigma_\eta = 2.4mm + 5.6mm/\sqrt{E}$ and $\sigma_\phi = 3.2mm + 5.8mm/\sqrt{E}$) shower profiles can be obtained by combining BSMD planes [80].

2.2.4 Heavy Flavor Tracker

The STAR experiment is upgrading with a group of inner tracking detectors, collectively refereed to as the Heavy Flavor Tracker (HFT), which will be essential for heavy flavor studies in the future. The HFT is designed to facilitate the reconstruction of the displaced decay vertices of heavy flavor decays with a point-

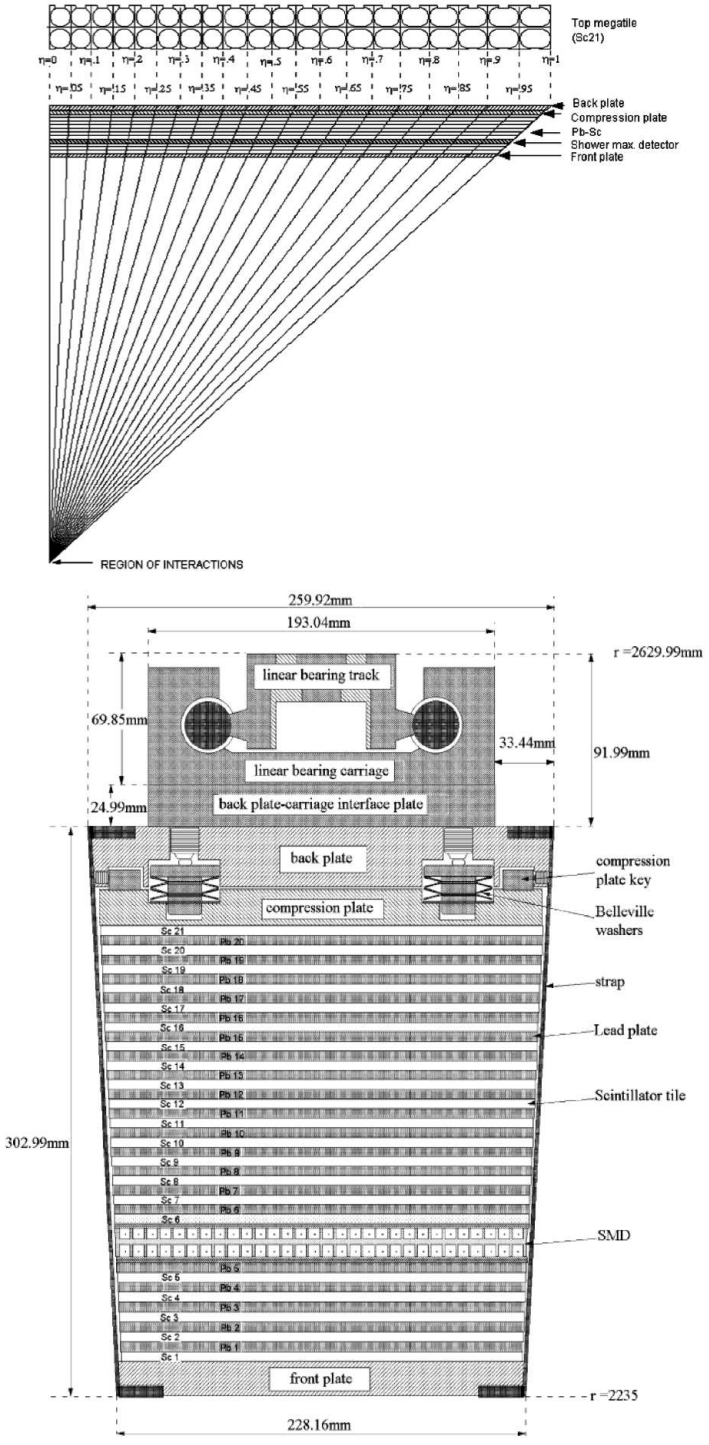

Figure 2.5: A side(end) view of a BEMC module in the upper(lower) plot. Figure taken from [80]

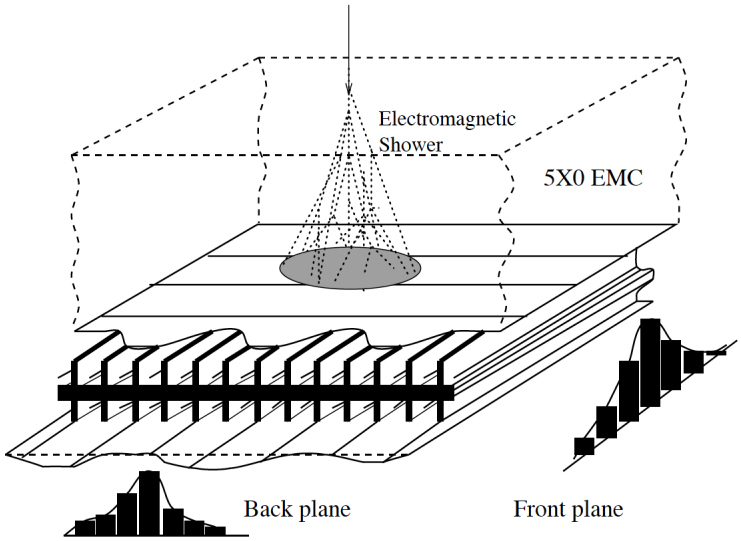

Figure 2.6: A illustration of the STAR BSMD. Figure taken from [80]

ing resolution of the order of 50 μm, so that charm and bottom hadrons can be topologically separated [86]. HFT consists of three sub-detectors at four different radius layers, as shown in Figure 2.7. Starting from the innermost, there are two layers of silicon pixel detector (PXL) at 2.5 and 8 cm radii, the Intermediate Silicon Tracker (IST) at 14 cm, and the Silicon Strip Detector(SSD) at 22 cm. The pointing resolution gradually increases from the outermost tracking detector towards the inner trackers, starting with about 1 mm for TPC pointing at the SSD and is expected to reach about 40 μm with the most inner layer PXL pointing at the displaced vertex. To reach such a good resolution, the Complementary Metal Oxide Semiconductor (CMOS) Active Pixel Sensor (APS) technology is used for the PXL, which will be a pioneering work in collider experiments [86]. An engineering run for HFT is planned for Run13 and HFT is expected to be fully completed in Run14.

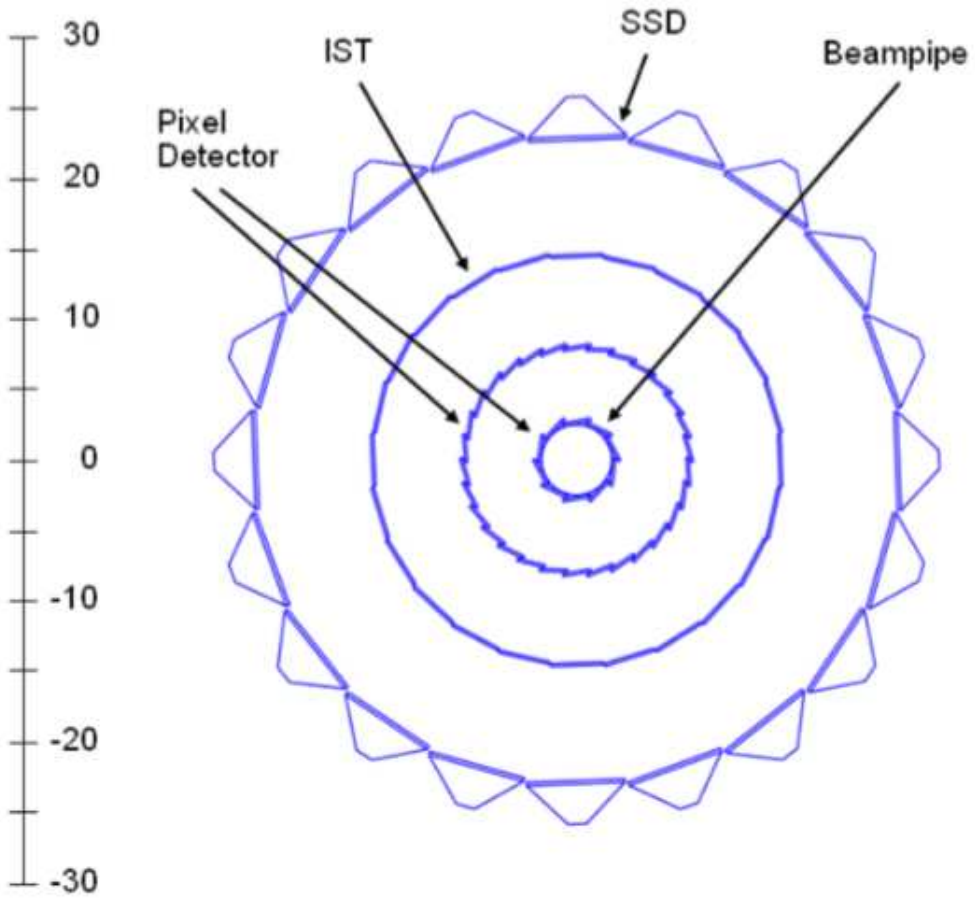

Figure 2.7: The design of the STAR HFT. Figure taken from [86]

CHAPTER 3

Analysis of Non-Photonic Electron spectrum

In this chapter, we will present the analysis of non-photonic electron (NPE) spectrum in Au+Au collisions at $\sqrt{s_{\rm NN}}$ = 200 GeV based on data taken during RHIC Run10 in 2010. The measurement of NPE spectrum in p+p collisions has been updated in a recent STAR paper [73]. Combining these two analyses, we will then calculate the nuclear modification factor R_{AA} for NPE. Most of the analysis procedures discussed here also apply to the NPE azimuthal anisotropy and correlation studies in the next chapter.

3.1 Overview of analysis procedures

The NPE analyses are essentially electron identification procedures plus statistical background subtractions. We firstly apply track quality and electron identification criteria to all reconstructed tracks to select a group of well reconstructed tracks with high electron purity, which is labeled as inclusive electrons. Within the inclusive electrons, the signal electrons are those from the semi-leptonic decays of open heavy flavor hadrons (*e.g.* $D \rightarrow Ke\nu_e$ and $B \rightarrow De\nu_e$). The main background is photonic electrons from photon conversions in the detector material and Dalitz decays of π^0 mesons. Therefore, the signal electrons are also called non-photonic electrons.

To handle the photonic electrons, every inclusive electron in each event is paired with oppositely charged partner electrons in the same event to reconstruct

their parent particles. The track quality and PID criteria for the partner track are not as rigid as those for the electron candidate in order to ensure high photonic background reconstruction efficiency. The combinatorial background can be accounted for by randomly pairing up electrons with the same charge. We then examine the properties of the electron pairs, such as the invariant masses of the reconstructed parents and the opening angles between the paired electrons, and we select photonic electron candidates based on these properties. Note that we do not tag every photonic electron in Au+Au collisions, and that the sample of opposite-sign (OS) pairs minus same-sign (SS) pairs is statistically a good representation of photonic electrons. This sample of OS minus SS pairs can be used to accurately extract not only the number but also the properties of photonic electrons, mostly just universal electron properties regardless of the origins of the electrons.

Additional electron sources, such as heavy quarkonia decays ($J/\psi \rightarrow e^- + e^+$, $\Upsilon \rightarrow e^- + e^+$), Drell-Yan processes ($q + \bar{q} \rightarrow e^- + e^+$), K_{e3} decays ($K \rightarrow \pi e \nu_e$), and light meson decays, also contribute to the inclusive electron sample, but at much lower levels.

3.2 Data sets

3.2.1 Triggers

In Run 2010, with a newly upgraded Data Acquisition (DAQ) system capable of handling event rates up to 1000 Hz (DAQ1000), the STAR detector collected about 830 Million Au+Au collisions with different trigger setups, including about 365 Million minimum bias (MinBias) Trigger events, about 255 Million Central Trigger events, and about 160 Million High Tower Trigger events, in an approximately 80-day period (Day 02 to Day 80). The MinBias trigger has been set up as the coincidence between the Vertex Position Detector (VPD) [78] and the Zero Degree

Calorimeter Detectors (ZDC) [84], aiming at triggering on most of the Au+Au collisions; the Central trigger selects the most central events (approximately 0∼10% centrality), by looking at ZDC and Time-of-Flight detector (TOF) signals; the High Tower triggers require at least one Barrel Electro-Magnetic Calorimeter (BEMC) tower passing a certain transverse energy threshold, selecting events with higher probability of having high p_T electrons than the MinBias events. In Run 2010, four different transverse energy thresholds were used for the study of NPE, providing four sets of High Tower triggers, NPE11, NPE15, NPE18, and NPE25, with the numbers indicating the actual thresholds applied to the Analog Digital Converters (ADC) readouts of the BEMC. The event rates for most triggers (MinBias, Central, NPE11, NPE15) are too large to record every event on tape, so only a certain fraction of such events are recorded, which is defined by the pre-scale factor of the trigger. Namely, one out of every pre-scale number of events is recorded.

3.2.2 Run selection

In the operation of the STAR detector, we often collect Au+Au events in groups of, say, half of a million, and we label them as one run. After each run, the DAQ system was stopped and then re-started to take the next run of data. Approximately 2400 runs were recorded for Run10 Au+Au collisions.

To reject bad runs, we firstly apply the STAR standard bad-run-list [87], which rejects:

- runs with charged track reference-multiplicity three Root-Mean-Square (RMS) away from the average over the entire Run10 Au+Au collisions,
- runs with no BEMC detector information,
- runs with 4 or more bad TPC Readout boards (RDO),

- runs with too few (less than one thousand) good MinBias events,
- runs with significant shift of primary vertex position and mean track p_T.

In Appendix A we list all the bad runs rejected in this STAR standard procedure. Secondly, we apply additional criteria to ensure better data quality. To ensure a uniform BEMC working condition over the whole Au+Au running period, we compare the number of high tower events in the NPE11 trigger with that of MinBias events. As shown in Figure 3.1, in the first 8 days of Run10, the ratio of number of events in NPE11 over number of events in MinBias is found to be higher than average, so all of those runs (covering run ID=11002000 to run ID=11009999) are rejected, along with some other outlier runs. We also require the collision positions in each run is consistent with the average, as we shall discuss later. In addition, very large pre-scale factors for the MinBias trigger were used during Day 55 to Day 65 and Day 75 to Day 80 to let some other triggers record more events. As a result, the recorded MinBias events during these days are much fewer than usual, with only about 4 million good MinBias events in total for these 15 days. These 15 days of MinBias data are skipped in the analyses, but the events of other triggers during these days are kept.

3.2.3 Event selection and centrality determination

For event selection, the only criteria for good quality we apply are on the primary collision vertex position. We require that the reconstructed vertex position based on reconstructed TPC tracks is no more than 30 cm away from the center of the STAR detector along the beam direction (the Z direction) and no more than 2 cm away along the radial direction, *i.e.* $|V_Z| < 30$ cm, $\sqrt{V_X^2 + V_Y^2} < 2$ cm where the center of the STAR detector is defined at X=0 Y=0 and Z=0. In addition, we require the reconstructed vertex based on TPC tracks and reconstructed vertex based on the Vertex Position Detector (VPD) to be consistent within 3 cm along

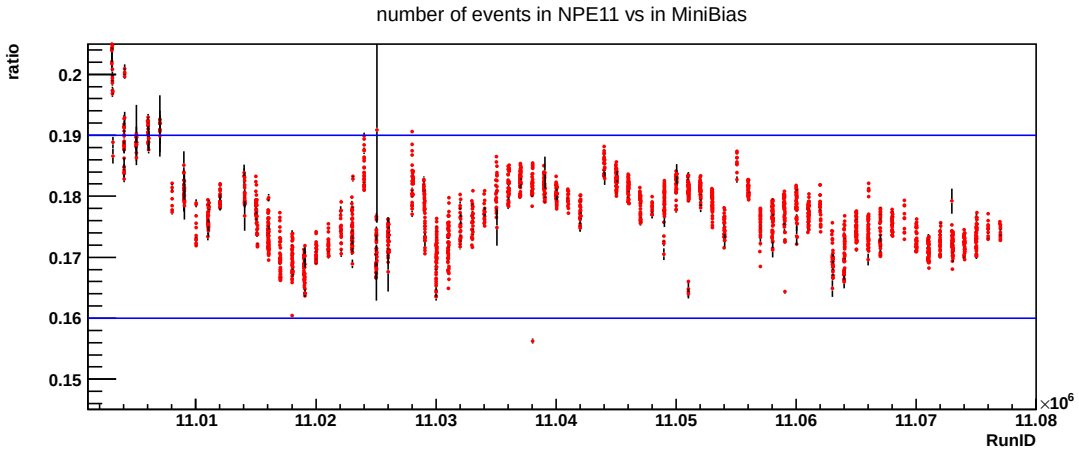

Figure 3.1: The number of actually occurred events in NPE11 trigger divided by that in MinBias trigger in each run. The horizontal lines indicate the range regarded as good runs, which is from 0.16 to 0.19. The outliers and run 1100200 to run 11009999 are rejected.

the Z direction, *i.e.* $|V_Z^{TPC} - V_Z^{VPD}| < 3$ cm. Figure 3.2 shows the distributions of reconstructed vertex positions based on TPC tracks and the difference between TPC vertex and VPD vertex. The efficiency of the $|V_Z| < 30$ cm cut is usually $80 \sim 85\%$, while the efficiency of the second cut is above 95%, and total efficiency is shown in Figure 3.3. To ensure a stable efficiency, we also reject those runs with abnormal efficiencies outside a 10% band. These requirements on the vertex positions correspond to those used in the STAR standard determination of event centrality. It is worth mentioning that the V_Z distributions depend on the centrality, and therefore the efficiencies of V_Z cuts also depend on centrality, as shown in Figure 3.4. The emphasis is that, in the calculation of number of events to be discussed below, efficiencies need to be applied centrality-by-centrality and run-by-run. After all the run selections and event selections, there are about 250 Million MinBias events and roughly 100 Million High Tower events left. The NPE18 trigger is only used for the elliptic flow and NPE-hadron correlation analyses in the next chapter. NPE25 trigger has too few events (a few Million), so it is not used at all. There are about 200 Million Central trigger events passing the run and event selection, 84 Million of which are the most central (0 to 5%) events

and are used in this analysis.

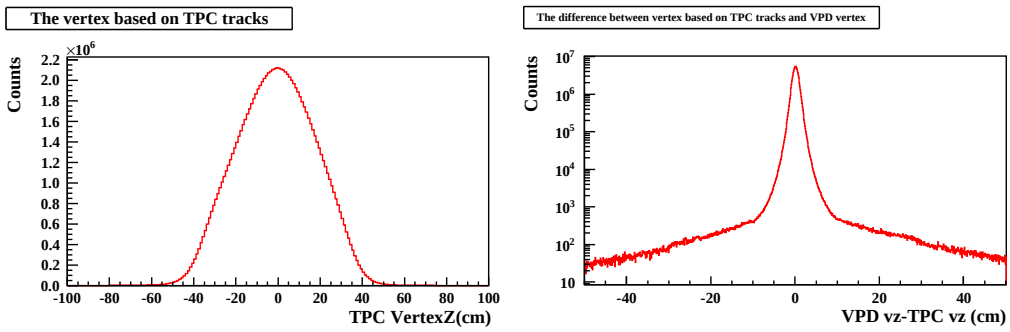

Figure 3.2: Left plot: Distribution of vertex position based on TPC tracks along the beam direction. Right plot: the difference between the TPC vertex and VPD vertex.

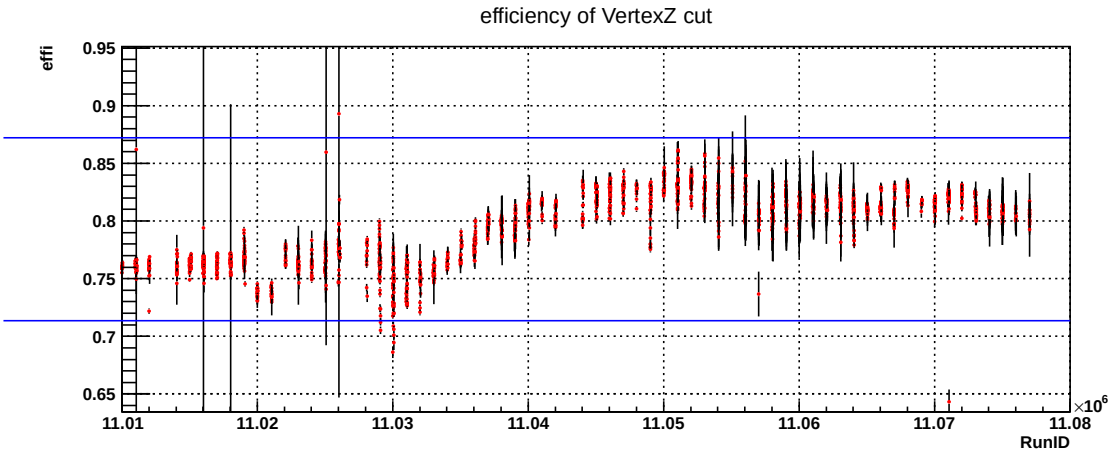

Figure 3.3: The efficiency of $|V_Z| < 30$ cm and $|V_Z^{TPC} - V_Z^{VPD}| < 3$ cm in each run. The horizontal lines indicate the $\pm 10\%$ range around the average, which defines the good runs. The outliers are rejected

The event centrality in this analysis is obtained with standard STAR centrality determination software, which classifies Au+Au events based on the (corrected) reference multiplicity. The reference multiplicity (RefMult) is the number of charged tracks at the center region inside TPC ($|\eta| < 0.5$). Because the west and east halves of TPC do not necessarily have the same efficiency, a TPC bias depending on the primary vertex position Z could occur. Also, there is a trigger bias even in the MinBias trigger, whose efficiency for very peripheral collisions is

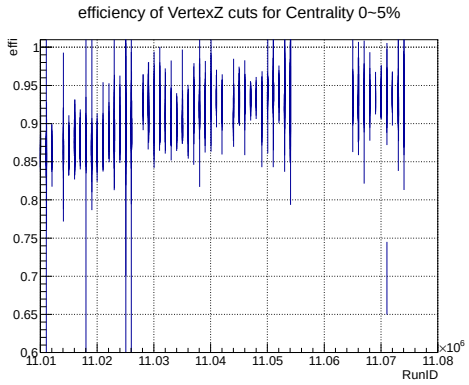

(a) 0% to 5%

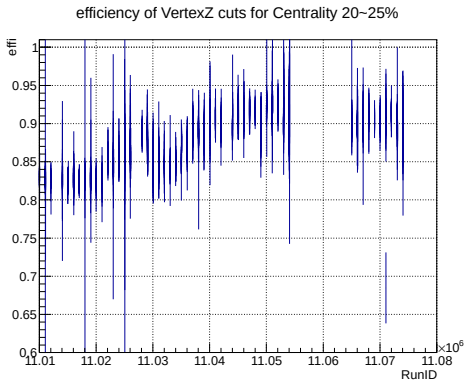

(b) 20% to 25%

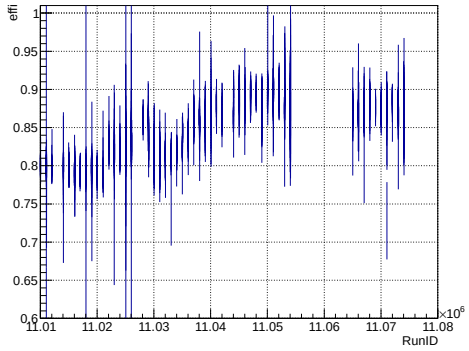

(c) 50% to 55%

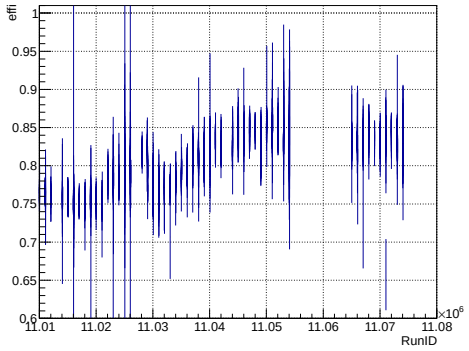

(d) 60% to 65%

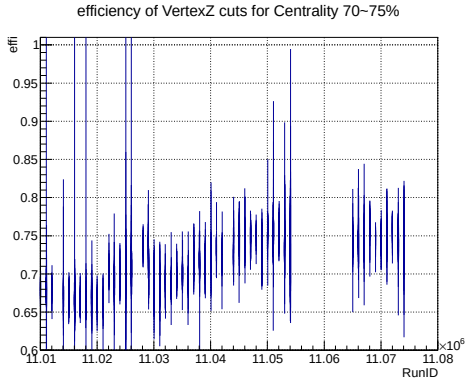

(e) 70% to 75%

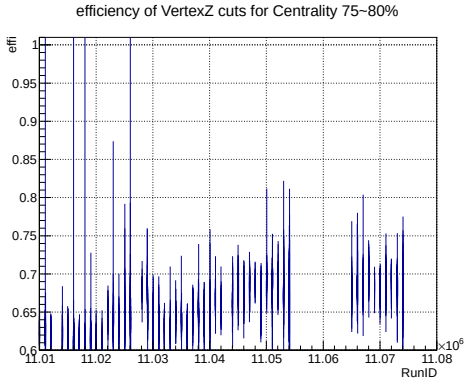

(f) 75% to 80%

Figure 3.4: The efficiency of $|V_Z| < 30$ cm, $\sqrt{V_X^2 + V_Y^2} < 2$ cm and $|V_Z^{TPC} - V_Z^{VPD}| < 3$ cm in each run for selected centrality. Days 55 to 65 and days 75 to 80 are not used in these plots.

lower. In addition, the pileup events, which depend on the luminosity, could modify the RefMult, although the pileup events are expected to be less important in Au+Au collision. Therefore, the STAR centrality determination software corrects the raw reference multiplicity in each event based on VertexZ positions and the event rates monitored by the ZDC.

Glauber model [43] Monte Carlo simulations of event RefMult are carried out by STAR, systematically scanning through all possible impact parameters, and are compared to the corrected RefMult distribution in MinBias events. RefMult ranges, each responding to 5% of the total cross section of Au+Au collisions in the Glauber simulations, are determined via the comparison [87]. In the meantime, the MinBias trigger inefficiency in data, considerable only in very peripheral collisions, is also determined from data-Glauber comparisons for each RefMult value. A weight to correct the inefficiency is assigned for each RefMult value, so that the data RefMult distribution is forced to match that in Glauber. The correction needed is less than 10% until very peripheral and the most peripheral events (approximately 10% geometrical cross section with biggest impact parameter) cannot be corrected reliably. This event by event re-weighting procedure only applies to events satisfying the aforementioned collision vertex position selections and after the re-weighting, the centrality bin $0 \sim 10\%$ and $10 \sim 20\%$ each counts for about 12% of all the final events, while the centrality bin $20 \sim 40\%$ and $40 \sim 60\%$ each counts for about 24%.

By definition, the number of events in MinBias trigger in the analysis is simply the number of events passing the vertex and centrality selections after the re-weighting. It is however more complicated for High Tower triggered events. During the data taking, the ratio of number of truly occurred (*i.e.* no matter whether the event is recorded on tape or not) High Tower events versus number of truly occurred MinBias events in each run was recorded. We apply this run-by-run ratio to convert the total number of High Tower events in each run

into equivalent total number of MinBias events ($N_{HT}^{MB-equiv}$) in each run before any cuts. Then, the vertex and centrality selections efficiency calculated from the MinBias trigger is multiplied to $N_{HT}^{MB-equiv}$ to obtain the equivalent number of MinBias events used in the analysis (*i.e.* after the cuts) for High Tower triggers. In short, even for High Tower events, what matters is the equivalent number of MinBias events and the selection efficiency based on MinBias events. The efficiency also depends on the centrality, as discussed above.

3.3 Track quality cuts

Although heavy quarks decay through the weak interaction, their life-times are usually relatively short, due to large heavy quark masses and large phase space available in the decays. The $c\tau$ of heavy flavor hadrons are on the order of 100 μm, much smaller than the tracking pointing resolution at STAR. As a result, the electron daughters of heavy flavor hadrons cannot be distinguished from the real primary particles, *i.e.* those coming from the primary vertices where the collisions occur. We only accept inclusive electron candidates from the primary vertices by requiring their distance-of-closest-approach (DCA) to the primary vertices being less than 1.5 cm. To ensure there are no badly reconstructed tracks nor track splitting, we require that each track should have at least 20 TPC hits used in track fitting/reconstruction (nHitsFit) but no more than 50, and nHitsFit should be at least over 52% of the maximum number of TPC hits possible. To ensure a good measurement of track energy loss in TPC, a minimum of 15 TPC hits has been used in the track energy loss calculation (nHitsDedx). For the partner electron candidates that will be used to for photonic electron reconstruction, we relax the requirements so that the minimum of nHitsFit is 15 and the minimum of nHitsDedx is 10. We require the partner electrons to be within a pseudo-rapidity range of $-1.3 < \eta < 1.3$ to have good tracking qualities, although the TPC covers

a large range. The pseudo-rapidity cut on the inclusive electron candidates is even tighter due to BEMC constrains and will be discussed later.

A critical advantage of recent data taken by STAR over the previous years is that the inner detectors, SVT and SSD, have been removed before the year 2008, resulting in a much lower detector material budget and much lower photonic electron background since 2008. However, the support structures have not been removed, and they cause a non-uniformity in the material budget distribution in the azimuthal angle. Therefore, in our analysis we avoid the support structures by rejecting certain azimuthal ranges, *i.e.* all electron candidates with $-1.84 < \phi < -1.2$ and $1.36 < \phi < 2.2$ are rejected. To further reject photonic electrons, we require the first TPC hit of each inclusive electron to be at a radius less than 73 cm from the center of TPC, before the fourth row of readout pads in the TPC inner sectors. It rejects the photon conversions in the TPC gas between radius 73 cm to 200 cm. As we discussed in chapter two, the TPC gas has a total thickness of 150 cm and has a $1.17\%X_0$ material budget, and this cut rejects approximately $(1 - 23/150) \times 1.17\%X_0 \sim 1\%X_0$ material budget. $1\%X_0$ is a significant amount considering the total material from the Inner Field Cage (IFC) to beam pipe is only $\sim 1.1\%X_0$ (IFC plus insulating gas is $\sim 0.65\%X_0$ [80] and the beam pipe and the wrap is $\sim 0.43\%X_0$ [73]). In addition, this cut ensures that the tracks travel a long path in TPC, therefore enhancing the probability for the tracks to be correctly reconstructed.

3.4 Electron identification

High p_T electrons can be effectively distinguished from hadrons by the electromagnetic calorimeter, due to the fact that almost all electrons deposit all of their energy in the calorimeter whereas hadrons deposit much less. To make sure that we understand the calorimeter responses well, we restrict the electrons to be within

$-0.7 < \eta < 0.7$, where the BEMC is well calibrated. We start electron identification by requiring certain energy thresholds to be met by the calorimeter, either already in the online triggers (*e.g.* in High Tower triggers, transverse energy thresholds applied on single tower) or in the analysis procedure (*e.g.* in MinBias and Central triggers, with much lower energy threshold than those used in High Tower triggers).

3.4.1 BEMC point reconstruction and track matching

Once a BEMC tower is identified with transverse energy (E_T) larger than a certain energy threshold (100MeV to begin with), we begin to gather more information around the tower to reconstruct the complete BEMC and BSMD responses to the triggering electromagnetic shower. The adjacent BEMC towers and BSMD strips are examined to form BEMC and BMSD clusters. Finally, BEMC and BMSD clusters from the same shower origin are associated together to form a BEMC point. The UCLA BEMC point reconstruction software and its advantages over other STAR software are discussed in detail in [88] and we will present a short summary here.

- In our analysis, one electromagnetic shower is represented by one BEMC point.
- In the chain of data analysis, the UCLA BEMC point reconstruction software is used after the standard STAR library codes finish analyzing the basic information from an event and return a complete collection of status and energy of each single tower/strip in the BEMC/BSMD for this event.
- The software begins with BEMC clustering. BEMC towers with energies higher than 0.1 GeV are identified as "seeds". Surrounding a "seed", towers with energies above a lower threshold are added to the "seed" to form clusters. The BSMD clustering procedure is very similar but with lower energy

thresholds, since BSMD is a wire proportional counter. A cluster, in either BEMC or BSMD, is always confined to within one BEMC/BSMD module *i.e.* no cross-module clustering, and therefore the BEMC point reconstruction software works on each individual module one by one.

- If no cluster can be formed for the BEMC, the software stops with no point found and moves onto the next module. Once a BEMC cluster is found, the software begins to reconstruct BSMD clusters particularly associated with *this* BEMC cluster. As a result, only those strips adjacent to this BEMC cluster are used to reconstruct the corresponding BSMD clusters. However, as long as there is a BEMC cluster, a BEMC point will always be reconstructed, no matter if, or how many BSMD clusters are found.

- If one of the two BSMD planes does not have any clusters whereas the other plane has, this plane will be analyzed again with the strip energy thresholds lowered. If there is more than one cluster on either BSMD plane, the clusters are also examined again and merged if certain criteria are met. This is necessary because the original criterion for BSMD clusters is rather strict. For example, there must be no "valley" in the strip energy profile, *i.e.* the further from the seed strip, the lower energy. However, this requirement is relaxed in the merging process of clusters.

- If there are still more than one cluster in either BSMD plane, the software will reconstruct more than one BEMC point, with the BEMC cluster energy shared among these points in a fashion that matches the energy distribution pattern of the BSMD clusters. This is based on the fact that the BSMD has much better spatial resolution and it is possible to distinguish two showers very close to each other. In this case, the software will sort the clusters on the BSMD-η and ϕ planes with both energy difference and η distance taken into consideration, and then associate them with each other properly. The

total energy of a BEMC point is solely from the BEMC cluster.

After all the BEMC points in one event are reconstructed, only those with all three planes, BEMC, BSMD-η and ϕ are used in Track-Point association. In this high p_T electron analysis, only TPC tracks with $p_T > 1.5$ GeV/c are used. The TPC track trajectories are modeled by helices in a magnetic field and projected onto the BSMD η and ϕ planes for η and ϕ positions respectively. These projected η and ϕ positions are compared with BEMC point η and ϕ positions, and the matching criterion is satisfied if the distance between the projected track and the BEMC point is smaller than 0.05 rad, *i.e.* $d = \sqrt{\Delta\eta^2 + \Delta\phi^2} < 0.05$. If there is more than one BEMC point close enough to the track, the closet point is associated with the track. See Figures 3.5, 3.6 and 3.7 for the distributions of the distance between a TPC track projection at the BSMD and the BEMC point associated with this track. In each figure, one plot is based on all the associated pairs of high p_T TPC tracks and BEMC points, and the other plot is based on a sample with enhanced electrons. The ΔZ distributions are separately drawn for positive and negative η sides, because there are different global offsets, likely due to a lack of accurate understanding of BEMC/BSMD geometry at the $\eta = 0$ ends. This can be inferred from the sudden jump of ΔZ at $\eta = 0$ in Figure 3.8. These offsets are small and do not impose any difficulties as long as we treat the two sides separately.

Two Gaussians are used in the fits shown in the Figures, the blue one representing electrons and the red one for non-electron contributions. The sum of the two Gaussians is in green, and the two magenta dotted vertical lines on each plot indicate the 3σ range around the center of the electron Gaussian. Based on the obtained fitting parameters, the association distance resolutions for electrons are determined to be consistent with the reported BSMD resolution [80]. In this analysis, additional cuts on the association distances are applied to reject non-electron contributions. The cuts are tighter than the $d = \sqrt{\Delta\eta^2 + \Delta\phi^2} < 0.05$ cut used

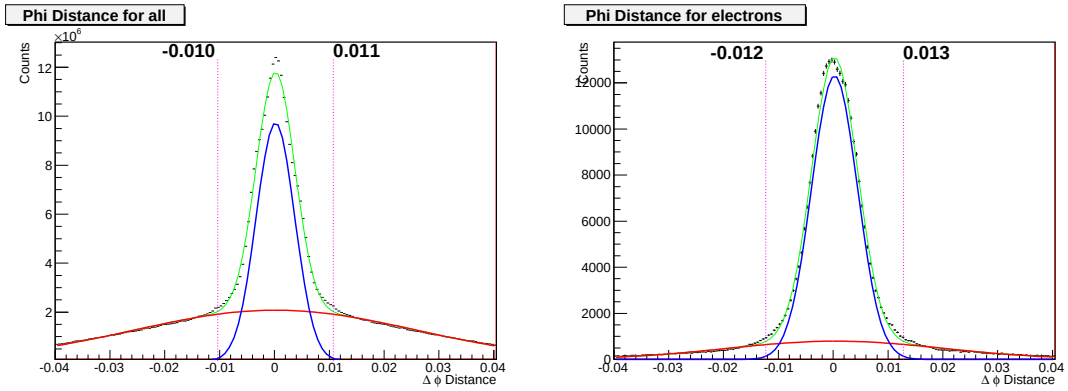

Figure 3.5: Left plot: Distribution of $\Delta\phi$ between associated pairs of TPC tracks and BEMC points. Right plot: Same distribution for an electron enhanced sample, where other electron identification cuts are applied.

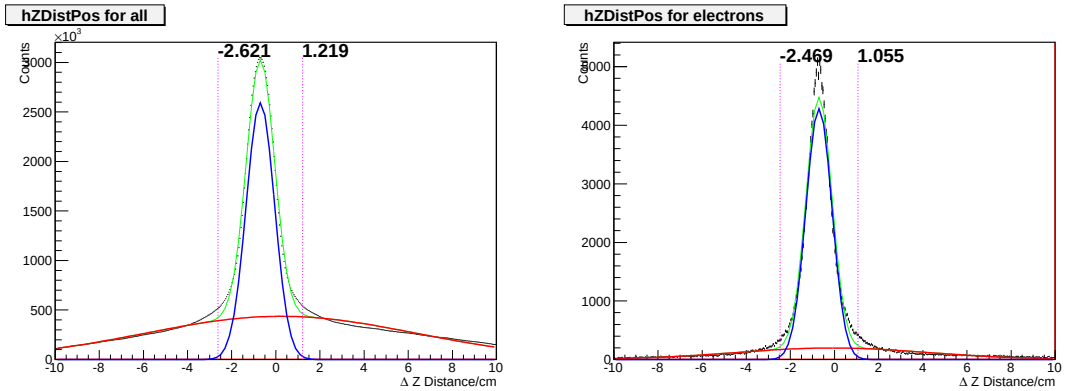

Figure 3.6: Left plot: Distribution of ΔZ between associated pairs of TPC tracks and BEMC points in the positive η side. Right plot: Same distribution for an electron enhanced sample, where other electron identification cuts are applied.

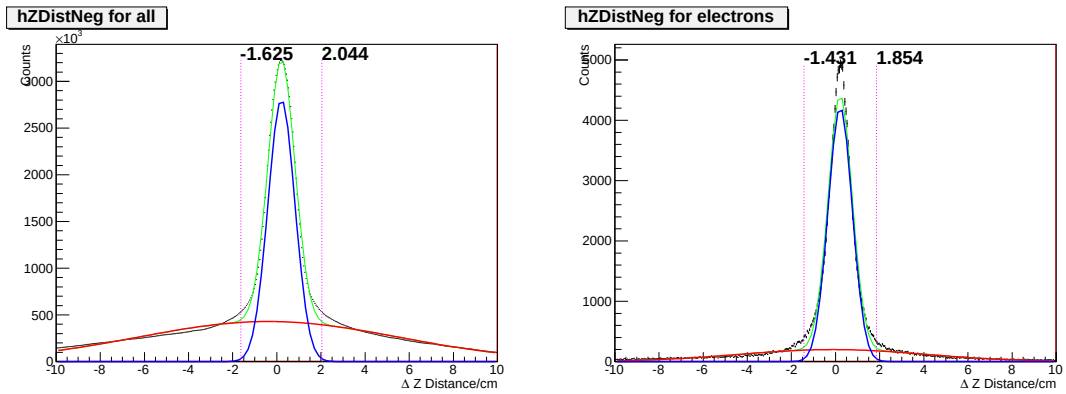

Figure 3.7: Left plot: Distribution of ΔZ between associated pairs of TPC tracks and BEMC points in the negative η side. Right plot: Same distribution for an electron enhanced sample, where other electron identification cuts are applied.

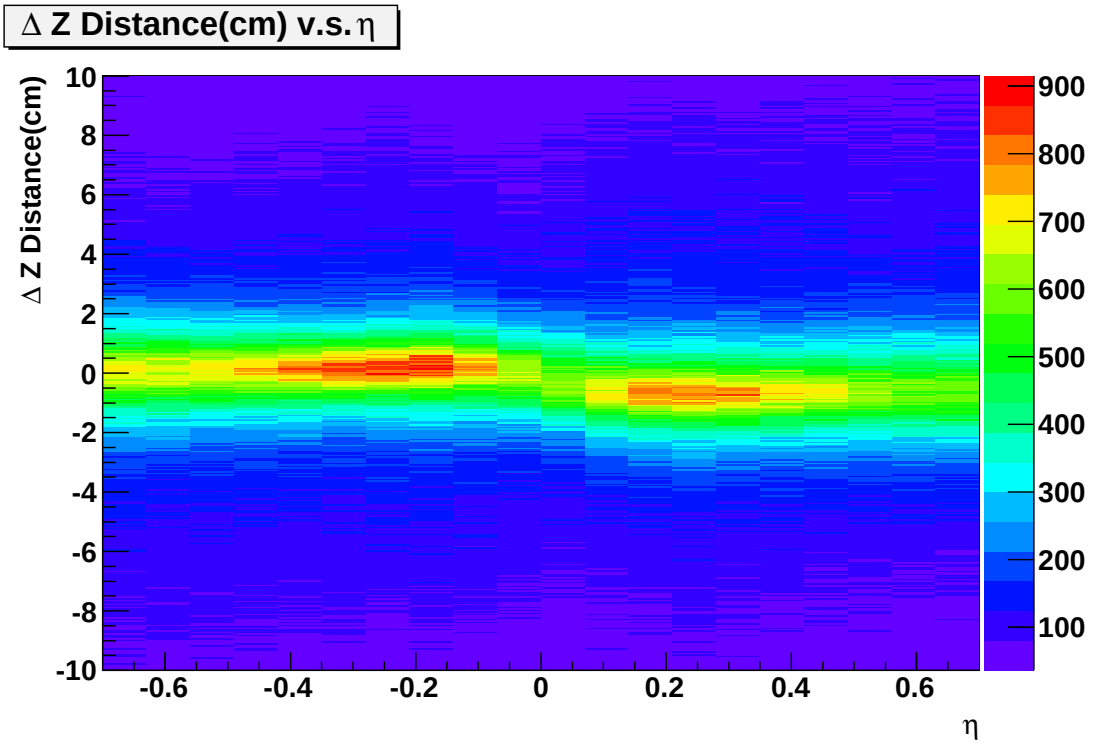

Figure 3.8: Two dimensional distribution of ΔZ between associated pairs of TPC tracks and BEMC points for different η. A jump of ΔZ is visible near $\eta = 0$.

in the initial association, but they still allow at least 99.7% of the electrons (3σ range around the center of a Gaussian distribution) to be included. The specific cuts ($-0.013 < \Delta\phi < 0.013$, -2.5 cm $< \Delta Z <$ 1.1 cm for positive η and -1.5 cm $< \Delta Z <$ 1.9 cm for negative η) are obtained based on the fitting parameters from the electron enhanced sample, but they are also checked against all the associated track-point pairs and against photonic electrons. The cut efficiencies are found to be always above 99.5% no matter what sets of parameters are used in the calculation. The overall efficiency of electrons matching BEMC points are complicated, involving many factors such as geometrical acceptance and detector unit performance, and we rely on simulations to study it. Only on the order of 1% of all the hadrons are associated with BEMC points.

In the High Tower triggered events, we further require the highest single-tower transverse energy in every accepted BEMC point to be larger than the equivalent High Tower trigger thresholds. During the data taking, the High Tower trigger thresholds (11, 15, 18 and 25) were applied to the Analog to Digital Converter (ADC) channels of the Photomultiplier Tubes (PMT) for BEMC towers and they are translated into tower transverse energy thresholds (2.64, 3.6, 4.3 and 5.98 GeV).

3.4.2 E/P and Number of BSMD strips

The electromagnetic showers of electrons are caused mostly by electron bremsstrahlung in the electromagnetic calorimeter and the emitted photons converting into pairs of electron and position, which emit more photons and so on. Electrons and photons deposit all of their energies in the electromagnetic calorimeter, whereas hadrons do not lose as much energy. Since the momentum of a relativistic electron equals to its energy, electrons should have $E/p \sim 1$, whereas hadrons do not, as shown in Figure 3.9. Therefore, we use $0.5 < E/p < 1.7$ to reject hadrons. The electromagnetic shower of electrons develops much broader at the depth where

the SMD is located ($\sim 5X_0$). We require that the shower profiles of electron candidates must be at least two-strip wide on both BSMD ϕ and η planes, *i.e.* firing at least two strips in both planes. In Figure 3.10, we compare BSMD showers for electrons and hadrons and the hadron showers are normally much smaller.

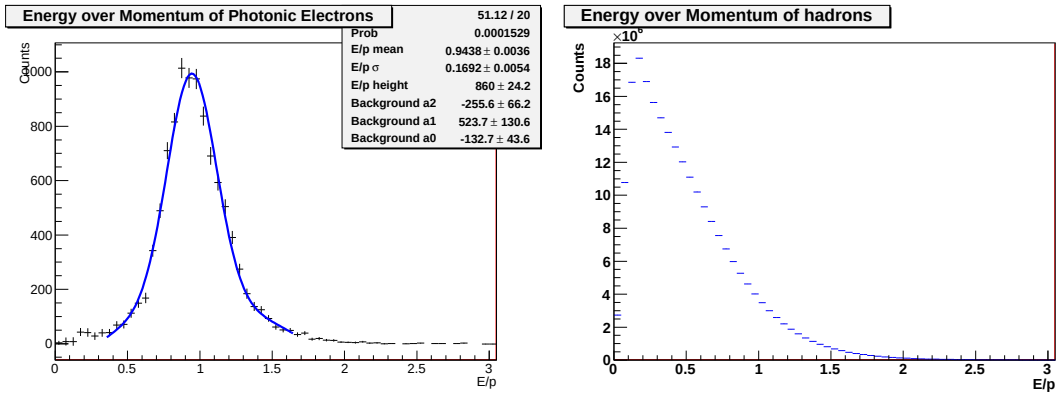

Figure 3.9: Left(Right) plot: Distribution of E/p for photonic electrons (hadrons, which are identified by their energy loss in TPC).

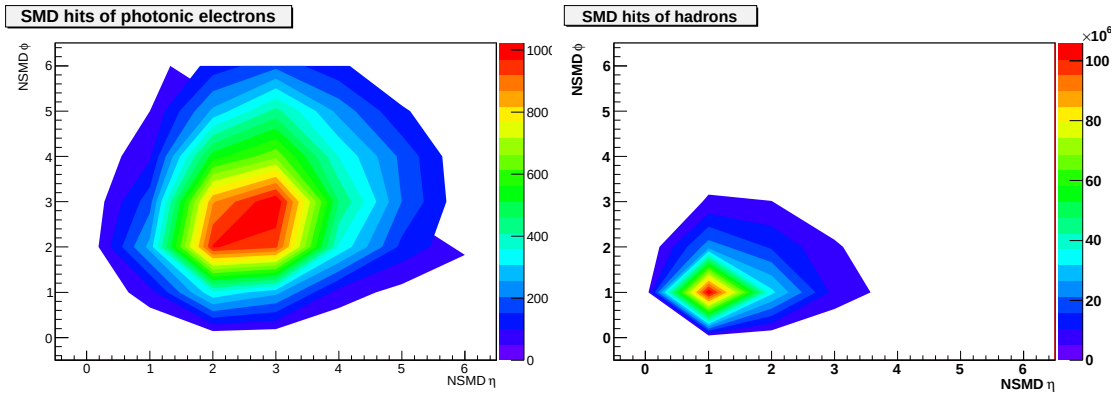

Figure 3.10: Left(Right) plot: Distribution of number of BSMD strips on the η and ϕ planes for photonic electrons (hadrons, which are identified by their energy loss in TPC) in MinBias events.

Since both energy measured by the calorimeter and $1/p$ measured by the TPC have Gaussian-like resolutions, the E/p distribution would be a Gaussian if there are no other effects. However, effects such as electron bremsstrahlung in the TPC, random tracks (*e.g.* π^0) hitting the same BEMC points coincidently with electrons and even the energy threshold cut on single-tower, distort the equality between

electron energy and momentum. These effects are slightly different for different p_T and centrality, but the differences are found to be very small. In Figure 3.9, the E/p distribution for photonic electrons is fitted with a Gaussian plus a second order polynomial. The width of this Gaussian is found to be about 17%, and it corresponds to the combination of track momentum resolution from TPC and energy resolution from BEMC. The efficiency of the E/p cut ($0.5 < E/p < 1.7$) is estimated to be above 99%. In MinBias events about 60% of the hadrons are rejected by this cut.

In contrast to E/p, number of BSMD strips has a strong dependence on p_T, since the size of electromagnetic showers depends on the energy deposited in the calorimeter. As a result, the distributions of the number of BSMD strips are different in MinBias and High Tower events, since the average p_T in MiniBias events is smaller than that in High Tower events. Based on photonic electrons, the total efficiency is estimated to be 86% (94%), with the individual plane cut efficiency around 92∼93% (96∼97%, in MinBias (High Tower) events. We show the distribution of the number of strips for each BSMD plane for photonic electrons in Figure 3.11. About 80% of the hadrons are rejected by these cuts in MinBias events.

In summary, combined requirements of BEMC matching, close-to-unity E/p and wide shower profiles, can achieve a hadron suppression factor on the order of 1000 at high p_T, while maintaining a reasonable electron efficiency. We do not apply any BEMC or BSMD related cuts to partner electrons.

In Table 3.1, we summarize all the electron identification cuts applied so far, except the $n\sigma_e$ cuts. The cuts listed here do not change with p_T, whereas the $n\sigma_e$ cuts will change.

Table 3.1: The electron identification cuts, except the $n\sigma_e$ cuts

Variable	Cut
Pseudo-rapidty η	$\in$ (-0.7, 0.7)
Azimuthal angle ϕ	$\notin$ (-1.84, -1.2)$\vee$(1.34, 2.2)
Radius of first TPC hit	$<$ 73 cm
Global DCA	$<$ 1.5 cm
Number of TPC hits	$\in$ [20, 50)
Number of TPC hits/Maximum hits possible	$\in$ (0.52,1.02)
Number of TPC hits used for energy loss	$\in$ [15,100)
Track-point association distance $d = \sqrt{\Delta\eta^2 + \Delta\phi^2}$	$<$ 0.05
Track-point association ϕ distance $\Delta\phi$	$\in$ (-0.013, 0.013)
Track-point association Z distance ΔZ	$\in$ (-2.5 cm, 1.1 cm) $\eta > 0$ $\in$ (-1.5 cm, 1.9 cm) $\eta < 0$
BEMC point energy over track momentum E/p	$\in$ (0.5, 1.7)
Number of BSMD η and ϕ strips	at least 2 for both planes

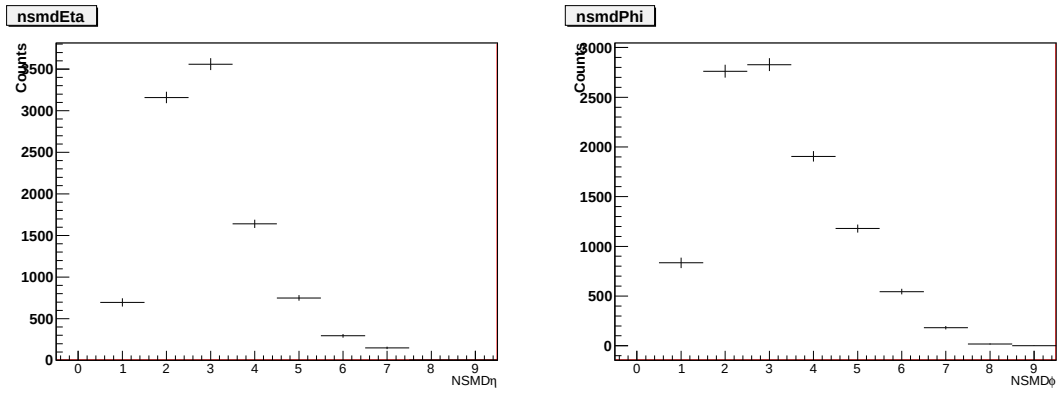

Figure 3.11: Left(Right) plot: Distribution of number of BSMD strips on the $\eta(\phi)$ plane for photonic electrons in Mini-Bias events.

3.4.3 TPC ionization energy loss $n\sigma_e$

In chapter two, we discussed track ionization energy loss in TPC. The STAR TPC measures track energy loss per unit distance dE/dx. Since charged particle ionization processes have been extensively studied for a long time, the theoretical calculations, *e.g.* Bichsel function [89], are rather accurate. The difference between the measured and calculated energy loss are divided by the TPC energy loss resolution, and thus converted into normalized ionization energy loss, $n\sigma$, for each particle species, usually including $\pi^{\pm}, k^{\pm}$, protons, and electrons. In particular, for electrons, we have $n\sigma_e$ according to Equation 3.4.1.

$$n\sigma_e \;=\; \frac{log[(dE/dx)/B_e]}{\sigma_e} \tag{3.4.1}$$

where B_e is from the Bichsel function prediction for electrons [73, 89].

After imposing the electron identification criteria discussed above, we examine the $n\sigma_e$ distribution of the electron candidates in p_T bins of 1 GeV each. We show some examples in Figure 3.12. At high p_T, electron energy loss is stable and has a very weak dependence on p_T, whereas the hadrons just pass the Minimum Ionization Position (MIP) and the hadron energy loss rises quickly with p_T and

approaches the electron energy loss. As a result, the hadron peaks are closer to the electron peak at higher p_T and we tighten the electron selection cuts at higher p_T to ensure a high purity. For example, we require electrons to have $n\sigma_e > -0.75$ at $2 < p_T < 3$ GeV/c and $n\sigma_e > -0.25$ at $4 < p_T < 5$ GeV/c. We fit the $n\sigma_e$ distributions with multiple-Gaussian functions, based on which we calculate the efficiency of the $n\sigma_e$ cuts and the contamination from hadrons in the accepted electron candidates. The hadron contamination is always less than 20% and much lower at low p_T. Due to the fact that the calorimeter enhances the probability of finding electrons, the $n\sigma_e$ distributions are different in High Tower and in MinBias, with the electron peak in High Tower trigger being much more prominent, also shown in Figure 3.12. As a result, although the efficiency of the $n\sigma_e$ cut is the same in High Tower and in MinBias, the hadrons contamination and the purity of selected electrons are different. Table 3.2 summarizes the efficiency and purity as a function of electron p_T.

We emphasize here two points for electron identification procedure. 1) in order to guide good fits to the $n\sigma_e$ distributions, we first study the $n\sigma_e$ distributions of photonic electrons, obtaining the mean and width of these distributions. We then fix the electron $n\sigma_e$ Gaussian parameters to be those obtained from photonic electrons. We assume there is no p_T dependence but consider the centrality dependence. Figure 3.13 shows the $n\sigma_e$ distributions of photonic electrons, along with the Gaussian mean and width obtained via fitting. 2) the $n\sigma_e$ selection is the last electron identification method to be applied. The selected particles are the inclusive electrons and the hadrons leaking into this selection is regarded as irreducible contamination, and the number of pure electrons is naturally the electron purity times the number of inclusive electrons.

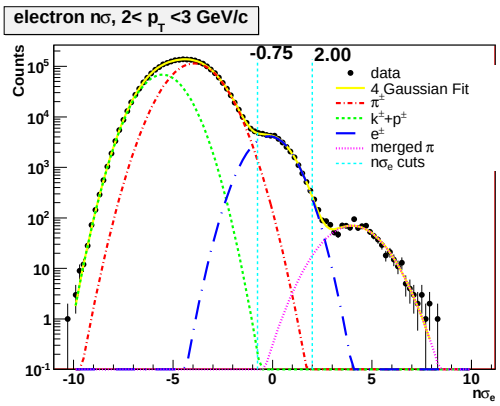

(a) MinBias $2 < p_T < 3$ GeV/c

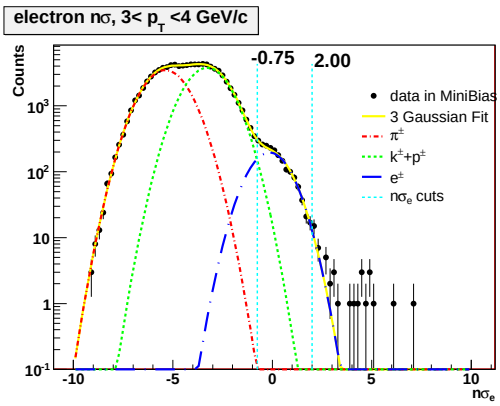

(b) MinBias $3 < p_T < 4$ GeV/c

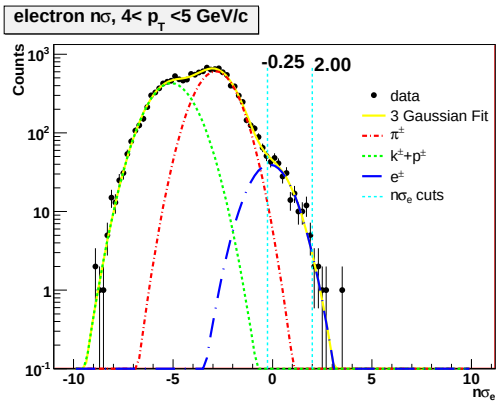

(c) MinBias $4 < p_T < 5$ GeV/c

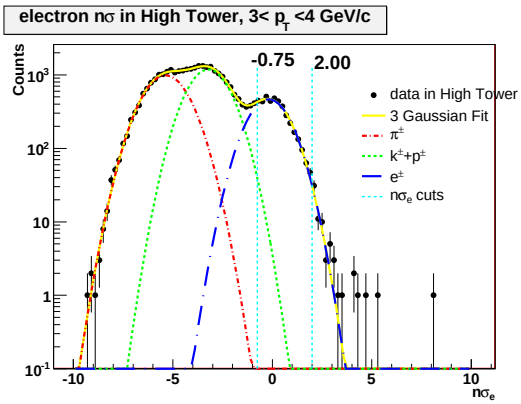

(d) High Tower $3 < p_T < 4$ GeV/c

Figure 3.12: Figures 3.12(a) to 3.12(c): Distributions of $n\sigma_e$ of electron candidates in 0% to 10% central events in the MinBias Trigger. Three Gaussians are used to fit the distribution, one for electrons, one for $\pi^{\pm}$ and the last one for the merged peaks of $K^{\pm}$ and $p^{\pm}$. In the top left plot, there is a fourth peak at the high $n\sigma_e$ end of the distribution due to merged $\pi^{\pm}$ tracks, which is approximated by a Gaussian here. Figures 3.12(d): same as Figure 3.12(b) except this is for High Tower Trigger.

Table 3.2: The efficiency of $n\sigma_e$ and the electron purity in the inclusive electrons as a function of electron p_T in different centrality. MB means MinBias triggered events, and NPE15 means High Tower NPE15 trigger. The values for NPE11 are only slightly different. N/A means cannot be fitted well.

p_T (GeV/c) selected range	2-3 (-0.75, 2)	3-4 (-0.75, 2)	4-5 (-0.25, 2)	5-6 (-0.25, 2)	6-8 (0.25, 2)	8-10 (0.5, 2)
MB $0 \sim 10\%$						
efficiency	0.74	0.74	0.53	N/A	N/A	N/A
purity	0.94	0.86	0.93	N/A	N/A	N/A
MB $10 \sim 20\%$						
efficiency	0.78	0.78	0.58	N/A	N/A	N/A
purity	0.95	0.88	0.92	N/A	N/A	N/A
MB $20 \sim 40\%$						
efficiency	0.80	0.80	0.61	N/A	N/A	N/A
purity	0.97	0.91	0.96	N/A	N/A	N/A
MB $40 \sim 60\%$						
efficiency	0.82	0.81	0.63	N/A	N/A	N/A
purity	0.98	0.94	0.91	N/A	N/A	N/A
NPE15 $0 \sim 10\%$						
efficiency	0.75	0.75	0.55	0.55	0.34	0.24
purity	0.98	0.99	0.99	0.97	0.98	0.94
NPE15 $10 \sim 20\%$						
efficiency	0.78	0.78	0.59	0.59	0.36	0.26
purity	0.99	0.99	0.99	0.94	0.97	0.95
NPE15 $20 \sim 40\%$						
efficiency	0.80	0.80	0.62	0.62	0.39	0.29
purity	0.99	0.99	0.99	0.98	0.98	0.93
NPE15 $40 \sim 60\%$						
efficiency	0.82	0.82	0.64	0.64	0.41	0.30
purity	1.00	1.00	0.99	0.98	0.98	0.92

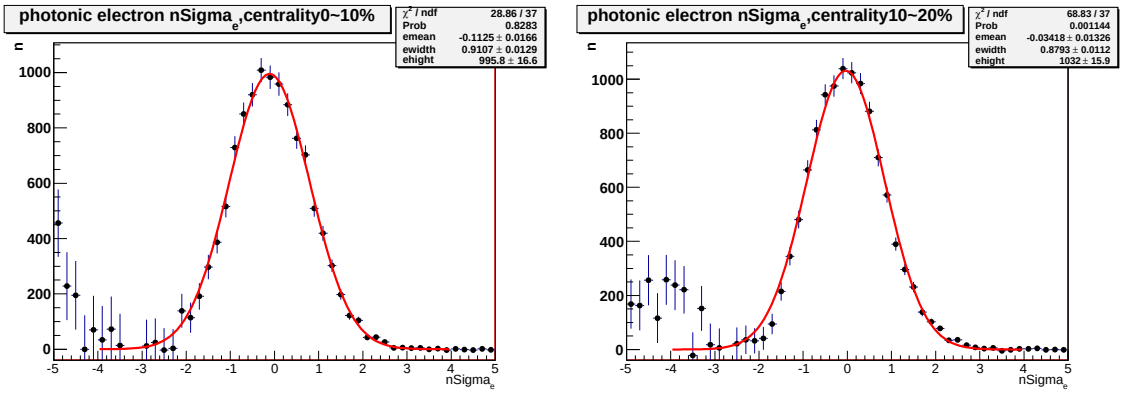

(a) centrality 0% to 10%

(b) centrality 10% to 20%

(c) centrality 20% to 40%

(d) centrality 40% to 60%

Figure 3.13: $n\sigma_e$ distributions of photonic electrons in different centrality. The parameters obtained here are used to constrain the fits to inclusive electrons $n\sigma_e$ distributions.

3.5 Photonic electron reconstruction

After all the track quality cuts and electron identification cuts are applied, the remaining sample is the inclusive electrons. As discussed above, the main background within the pure electrons are the so called photonic electrons from photon conversions (Equation 3.5.2) and π^0 Dalitz decays (Equation 3.5.3). The photons come not only directly from the Quark-Gluon Plasma (QGP) but also from particle decays, mainly π^0 mesons.

$$\gamma \rightarrow e^+ \ + \ e^- \tag{3.5.2}$$

$$\pi^0 \rightarrow e^+ \ + \ e^- \ + \gamma \qquad (1.174 \pm 0.035)\% \tag{3.5.3}$$

We try to reconstruct the parent γ and the Dalitz e^+e^- pair by pairing inclusive electrons with partner electrons in the same event. The partner electrons have looser track quality cuts, as discussed above, and they are not required to come from the collision vertices, since photon conversions only happen in detector materials, the majority of which are some distance away from collision vertices. The partner electrons are required to have a TPC energy loss within $-3 < n\sigma_e < 3$. We use helices to model the electron bending in the magnetic field. The p_T of partner electrons are required to be above 0.3 GeV/c to ensure a good modeling with helices. The cuts to select partner electrons are listed in Table 3.3.

Every track in the inclusive electron sample is paired with all the qualified electrons in the same event, including both oppositely charged (forming opposite-sign pairs, *i.e* electron-positron pairs) and same charged (forming same-sign pairs, *i.e* electron-electron and positron-positron pairs). The electron and positron in an opposite-sign pair could be either truly correlated, *i.e* come from the same parent, or not correlated at all but as a result of the random pairing process.

Table 3.3: The partner electron identification cuts

Variable	Cut
Number of TPC hits	≥ 15
Number of TPC hits used for energy loss	≥ 10
Pseudo-rapidty η	$\in$(-1.3, 1.3)
Transverse momentum p_T	>0.3 GeV/c
Normalized energy loss nσ_e	$\in$(-3, 3)

The latter contribution, referred to as the combinatorial background, can be well estimated by the same-sign pairs. This is because the correlation between same-charged electrons are expected to be extremely small, if any, coming from some very rare decays. As a result, the possibility of an electron being paired with an uncorrelated positron should be, on average, the same as the possibility of it being paired with another electron. Therefore, the opposite-sign (OS) pairs subtracting the same-sign (SS) pairs represents the amount of photonic electrons.

Although the combinatorial background can be well estimated on average, it could be very significant if no constraints were applied, and the statistical uncertainty would be overwhelming. We examine the properties of each OS and SS pair to decide whether the paired electrons are likely to come from a common parent or not. The properties to be examined are pair opening angles, pair distance and parent mass. The cuts on the pairs are exactly the same for OS and SS, so that the good estimation of the combinatorial background will not be affected.

Firstly, the opening angles between the paired tracks are examined, as shown in Figure 3.14. The random combinations, represented by the same-sign pairs,

increase rapidly with growing opening angle. We cut the opening angle at 0.1 rad where the photonic electron distribution (OS-SS) approaches zero. Furthermore, we examine the opening angles in both ϕ plane ($\eta = 0$) and θ plane ($\phi = 0$), shown in Figure 3.15. Similarly, we always cut those angles where photonic electron distributions approach zero, 0.1 and 0.05 rad for ϕ plane and θ plane, respectively. These cuts reject a large number of random combinations.

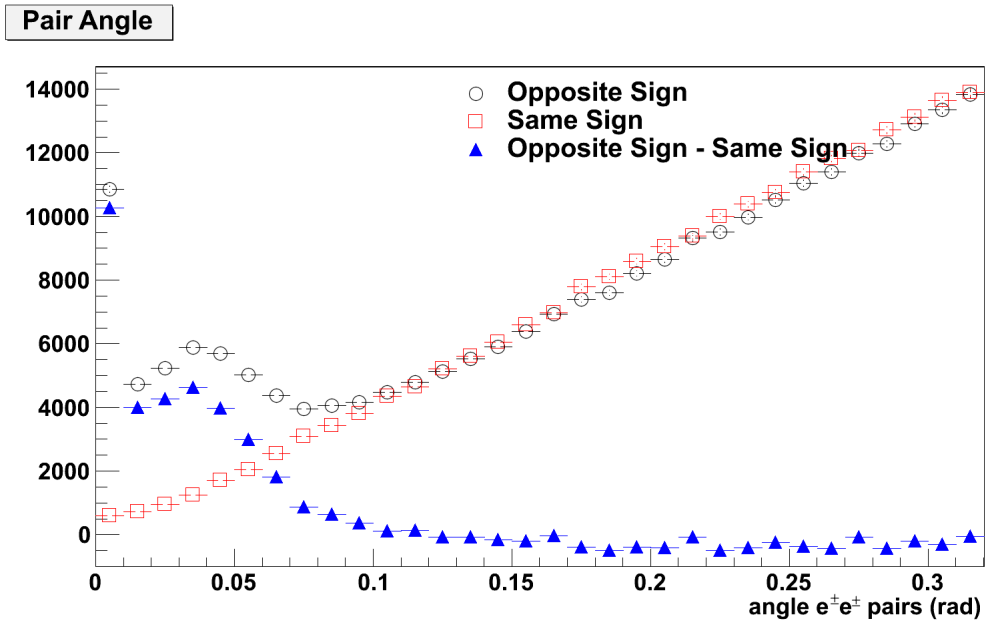

Figure 3.14: The opening angle between two paired tracks. The photonic electrons are the opposite-sign pairs subtract same-sign pairs. No other pair cuts are applied.

Secondly, if the paired tracks are truly from a common parent, the measured distance-of-closest-approach (DCA) between them should be very small, being non-zero only due to detector resolution. We require the DCA less than 1cm, and this cut accepts the majority of the photonic electrons as shown in Figure 3.16. By doing so, we avoid the need of very accurate simulations of this particular detector resolution.

Finally, instead of the normal invariant mass, we examine a two-dimensional (2-D) invariant mass, where we ignore the opening angle between the two paired

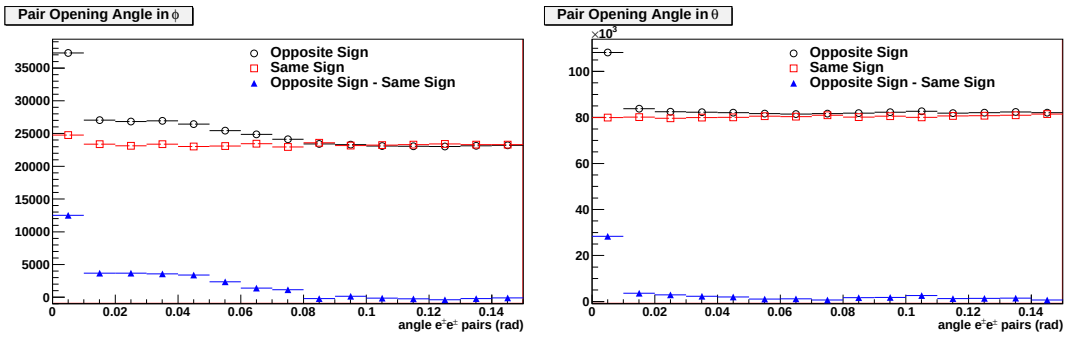

Figure 3.15: The opening angle between two paired tracks in ϕ plane (in the left plot) and θ plane (in the right plot). The photonic electrons are the opposite-sign pairs subtracting same-sign pairs. No other pair cuts are applied.

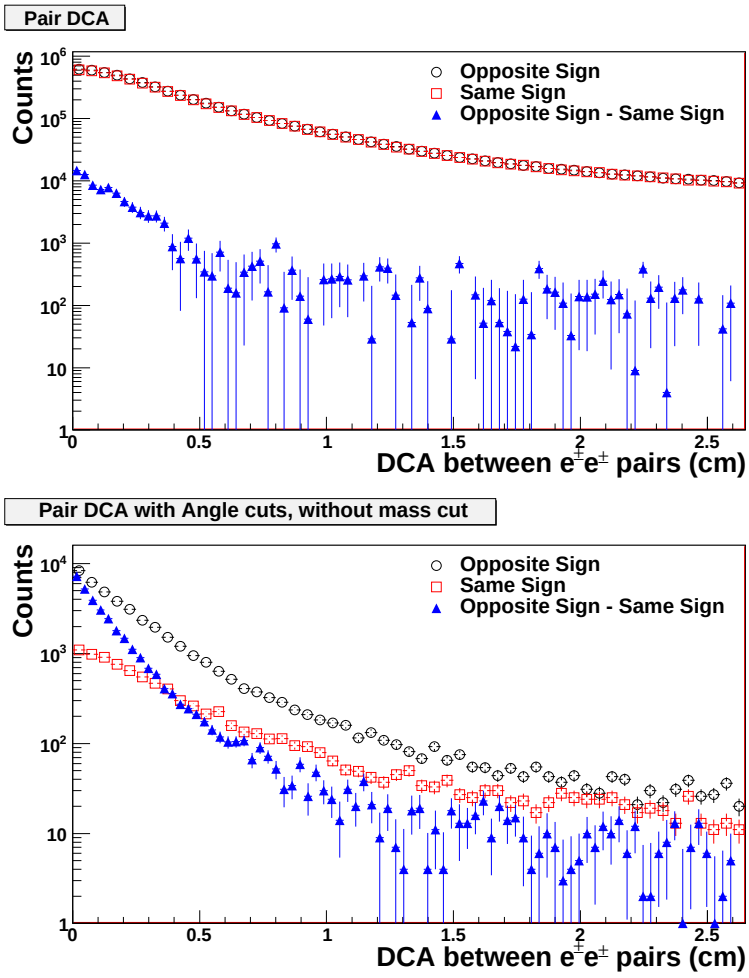

Figure 3.16: The DCA between two paired tracks. The photonic electrons are the opposite-sign pairs subtracting same-sign pairs. Upper: No other pair cuts are applied. Lower: pair opening angle cuts are applied.

tracks in the ϕ direction. The momenta of the paired tracks are rotated to a common plane with $\phi = 0$ and since it is a rotation, the magnitudes of the momenta are conserved. In other words, *two dimensional* means that track momentum is rotated and confined into a two-dimensional space. The purpose is to reduce the impact of the limited resolution of the opening angle in ϕ direction, which in turn is caused by limited tracking resolution [88]. The limited tracking resolution makes it difficult to reconstruct the exact position of DCA between the two paired tracks, *i.e.* the secondary vertex where the potential parent particle decays. The badly reconstructed secondary vertex results in a bad estimation of opening angle in ϕ direction, which can be seen as shown in Figure 3.17.

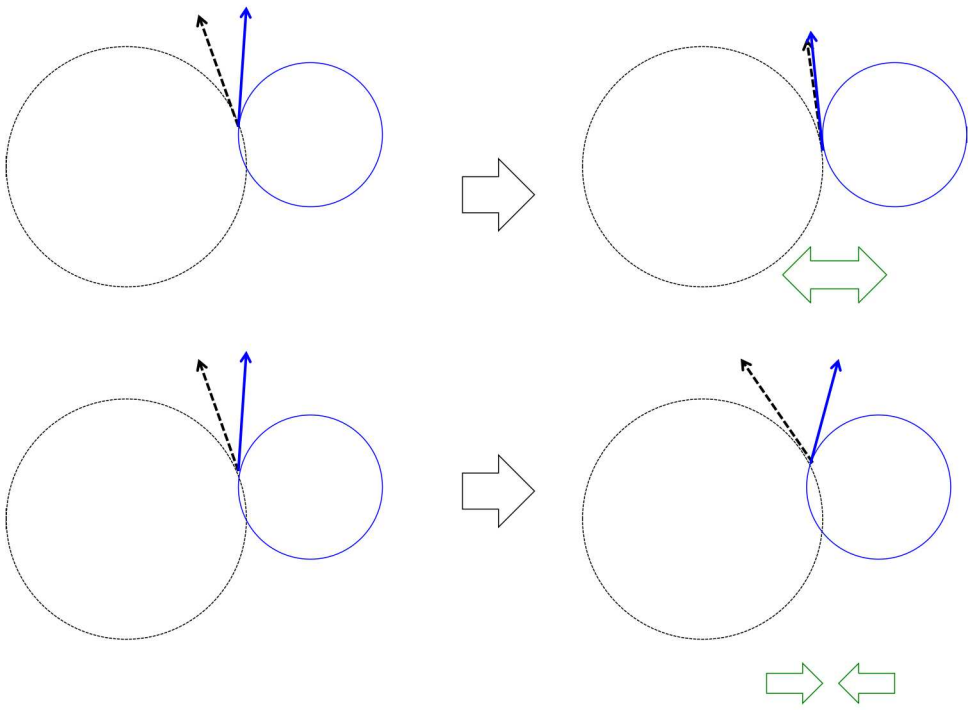

Figure 3.17: The two scenarios of mis-reconstructed DCA position between two paired helices (circles in this figure are viewed from the Z axis) and the effects on the ϕ opening angle.

Figure 3.18 shows both the normal invariant mass and 2-D invariant mass of electron pairs in MinBias events. The photonic electrons are the opposite sign pairs subtracting the same sign pairs (OS-SS). The normal invariant mass of

photonic electrons spans a much wider range than the 2-D invariant mass does. The π^0 Dalitz decay is a three-body decay and the photon daughter is missed in the invariant mass reconstruction. This incomplete reconstruction gives rise to the broad peak at around 0.05 GeV in the invariant mass distribution, and it also contributes to the peak around zero invariant mass, which is mainly from photon conversions. If we used the normal invariant mass to select the photonic electrons, then we would have to accept a wide mass range to contain the π^0 Dalitz peak, and this introduces more combinatorial background, which also has a broad mass distribution. If we use a narrow mass range, we would need accurate simulation to know the mass cut efficiency exactly, which is a difficult task. By using the 2-D invariant mass, we only need a small mass range to contain most of photonic electrons. We do not rely on the accuracy of the simulations, but instead we rely on the cancellation between the OS pairs and the SS pairs. We require the 2-D invariant mass of photonic electrons to be smaller than $100\text{MeV}/c^2$.

In short, we studied the photonic electron pairs' properties based on opposite-sign pairs subtracting same-sign pairs, and we apply loose cuts on pair properties so that the selection efficiency is high enough. In doing so, we reduce the dependence on accuracy of simulations. Table 3.4 summarizes the cuts.

In addition, not every partner electron can be reconstructed by the TPC, nor can they all pass the geometry and kinematic cuts. These inefficiencies are studied by simulations, to be discussed in detail later. The true number of photonic electrons is the number of reconstructed photonic electrons corrected for the photonic electron reconstruction efficiency, and the number of reconstructed non-photonic electrons equals the number of inclusive electrons after subtracting the efficiency-corrected number of photonic electrons, summarized as in Equation 3.5.4, where the superscript "rec" indicates the amount being reconstructed. The total NPE would be the reconstructed NPE divided by single electron efficiency.

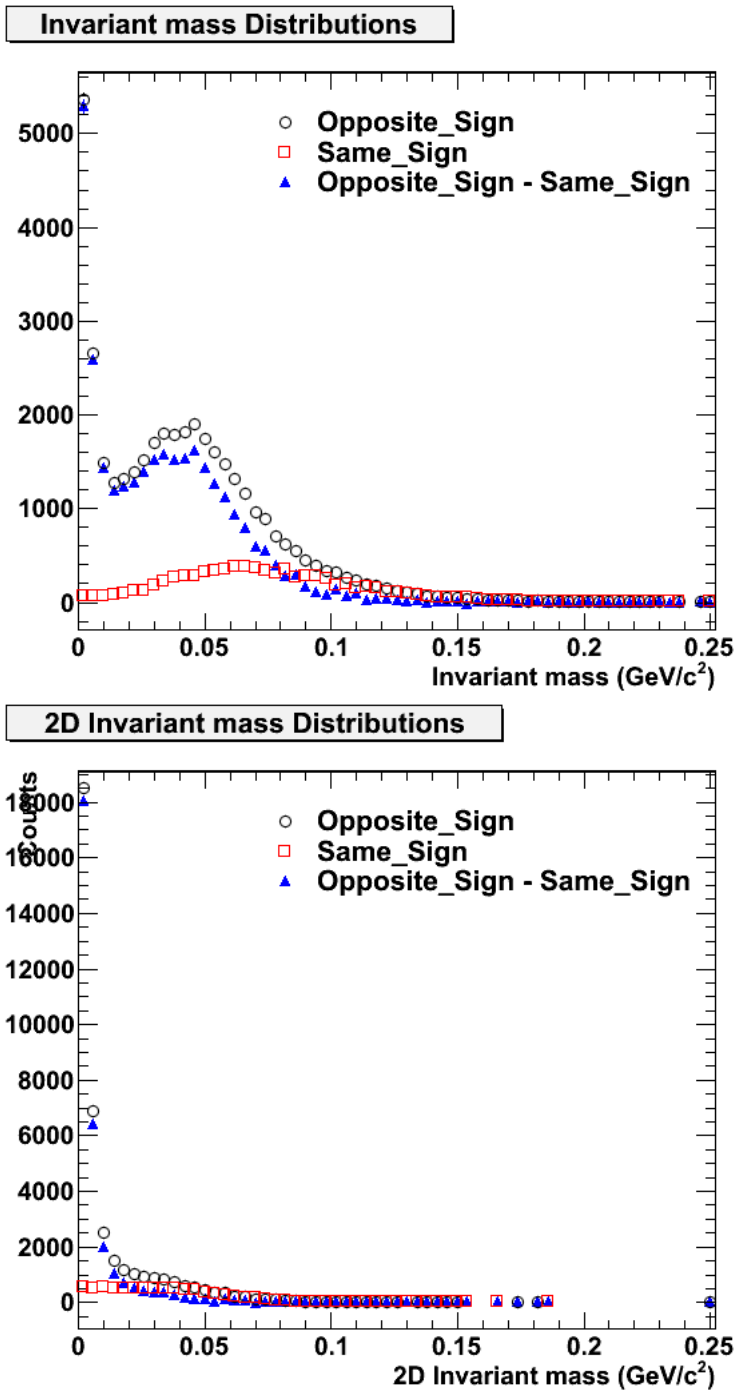

Figure 3.18: The invariant mass distribution (upper plot) and 2-D invariant mass distribution (lower plot) for oppositely signed pairs and same signed pairs in Mini-Bias events. The photonic electrons are the opposite sign pairs after subtracting same sign pairs from them. The pair opening angle cuts and pair DCA cuts have been applied.

Table 3.4: The cuts applied to identify photonic electrons

Variable	Cut
Pair DCA	≤ 1 cm
Pair Opening Angle	≤ 0.1 rad
Pair Opening Angle in θ plane	≤ 0.05 rad
Pair Opening Angle in ϕ plane	≤ 0.1 rad
Pair 2-D invariant mass	≤ 0.1 GeV/c^2

$$N_{NPE}^{rec} = N_{inc} \times purity - N_{PE}^{rec}/\varepsilon_{PE} \tag{3.5.4}$$

3.6 Heavy quarkonia decay and Drell-Yan

Before we proceed to detailed discussions of simulation studies of efficiencies including ε_{PE}, we here discuss some other sources contributing to the electrons. The second largest background, other than the photonic electrons discussed above, is the electrons from heavy quarkonia, *i.e* J/Ψ and Υ decays and Drell-Yan processes. While heavy quarkonia also consist of heavy quarks, their energy loss mechanisms are different from single heavy quarks, and model calculations have to treat them separately. Electrons from J/Ψ and Υ decays should be subtracted from the final non-photonic electrons, in both p+p and Au+Au collisions. The Drell-Yan processes should also be subtracted since they are initial state processes and not affected by the QGP, although they could be affected by cold nuclear effects.

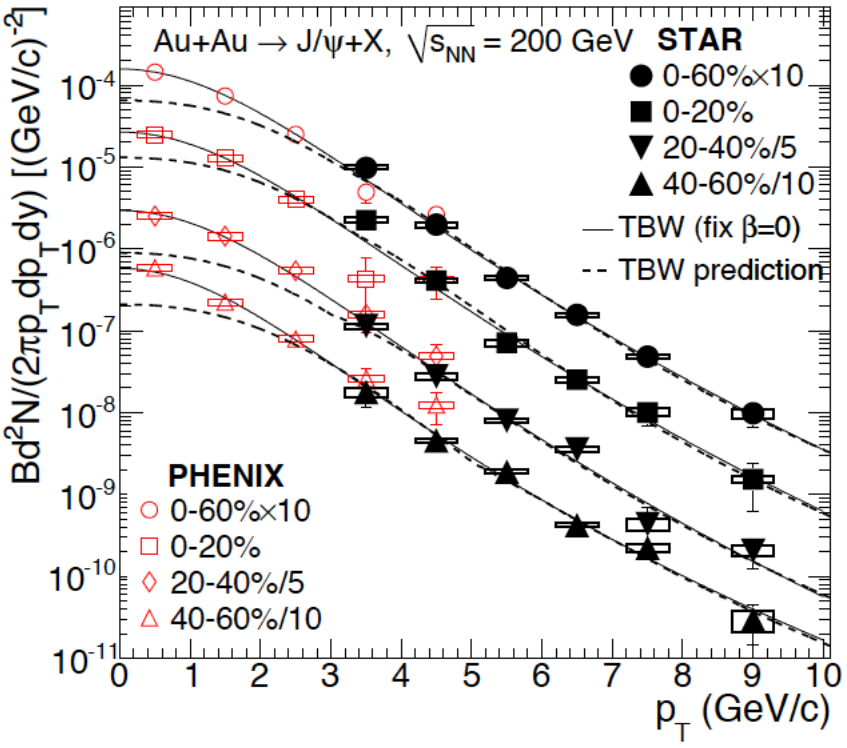

Figure 3.19: The J/Ψ spectra at mid-rapidity measured by STAR [90] and PHENIX [91]. The spectra is multiplied by the branching ratio of J/Ψ decaying to e^+ and e^-. Figure taken from [90].

J/Ψ spectra have been measured in Au+Au collisions at middle rapidity by both STAR [90] and PHENIX [91] collaborations, and the results are fitted with the Tsallis statistics Blast-wave (TBW) model with β fixed to zero, as shown in Figure 3.19. Since these spectra are only measured at mid-rapidity, we rely on PYTHIA [92] to estimate the rapidity distributions [93]. Although we assume the p_T spectra is rapidity-independent, the J/Ψ rapidity distributions from PYTHIA have a p_T dependence, and thus they cannot be factorized. We randomly generate one billion J/Ψ for each centrality bin, according to the measured p_T spectra and PYTHIA rapidity distributions, and feed them into PYTHIA8 [94], in which J/Ψ decays to an pair of electron and positron. These J/Ψ electrons within $\pm$0.5 rapidity range are recorded and we also keep track of the number of J/Ψ decays. The normalization is based on the matching between p_T integrated J/Ψ spectra and number of J/Ψ decays in PYTHIA. Since we lack J/Ψ measurements at non-mid-rapidity, and the p_T and rapidity distributions are correlated, the p_T range used in the normalization affects the normalization scales. We choose a normalization range of $5 < p_T < 15$ GeV/c to be the nominal case and different choices of normalization p_T range yield a systematic uncertainty up to the order of 30% on the J/Ψ decay electron spectra. Figure 3.20 shows the J/Ψ decay electron spectra at middle rapidity in different centrality bins.

Our previous study of Υ decay electrons [73] found that it contributes at most 10% to J/Ψ decay electrons. Since Υ is also suppressed in Au+Au collisions, its contribution is even smaller than the uncertainty of J/Ψ decay electrons and thus is neglected here.

Although the Drell-Yan contribution is also small, it is not supposed to be affected by the QCD medium and may be important. Therefore, we scale up its contribution in p+p collisions [73] by the number of binary collisions in Au+Au collisions, and subtract its contribution from the total NPE. The Drell-Yan contribution to electrons has a hard p_T spectra, and it has been found to be very small

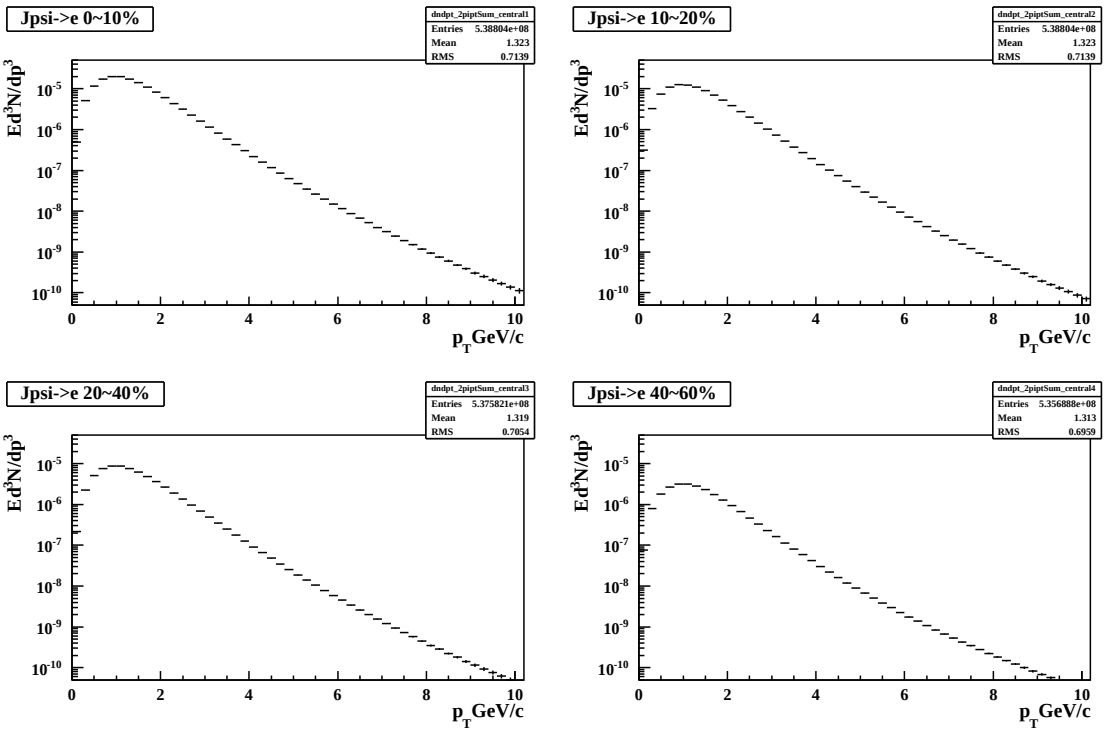

Figure 3.20: The J/Ψ decay electron spectra at middle rapidity studied by PYTHIA. The four panels represent four different centrality bins.

at low p_T, *e.g.* less than 1% at p_T=2.75 GeV/c. Its relative contribution should be even smaller at lower p_T, and thus neglected at p_T<2.75 GeV/c.

3.7 K_{e3} decay

A PHENIX study [95] concludes K_{e3} decay electrons contribute less than 10% of heavy flavor decay electrons at $p_T > 1$ GeV/c. STAR simulation studies [96] confirm this and indicate the kaon contribution is several times smaller at STAR thanks to the global DCA cut we apply, which significantly rejects kaon decay products, since kaons decay through the weak interaction and have large $c\tau$. Therefore K_{e3} decay electrons have negligible contribution to the measured electron yield in this analysis.

3.8 Efficiency studies

As discussed in the previous chapters, we can use photonic electrons to study the efficiency of a given cut. We can firstly relax the cut and then apply the cut to study the difference it makes. However, this depends on the good cancellation between the opposite sign pairs and the same sign pairs and it might be biased by possible correlations between different cuts, *e.g.* the correlation between E/p and number of BSMD strips, and one needs to use this method with care. In our analysis, we calculate cut efficiencies with Monte Carlo simulations and only use photonic electrons as a cross check.

3.8.1 Introduction to embedding

The whole procedure of Monte Carlo simulations used in STAR is called *embedding*, because the simulated tracks are embedded into real data and then analyzed. Embedding into real events is critically important for TPC tracking, because one of

the reasons for tracking inefficiency in the TPC is that two adjacent TPC hits cannot always be distinguished in a very busy environment and could be merged into one [80]. By placing simulated tracks into real events, the multi-particle and large-detector-occupancy environment in heavy ion collisions is preserved and the corresponding effects are well simulated. The simulation is based on GEANT3 [97] where Monte Carlo particles of interest go through a detailed GEANT simulation of the STAR detector. The GEANT simulations of raw detector responses, such as the TPC hits, are mixed with real data at the raw detector response level. The TPC hits, both simulated and real, are reconstructed with the same code as used in the real data production. We associate the reconstructed tracks with Monte Carlo tracks by comparing their TPC hits. We apply the same cuts to those reconstructed tracks originating from Monte Carlo tracks and calculate the cut efficiencies based on these tracks.

For some of the cuts, such as E/p and number of BSMD strips, after obtaining the efficiencies from photonic electrons, we verify that the embedding gives consistent efficiencies, or we improve the simulation. For $n\sigma_e$ distributions, accurate simulation is difficult, although the STAR simulation team is currently trying to improve this and the results look promising. The $n\sigma_e$ cut efficiencies are obtained from the multi-Gaussian fits, as discussed above.

3.8.2 Single electron efficiency

The single electron efficiency includes the detector acceptance, general tracking efficiency, and electron identification cuts efficiencies. In the embedding, electrons are simulated with flat p_T, flat η and flat ϕ distributions. Flat p_T distribution is necessary to ensure enough statistics at high p_T and thus enough precision can be achieved. Intermediate NPE spectra will be firstly calculated without re-weighting the flat p_T electrons in emebedding. Then the intermediate NPE spectra will be corrected for the finite resolution of the reconstructed p_T. In the embedding,

roughly same amounts of tracks are shifted to lower and higher p_T due to the flat input spectra. However, in reality there are more tracks being shifted to higher p_T than those being shifted lower, as a result of the falling p_T spectra at not-so-low p_T. To account for this effect, we will re-weight the input electrons in the embedding according to the intermediate NPE spectra and obtain a set of new efficiencies, which are used as the nominal values to obtain the final NPE spectra.

In Figure 3.21, we compare the η and ϕ distributions of reconstructed tracks from embedding with data. The non-uniformities in both cases are due to detector acceptances and the embedding distributions reasonably match the data. The sharp dips in the ϕ distribution are due to TPC sector boundaries and the drop in ϕ between roughly $-1 \sim 0$ rad is due to one TPC sector being removed from data production as a result of its bad calibration. The TPC tracking efficiency is shown in Figure 3.22. As mentioned before, the tracking efficiency depends on the TPC occupancy and the most central events have the lowest efficiency, as we shall see in Figure 3.25. We study the efficiencies from embedding for different centrality ranges, corresponding to the real-event analysis.

The simulated BEMC responses are also analyzed by the same codes as in the data analysis, including the BEMC Point Maker and the same track-point association algorithm. The efficiency of an electron being associated with its BEMC point is shown in Figure 3.24. As in the data analysis, the BEMC points in embedding also must have all three planes of BTOW, BSMD-η and BSMD-ϕ. In embedding, the E/p cut has a 95% efficiency over the whole p_T range, while it is 99% from data as we discussed before.

We recently improved the BSMD simulation by correctly implementing the energy leakage between adjacent BSMD-η strips, which is due to channels picking up the signals from neighboring channels (cross-talk). From the design of the BSMD, this cross-talk effect was expected to be present but small, approximately $4 \sim 5\%$ at the low η end and decreasing to 0% at the high η end of a BSMD

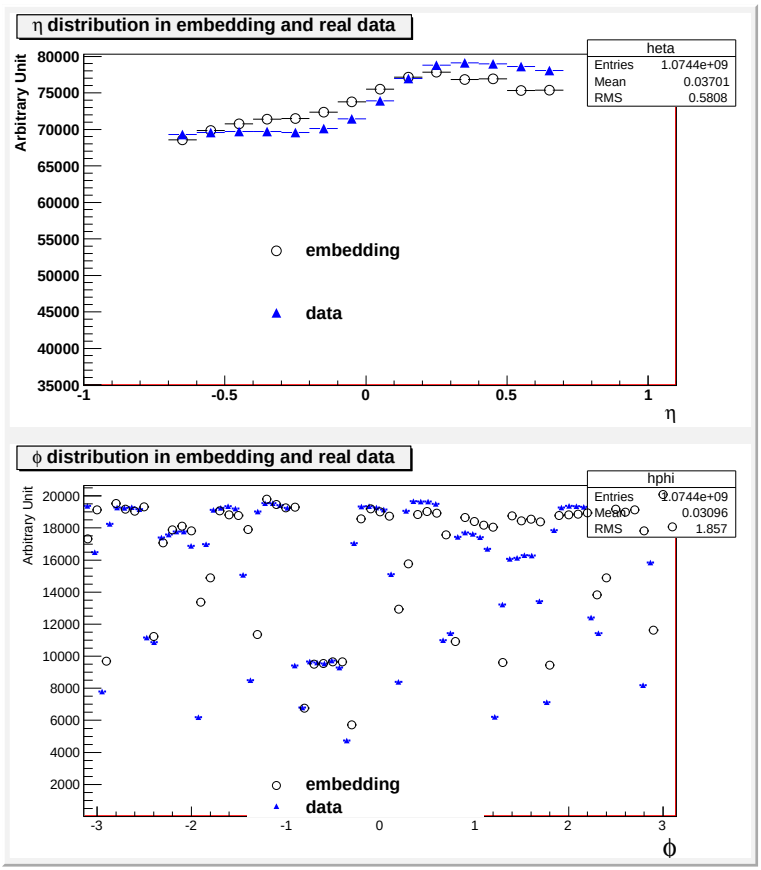

Figure 3.21: η and ϕ distributions of tracks in embedding and in data.

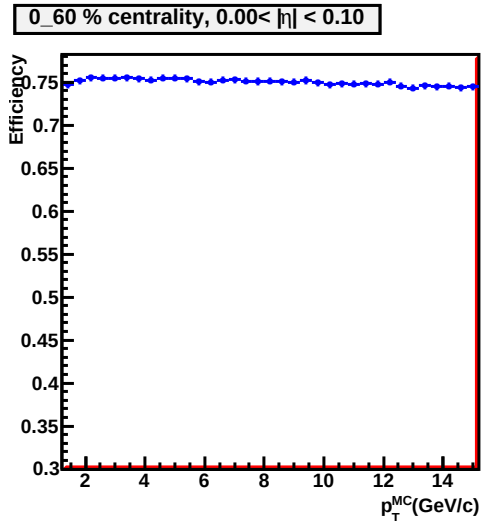

Figure 3.22: TPC tracking efficiency in 0∼60% centrality.

module [98]. We found if we introduce a 3% cross-talk at the low η end of the BSMD-η plane, and this cross-talk decreases linearly with respect to η, then the simulation can reproduce the distributions of the BSMD-η strips very well. The cross-talk for BSMD-ϕ is more complicated, but seems less important, since the simulation can reasonably reproduce the data with or without cross-talks. In Figure 3.23, we compare the number of BSMD-η and -ϕ strips for p_T 2 to 4 GeV/c from simulation with data for photonic electrons. In the photonic electron sample from data, the chance that two electrons matching to one BEMC point is small, since the energy over momentum for photonic electron, shown in Figure 3.9, peaks at one. To double check this, we make a special photonic electron sample by requiring that the opening angle in θ between the paired electrons to be larger than 0.02 rad, and smaller than 0.05 rad. In this sample, the two electrons are at least about 5 cm apart on the BSMD planes, largely reducing the chance of both firing the same BEMC point. We found consistent results, but the statistics are limited. From single electron simulation/embedding, the efficiency for an individual BSMD plane cut is around 90% at 2 to 3 GeV/c, and above 95% at above 5 GeV/c, consistent with what we obtained from data, as discussed before.

The performance of BEMC and BSMD has been studied and propagated into the embedding. To make sure the consistence, we further study the performance of BEMC and BSMD in both data and the embedding by calculating the fraction of bad channels. A bad channel is defined as a channel with number of hits less than 10% of the average. We find the combined effect of bad channels on three planes is about 20% in data and about 10% in embedding. The difference is corrected and the uncertainty in the correction procedure is accounted for. In Figure 3.24, the total BEMC related efficiency is shown. At very high p_T , this efficiency closely reflects the acceptance of the BEMC and BSMD.

As a summary to the discussion of the single electron efficiency, we plot the overall efficiencies, excluding the efficiencies of $n\sigma_e$ cuts, in each centrality range

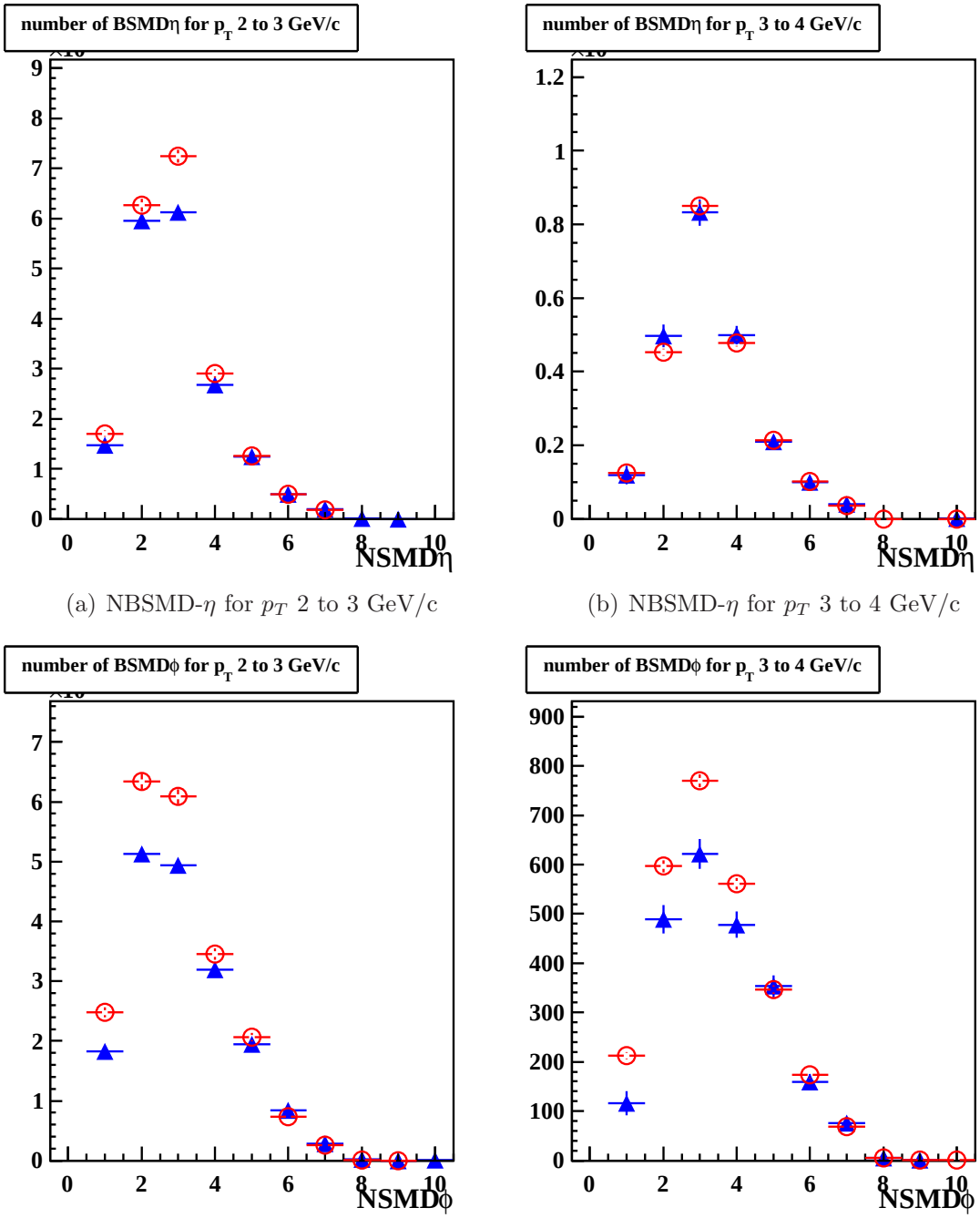

(a) NBSMD-η for p_T 2 to 3 GeV/c

(b) NBSMD-η for p_T 3 to 4 GeV/c

(c) NBSMD-ϕ for p_T 2 to 3 GeV/c

(d) NBSMD-ϕ for p_T 3 to 4 GeV/c

Figure 3.23: Number of BSMD-η and -ϕ strips for p_T 2 to 4 GeV/c. The blue triangles are from photonic electrons in data, and the red circles are from single electron simulation.

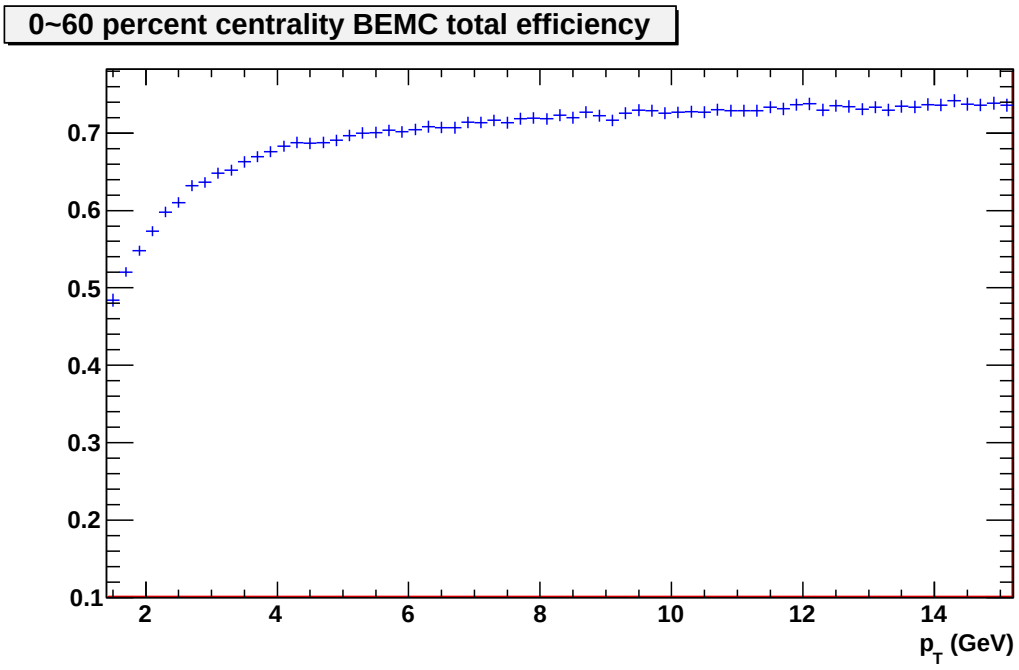

Figure 3.24: The combined efficiency for an electron matched to a BEMC point, passing both the E/p cut and number of BSMD-η and -ϕ strips cuts. This efficiency does not include any TPC-related efficiencies.

in Figure 3.25. The ordering of centrality seen in the overall efficiency is a direct result of the centrality dependence of the TPC tracking efficiency.

3.8.3 Photonic electron reconstruction efficiency

Similar to the single electron embedding, we simulate gamma conversions and π^0 Dalitz decays in the STAR detector and the decay daughters are embedded into real events. While the gamma conversions are well simulated processes, which do depend on an accurate accounting of the material budget at STAR, the original π^0 Dalitz decay in GEANT only accounts for the phase space factor of the decay process. As a result, π^0 Dalitz decay in our GEANT simulation has been modified from a simple 3-body decay in phase space to the correct Kroll-Wada decay formalism [73, 99]. After the modification, the invariant mass of Monte Carlo e^+ and e^- from Dalitz decays in simulation is shown in Figure 3.26. In comparison,

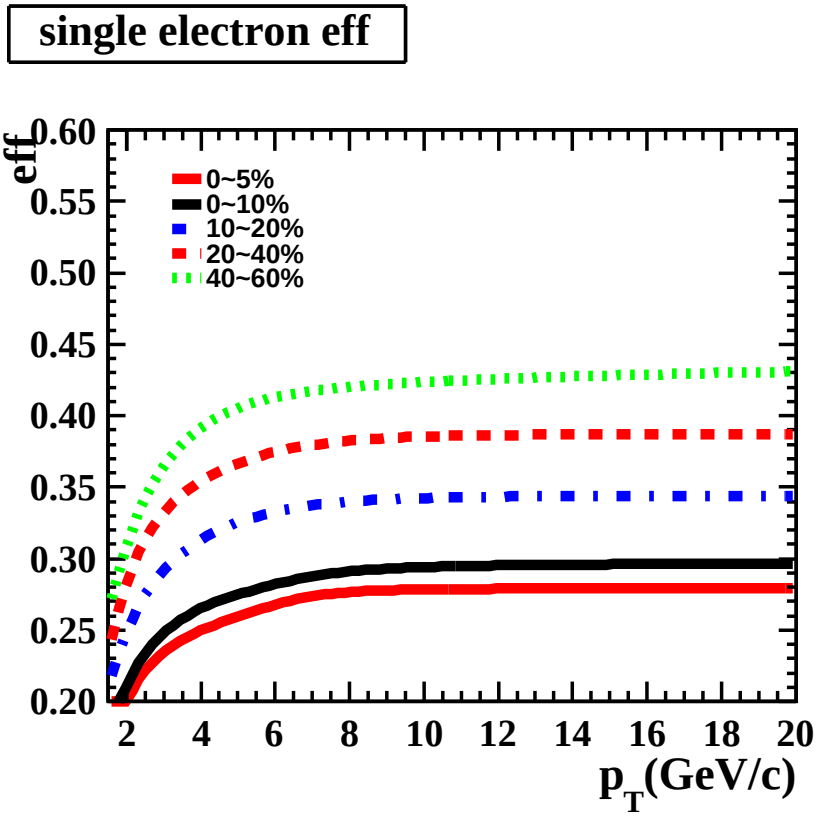

Figure 3.25: The overall electron efficiency, excluding the efficiencies of $n\sigma_e$ cuts: the overall efficiency for an electron being reconstructed by TPC with good qualities within our geometrical and kinematics range, and matched to a BEMC point, passing both the E/p cut and number of BSMD-η and -ϕ strips cuts. From bottom to top, it is for increasing centrality.

the reconstructed invariant mass and two dimensional (2-D) invariant mass distributions in simulation are shown in Figure 3.27. In the analysis, we accept a 2D invariant mass less than 0.1 GeV/c^2, which accepts the majority of π^0 Dalitz decays.

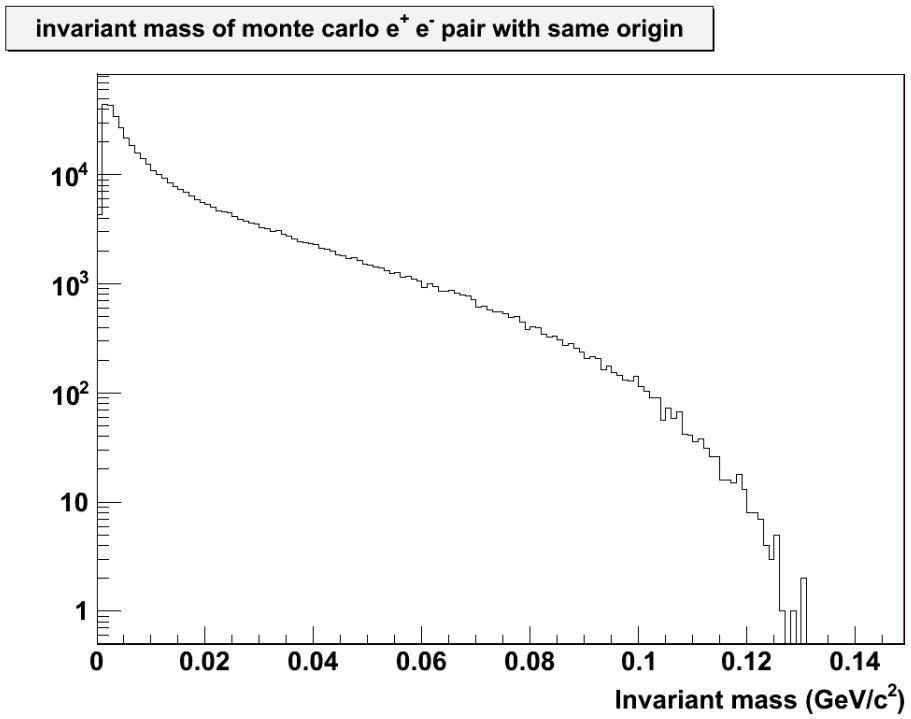

Figure 3.26: The invariant mass of e^+ and e^- pairs from the Dalitz decays in simulation.

In Figure 3.28, we show some examples of the opening angles between the Monte Carlo e^+ and e^- pairs from Dalitz decays in the simulation. The distance-of-closest-approach (DCA) between Monte Carlo e^+ and e^- pairs from Dalitz decays is zero by default, so in Figure 3.29, we show the DCA between reconstructed e^+ and e^- pairs from Dalitz decay, which represents the distance resolution. From these plots, we show that our choices of pair property cuts accept the majority of photonic electron pairs and thus the the background reconstruction efficiency does not depend significantly on accuracy of simulation.

The separated photonic electron reconstruction efficiencies for γ conversion and

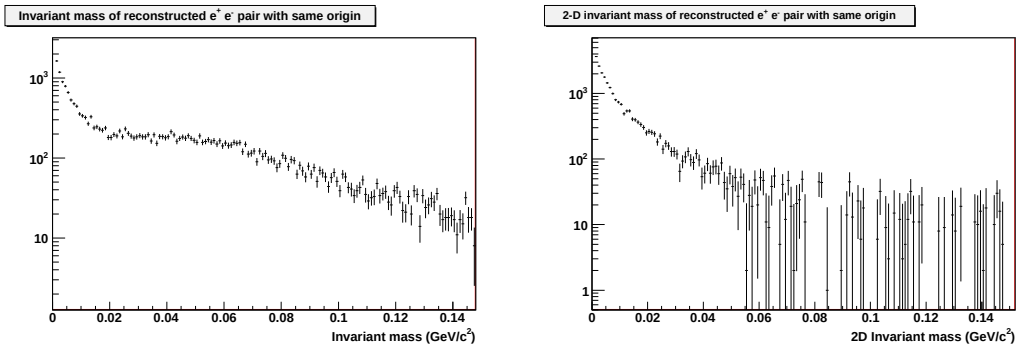

Figure 3.27: Left Plot: The invariant mass of reconstructed e^+ and e^- pairs from the Dalitz decays in simulation. Right Plot: same as the Left Plot, except plotting the 2D invariant mass.

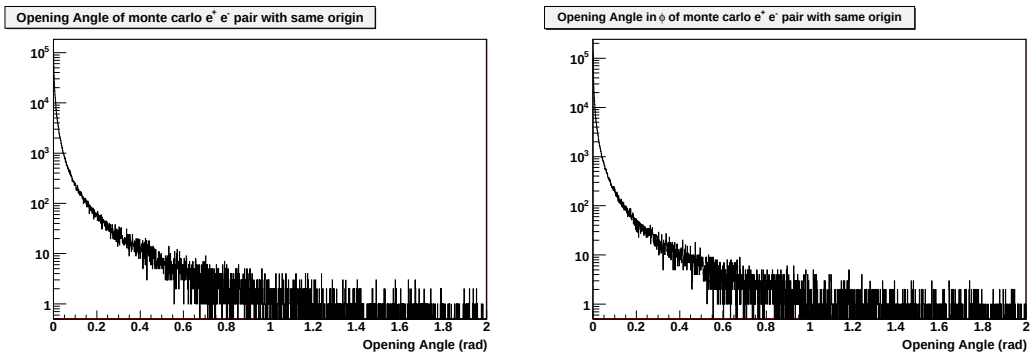

Figure 3.28: Left Plot: The opening angle of Monte Carlo e^+ and e^- pairs from the Dalitz decays in simulation. Right Plot: same as the Left Plot, except plotting the opening angle in the ϕ direction (transverse plane) alone.

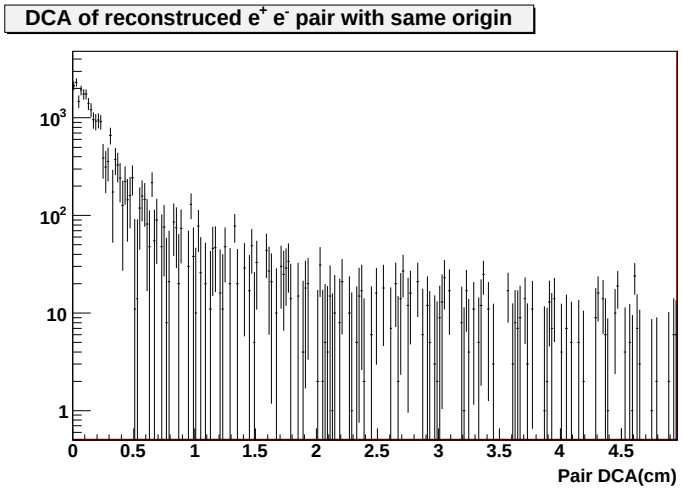

Figure 3.29: The distance-of-closest-approach of reconstructed e^+ and e^- pairs from the Dalitz decays in simulation.

π^0 Dalitz decays are studied, typical examples shown in Figure 3.30, and they are then combined together. Since photonic parents at different p_T will give rise to different properties of the daughter electron-positron pairs, the real p_T spectra of photonic parents must be correctly reflected in the embedding. We use the γ and π^0 spectra measured by the PHENIX experiment at RHIC [100] to weight the flat input γ and π^0 in the simulation. A large fraction of the photons come from $\pi^0 \rightarrow \gamma + \gamma$ decays. Figure 3.31 shows a typical ratio of the gamma conversion contribution divided by the total photonic electrons, which are identified as part of the inclusive electrons in the embedding, *i.e.* the material budget factor has been applied for gamma conversions. We have required the parent γ and π^0 to have at least p_T>0.2 GeV, because 1) low p_T γ and π^0 should have very small probability to produce high p_T electrons 2) there are no reliable measurements below this p_T and the weighting functions used here continue increasing unrealistically at lower p_T .

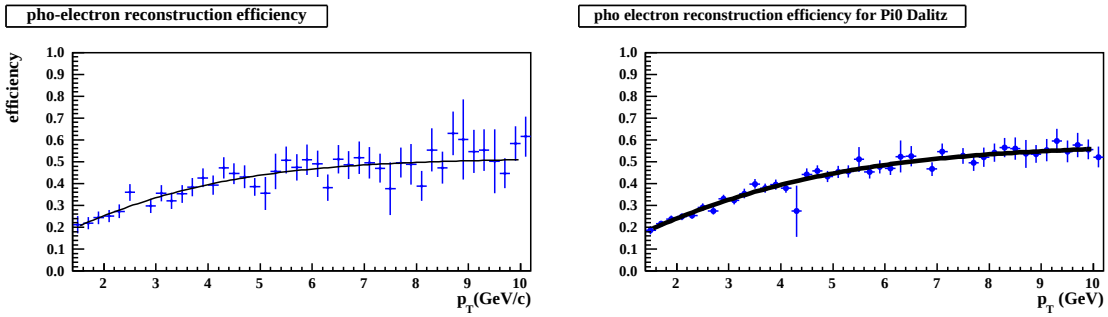

(a) efficiency for γ conversion

(b) efficiency for π^0 Dalitz decays

Figure 3.30: The overall photonic electron reconstruction efficiency for γ conversion on the left and for π^0 Dalitz decays on the right, in embedding, centrality 0-10%.

In summary, the photonic electron reconstruction efficiency ε_{PE} from combined γ and π^0 in embedding is shown in Figure 3.32. The fitting function used in the plots is $\frac{p_0}{e^{-(p_T-p_1)/p_2}+1} + p_3$, where p_0 to p_3 are fitting parameters.

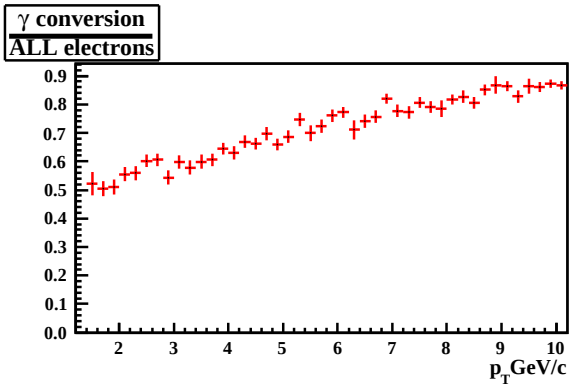

Figure 3.31: Ratio of the gamma conversion electrons to the total photonic electrons that are identified as part of the inclusive electrons, in the embedding for centrality 0∼10%. Binomial errors are used. The γ conversion fractional contribution rises with p_T as a result of the direct photons becoming dominant at high p_T.

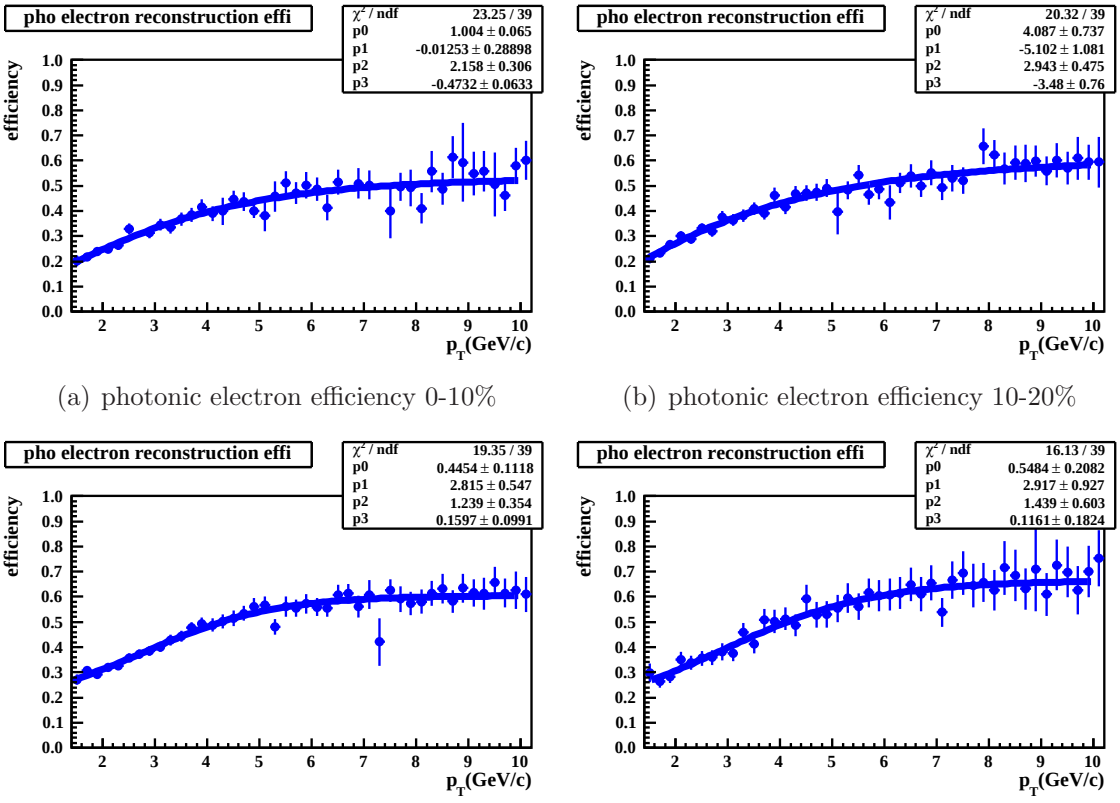

(a) photonic electron efficiency 0-10%

(b) photonic electron efficiency 10-20%

(c) photonic electron efficiency 20-40%

(d) photonic electron efficiency 40-60%

Figure 3.32: The overall photonic electron reconstruction efficiency based on combined γ and π^0 in embedding in each centrality

3.9 High tower trigger efficiency

We can obtain the High tower trigger efficiency from either MinBias-High Tower comparisons or from the embedding. Our nominal method is the former one. For the first High Tower trigger, NPE11, we directly compare the spectrum of electrons in the inclusive electron sample in NPE11 with that in MinBias, and this ratio is shown in Figure 3.33. There is not enough statistics in NPE11 at p_T below 2 GeV/c, while MinBias events run out of statistics at p_T above 5 GeV/c, *esp.* not enough for the electron purity determination. The p_T distribution of the ratio of these two spectra, NPE11 divided by MinBias, presents the trigger efficiency of NPE11. An error function can usually be used to describe the turn-on of a threshold, *e.g.* the trigger threshold here. The error function erf, with two parameters, is -1 at negative infinity and +1 at positive infinity. Therefore, we use $0.5 \times (1 + erf)$ to fit the ratio distribution, so that it is approaching zero at low p_T and approaching unity at high p_T . One of the parameters, labeled as "1/2-eff p_T" since it is the p_T where the efficiency is 50% (roughly the "turn-on" point of the trigger), is fitted to be around 3.0 GeV/c, approximately 0.5 GeV higher than the E_T cut used in the high tower trigger. The other parameter, labeled as "width", indicating the rough range of trigger inefficiency, is fitted to be around 0.69 GeV/c. As discussed before, we rely on fittings to the $n\sigma_e$ distributions to obtain the purities of inclusive electrons and to calculate the number of electrons in the inclusive electron sample. Since the $n\sigma_e$ distributions are different in High Tower and in MinBias, due to the fact that BEMC enhances electrons, the electron purities are also different in the two triggers. Furthermore, the uncertainties on the resulting purities are also different in High Tower and MinBias sample, and are not correlated. Figure 3.33, however, only includes statistical uncertainties. As we shall see, we do not use any p_T range where the statistical precision is very limited.

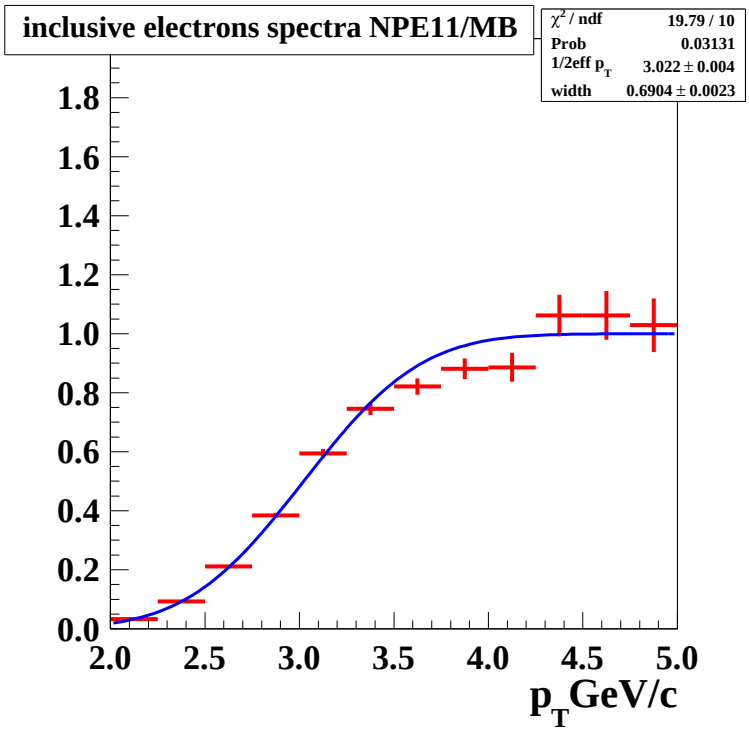

Figure 3.33: The spectrum of pure electrons in the inclusive electron sample in the NPE11 trigger divided by that in the MinBias trigger. The event centrality is 0 to 60%.

Several aspects of the trigger efficiency have been cross checked. First of all, there are substantial energy deposits in the BEMC from the underlying event in Au+Au collisions. These energy deposits are random, but they do depend on the particle density and thus on the event centrality. We repeat the fitting procedure for each individual centrality and compare each individual result with the average one for 0 to 60% centrality, as shown in Figure 3.34. As expected, a systematic evolution of the trigger efficiency with respect to centrality is seen. The most central events have a higher trigger efficiency than average, since there are more random energy depositions in the more central events, whereas the most peripheral events have lowest trigger efficiency. We find that for electron $p_T > 3.5$ GeV/c the differences are smaller than 5%.

Secondly, the inclusive electrons include both photonic electrons and non-photonic electrons, which do not necessarily have exactly the same trigger efficiency. Thus, we also check the trigger efficiency based on photonic electron spectrum, as shown in Figure 3.35. The photonic electron sample is based on opposite sign pairs minus same sign pairs, which provides pure photonic electrons without hadron contamination, so there is no issue with the electron purity estimation. Since the nσ_e cuts used in High Tower and MinBias triggers are exactly the same, there is no issue with the nσ_e cut efficiency estimation either. As a result, statistical error bars represent the true uncertainties, and thus the goodness-of-fit is very close to one ($\chi^2/ndf = 10.04/10$). However, we still use the trigger efficiency based on inclusive electrons as the nominal value. Comparison between the trigger efficiency based on photonic electrons and the nominal efficiency indicates they are almost identical with each other for $p_T > 3.5$ GeV/c.

In short, by comparing NPE11 trigger efficiencies obtained with different electrons samples, we now have a good control of the NPE11 trigger efficiency at $p_T > 3.5$ GeV/c, so we will begin to use NPE11 data at $p_T = 3.5$ GeV/c, without using the MinBias data.

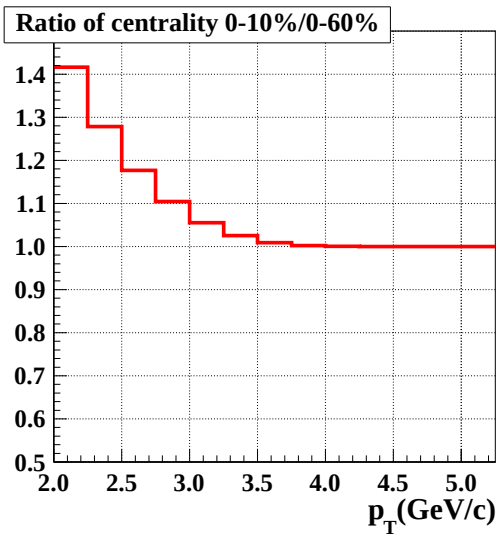

(a) NPE11 trigger efficiency 0-10%/0-60%

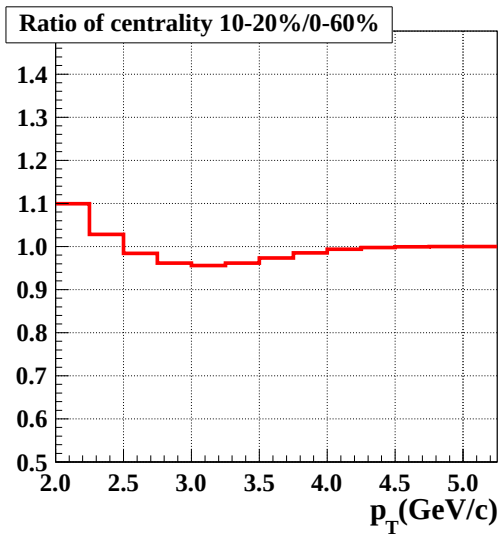

(b) NPE11 trigger efficiency 10-20%/0-60%

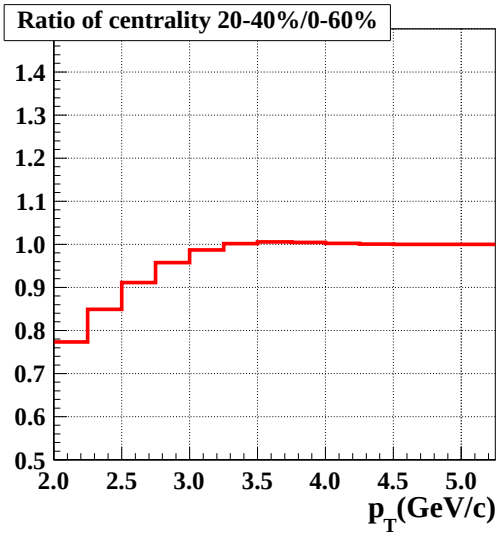

(c) NPE11 trigger efficiency 20-40%/0-60%

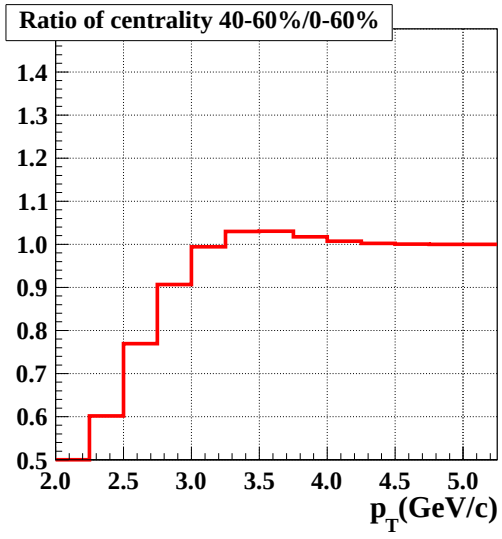

(d) NPE11 trigger efficiency 40-60%/0-60%

Figure 3.34: The NPE11 trigger efficiency based on inclusive electron spectrum in each centrality divided by that in 0∼60% centrality. The four panels represent four individual centrality bins.

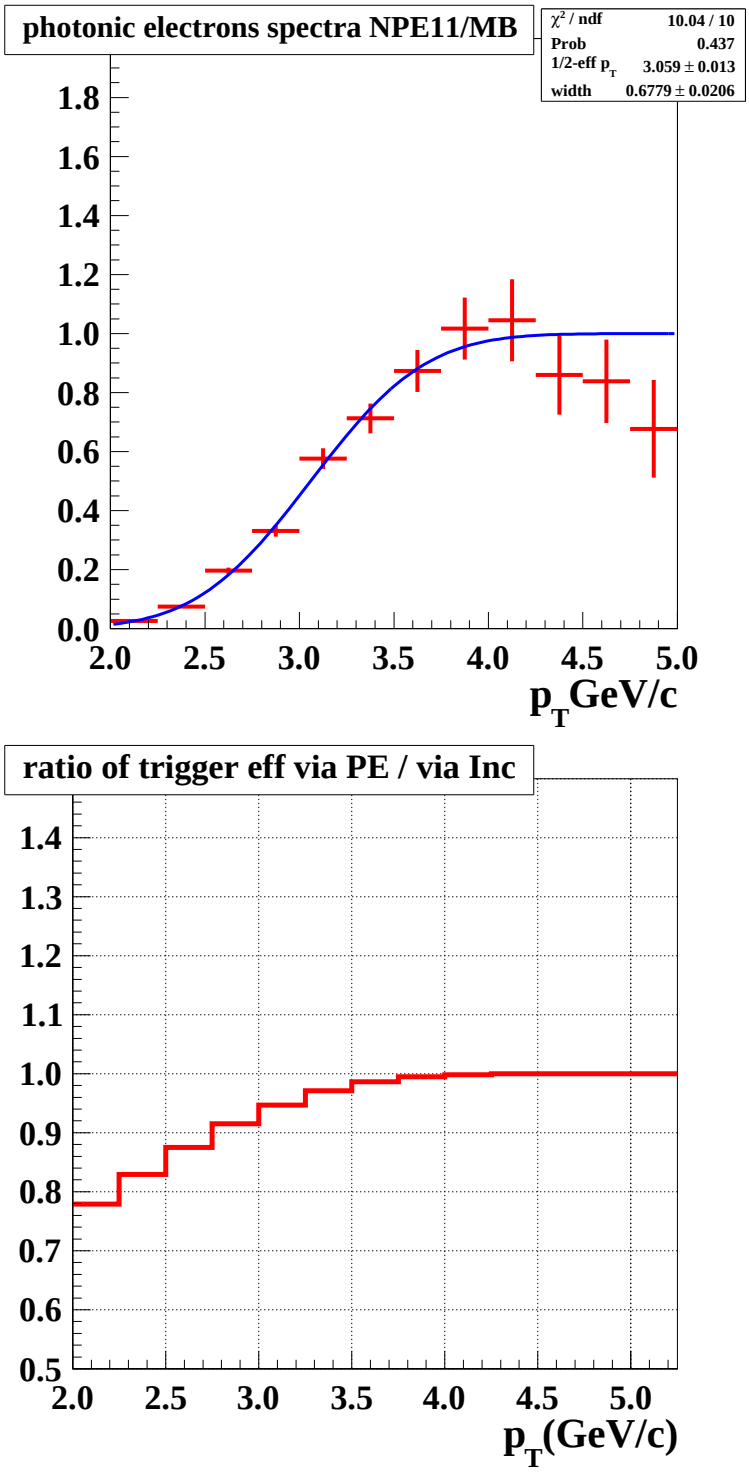

Figure 3.35: Upper: The NPE11 trigger efficiency based on photonic electron spectrum, fitted by error function. Lower: The NPE11 trigger efficiency based on photonic electron spectrum divided by the nominal trigger efficiency.

Now we repeat a similar procedure for the second High Tower trigger, NPE15. Since the MinBias trigger is essentially out of statistics, we compare NPE15 with NPE11 instead, with the raw NPE11 inclusive and photonic electron spectra being corrected by the NPE11 trigger efficiency obtained above. We show the NPE15 trigger efficiency based on the electrons in the inclusive electron sample in Figure 3.36. We compare the NPE15 trigger efficiency obtained for each individual centrality with the nominal one in 0 to 60% in Figure 3.37, where the centrality-dependent deviations from the nominal one follow the same pattern as seen for the NPE11 trigger. We also compare the efficiency based on photonic electrons with the nominal one in Figure 3.38. For p_T>5 GeV/c, the largest deviation, about 15%, from the nominal efficiency is seen in Figure 3.38. Based on these comparisons, we will begin to use NPE15 at p_T>5 GeV/c, dropping NPE11 at the same time, with a proper systematic uncertainty assigned to cover the difference.

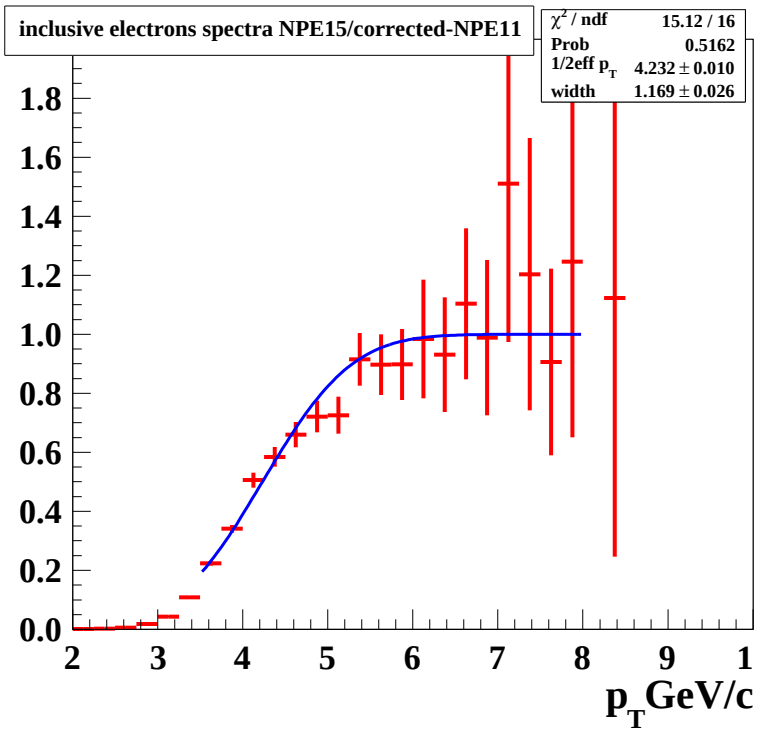

Figure 3.36: The spectrum of electrons in the inclusive electron sample in NPE15 trigger divided by that in NPE11 trigger after correction. The event centrality is 0 to 60%.

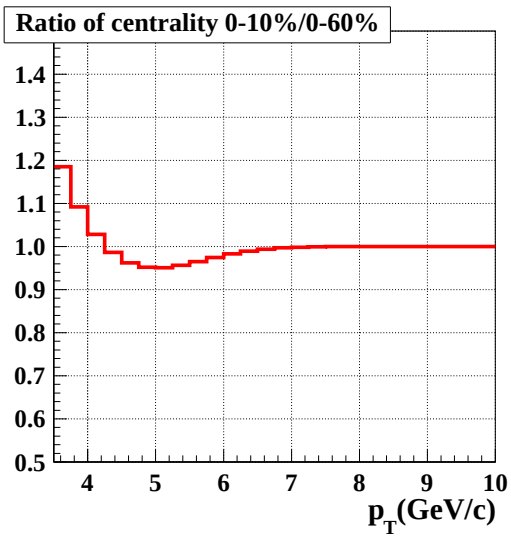

(a) NPE15 trigger efficiency 0-10%/0-60%

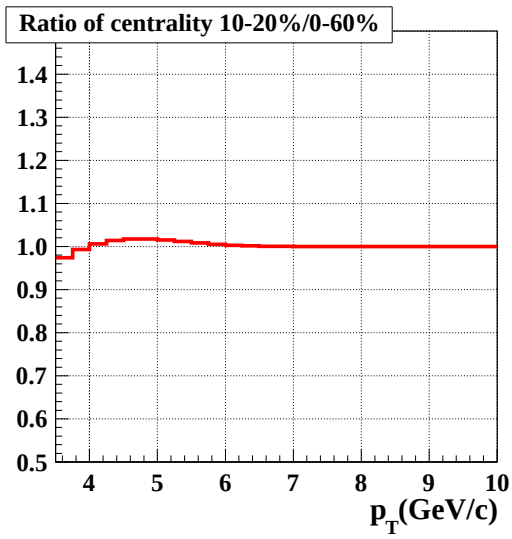

(b) NPE15 trigger efficiency 10-20%/0-60%

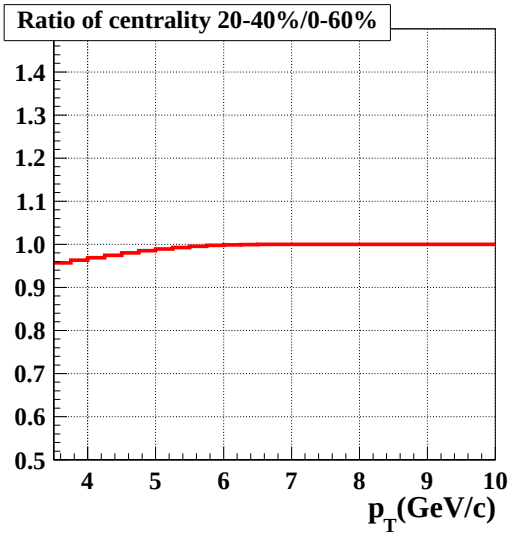

(c) NPE15 trigger efficiency 20-40%/0-60%

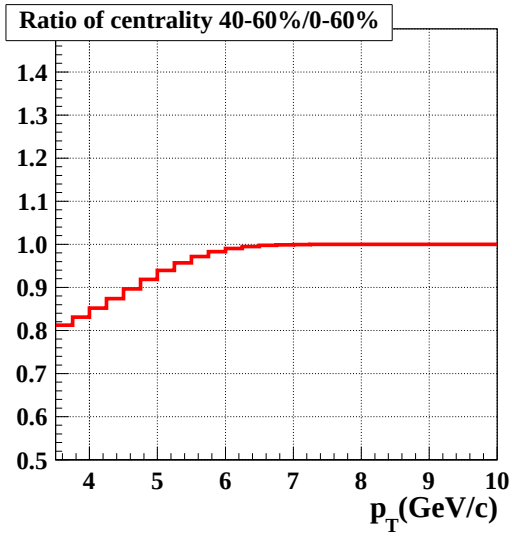

(d) NPE15 trigger efficiency 40-60%/0-60%

Figure 3.37: The NPE15 trigger efficiency based on inclusive electron spectrum in each centrality divided by that in centrality range 0∼60%. The four panels represent four different centrality bins.

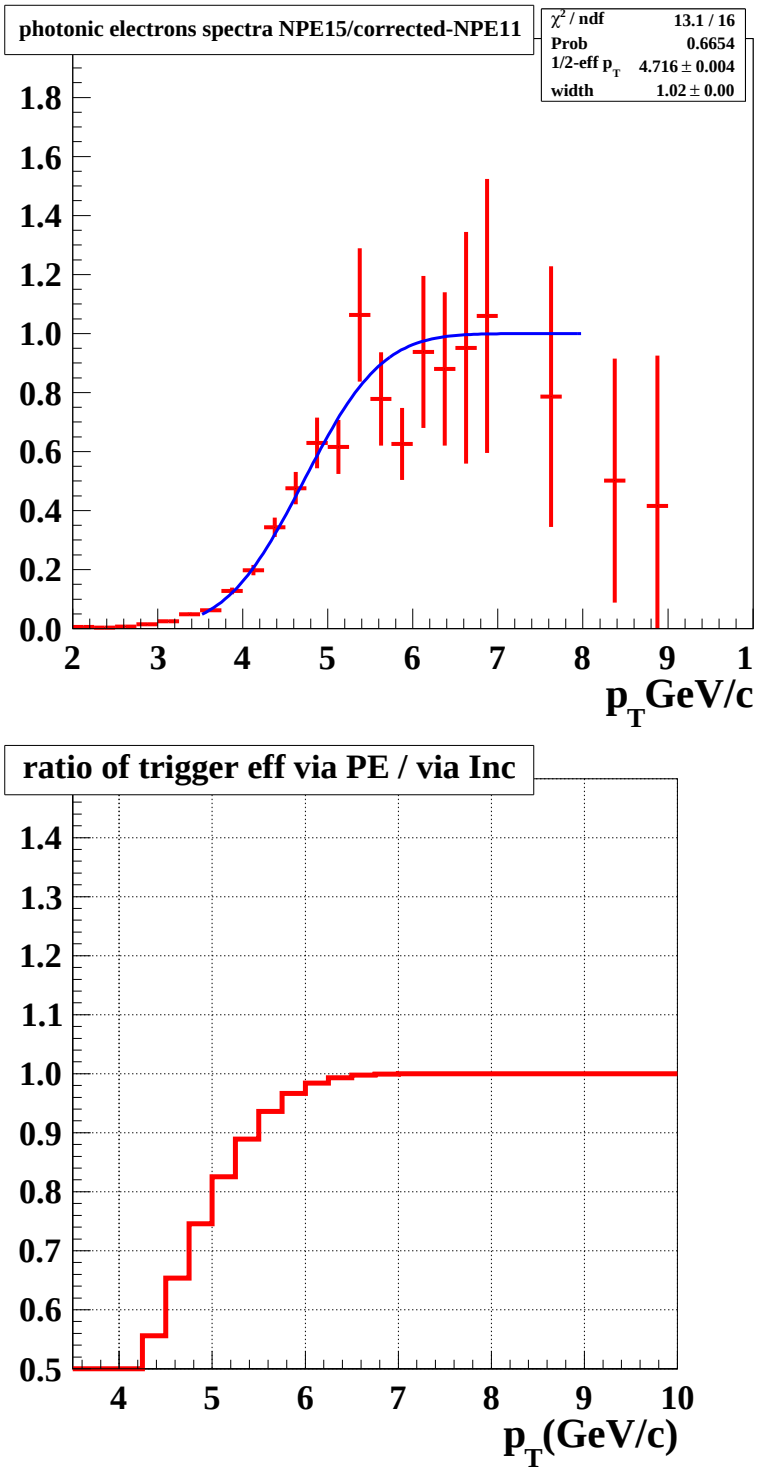

Figure 3.38: Upper: The NPE15 trigger efficiency based on photonic electron spectrum, fitted by error function. Lower: The NPE15 trigger efficiency based on photonic electron spectrum divided by the nominal efficiency.

3.10 Systematic uncertainties

3.10.1 From photonic electron reconstruction efficiency

There are several sources for uncertainties in the photonic electron reconstructions, including the input γ and π^0 spectra used as the weights, the partner electron reconstruction/selection, and the photonic electron pair selection criteria. We have demonstrated that the criteria to select the photonic electron pairs in this analysis are loose enough so that our results will not be sensitive to details of cuts. We also vary parameters and criteria directly related to the former two sources. For example, the input spectra have been varied from π^0+ direct γ to π^0 alone, and also to $\pi^0 + 2\times$ direct γ, etc. The photonic electron reconstruction efficiency responds to these variations in complicated ways, but almost always within 10% of the nominal values. The ratio of electrons from π^0 Dalitz contribution to those from γ conversions has also been varied up and down by a factor of two, and the combined photonic electron efficiency changes by less than 5%. Overall, we assign a 10% systematic uncertainty to the photonic electron reconstruction efficiencies, and after being propagated to the NPE spectra, results in a relative uncertainty of about 10% to 15% depending on p_T.

3.10.2 From single electron efficiency

Another very important source of systematic uncertainty is from the single electron efficiency, *esp.* from nσ_e fittings and the High Tower trigger efficiency. To understand the former, we relax the nσ_e cuts used in the analysis so that the efficiency of the cuts are higher but more hadrons are allowed to leak into the inclusive electron sample. The difference between the NPE spectra with relaxed cuts and that with nominal cuts is regarded as the systematic uncertainty and we find it is typically at approximately 10% level, but it occasionally becomes more than 20%. As aforementioned, we corrected the BEMC and BSMD performance

in the embedding to match that in data, and this procedure gives rise to systematic uncertainties. We re-defined a bad channel as a channel with number of hits less than 50% of the average, a tight requirement, to obtain the upper limit of the correction. We obtained the lower limit by assuming no correction is needed. This systematic uncertainty is roughly 10%. In addition, we studied both electrons and positrons, separately, in the embedding and the small difference between them is accounted for in the systematic uncertainty.

The uncertainty on the High Tower trigger efficiency, coming from the various ways we calculate the trigger efficiency, only exists at the trigger transitions and it has been fully discussed above. Namely, we start to use NPE11 at p_T >3.5 GeV/c, and there is only about 2% uncertainty on the trigger efficiency; however, the trigger efficiency for NPE15 has a $\frac{1}{0.84} - 1 \sim 20\%$ uncertainty at p_T =5.25 GeV and a $\frac{1}{0.95} - 1 \sim 5\%$ uncertainty at p_T =5.75 GeV due to the discrepancy between the efficiency based on photonic electrons and the nominal efficiency. The differences on the trigger efficiency found in individual centrality are much smaller and neglected.

The uncertainties from other sources, including number of BSMD strips, E/p, and the TPC tracking, typically are at most a few percent, and are neglected. For example, based on the comparison of BSMD strips distributions in data and in embedding, as discussed before, we find the uncertainty of the efficiency of the number of BSMD strips cut is on the level of approximately 4%, and no obvious dependence on p_T. Similarly, the uncertainty is about 1% for the E/p cut efficiency, thanks to our rather loose cut choices for both E/p and BSMD.

3.10.3 From J/Ψ and other feed down

The systematic uncertainty for J/Ψ feed down is due to lack of experimental data at full rapidity range, which overwhelms the uncertainty of the fitted J/Ψ spec-

tra at mid-rapidity [90]. This systematic uncertainty is obtained using different p_T ranges for PYTHIA normalization, which could be as large as 30% as mentioned previously. Figure 3.39 shows the J/Ψ decay electrons divided by the total NPE, and only this J/Ψ uncertainty due to normalization is shown, in order to emphasize it. There is a 50% uncertainty for the Drell-Yan contribution, but this is already included as part of the statistical error.

3.11 Additional ingredients for NPE R_{AA}

To obtain the NPE Nuclear Modification Factor R_{AA}, the NPE spectrum in p+p collisions $E\frac{d^3\sigma_{pp}}{d\vec{p}^3}$ and the average number of binary nucleon-nucleon collisions for each Au+Au centrality class must be utilized, as in Equation 3.11.5,

$$R_{AA}^{NPE}(p_T) = \frac{dN_{AA}^2/(dp_T dy)}{< N_{coll} > dN_{pp}^2/(dp_T dy)} = \frac{\frac{1}{2\pi}\frac{d^2N_{AA}}{p_T dp_T dy}}{< N_{coll} > \frac{1}{2\pi}\frac{d^2N_{pp}}{p_T dp_T dy}} \qquad (3.11.5)$$

where $\frac{1}{2\pi}\frac{d^2N_{pp}}{p_T dp_T dy} = E\frac{d^3\sigma_{pp}}{d\vec{p}^3}/\sigma_{pp}$, and we use σ_{pp} = 42mb, consistent with the Glauber calculations where the number of binary collisions $< N_{coll} >$ are obtained.

A precision measurement of the NPE spectrum in $p+p$ collisions at $\sqrt{s}$ = 200 GeV has already been published recently based on STAR data taken during RHIC Run05 and Run08 [73], as shown in Figure 3.40, and is also listed in Table 3.5. A pQCD prediction [59] is found to be consistent with the measurements. This p+p spectrum has a 8.1% global uncertainty in additional to point-by-point systematic uncertainties, which are typically close to 20% but as much as 34% at p_T=7 GeV/c and 66% at p_T=9 GeV/c. The number of binary collisions $< N_{coll} >$ also gives rise to considerable uncertainty in the peripheral centrality bins, as shown in Table 3.6.

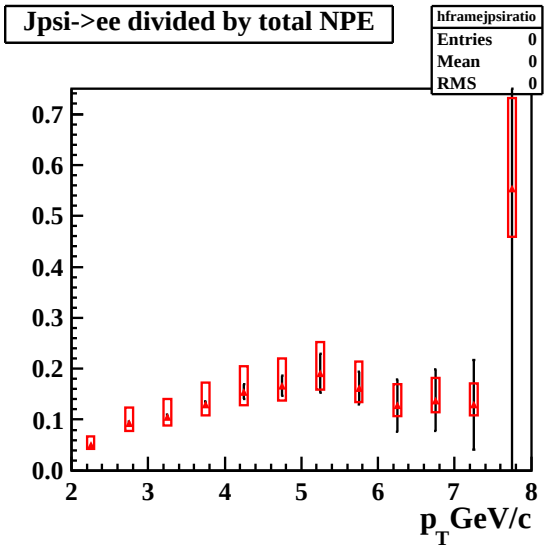

(a) $(J/\Psi \rightarrow e)$/NPE for centrality 0% to 5%

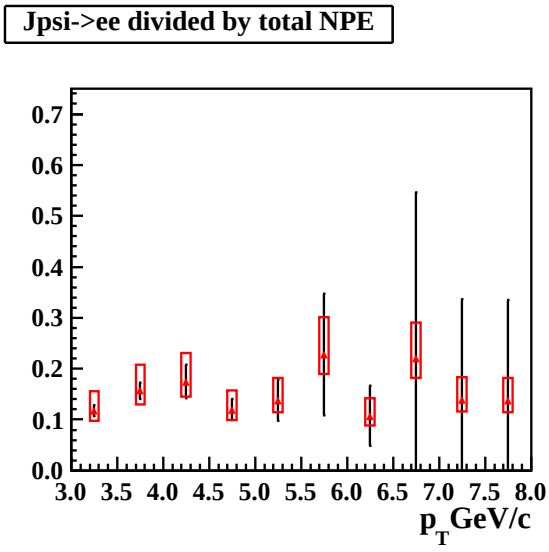

(b) $(J/\Psi \rightarrow e)$/NPE for centrality 0% to 10%

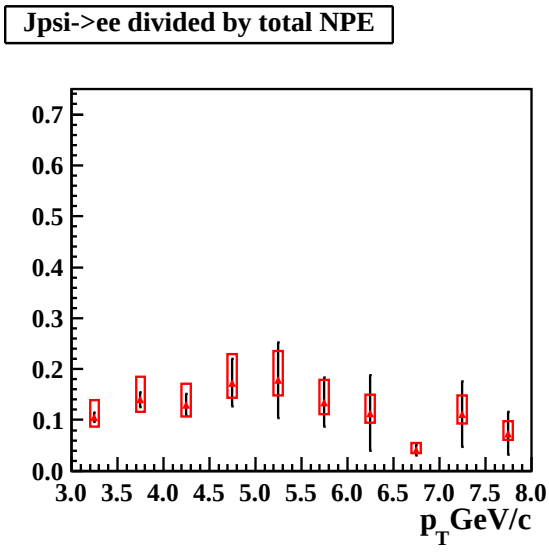

(c) $(J/\Psi \rightarrow e)$/NPE for centrality 10% to 20%

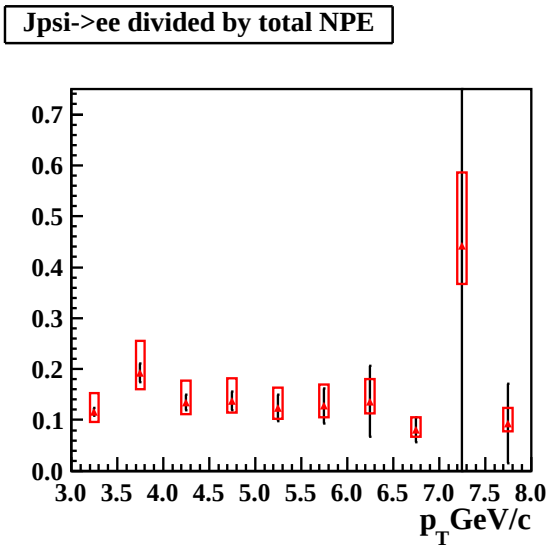

(d) $(J/\Psi \rightarrow e)$/NPE for centrality 20% to 40%

Figure 3.39: Representative plots of J/Ψ decay electron divided by total NPE for different centrality. The systematic uncertainties come from the different choices of normalization range.

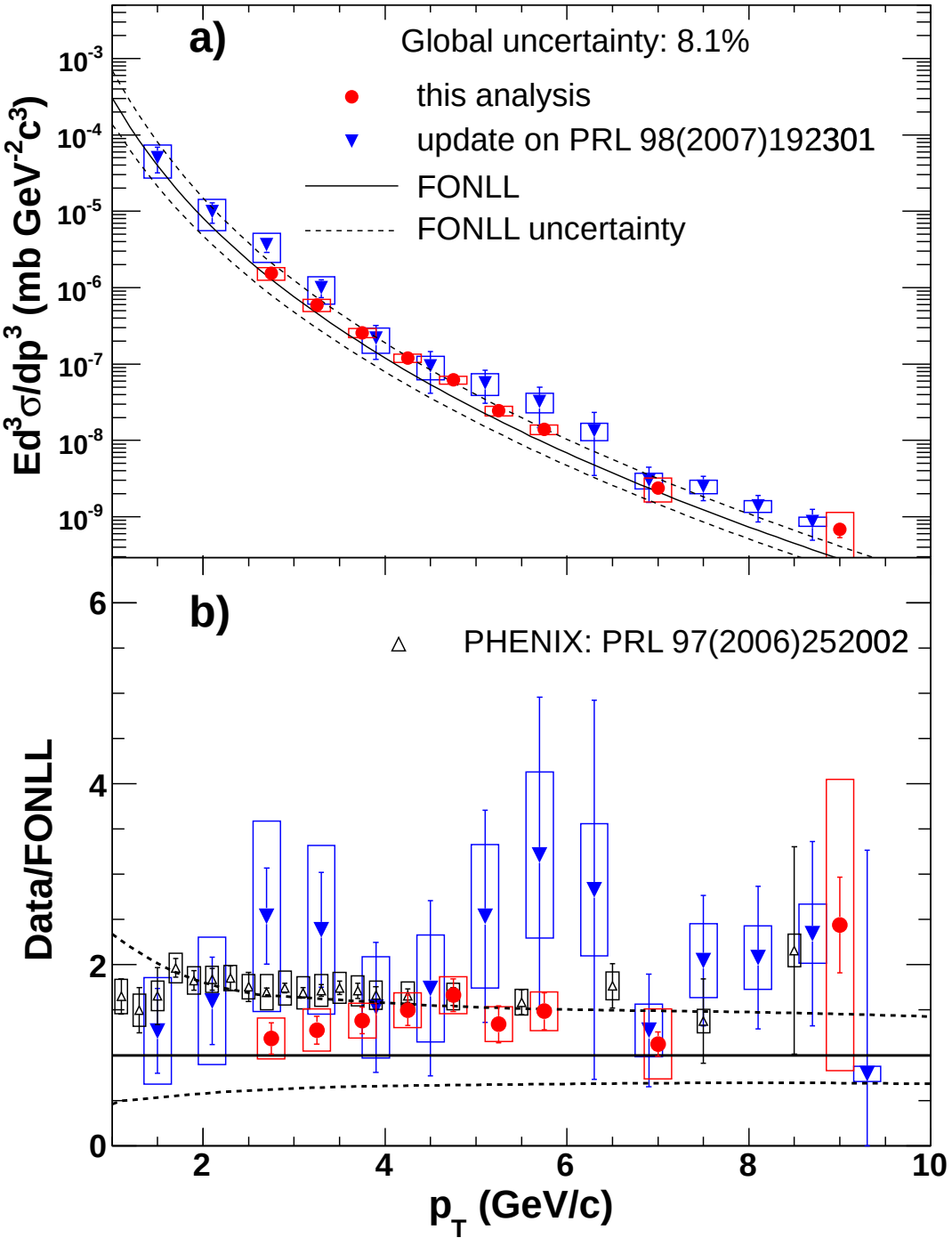

Figure 3.40: (color online) (a) NPE invariant cross section in $p + p$ collisions from a previous STAR measurement [101](closed triangles), a PHENIX measurement [102] (open triangles) and the recent STAR measurement [73] (closed circles). (b) Comparison to the FONLL calculations in [59]. Figure taken from [73].

Table 3.5: Invariant cross section for non-photonic electron production ($\frac{e^+ + e^-}{2}$) in $p+p$ collisions measured in [73] and used for this analysis.

p_T(GeV/c)	$E\frac{d^3\sigma}{d\vec{p}^3}(mb\ GeV^{-2}\ c^3)$	stat. uncertainty	syst. uncertainty
2.75	1.536747e-006	2.261030e-007	2.946275e-007
3.25	5.944377e-007	7.145496e-008	1.085212e-007
3.75	2.564046e-007	2.716573e-008	3.560173e-008
4.25	1.201271e-007	1.340690e-008	1.549221e-008
4.75	6.186093e-008	6.731042e-009	7.622289e-009
5.25	2.450933e-008	3.723545e-009	3.498343e-009
5.75	1.397378e-008	1.900307e-009	2.003147e-009
7.00	2.384259e-009	2.850461e-010	8.178320e-010
9.00	6.858185e-010	1.481453e-010	4.521734e-010

Table 3.6: Number of binary nucleon-nucleon collisions for each Au+Au centrality [103]

Centrality	N_{binary}	Uncertainty
0∼5%	1048.11384	27.46719
0∼10%	941.23714	26.27357
10∼20%	593.66913	30.17927
20∼40%	290.87634	30.46602
40∼60%	91.33495	20.00852

3.12 Results and discussion

3.12.1 NPE p_T spectrum and R_{AA} Results

The NPE spectrum can be written as Equation 3.12.6, and the NPE p_T spectrum is calculated using Equation 3.12.7.

$$E\frac{d^3N_{AA}^{NPE}}{d\vec{p}^3} = \frac{1}{2\pi}\,\frac{d^2N_{AA}^{NPE}}{p_T dp_T dy}\,\{1+\sum_{n=1}^{\infty} 2v_n\cos[n(\phi-\Psi_r)\} \tag{3.12.6}$$

$$\begin{aligned}\frac{1}{2\pi}\,\frac{d^2N_{AA}^{NPE}}{p_T dp_T dy} &= \frac{1}{2\pi}\,\frac{N^{NPE}}{\delta_{binshift}\,N_{event}\,p_T\,\Delta p_T\,\Delta y} \\ &= \frac{1}{2\pi}\,\frac{N_{inc}\cdot purity - N_{PE}^{rec}/\varepsilon_{PE}}{\varepsilon_e\,\delta_{binshift}\,N_{event}\,p_T\,\Delta p_T\,\Delta y}\end{aligned} \tag{3.12.7}$$

where $\Delta y = 1.4$ since we approximate electron rapidity with electron pseudo-rapidity, and we have extensively discussed the counting of N_{event} in both MinBias and High Tower triggers. What we directly measure in the analysis is the average NPE cross section in each p_T bin, whereas what we want to represent in terms of spectra is the NPE cross section at the exact center of each p_T bin, which are two different variables. A shifting factor $\delta_{binshift}$ is used to convert the former to the latter. $\delta_{binshift}$ is determined by the spectrum shape, *esp.* the deviations from linearity, whereas the spectrum scale is not important. We assume that the spectrum shape is of the functional form Equation 3.12.8 and indeed we find that the raw NPE spectra can be fitted very well with such a functional form (very small χ^2/ndf). Based on the fitted spectra, we calculate a tentative set of $\delta_{binshift}$ by dividing the bin average values by the values at the center of each p_T bin. We apply these tentative $\delta_{binshift}$ to obtain new spectra and fit the new spectra again and obtain a new set of $\delta_{binshift}$. We repeat the procedure for three iterations, after which the shifting factors $\delta_{binshift}$ are stabilized. The final $\delta_{binshift}$ factors

Table 3.7: $\delta_{binshift}$: p_T bin average of NPE cross section divided by NPE cross section values at the center of each p_T bin

p_T(GeV/c)	2.75	3.25	3.75	4.25	4.75	5.25	5.75	7.00	9.00
$0 \sim 5\%$	1.07	1.06	1.05	1.04	1.03	1.03	1.02	1.30	N/A
$0 \sim 10\%$	1.07	1.06	1.05	1.04	1.03	1.03	1.02	1.32	1.21
$10 \sim 20\%$	1.07	1.06	1.04	1.03	1.02	1.02	1.02	1.26	1.16
$20 \sim 40\%$	1.06	1.05	1.04	1.03	1.03	1.02	1.02	1.26	1.16
$40 \sim 60\%$	1.06	1.05	1.04	1.03	1.03	1.02	1.02	1.27	1.17

are listed in Table 3.7.

$$\frac{1}{2\pi}\frac{d^2N_{AA}^{NPE}}{p_T dp_T dy} = \frac{A}{(1+p_T/p_0)^n} \tag{3.12.8}$$

After the $\delta_{binshift}$ corrections, Figure 3.41 to 3.45 show the final spectra of non-photonic electrons from the decays of open heavy flavor hadrons in Au+Au collisions in different centrality bins and the corresponding nuclear modification factor R_{AA}. Scaled NPE spectra in p+p collisions are also plotted for comparison, but their systematic uncertainties are not drawn in the figure in order to give a clear view of the Au+Au results. The NPE production is found to be highly suppressed in central and semi-central Au+Au collisions, and moderately suppressed in semi-peripheral collisions.

3.12.2 Model comparison

Now we compare our results to some recent model calculations. As we discussed in the Introduction chapter, early model calculations indicate that radiative energy loss alone cannot explain the large heavy flavor electron suppression observed experimentally. Many efforts have been made to improve model calculations, and at the same time, additional mechanisms have also been proposed. Particularly, collisional energy losses due to heavy quark elastic scatterings are thought to be very important and the details of such processes are carefully examined.

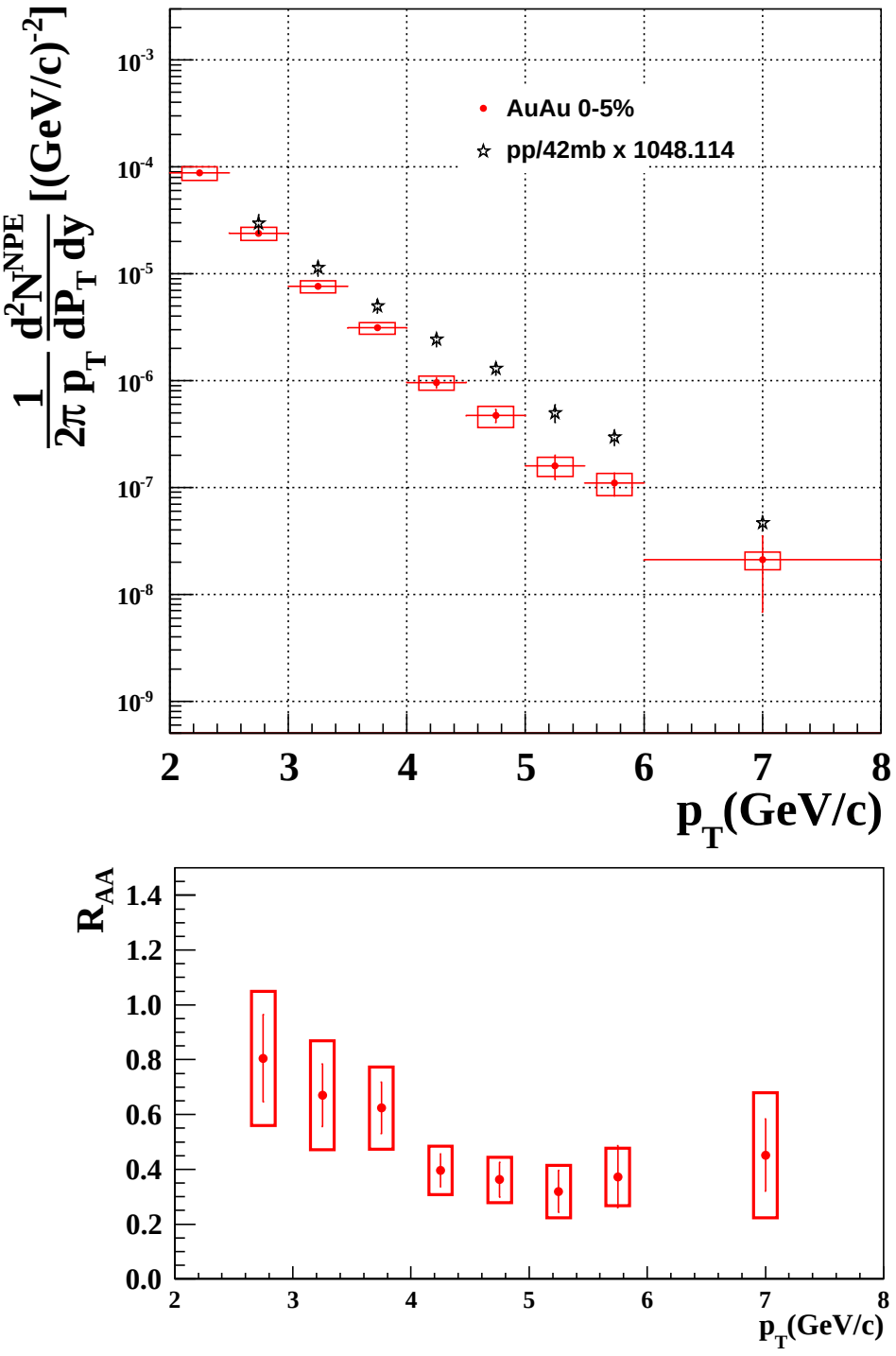

Figure 3.41: The NPE spectrum and R_{AA} in 0 to 5% centrality.

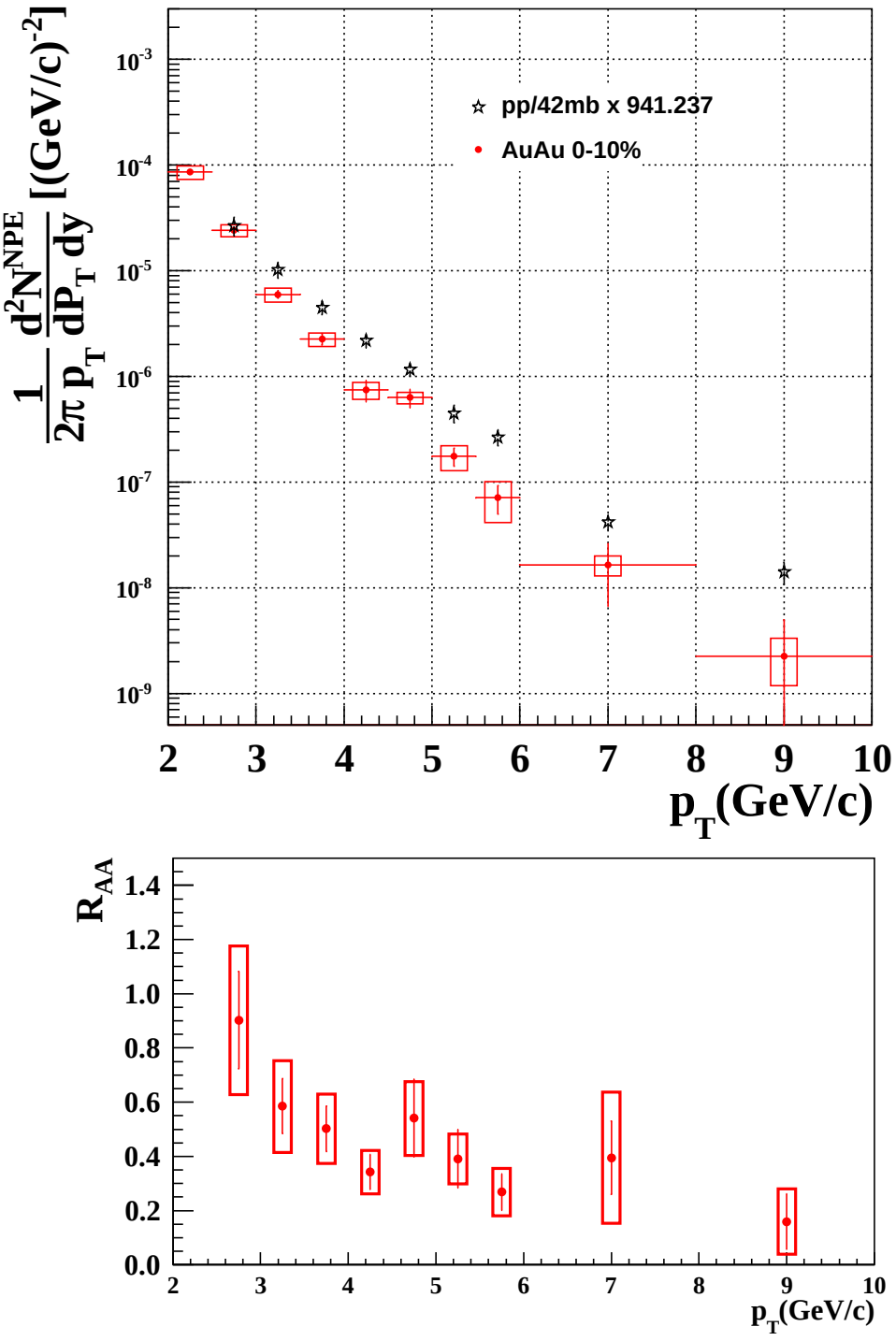

Figure 3.42: The NPE spectrum and R_{AA} in 0 to 10% centrality.

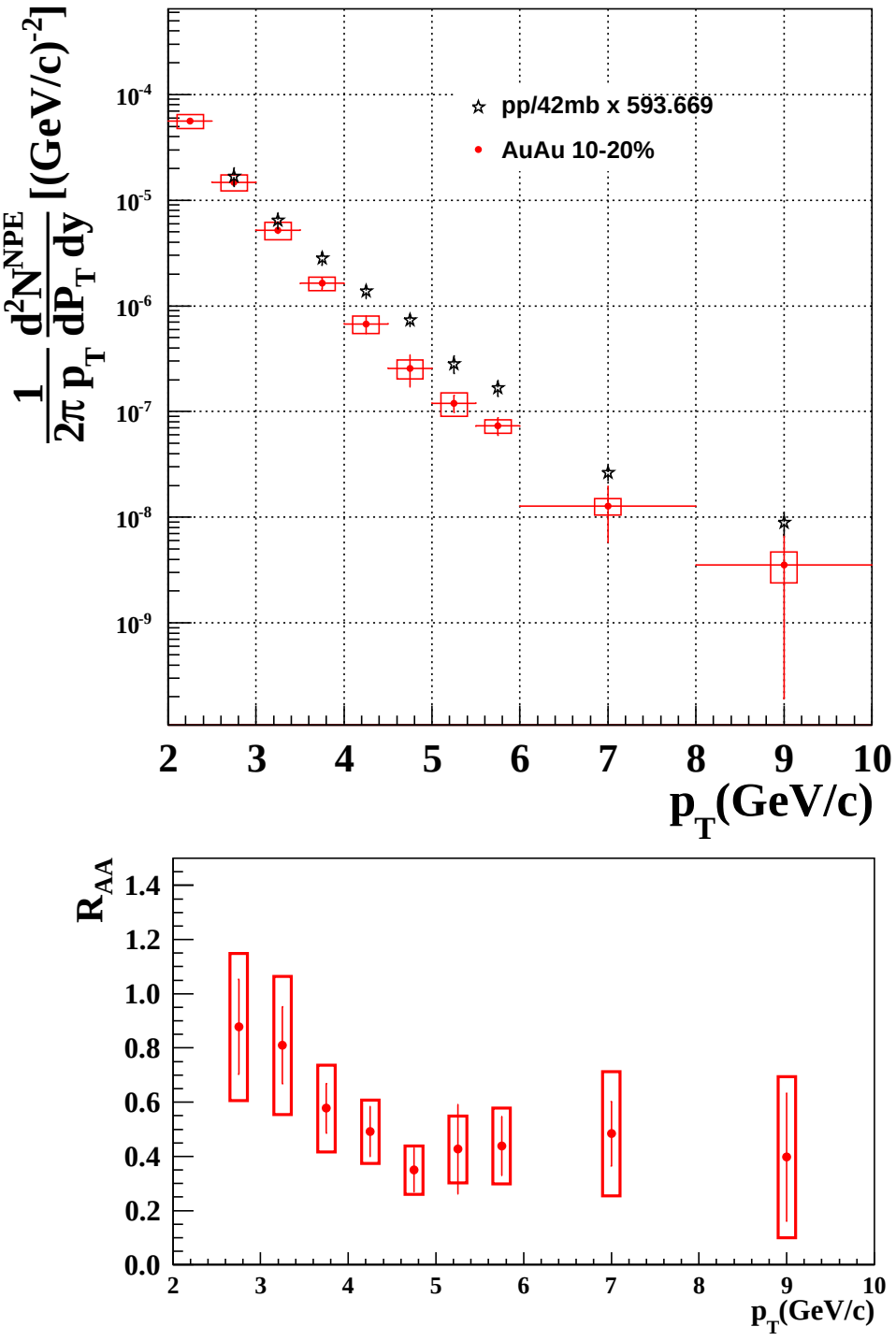

Figure 3.43: The NPE spectrum and R_{AA} in 10 to 20% centrality.

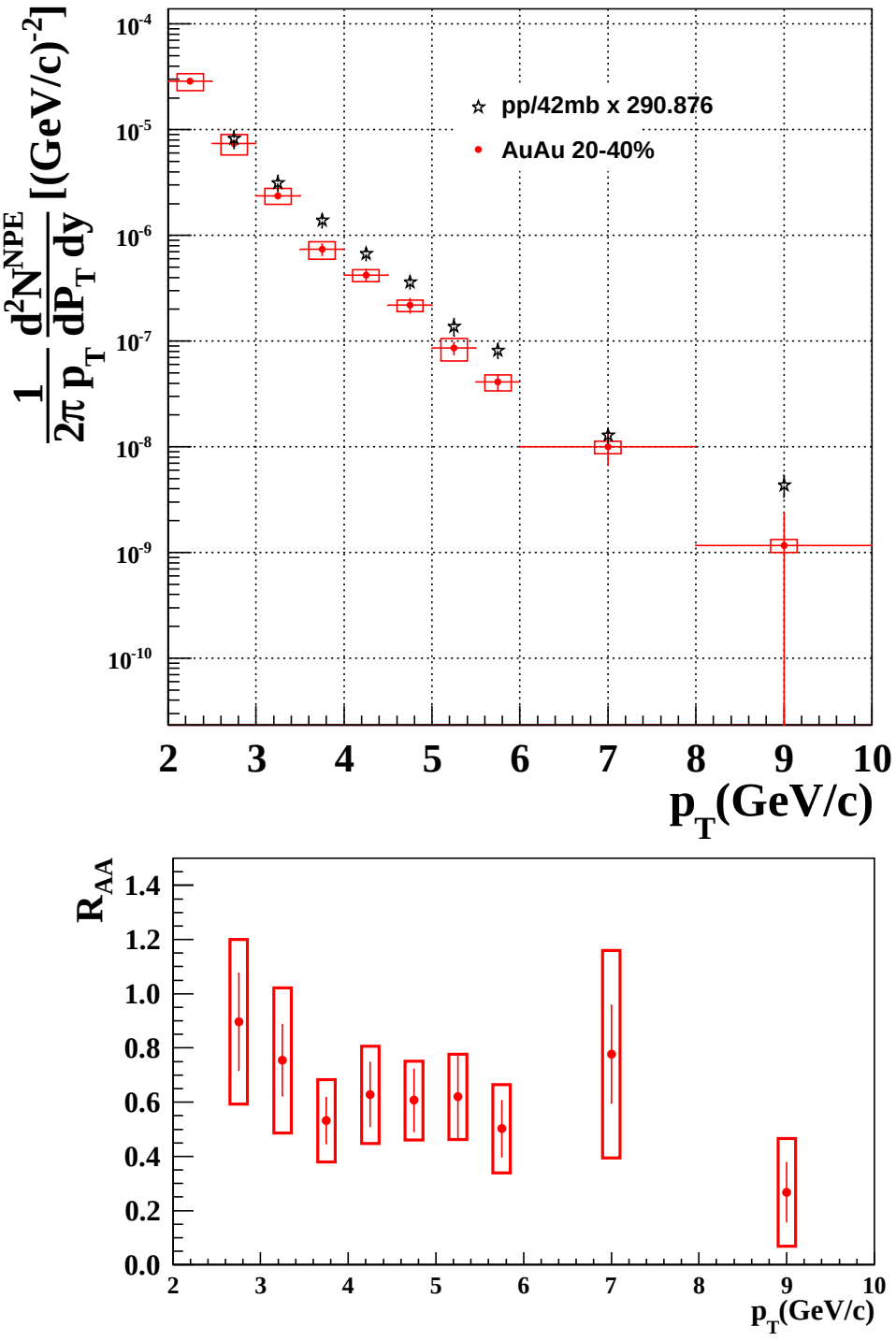

Figure 3.44: The NPE spectrum and R_{AA} in 20 to 40% centrality.

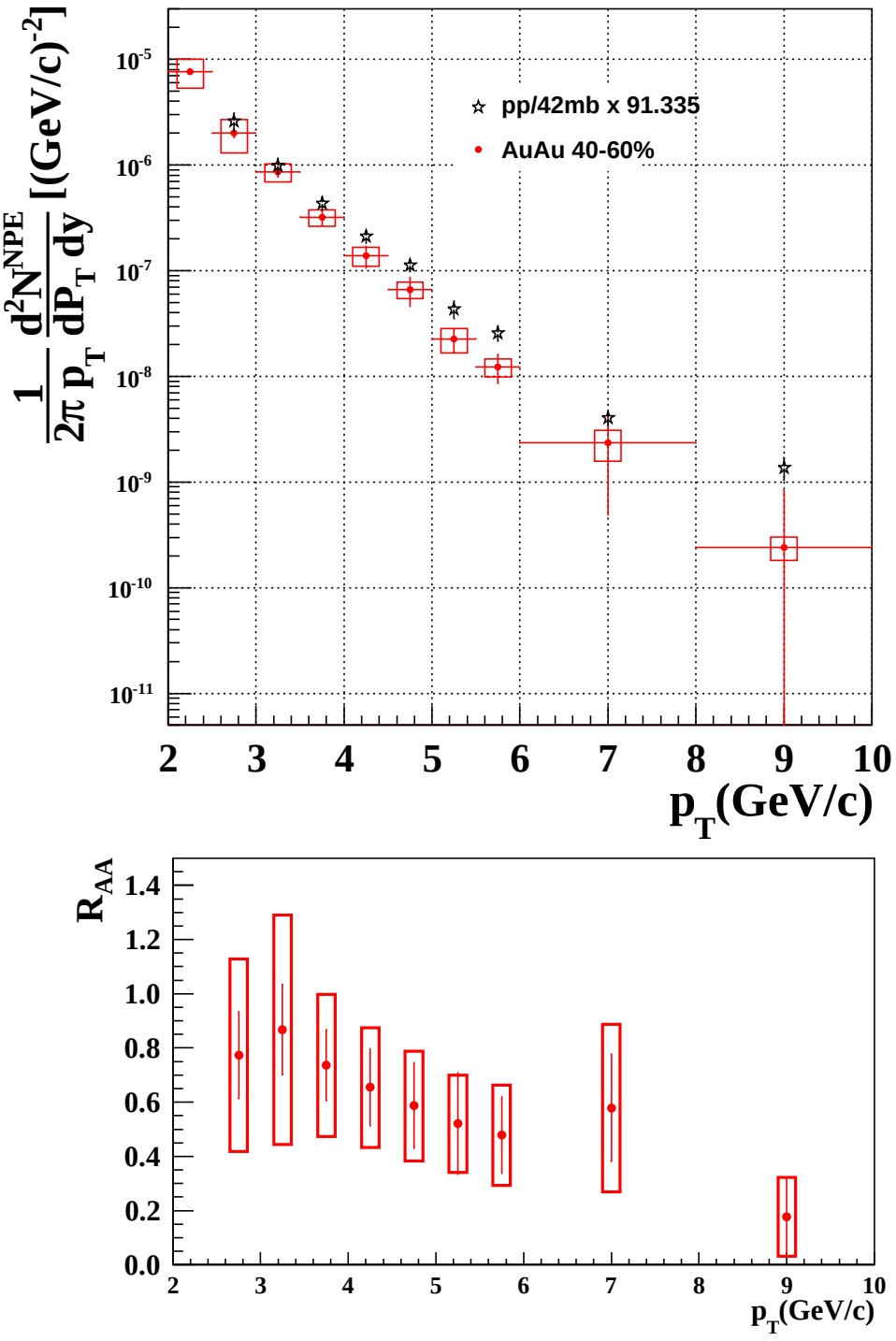

Figure 3.45: The NPE spectrum and R_{AA} in 40 to 60% centrality.

For example, the GBA model calculation [67] shown in Figure 3.46 considers the running of the strong coupling constant and uses a physically determined infrared regulator in the t channel scattering processes [104]. This model finds that a factor of around 2 (the K factor) larger coupling is required to explain the data, and it attributes this deficit to be exactly what radiative energy loss should contribute. Differences between bottom mesons and charm mesons are observed in this calculation, calling for the experimental disentanglement of charm and bottom contributions.

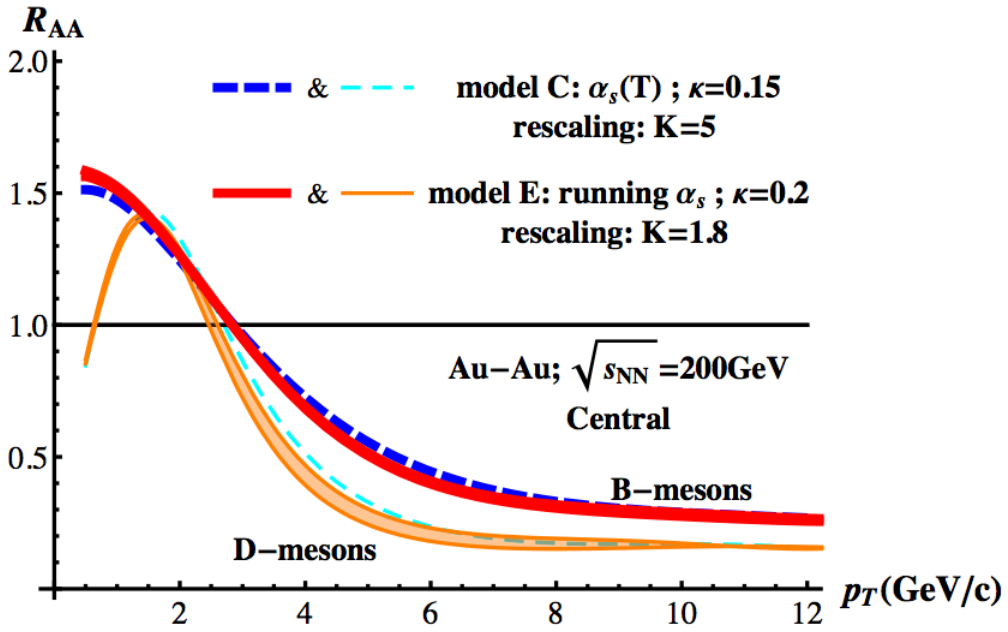

Figure 3.46: The heavy flavor meson R_{AA} in a pQCD calculation of heavy quark collisional energy loss in QGP. Model E is with a running strong coupling constant and it requires a K factor of 2 to explain the data, leaving reasonable room for radiative energy loss; and Model C is without such running and requires a K factor of 5, which is too large to be filled by radiative energy loss. The k value is related to the value of the infrared regulator in the t channel [104]. Although this is for heavy mesons, the flat feature of this R_{AA} calculation makes it comparable to NPE R_{AA}, which is essentially p_T shifts. Figure taken from [67].

Other models, *e.g.* the HFR model [52], considered collisional processes between heavy and light quarks involving (quasi-)heavy flavor hadrons forming inside the QGP. Due to their small Lorenz time dilation from their heavy mass and low

speed, the formation time of heavy flavor hadrons could be short enough so that they are formed inside the QGP. Although such quasi-hardon formations involve non-perturbative processes, HFR utilized the potential between heavy and light quarks estimated from finite-temperature lattice QCD to make quantitative predictions. HFR pointed out that these quasi-hadrons can significantly enhance the coupling between the heavy quarks and the medium by a factor of about 4 compared with pure elastic pQCD scattering. The medium evolution is treated with different approaches in this calculation to explore the consequence of medium properties. Shown in Figure 3.47, the results labeled as "fireball" are based on a simple modeling of the QGP with the bulk elliptic flows, and the results labeled as "AZHYDRO" are based on a more realistic 2+1 dimensional hydrodynamics modeling of the QGP. Different values of the impact parameter are also used to represent different centrality classes, including the most central collisions ($b = 0$ fm) and more peripheral collisions ($b = 7$ fm). The calculated NPE R_{AA} with $b = 0$ fm shown in Figure 3.47 is in good agreement with the data for 0 to 5% central events measured in this dissertation within the uncertainties.

The individual suppressions for charm mesons and bottom mesons calculated by the HFR model are significantly different from each other, as shown in Figure 3.48(a), and thus a small variation of bottom/charm ratio could change the combined R_{AA} considerably. In particular, this calculation combines electrons from charm decays with those from bottom decays according to PYTHIA generated spectra for the hard scatterings, which are slightly different from the recent STAR measurements of bottom/charm ratios in p+p collisions [72], *esp.* at 3 and 4 GeV/c as shown in Figure 3.48(b). As a result, it is still critical to separately measure charm and bottom decay electrons in Au+Au collisions, before definitive conclusions can be drawn.

The SVZ model [66] has also studied the heavy quark hadron formations inside the QGP medium, and furthermore considered the subsequent dissociations of

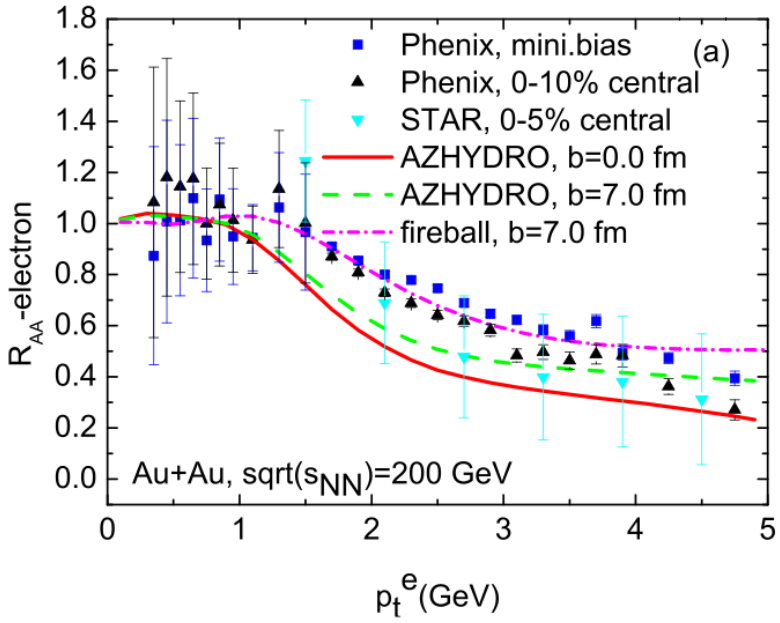

Figure 3.47: The NPE R_{AA} from a calculation of heavy quark collisional energy loss in a hydrodynamic background, which considers heavy quarks forming Feshbach resonances inside the QGP, on top of pQCD elastic scattering. Results involving different treatments of the QGP medium and different impact parameters are drawn together for comparison. Figure taken from [52]. The STAR data shown in this plot is from a previous measurement, not from this dissertation.

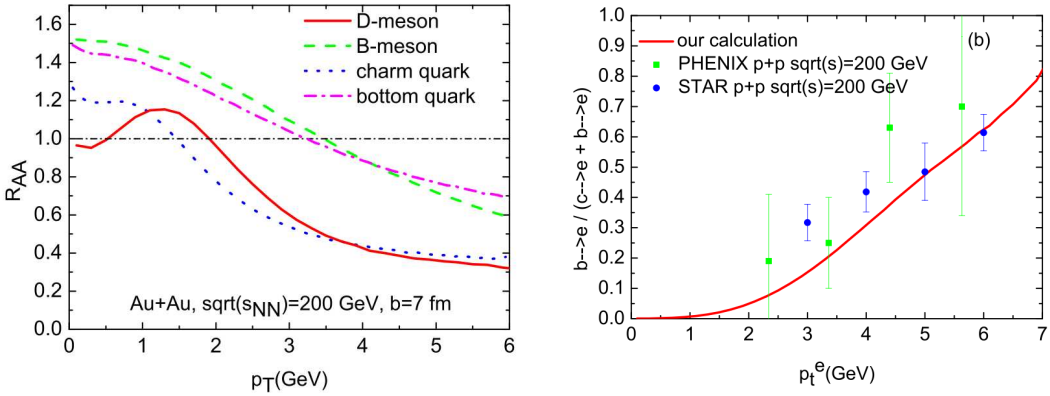

(a) Separated charm and bottom R_{AA}

(b) The bottom fractional contribution

Figure 3.48: a)The charm quark (meson) and bottom quark (meson) R_{AA} calculated in [52]. b) The bottom fractional contribution to total NPE in the model calculation, compared with RHIC measurements (see [52] and references therein). Both figures are taken from [52].

the heavy quark hadrons within the medium. Shown in Figure 3.49, the SVZ model adds the heavy hadron forming-dissociation energy loss on top of the gluon radiation energy loss of the heavy quarks prior the forming of hadrons. The results are consistent with our data within the uncertainties. We note that, while the collisional energy loss can explain the data so far, it is expected to yield to radiative energy loss at higher p_T, and the SVZ model has both built in. However, the current experimental data at STAR only effectively covers up to $p_T \sim 6$ GeV/c, and the direct test of radiative energy loss at higher p_T remains an experimental challenge.

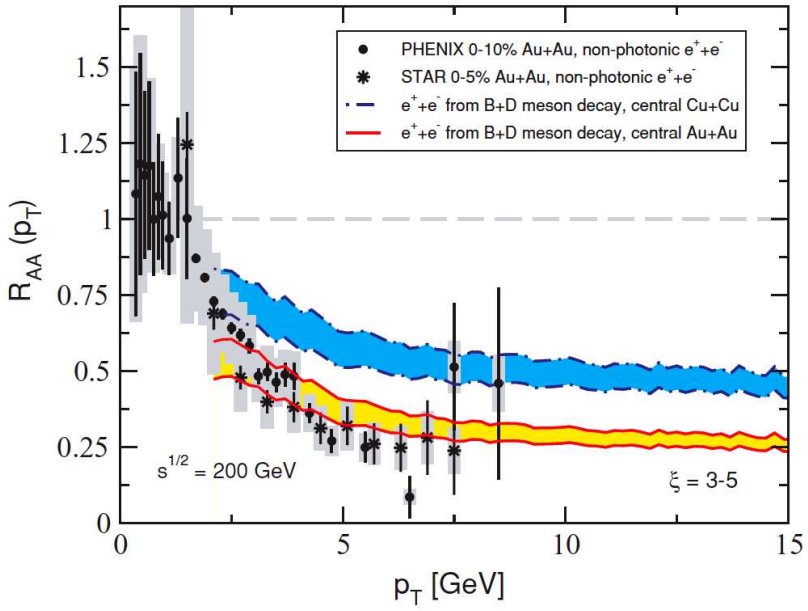

Figure 3.49: The NPE R_{AA} from the SVZ model calculation of heavy quark hadronization inside the QGP, on top of heavy quark radiative energy loss. The results for both Au+Au and Cu+Cu collisions are shown. Figure taken from [66]. The STAR data shown in this plots is from a previous measurement, not from this dissertation.

In conclusion, while the radiative energy loss alone cannot explain the significant suppressions of NPE in central Au+Au collisions observed in the experiments, the recent model calculations involving collisional energy loss seem to be able to match the data up to $p_T \sim m_{HQ}$. However, the energy losses for charm and

bottom are often vastly different in the model calculations, and a precise experimental measurement of charm/bottom ratios is critical, which will be fulfilled by the incoming STAR HFT upgrade. In addition, to further test and discriminate the models, larger dynamical range and more powerful heavy flavor observables, such as the elliptic flow, should be explored in both models and experiments.

CHAPTER 4

NPE azimuthal anisotropy and correlation

In the last chapter, we presented our measurement of the NPE spectra in Au+Au collisions. The suppression of NPE at high p_T indicates that heavy quarks lose considerable energy inside the QGP medium. Recent model calculations are able to reasonably explain such suppressions, though details of the models remain to be confronted experimentally. For example, non-perturbative features and/or parameter tunings are often involved in the models. To better understand the mechanism of heavy quark energy loss and to better constrain dynamical models, we should investigate the QGP medium with more differential probes. We present the first exploration of the NPE azimuthal anisotropy and NPE-hadron azimuthal correlation measurement from STAR.

4.1 NPE azimuthal anisotropy

Two dynamical processes could cause a finite heavy quark azimuthal anisotropy, which could be measured in terms of an elliptic flow as we discussed in chapter one. Firstly, if the coupling between the heavy quarks and the QGP medium is strong enough, the heavy quarks could more or less thermalize inside the medium and gain collectivity, just like the light quarks do. Secondly, when the heavy quarks traverse the medium, their path lengths within the medium vary azimuthally and the path-length dependence of heavy quark energy loss could give rise to an effective azimuthal anisotropy as shown in Figure 1.14. While the former process could dominate for low p_T heavy quarks, the latter is expected to be

more important at high p_T, since high p_T heavy quarks may be too energetic to be thermalized. Both processes are based on heavy quark interacting with the QGP medium. Simultaneous measurements of R_{AA} and v_2 over a broad p_T range can shed light on our understanding of heavy quark energy loss and heavy quark propagation in the QGP.

Since we use the electrons from heavy quark decays as the proxies for heavy quarks, it is necessary to examine how good the approximation is, which can be studied in PYTHIA since it is mainly determined by the decay kinematics. In Figure 4.1, the azimuthal angles of bottom quarks and their daughter electrons are found to be very consistent with each other once electron p_T is high enough, approximately at p_T> 3 GeV/c. For charm quarks, the consistence begins earlier at p_T > 1.5 GeV/c. For this reason, we will focus on high p_T electrons in the elliptic flow and correlation studies, and we will only use High Tower triggered events.

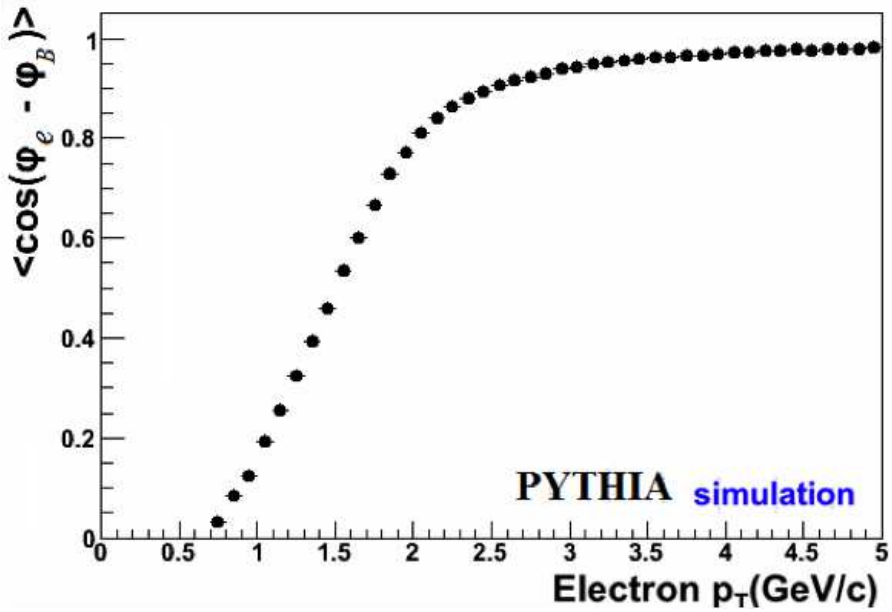

Figure 4.1: The cosine of the difference between the azimuthal angles of bottom quarks and the decay electron daughters, as a function of electron p_T, as studied in PYTHIA. At high electron p_T, the cosine approaches one, meaning the angle difference approaches zero.

4.1.1 Event Plane Reconstruction

The first step of the elliptic flow measurement is to reconstruct the event plane Ψ_{EP}, which is an estimation of the unmeasurable true reaction plane. There are several sub-steps to measure Ψ_{EP}, which are summarized as the following:

- ϕ-angle weighting. Since the detectors are not perfectly uniform along the azimuthal angle ϕ, we apply a weight to each ϕ angle so that the track ϕ distribution is forced to be flat. The weight assigned to each ϕ angle is proportional to the inverse of track multiplicity found in this angle over all the events. Since the track curvatures are different depending on the p_T, this weighting is done individually for each p_T range.

- We use all the primary tracks, with $0.15 < p_T < 1.5$ GeV/c within $|\eta| < 1$, to reconstruct the event plane. All the tracks with $|n\sigma_e| < 3$ are excluded to avoid the possible auto-correlations due to electrons.

- The tracks are randomly divided into two equal sub-groups and a sub-event plane is calculated for each group, based on which the resolution of event plane can be calculated. For each sub-event plane, two vectors are defined as $X = \sum_i \omega_i \cos(2 \times \phi_i)$ and $Y = \sum_i \omega_i \sin(2 \times \phi_i)$, where i goes through all tracks in the group, and ω_i is a weight, usually chosen to be p_T. The event plane is then calculated as $\Psi_{EP} = \arctan(\frac{X}{Y})/2$ [25].

- From a physics point of view, the (sub)event plane must be truly random across all the events, as a result of the truly random collision impact parameter. To make sure the randomness and to cancel any residual effects of detector non-uniformity, we force the calculated (sub)event planes to be flat via a shifting method. For more details of the shifting method, see [105].

In Figure 4.2, we show an example of the event plane distribution after the shifting, which is fitted by a Fourier expansion up to the 16th order and all the

coefficients are found to be very small, indicating the flatness of the distribution.

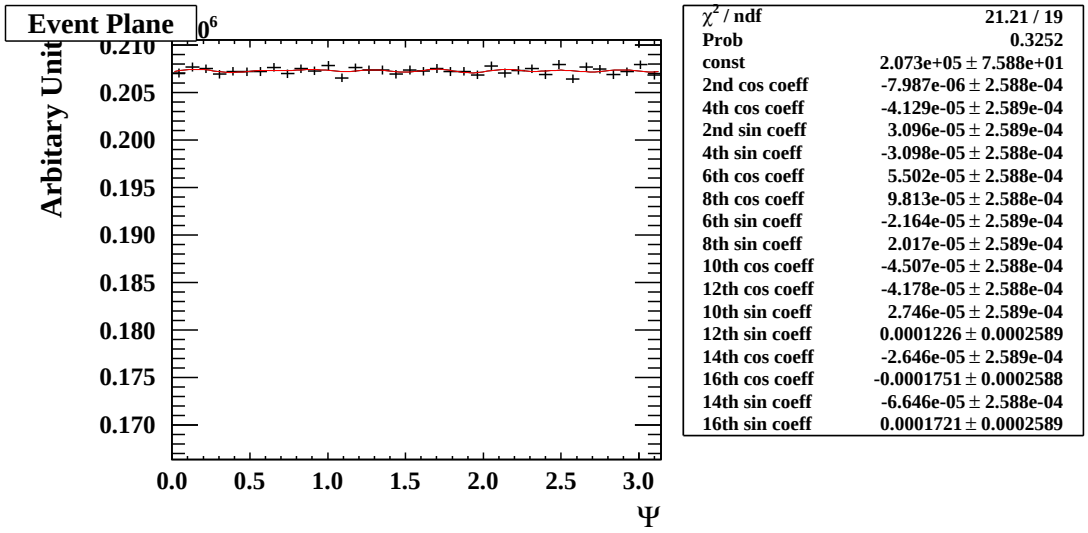

Figure 4.2: The event plane Ψ_{EP} distribution.

4.1.2 Hadron flow

There are two common methods to measure the elliptic flow. In the first method, we measure the particle production differentially at all azimuthal angles with respect to the event plane, and fit the distribution with Equation 4.1.1.

$$\frac{dN}{d\Delta\phi} = const \times [1 + 2 \times v_2 \times \cos(2 \times \Delta\phi)] \tag{4.1.1}$$

where $\Delta\phi \equiv \phi - \Psi_{EP}$ is the particle azimuthal angle ϕ with respect to the event plant Ψ_{EP}, reconstructed event by event as discussed above. We refer to this method as the fitting method.

The second method utilizes the fact that each coefficient of the Fourier expansion of particle production (see Equation 1.3.1) can be expressed as Equation 4.1.2. We refer to this method as the calculation method. These two methods are essentially the same, mathematically speaking. However, the uncertainties of the

fitting method come from the CERN ROOT Toolkit [106] we are using, and we manually calculate the statistical uncertainty for the other method. By using both methods, we have a cross-check, *esp.* on the uncertainty estimation.

$$v_n = \frac{\int_{-\pi}^{\pi} \cos(n \times \Delta\phi) \cdot dN/d\Delta\phi \cdot d\Delta\phi}{\int_{-\pi}^{\pi} dN/d\Delta\phi \cdot d\Delta\phi} \tag{4.1.2}$$

Before measuring the NPE elliptic flow, we first cross-check the elliptic flows of hadrons in this analysis, which are shown in Figure 4.3. They are consistent with previously published STAR results [26].

4.1.3 NPE elliptic flow

Similar to NPE spectrum analysis, in order to access NPE elliptic flow, we have to identify inclusive electrons and reconstruct photonic electrons. In the fitting method, we directly measure the number of NPE in each $\Delta\phi$ bin, in exactly the same way used in the spectrum analysis, and then we fit the resulting NPE $\Delta\phi$ distribution to extract NPE v_2. A typical NPE $\Delta\phi$ distribution is shown in Figure 4.4, where the fit and the extracted v_2 value are also shown. In the calculation method, we separately calculate the elliptic flows of inclusive electrons, opposite-sign pairs, same-sign pairs, and hadrons, and then the NPE elliptic flow is obtained using Equation 4.1.3

$$N^{NPE} v_2^{NPE} = N^{inc} v_2^{inc} - \frac{N^{OS} v_2^{OS} - N^{SS} v_2^{SS}}{\varepsilon_{PE}} - N^h v_2^{BEMCh} \tag{4.1.3}$$

where OS and SS are opposite-sign and same-sign pairs, and N^h is the number of hadrons in the inclusive electron sample, which is about 3% of all inclusive electrons since tight $n\sigma_e$ cuts are applied. The superscript $BEMCh$ means that only those hadrons that satisfy BEMC trigger conditions are used here to calcu-

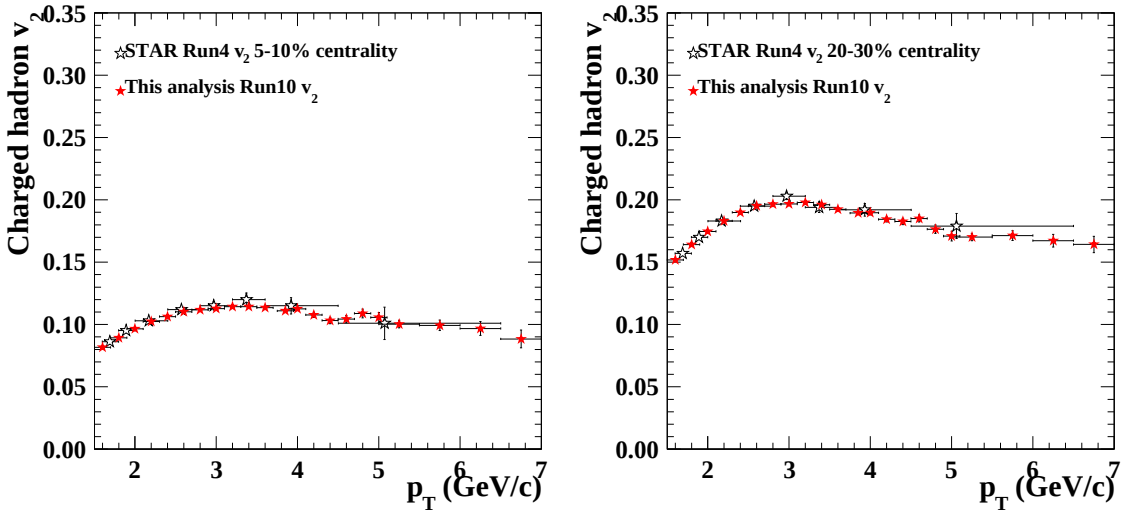

(a) hadron v_2 5-10%

(b) hadron v_2 20-30%

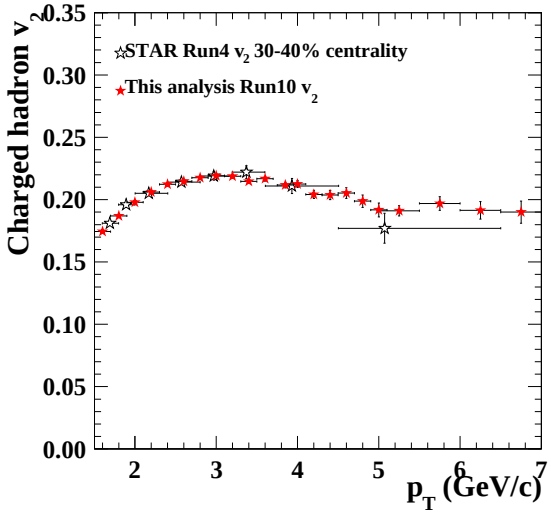

(c) hadron v_2 30-40%

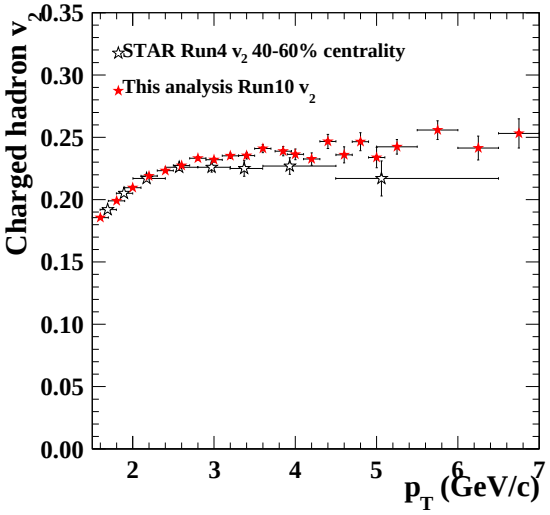

(d) hadron v_2 40-60%

Figure 4.3: The charged hadrons elliptic flows at high p_T in different centrality bins measured in this analysis, compared with earlier published STAR results based on Run04. The STAR Run04 data are from [26].

late the v_2 contribution of the hadron contamination. The statistical uncertainty calculation and propagation are discussed in detail in Appendix B. The main systematic uncertainties are from the photonic electron reconstruction efficiency ε_{PE}, which has a relative 10% uncertainty as in the spectrum analysis, and from the electron purity estimation.

In addition, we note that the elliptic flow of $BEMCh$ is always larger than that of regular hadrons, which do not trigger the BEMC. We understand this as many of the $BEMCh$ hadrons are associated with jets, which trigger the BEMC. The reason is that in our event plane determination using TPC, the presence of jets can bias the event plane Ψ_{EP} towards the jet axis since the jet-associated hadrons have been used in the event plane reconstruction, resulting in an overestimation of the elliptic flow of the jet-associated hadrons, see for example [107] for more discussion. As a result, when we subtract the elliptic flow contribution of $BEMCh$ hadrons, not regular hadrons; we also expect the NPE elliptic flow could be overestimated in the same way, since the NPE come from heavy quark jets. This, and other possible correlations between heavy quark jets and the event planes, are often referred to as "non-flow". Methods involving multi-particle correlations and event plane reconstruction with tracks measured by detectors other than the TPC could help deal with the "non-flow", but the required statistics are currently too large to be feasible at high p_T.

Figure 4.5 shows the NPE v_2 with respect to both centrality and p_T, in which both results from the fitting and calculation methods are shown. The results from the fitting method and the calculation method are consistent with each other. More importantly, the statistical uncertainties, one set from ROOT and the other from our manual calculations, are also very consistent. A sizable $v_2 = 5\% \sim 10\%$ is seen for all considered centrality ranges at high p_T. The NPE v_2 in 20$\sim$40% centrality bin is likely to be larger than that in 0$\sim$20% centrality bin and exhibits no obvious p_T dependence, although the data are statistically limited.

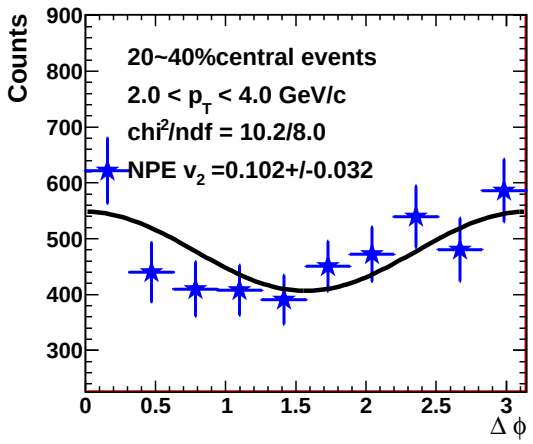

Figure 4.4: A typical $\Delta\phi = \phi - \Psi_{EP}$ distribution for NPE. A fit with Equation 4.1.1 and the extracted NPE v_2 are also shown. The event centrality is $20 \sim 40\%$ and electrons are with $4 < p_T < 6$ GeV/c.

4.1.4 Model comparison

Now we compare our results to the HFR model [52] discussed in the last chapter, which is based on collisional energy loss and whose NPE R_{AA} calculations are consistent with the experimental results. This model is build upon full hydrodynamics simulations of the medium, and it provides v_2 calculations explicitly for heavy flavor decay electrons, as shown in Figure 4.6. The impact parameter, $b = 7$ fm, used in the model represents centrality class roughly around 20% based on the Glauber Model [43]. The model predictions are mostly below 5% and thus under-estimate the elliptic flow a little if compared with, for example, Figure 4.5(d). The imperfect match of event centrality in model and data could be the reason for the difference, as pointed out in [52]. From the experimental side, the heavy quark jets could bias the event planes, such that the NPE elliptic flow is overestimated by the standard elliptic flow methods used in the analysis. However, the PHENIX results shown in Figure 4.6 are obtained with this bias suppressed because different detectors are used to reconstruct the event planes and to measure the electrons [62].

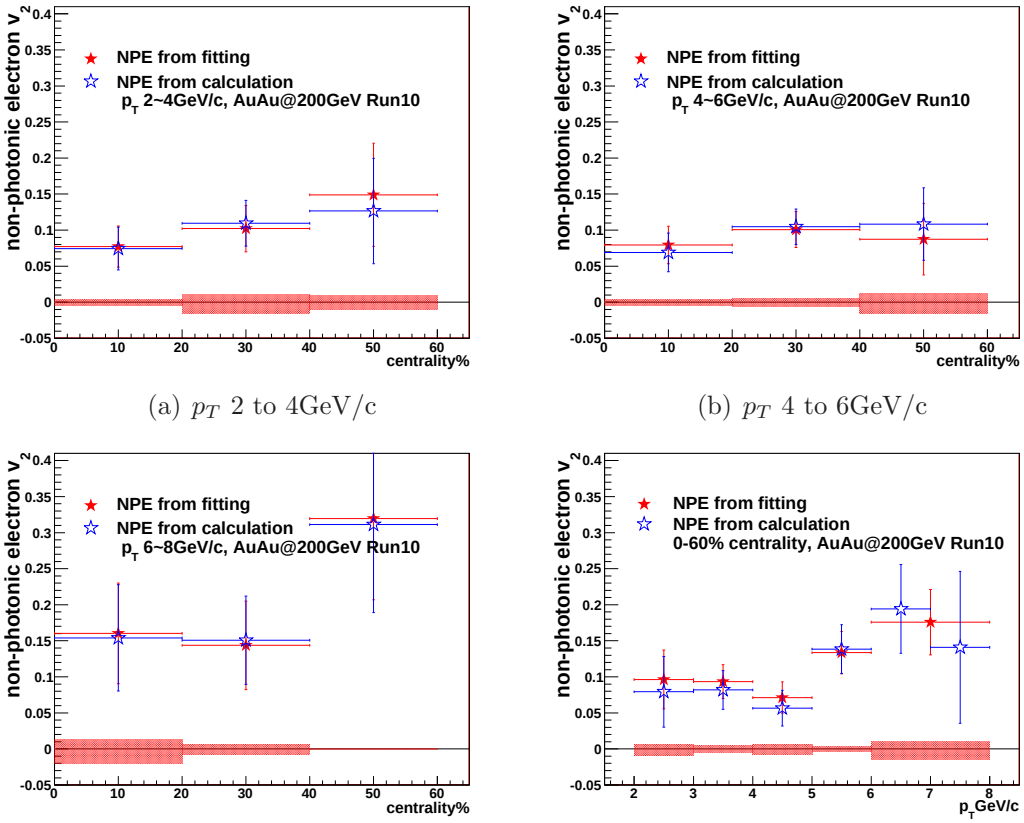

(a) p_T 2 to 4GeV/c

(b) p_T 4 to 6GeV/c

(c) p_T 6 to 8GeV/c

(d) centrality 0 to 60%

Figure 4.5: The elliptic flows of NPE as a function of centrality and p_T. The red shaded bands around zero are systematic uncertainties calculated for the fitting method, accounting for the uncertainties from the photonic reconstruction efficiency and electron purity, but should be common to both methods.

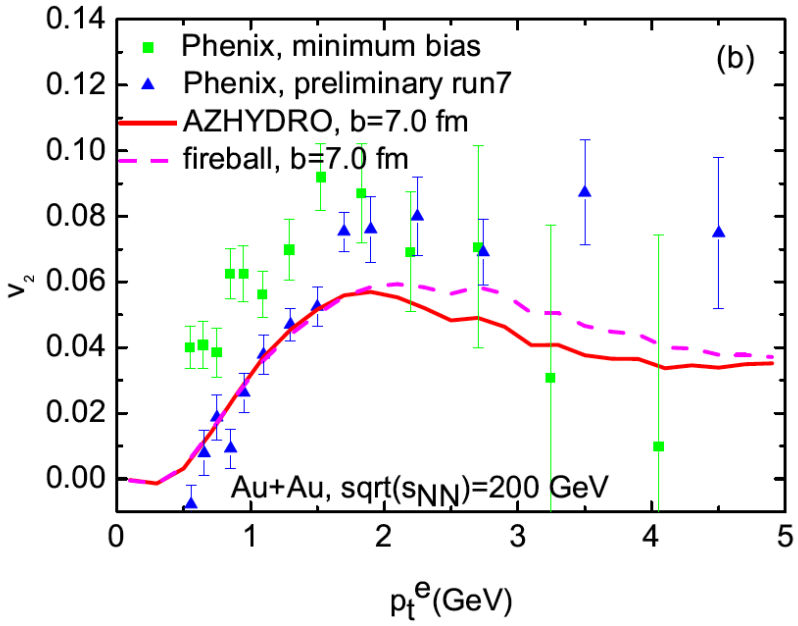

Figure 4.6: NPE v_2 in the HFR model based on collisional energy loss, as a function of p_T. Figure taken from [52]. The PHENIX results are from [62].

4.2 NPE-hadron azimuthal correlation

4.2.1 Measurements of the NPE-hadron azimuthal correlation

As previously mentioned, a high p_T NPE can reflect the direction of its parent heavy quark reasonably well. As a result, the high p_T NPE-hadron azimuthal correlation is a proxy of the correlation between heavy flavor jets and hadrons, which can be used to probe the heavy quark jet-medium interaction if the associated hadrons are related to the heavy quark-medium interaction, either from radiation of heavy quark jets or from the medium interacted with the jet. The steps of measuring NPE-hadron azimuthal correlation are similar to the NPE v_2 measurement, except that the azimuthal angle difference is calculated with respect to the associated hadrons $\Delta\phi_{eh} = \phi_e - \phi_h$, instead of with respect to the event plane as in the case of v_2 measurement. However, there are several additional points worth mentioning here.

Firstly, we need to subtract the intrinsic electron-positron correlation for each

photonic electron pair. When we correlate electrons with hadrons, no identification is applied to the associated hadrons to maximum the statistics, and thus the associated hadron include electrons. If an electron (or positron) is photonic, its partner positron (or electron) will produce a very prominent correlation at very small angle, which is a background of the electron-hadron correlation. Therefore, during the photonic electron reconstruction process, we record the $\Delta\phi_{ee} = \phi_e - \phi_{partner\ e}$ distributions for both opposite-sign and same-sign pairs, and the $\Delta\phi_{ee}$ distributions are later subtracted from the $\Delta\phi_{eh} = \phi_e - \phi_h$ distributions of opposite-sign and same-sign pairs.

Secondly, detector non-uniformity gives rise to artificial correlations and these are studied via a mixed-event correction method. For tracks in different events, there are no physical correlations between them, but correlations due to detector geometry and acceptance are kept. We choose an inclusive electron from one event and choose hadrons from other events, and the resulting $\Delta\phi_{eh}^{mix} = \phi_e - \phi_{h,otherevent}$ distribution is artificially induced by the detectors, as shown in Figure 4.7(b). The scale of this correction is on the order of 5% due to a problematic calibration of one TPC sector, and the physical correlations we want to study are on the order of 5% as well. Although we made many efforts to systematically understand this correction with respect to collision centrality, primary vertex positions and p_T of relevant particles, all of which affect the correction a bit, hidden systematic uncertainties could still distort the physics correlations. This is one of the reasons we will not give the finalized NPE-hadron correlations based on Run10 data in this dissertation. The STAR TPC in Run11 has no such calibration problem and will be the ideal data set to finalize this measurement.

Thirdly, the physical background in NPE-h correlation needs to be treated carefully. It is easy to see there is a flat pedestal background in the NPE-h correlation distribution due to random combination of uncorrelated electrons and hadrons. We use hadrons with $0.5 < p_T < 1$ GeV/c since this flat combinatorial

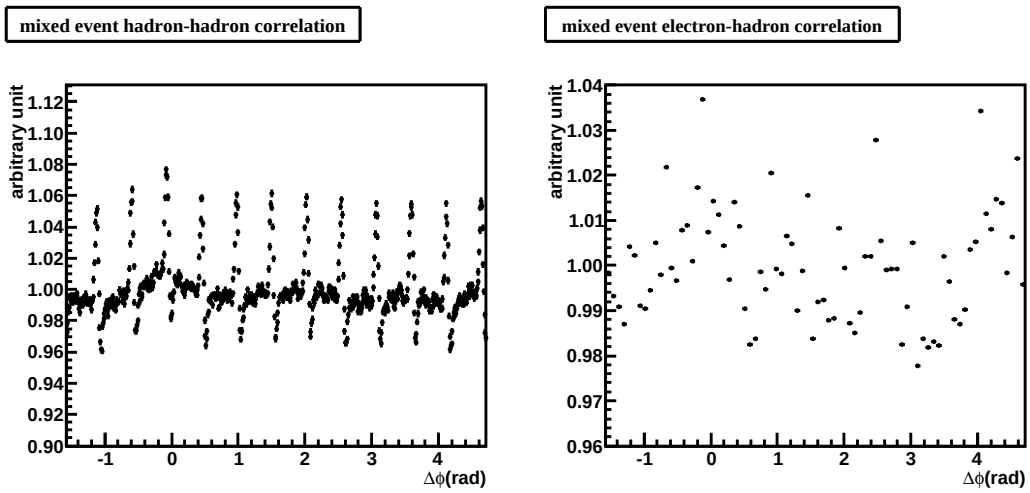

(a) Di-hadron correlation in mixed events.

(b) Electron-hadron correlation in mixed events.

Figure 4.7: Artificial correlations due to detector non-uniformity. Figure 4.7(a) shows two hadron correlations in mixed events, where the hadrons are just regular hadrons reconstructed by TPC and not required to match the BEMC, and therefore represents the artificial correlation due to the TPC. The series of peaks seen in the figure are 30 degrees apart and are caused by a correlation between the empty TPC sector (removed from data due to its calibration problem) and all the remaining TPC sector boundaries, which are 30 degrees apart and sharp. There is a slight enhancement underneath the peak at $\Delta\phi = 0$ which is due to the self-correlation of the empty TPC sector. Figure 4.7(b) shows the electron-hadron correlation in mixed events, where electrons are very loosely selected to allow copious statistics but still required to satisfy the BEMC trigger condition. This represents BEMC effects on top of the TPC effects. The statistics error bars are too small to be seen.

background would become overwhelming if hadrons with lower p_T are used. At the same time, the collectivity in Au+Au collisions also creates a considerable modulated background. For example, the elliptic flow of the trigger NPE and associated hadrons creates a background that amounts to Equation 4.2.4 [108]. Furthermore, recently it has been argued that the coefficient for the third harmonic term (v_3) in the Fourier expansion of hadron azimuthal distribution should not be zero due to asymmetric shape of the initial collision geometry. This is called the triangular flow [109]. While the debate regarding the hadron triangular flow is still on-going, there is little known about the NPE triangular flow. In addition, while the constant A in Equation 4.2.4 is normally determined via the so called Zero Yield At Minimum (ZYAM) method [108], the systematic uncertainty related to this method has not been adequately addressed experimentally.

$$A \cdot [1 + 2 \cdot v_{2,\ npe} \cdot v_{2,\ h} \cdot \cos(2 \cdot \Delta\phi)] \tag{4.2.4}$$

In Figure 4.8(a), we present the NPE-h correlation in 10∼40% centrality with the mixed event background correction but without any further background subtractions. From the NPE elliptic flow measurements presented above, the NPE v_2 is around 5 to 10 percent for p_T between 2 to 6GeV/c, therefore we calculate two sets of modulated elliptic flow background, one with NPE v_2 assumed to be 5% and the other with NPE v_2 = 10%. We subtract these two sets of elliptic flow background via the ZYAM method in Figure 4.8(b). The hadron elliptic flow $v_{2,\ h}$ used here is a weighted average over the hadron p_T range and the event centrality range used in the analysis. The weight is the number of hadrons multiplied by number of NPE in each centrality, since the modulated background is proportional to number of hadrons times number of NPE. The obtained value is $v_{2,\ h} = 0.066$. The electrons are selected with tight $n\sigma_e$ cuts so that a purity of 99% is achieved, and thus no correction is made to account for the remaining

hadron contamination.

No systematic uncertainties are drawn in the figures, since we do not have sufficient statistics to study the systematics thoroughly. Nevertheless, in both cases, the NPE-h azimuthal correlation indicate a broadening in the away side peak, compared with the near side peak. Qualitatively, this broadening is likely to be caused by the heavy quark jet-medium interactions and thus reflects the imprints of such interactions. The contribution to the correlation from a modulated triangular flow background remains to be investigated with more STAR data in the coming years.

4.2.2 Models of the NPE-hadron azimuthal correlation

The advantage of the NPE-hadron correlation is that it probes many aspects of the dynamics of heavy quark jet-medium interactions, including both the affected heavy quarks and the response of the QGP medium to the heavy quarks. As pointed out by recent AdS/CFT calculations, several factors could affect the shape and magnitude of the medium responses to the punching through of the heavy quark jets. For example, while heavy quarks could generate strong diffusion wakes as well as shock wave patterns (*i.e.* two symmetric peaks at the Mach cone angle around a valley at $\Delta\phi_{eh} = \pi$) in the azimuthal correlation [110], the heavy flavor mesons could only generate the shock wave patterns but no diffusion wakes [111]. In addition, the degree of equilibrium in the medium and the speed of heavy quarks also affect the azimuthal correlation [112]. In short, the exact modification of the away side peak could provide an independent way to test our understandings of heavy quark interactions with the QGP medium, including the important question of whether the energy loss processes are related to the formation time of heavy flavor hadrons.

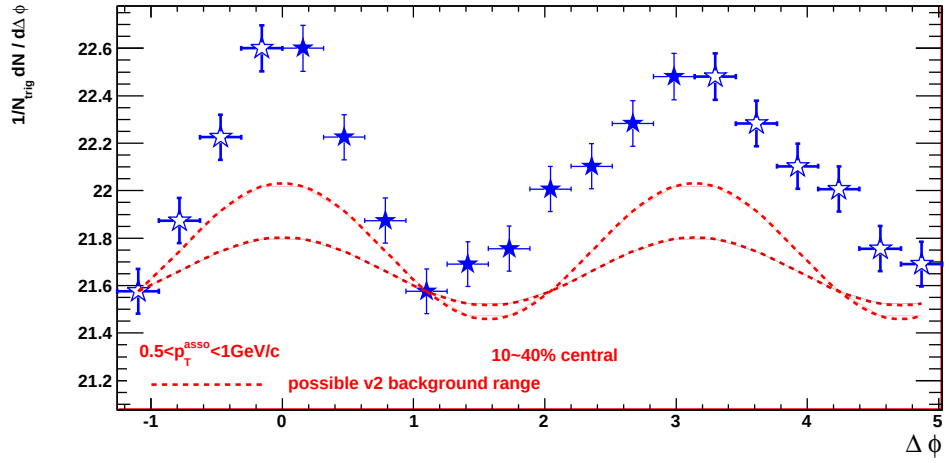

(a) NPE-hadron correlation, raw

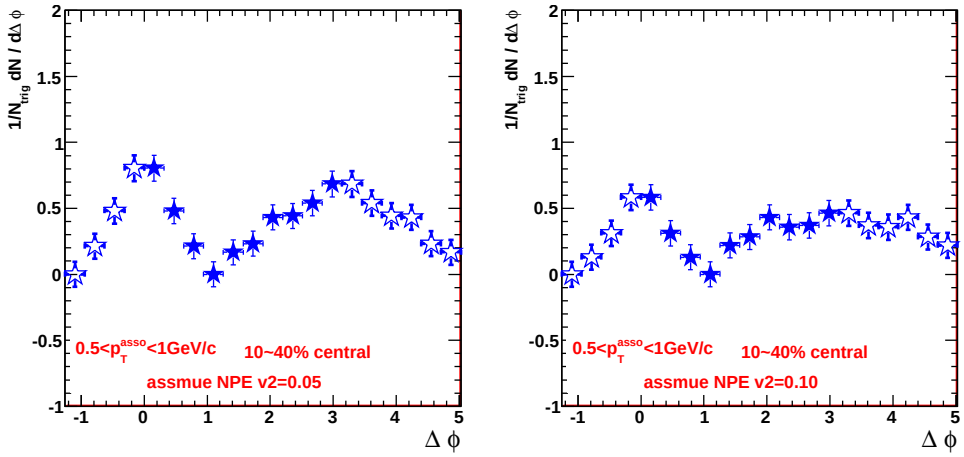

(b) NPE-hadron correlation, subtracted

Figure 4.8: The NPE-hadron correlations without any background subtraction in Figure 4.8(a) and with elliptic flow background subtracted in Figure 4.8(b). The two dashed red lines in Figure 4.8(a) correspond to elliptic flow backgrounds with NPE $v_2 = 0.05$and $v_2 = 0.1$. The centrality is 10∼40% and NPE p_T is 3∼6 GeV/c. The measurement over the entire 2π range has been folded into π to enhance the statistics, considering the symmetry around the heavy quark jets over many events. The open stars are just a reflection of the closed stars.

CHAPTER 5

Measurement of Charm/Bottom Ratios and Bottom quark production in p+p collisions

A precision measurement of NPE spectrum in $p+p$ collisions at $\sqrt{s} = 200$ GeV has been performed by STAR with data from year 2005 and 2008 runs [73]. While the disentanglement of bottom and charm quark decay contributions to electrons in Au+Au collisions cannot be achieved with the exsiting detector capability, the disentanglement in p+p collisions has been performed by the UCLA group using the NPE-hadron azimuthal correlation [72] (we will refer to this as the e-h paper).

In this chapter, we will combine the results of p+p NPE spectrum reported in [73] with the fractional bottom and charm contributions reported in [72] to obtain the spectra of electrons originated from bottom hadrons and from charm hadron, separately. We will then show that the cross sections of bottom and charm decay electrons are, respectively,

$$\frac{d\sigma_{B\to e+B\to D\to e}}{dy_e}|_{y_e=0}(3GeV/c < p_T < 10GeV/c) = 4.0 \pm 0.5(stat.) \pm 1.1(syst.)nb$$

and

$$\frac{d\sigma_{D\to e}}{dy_e}|_{y_e=0}(3GeV/c < p_T < 10GeV/c) = 6.2 \pm 0.7(stat.) \pm 1.5(syst.)nb$$

in p+p collisions at $\sqrt{s} = 200$ GeV.

Furthermore, based on various theoretical calculations, we will project the total

bottom quark production cross section in p+p collisions at $\sqrt{s} = 200$ GeV to be $\sigma_{b\bar{b}} = 1.34$ μb with a PYTHIA [92] calculation in the minimum-bias production mode and 1.83 μb with the same PYTHIA calculation in the bottom-triggered production mode. A Fixed Order plus Next to Leading Logarithm (FONLL) prediction [59] is also normalized to data and gives $\sigma_{b\bar{b}} = 1.93$ μb. These total cross section projections would also inherit the same experimental uncertainties on bottom electron cross section at high p_T, *i.e.* 12.5% statistical and 27.5% systematic.

We will start with discussing the experimental measurements, and then we will describe the PYTHIA and FONLL calculations, as well as the normalization procedures and corrections. At the end of this chapter, we will return to the results.

5.1 Bottom decay electrons

5.1.1 High p_T e_B/e_{npe} in p+p

To disentangle bottom and charm quark decay contributions to electrons, the e-h paper [72] noticed that in the decay processes, charm hadrons and bottom hadrons provide different boosts to their daughters and thus the angular correlations between the daughters are different in the two cases, with the angular correlation in charm hadron decays being narrower. By comparing experimentally measured azimuthal correlations with theoretical calculations, the fractions of bottom decays and charm decays were obtained. The results, shown in Figure 5.1, are presented as e_B/e_{npe} (the ratio of electrons from bottom quark decays over the total non-photonic electrons) in each p_T bin. This method is not expected to work in Au+Au collisions because even the near side of the NPE-hadron correlation could be modified by the QGP medium, and more importantly, the modification could depend on the charm or bottom origin of the NPE.

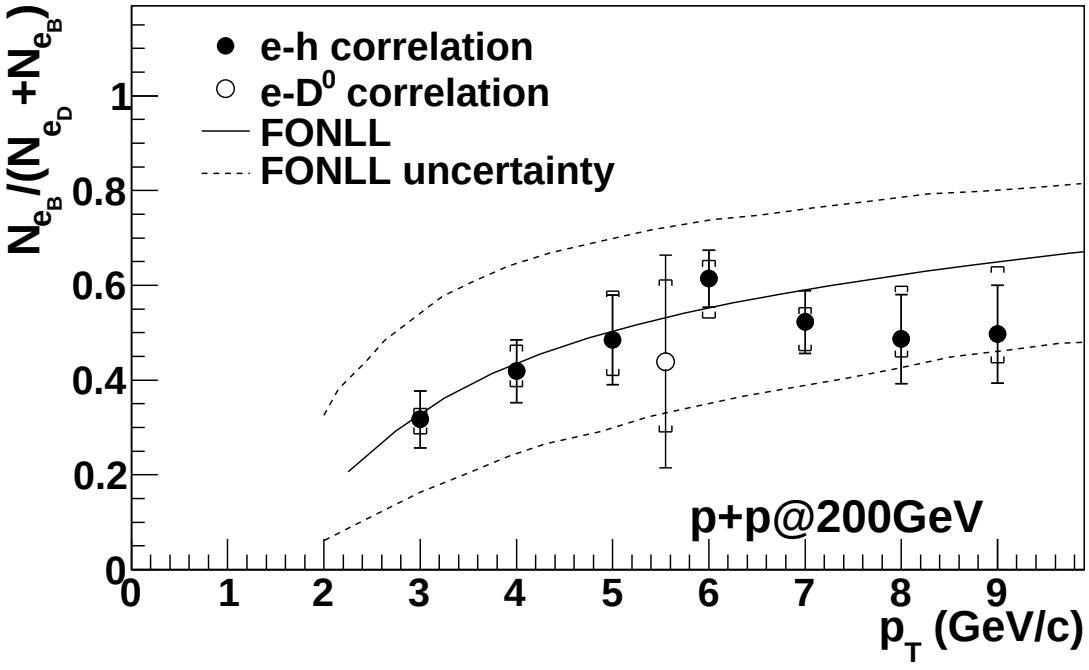

Figure 5.1: The relative contribution from bottom mesons to the total NPE yields. The curves are the central value (solid curve) and theoretical uncertainties (dashed curves) of a FONLL prediction [59]. Figure taken from [72].

Table 5.1: The bottom decay contributions to non-photonic electrons, linearly interpolated to the p_T positions where the NPE cross sections are measured. The 7 GeV/c and 9 GeV/c data points are the original ones in [72].

p_T(GeV/c)	e_B/e_{npe}	stat. err	lower bound	upper bound
3.25	0.342	0.062	0.312	0.374
3.75	0.393	0.065	0.362	0.440
4.25	0.435	0.073	0.392	0.502
4.75	0.468	0.087	0.404	0.559
5.25	0.517	0.086	0.440	0.604
5.75	0.582	0.069	0.501	0.636
7.00	0.522	0.066	0.462	0.552
9.00	0.497	0.104	0.436	0.639

The differential cross section of electrons from bottom decays in each p_T bin is just the NPE differential cross section (shown in Figure 3.40 and Table 3.5) times e_B/e_{npe} in that p_T bin. The contributions from J/ψ, Υ decay and Drell-Yan processes are subtracted from the NPE cross sections based on data in [73]. However, the NPE differential cross sections and the e_B/e_{npe} ratios are usually not measured at exactly the same p_T, so interpolations are necessary. We interpolate the measured e_B/e_{npe} to get values at p_T= 3.25, 3.75, 4.25, 4.75, 5.25 and 5.75 GeV/c. At 7 GeV/c and 9 GeV/c, original e_B/e_{npe} data points are available, and no interpolations are needed. Two different methods are used for the interpolation.

- Interpolation method 1: a simple linear interpolation, the results of which are listed in Table 5.1. This is the nominal method. The statistical and systematic uncertainties are also interpolated according to the neighboring uncertainties.

- Interpolation method 2: As a cross-check and a way to estimate the systematic uncertainty on the interpolation, we also use the functional form of the FONLL prediction [59] of e_B/e_{npe}. Because the FONLL prediction was originally available as discrete points, instead of curves, we firstly parameterize

the points of the FONLL prediction with both a third order polynomial and a fifth order polynomial, shown in the upper row of plots in Figure 5.2. We then compare the two different FONLL parameterizations with the measured e_B/e_{npe}, shown in the lower row of plots in Figure 5.2. We use the parameterized polynomials, each multiplied with an overall scaling factor, to fit the measured e_B/e_{npe}. We find the overall scaling factors for both parameterizations should be 0.93 in order to match the data. We use the scaled FONLL parameterizations to calculate e_B/e_{npe} at desired p_T positions and find the e_B/e_{npe} ratios obtained in this way are almost identical to the corresponding ones from linear interpolations. It is estimated that the differences on the ratios only cause a 3% difference on the integrated bottom decay electron cross section.

5.1.2 Differential cross section of bottom decay electrons

Based on the linear interpolation, we measured the differential cross sections of electrons from bottom decays, listed in Table 5.2 for the nominal values and statistical uncertainties and in Table 5.3 for systematic uncertainties. Both the e_B/e_{npe} and NPE cross section measurements contribute similarly to the statistical uncertainties. The combined bin-by-bin statistical uncertainty (not listed in the table) is the sum in quadrature of the two. The dominant systematic uncertainty is associated with the NPE cross section measurement (column E in Table 5.3). Some of the systematic uncertainties are asymmetric. Column A (B) in Table 5.3 corresponds to the upper (lower) uncertainty on the measured e_B/e_{npe}. Column C (D) is due to the lower (upper) limit of J/ψ, Υ decay and Drell-Yan contributions. Column E is the systematic uncertainty of the p_T interpolation, estimated by the two different interpolation methods. The combined bin-by-bin upper (lower) systematic uncertainty is the square root of the quadratic sum of column A (B), column C (D), and column E. In addition, the NPE cross section measurement

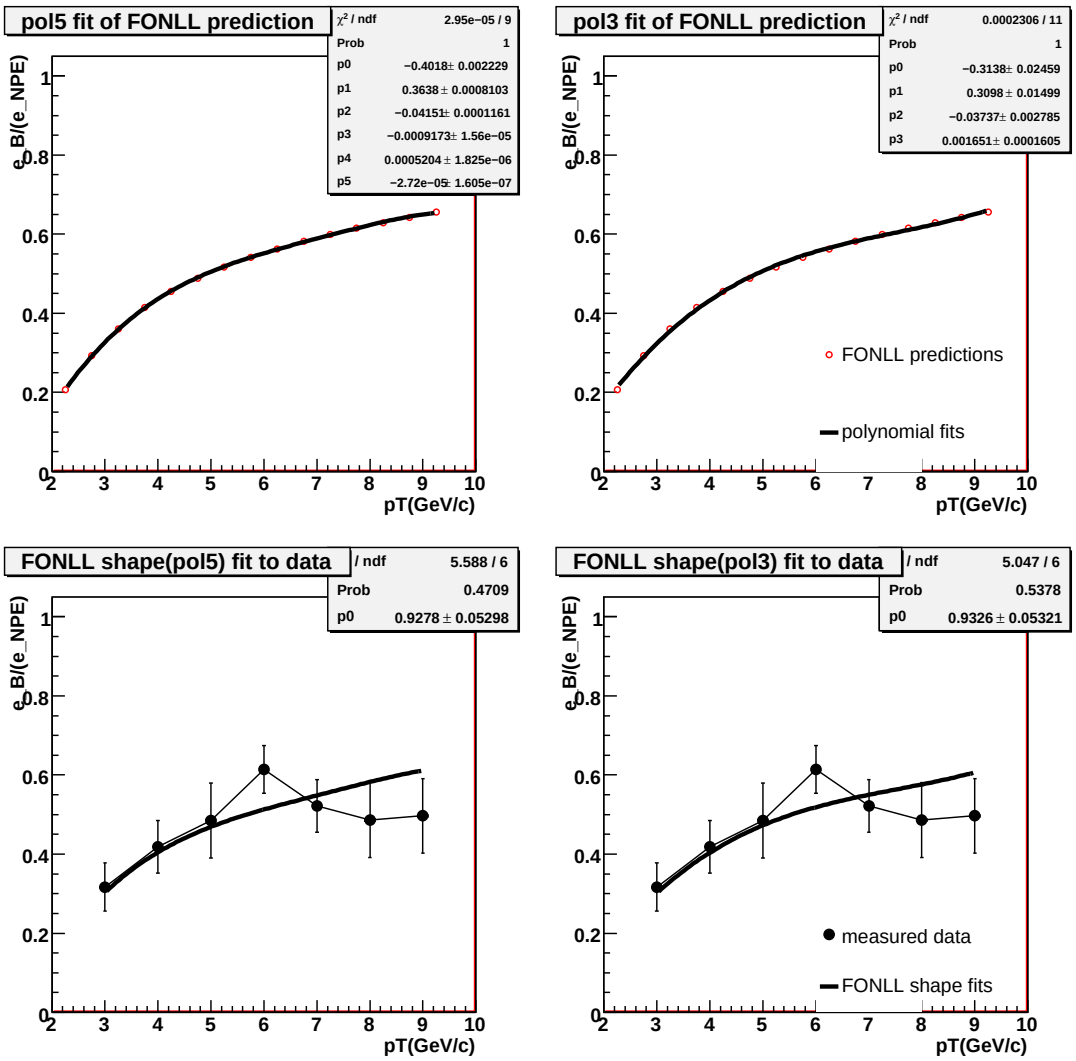

Figure 5.2: Upper Row: FONLL prediction [59] of e_B/e_{npe} (red open circles) is parameterized by, *i.e.* by fitting a fifth order polynomial in the left plot and a third polynomial in the right plot. Lower Row: The parameterized FONLL predictions multiplying overall scaling factors are used to fit the measured e_B/e_{npe} [72] (black solid circles). The fifth (third) polynomial parameterization are shown in the left (right) plot. In both cases, the scaling factor is fitted to be 0.93.

Table 5.2: The cross section of electrons from bottom hadron decays and the relative statistical uncertainties. A: from e_B/e_{npe}; B: from NPE cross section measurement.

p_T(GeV/c)	$E\frac{d^3\sigma}{dp^3}(nb\ GeV^{-2}\ c^3)$	stat. A	stat. B
3.25	0.155699	18.1%	15.7 %
3.75	0.0785945	16.5%	13.6%
4.25	0.0422377	16.9%	13.8%
4.75	0.0242966	18.7%	13.0%
5.25	0.010306	16.6 %	18.7%
5.75	0.0068635	11.8 %	16.1 %
7	0.00103383	12.7%	14.4 %
9	0.000314954	20.9%	23.4%

Table 5.3: The relative systematic uncertainties on the cross section of electrons from bottom hadron decays. A (B): from e_B/e_{npe} lower (upper) bound; C (D): from higher (lower) estimation of J/ψ, Υ decay and Drell-Yan processes contributions E: from the interpolation of e_B/e_{npe} if interpolation is used; F: from the luminosity uncertainty in the NPE cross section measurement.

p_T(GeV/c)	syst. A	syst. B	syst.C	syst.D	syst. E	syst. F
3.25	8.9%	9.1%	6.0%	5.7%	1.9%	23.9%
3.75	8.0%	11.9%	5.5%	5.2%	2.1%	17.8%
4.25	9.8%	15.3%	4.4%	4.2%	2.7%	16.0%
4.75	13.7%	19.4%	3.5%	3.3%	3.0%	14.7%
5.25	14.9%	16.8%	4.2%	3.8%	7.0%	17.5%
5.75	13.9%	9.3%	3.4%	3.0%	13.5%	17.0%
7	11.6%	5.7%	3.7%	3.1%	0%	41.3%
9	12.1%	28.7%	1.4%	1.2%	0%	71.3%

has a 8.1% global scale uncertainty due to the luminosity uncertainty. This will be quadratically added during the integrated cross section calculation. One can repeat this for the electrons from charm decays, with $e_D/e_{npe} = (1 - e_B/e_{npe})$. The corresponding results are listed in Table 5.4 and Table 5.5. The measured differential cross sections of electrons from bottom decays and charm decays are shown separately in Figure 5.3.

Table 5.4: The cross section of electrons from charm hadron decays and the relative statistical uncertainties. A: from e_D/e_{npe}; B: from NPE cross section measurement.

p_T(GeV/c)	$E\frac{d^3\sigma}{dp^3}(nb\ GeV^{-2}\ c^3)$	stat. A	stat. B
3.25	0.299057	18.1%	15.7 %
3.75	0.121292	16.5%	13.6%
4.25	0.0548299	16.9%	13.8 %
4.75	0.0275965	18.7%	13.0%
5.25	0.00962796	16.6 %	18.7%
5.75	0.00493872	11.8 %	16.1 %
7	0.000945195	12.7 %	14.4 %
9	0.0003192	20.9%	23.4%

Table 5.5: The systematic uncertainties of the cross section for electrons from charm hadron decays. A (B): from e_D/e_{npe} lower (upper) bound; C (D): from higher (lower) estimation of J/ψ, Υ decay and Drell-Yan processes contributions E: from interpolation of e_D/e_{npe} if interpolation is used; F: from the luminosity uncertainty in the NPE cross section measurement

p_T(GeV/c)	syst. A	syst. B	syst. C	syst. D	syst. E	syst. F
3.25	4.7%	6.0%	4.7%	5.7%	1.0%	23.9%
3.75	7.7%	5.5%	7.7%	5.2%	1.3%	17.8%
4.25	11.8%	4.4%	11.8%	4.2%	2.1%	16.0%
4.75	17.1%	3.5%	17.1%	3.3%	2.6%	14.7%
5.25	18.0%	4.2%	18.0%	3.8%	7.5%	17.5%
5.75	13.0%	3.4%	13.0%	3.0%	18.7%	17.0%
7	6.3%	3.7%	6.2%	3.1%	0%	41.3%
9	28.3%	1.4%	28.3%	1.2%	0%	71.3%

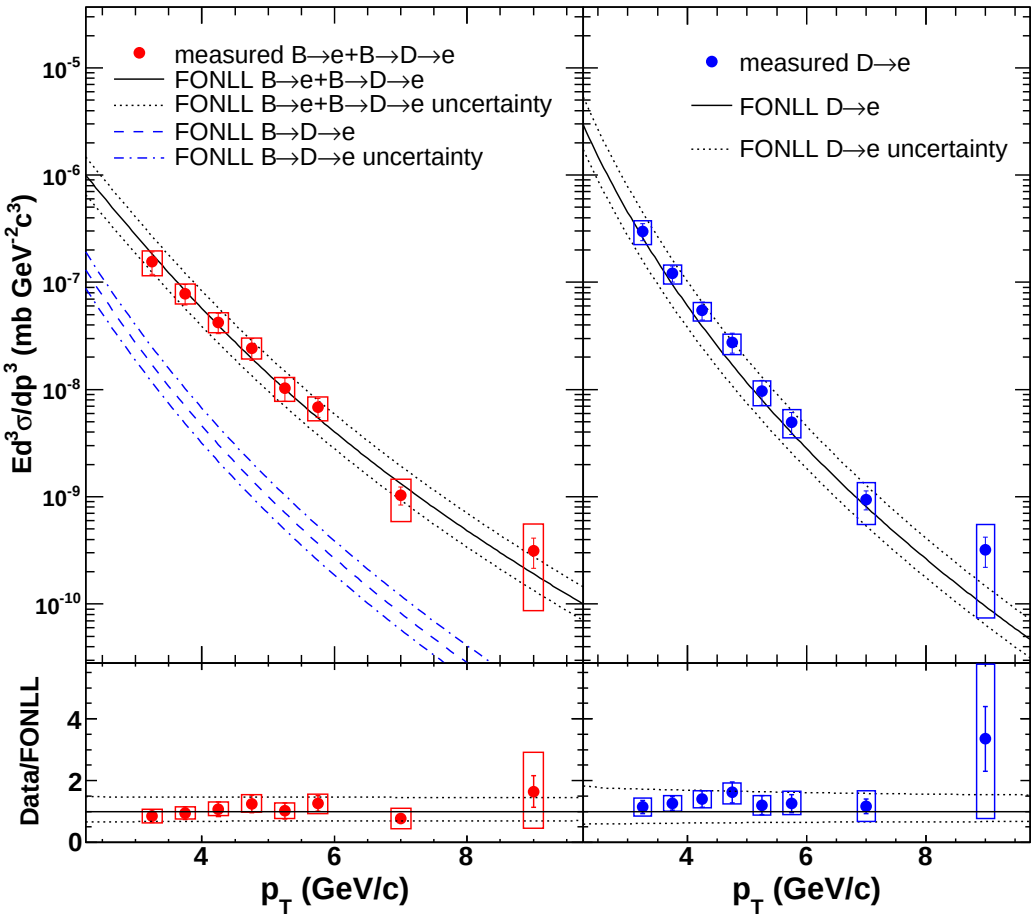

Figure 5.3: Separated spectra of electrons originating from bottom (charm) quarks in the upper left (right) panels. The solid red (blue) circles are experimental measurements of bottom (charm), and the surrounding boxes are the systematic uncertainties. The curves are FONLL predictions in [59], presented as central predictions sandwiched between the upper and lower boundaries. B→D→e means a chain of bottom hadrons decaying to charm hadrons that decay subsequently to electrons. The ratios of bottom (charm) electron data over FONLL are shown in the lower left (right) panels.

5.1.3 FONLL calculations of NPE

A recent Fixed-Order plus Next-to-Leading-Logarithm (FONLL) calculation of NPE is reported in [59]. We compare the original FONLL predictions without any rescaling with the measured data in Figure 5.3, with bottom decays on the left and charm decays on the right, and we find the predictions agree with the data within the uncertainties. We divide the measured data by the FONLL prediction to get the data/FONLL ratio and find it is around 1.03 for most p_T, which indicates the measured data of bottom decay electrons is very close to the central value of the FONLL calculations. For charm decay electrons, the measured data is however between the central value and the upper limit of FONLL calculations.

5.1.4 Integrated cross section of bottom decay electrons

For bottom decay electrons, the differential cross sections at high p_T from 3 GeV/c to 10 GeV/c are summed together to get the integrated cross section according to Equation 5.1.1

$$\frac{d\sigma}{dy_e}|_{y_e=0}\,(p_T = 3-10GeV/c) \;=\; \sum E\frac{d^3\sigma}{d\vec{p}^3}\delta_{binshift}\,p_T\,2\pi\,\Delta p_T \tag{5.1.1}$$

where $E\frac{d^3\sigma}{d\vec{p}^3}$ is the differential cross section at p_T bin center, already listed in Table 5.2. The term $\delta_{binshift}$, which has been discussed in the Au+Au spectrum analysis, converts the cross section at bin center to bin average. The integrated cross section is proportional to the sum of bin average, not bin center values. For the completeness, the $\delta_{binshift}$ are 1.038 at 3.25 GeV/c, and then 1.039, 1.028, 1.030, 1.026, 1.027, 1.339, 1.233 for the following bins [73]. The relative large values 1.339 and 1.233 at 7 and 9 GeV/c have very small effect due to their very small contributions to the total cross section.

With the discussion above, we obtain the middle rapidity cross sections:

$$\frac{d\sigma_{B\to e+B\to D\to e}}{dy_e}|_{y_e=0}(3 < p_T < 10GeV/c) = 4.0 \pm 0.5(stat.) \pm 1.1(syst.)nb \quad (5.1.2)$$

and

$$\frac{d\sigma_{D\to e}}{dy_e}|_{y_e=0}(3 < p_T < 10GeV/c) = 6.2 \pm 0.7(stat.) \pm 1.5(syst.)nb \quad (5.1.3)$$

where we assumed that there is no correlation between the bin-by-bin uncertainties, so the uncertainties of different p_T bins are added in quadrature and the 8.1% global luminosity uncertainty is then added as an overall uncertainty.

It is important to note here the e_B/e_{npe} ratios reported in [72] include indirect contributions from the decay chain of bottom quarks decaying to charm quarks, which in turn decay to electrons, denoted by $B \to e + B \to D \to e$. Therefore, the bottom electron cross sections measured here, both differential and integrated, also include such indirect contributions.

5.2 PYTHIA calculations

In the last section, we introduced the experimental measurement of electrons from bottom decays alone. In this section, we will discuss this from a theoretical point of view. In $p + p$ collisions at $\sqrt{s} = 200$ GeV, the bottom quarks are mainly produced via gluon fusion to bottom and anti-bottom quark pairs, the majority of which then fragment into open bottom hadrons. The cross section for hidden bottom systems (bottomonium states) is ~ 0.1 nb [113], below the 1% level of bottom quark production.

We use the PYTHIA event generator [92] version 6.409 to simulate $p + p$ collisions at $\sqrt{s} = 200$ GeV and select electrons from open bottom hadron decays. The bottom hadrons include B^0, B^+, B_s^0, Λ_b^0, Σ_b^0, Σ_b^-, Σ_b^+, Ξ_b^0, Ξ_b^- and Ω_b^- (and

the charge conjugates, same for the rest of the chapter). We denote all of the direct bottom decaying to electron processes by $B \rightarrow e$. We also select electrons which come from open charm hadrons as long as the parent charm hadrons originate from open bottom hadrons (within 3 generations in the decay chain identified in PYTHIA), and we denote this part by $B \rightarrow D \rightarrow e$. The combined cross section of these two types of processes is calculated in each p_T bin as Equation 5.2.4.

$$E\frac{d^3\sigma_{(B\rightarrow e+B\rightarrow D\rightarrow e)}}{dp^3} = \sigma_{pp}\frac{N_{(B\rightarrow e+B\rightarrow D\rightarrow e)}}{N_{evt}2\pi\, p_T\, \Delta p_T\, \Delta y} \tag{5.2.4}$$

where N_{evt} is the number of events generated by PYTHIA and $N_{(B\rightarrow e+B\rightarrow D\rightarrow e)}$ is the number of electrons (plus positrons, and then divided by two) from the $B \rightarrow e$ process and the $B \rightarrow D \rightarrow e$ process within $|y_e| < 0.5$ in each p_T bin, Δp_T is the size of the p_T bins, and Δy equals $2 \times 0.5 = 1$ since we choose a rapidity range of $|y_e| < 0.5$ in accordance with the experimental measurements. σ_{pp} is an overall factor related to the modes of p+p collisions in PYTHIA calculations, *e.g.* minimum-bias mode or bottom-triggered mode, and is used to normalize the simulated spectrum to the measured spectrum.

To do the normalization, we also calculate the integrated bottom decay electron cross section from p_T = 3 GeV/c to p_T = 10 GeV/c in the PYTHIA calculation, which depends on the global factor σ_{pp} as mentioned. We determine the value of σ_{pp} so that the integrated cross section of electrons from bottom decays here in PYTHIA is the same as the experimental value obtained in the previous section, *i.e.* 4.0nb. Figure 5.4 shows the normalized spectrum from PYTHIA calculation as well as the measurement itself (closed red circles). The solid black curve is for the normalized PYTHIA calculation of $B \rightarrow e$ plus $B \rightarrow D \rightarrow e$, with the dotted red curve for $B \rightarrow e$ and the dashed blue curve for $B \rightarrow D \rightarrow e$ only. The parameters used in this PYTHIA calculation are all default except we use the CTEQ5M1 set of parton distribution functions (PDF). This set of parameters is referred to as

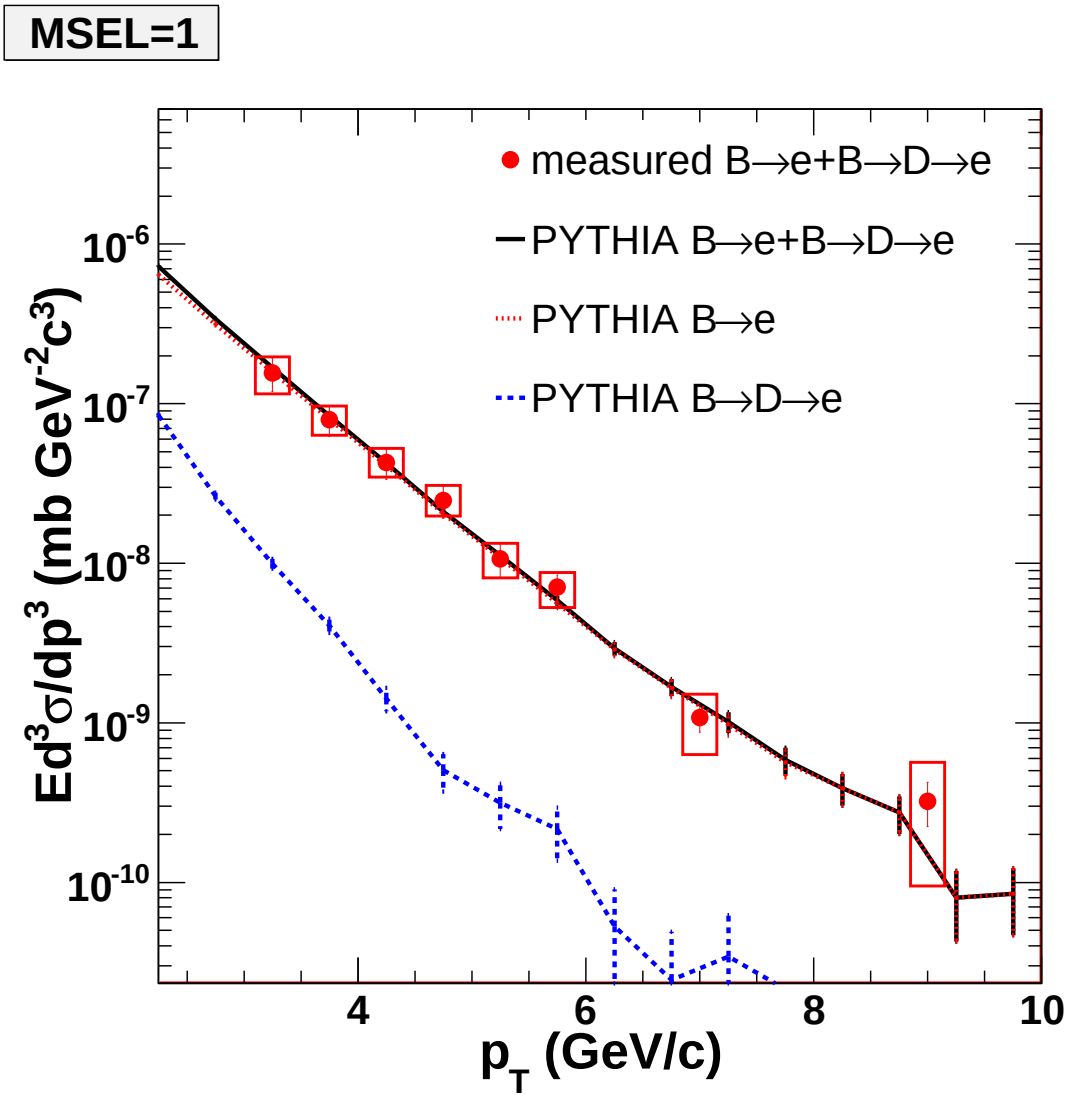

Figure 5.4: Spectra of electrons originating from bottom quarks. The closed red circles are measured bottom decay electron cross sections as described in the text and in Table 5.2, and the surrounding boxes are systematic uncertainties. The solid black curve is the sum of $B \rightarrow e$ plus $B \rightarrow D \rightarrow e$ processes from the nominal PYTHIA calculation normalized to data, with the dotted red curve for the direct process of $B \rightarrow e$ only and the dashed blue curve for $B \rightarrow D \rightarrow e$ only.

the nominal parameter set and it was used in a previous STAR paper [114] with an earlier PYTHIA version. In particular, we point out MSEL= 1 is being used. The spectra from PYTHIA calculations are sensitive to MSEL, which controls the type of pp interactions in PYTHIA simulations. We favor PYTHIA simulations with MSEL= 1 because it provides minimum-bias p+p interactions that include processes beyond the leading order ones.

We note that, although over the entire electron p_T range, the $B \rightarrow D \rightarrow e$ contribution is close to that of $B \rightarrow e$ alone, which is an expected coincidence based on the known branching ratios, it is only about 5% of $B \rightarrow e$ at high electron p_T 3 GeV/c to 10 GeV/c. This is because the electron spectrum of the indirect $B \rightarrow D \rightarrow e$ process is much softer than that in the direct process. Once the overall normalization is done, for example the global factor σ_{pp} is determined to be 23.7 mb in this case, we assume both the direct $B \rightarrow e$ and indirect $B \rightarrow D \rightarrow e$ decay processes are normalized to data. Although both processes can be projected back to low p_T, we will only use the direct $B \rightarrow e$ process to project the total bottom cross section for simplicity, and more importantly, for the measured indirect $B \rightarrow D \rightarrow e$ cross section at high p_T accounts for too little of the total cross section of such processes.

Corresponding to the experimental data Table 5.2 in the previous section, here in Table 5.6 we list the cross sections from the PYTHIA calculation discussed above with the global factor $\sigma_{pp} = 23.7$ mb. The statistical uncertainties are calculated according to the number of electrons plus positrons. Based on this PYTHIA calculation, we project the integrated cross section of electrons directly from bottom hadrons (*i.e.* $B \rightarrow e$ processes only, excluding $B \rightarrow D \rightarrow e$) over the entire p_T range (0 to 10 GeV/c) to be $\frac{d\sigma_{B\rightarrow e}}{dy_e}|_{y_e=0} = 40.2$ nb, which is about 10 times of the integrated cross section at high p_T (3 to 10 GeV/c). There is a very small, 0.4%, statistical uncertainty in PYTHIA since we produced 30 Billion minimum-bias PYTHIA events. The integrated cross section in the 3 GeV/c to

Table 5.6: The electron from bottom decay differential cross sections and the relative statistical uncertainties in a normalized PYTHIA calculation with MSEL= 1. The differential cross sections are bin averages and therefore the p_T bin ranges are listed, instead of the bin centers. The unit for the cross sections is nb GeV^{-2} c^3

p_T range(GeV/c)	$E\frac{d^3\sigma_{B\to e}}{d\vec{p}^3}$	stat. err	$E\frac{d^3\sigma_{B\to D\to e}}{d\vec{p}^3}$	stat. err
0-0.5	3.923	1.3%	26.73	0.5%
0.5-1	3.990	0.7%	5.334	0.6%
1-1.5	2.445	0.7%	1.087	1.1%
1.5-2	1.275	0.9%	0.2759	1.8%
2-2.5	0.6435	1.1%	0.08474	2.9%
2.5-3	0.3148	1.4%	0.02643	4.8%
3-3.5	0.1585	1.8%	0.009964	7.1%
3.5-4	0.07984	2.3%	0.004076	10.4%
4-4.5	0.04111	3.1%	0.001419	16.6%
4.5-5	0.02049	4.1%	0.0005044	26.3%
5-5.5	0.01084	5.4%	0.0003147	31.6%
5.5-6	0.005632	7.1%	0.0002155	36.5%
6-6.5	0.002882	9.6%	5.287e-05	70.7%
6.5-7	0.001652	12.2%	2.448e-05	100%
7-7.5	0.0009800	15.2%	3.419e-05	81.6%
7.5-8	0.0005650	19.4%	2.132e-05	100%
8-8.5	0.0003905	22.6%	0	–
8.5-9	0.0002738	26.3%	0	–
9-9.5	8.038e-05	47.1%	0	–
9.5-10	8.473e-05	44.7%	0	–

Table 5.7: The integrated cross section of electrons from bottom decays (0 GeV/c< p_T <10 GeV/c) in PYTHIA calculations with various parameters. A value denoted by (D) means it is the PYTHIA default value. The deviations listed are relative to the nominal set in first row.

$\langle k_T \rangle$	Max.k_T	PDF	$\frac{d\sigma_{B\to e}}{dy_e}\|_{y_e=0}(nb)$	deviation
2.0GeV(D)	5.0GeV(D)	CTEQ5M1	40.2	0
0.5GeV	5.0GeV(D)	CTEQ5M1	41.6	+3.5%
1.5GeV	10.0GeV	CTEQ5M1	38.5	-4.3%
3.0GeV	15.0GeV	CTEQ5M1	42.2	+5%
4.5GeV	20.0GeV	CTEQ5M1	36.0	-10.5%
2.0GeV(D)	5.0GeV(D)	CTEQ5L (D)	38.8	-3.5%
	CDF tuneA		45.7	+14%

10 GeV/c range has a 1.2% statistical uncertainty in PYTHIA. Therefore, the statistical uncertainties in PYTHIA can be neglected and the statistical uncertainties associated with these cross section values are just the statistical uncertainties inherited from data. In short, for the projected $B \to e$ cross section at high p_T, we estimate the statistical uncertainty is 12.5% and the systematic uncertainty is 27.5%.

To explore the theoretical uncertainties, we use other parameter sets for PYTHIA calculations. Firstly, we vary the intrinsic k_T and the PDF used in the PYTHIA calculations and find they do not change the results by more than 10%. We list the results with various k_T and PDF in Table 5.7, including the nominal parameter set as the first row of the table. The intrinsic k_T is a Gaussian distribution with its width set by parp(91) and the upper cut off set by parp(93). The PDF is set by mstp(51)=8 for the CTEQ5M1 case, and mstp(51)=7 for the PYTHIA default CTEQ 5L.

Secondly, we also utilize the parameter set used in the e-h paper, and find that it gives $\frac{d\sigma_{B\to e}}{dy_e}\|_{y_e=0}$ = 28.1 nb, 30% lower than the nominal value. Since this is a large variation, we list the details of this parameter set in Table 5.8 and the normalized cross sections from this calculation in Table 5.9, which are also shown in Figure 5.5. 10 billion PYTHIA minimum-bias events were produced for this

Table 5.8: The parameters set in the NPE-hadron correlation study

e-h paper [72] PYTHIA parameter	value	comment
MSEL	1	Minimum-bias
parp(91)	1.5	inital p_T
parp(93)	10.	maximum p_T
pmas(4,1)	1.25	mass of charm
pmas(5,1)	4.8	mass of bottom
mstp(33)	1	using K factor
parp(31)	3.5	K factor, default=1.5
mstp(32)	4	definition of Q^2
parp(67)	4	a factor multiplied to Q^2
mstp(51)	7	CTEQ5M1
MSTJ(11)	3	peterson function used
PARJ(54)	-1.0×10^{-5}	ϵ for charm
PARJ(55)	-1.0×10^{-5}	ϵ for bottom

calculation.

In addition, the CDF PYTHIA tuneA [115] parameter set has also been used, and it gives an integrated cross section of 45.7 nb, which is 14% higher than the nominal value of 40.2 nb.

One important point we notice is that PYTHIA can simulate different p+p scattering processes, so one needs to make a choice. In the PYTHIA calculations presented above, we always use the minimum-bias processes, *i.e.* both high Q^2 processes and low Q^2 processes [92], and the control parameter MSEL is always 1. Below we will use a different process, namely the triggered bottom quark production mode with MSEL=5, which only has leading order processes, *e.g.* $q\bar{q}$ and gg scatterings. With exactly the same parameters as the nominal PYTHIA calculation, except MSEL=5, this mode produces a much softer spectrum shape, and thus a much higher integrated cross section. $\frac{d\sigma_{B\to e}}{dy_e}|_{y_e=0} = 53.8nb$ is obtained after being normalized to the experimental data at high p_T. Only 10 million such PYTHIA events are produced, but since all of them have bottom quarks, the statistical uncertainty from PYTHIA is even smaller than the previous calculations. The details are listed in Table 5.10 and plotted in Figure 5.6. We emphasize the

Table 5.9: The electron from bottom decay differential cross sections from a PYTHIA calculation with parameters in the NPE-hadron correlation study [72], listed in Table 5.8. The unit for the cross sections is nb GeV^{-2} c^3

$p_T$range(GeV/c)	$E\frac{d^3\sigma_{B\to e}}{d\vec{p}^3}$	stat. err	$E\frac{d^3\sigma_{B\to D\to e}}{d\vec{p}^3}$	stat. err
0-0.5	2.723	1.7%	17.64	0.7%
0.5-1	2.585	1.0%	3.731	0.9%
1-1.5	1.564	1.0%	0.8490	1.4%
1.5-2	0.8389	1.2%	0.2455	2.2%
2-2.5	0.4553	1.4%	0.08174	3.3%
2.5-3	0.2427	1.7%	0.03018	5.0%
3-3.5	0.1346	2.2%	0.01101	7.5%
3.5-4	0.07413	2.7%	0.004839	10.6%
4-4.5	0.04265	3.4%	0.002303	14.4%
4.5-5	0.02470	4.2%	0.001352	17.8%
5-5.5	0.01334	5.4%	0.0005631	26.3%
5.5-6	0.008315	6.5%	0.0002305	39.2%
6-6.5	0.004290	8.7%	0.0001957	40.8%
6.5-7	0.002628	10.7%	7.551e-05	63.2%
7-7.5	0.001547	13.5%	7.031e-05	63.2%
7.5-8	0.0009997	16.2%	2.631e-05	100%
8-8.5	0.0004943	22.4%	0	–
8.5-9	0.0003146	27.2%	0	–
9-9.5	0.0003416	25.4%	1.102e-05	141.4%
9.5-10	0.0001464	37.8%	0	–

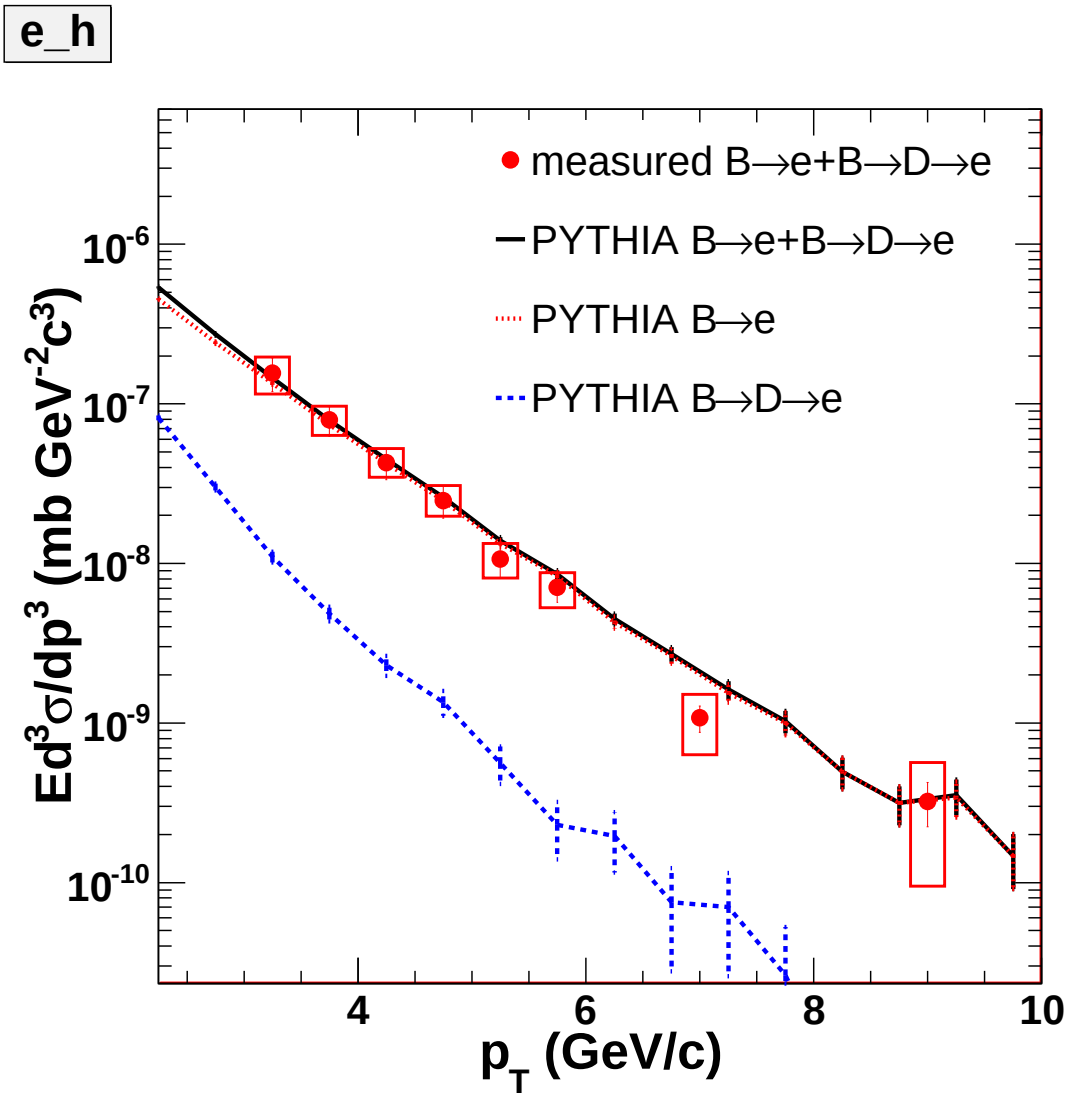

Figure 5.5: Same as Figure 5.4, but from a normalized PYTHIA calculation with parameters used in the NPE-hadron correlation study [72].

Table 5.10: The electron from bottom decay differential cross sections from a normalized PYTHIA calculation with the same nominal parameters except in a bottom production mode. The unit for the cross sections is nb GeV^{-2} c^3

$p_T$range(GeV/c)	$E\frac{d^3\sigma_{B\to e}}{d\vec{p}^3}$	stat. err	$E\frac{d^3\sigma_{B\to D\to e}}{d\vec{p}^3}$	stat. err
0-0.5	5.324	0.7%	36.93	0.3%
0.5-1	5.604	0.4%	7.192	0.3%
1-1.5	3.486	0.4%	1.330	0.6%
1.5-2	1.761	0.4%	0.3094	1.0%
2-2.5	0.8337	0.6%	0.08253	1.8%
2.5-3	0.3807	0.7%	0.02580	2.9%
3-3.5	0.1740	1.0%	0.00891	4.5%
3.5-4	0.08026	1.4%	0.003206	6.9%
4-4.5	0.03869	1.9%	0.001269	10.3%
4.5-5	0.01870	2.5%	0.0004674	16.1%
5-5.5	0.009073	3.5%	0.0002636	20.4%
5.5-6	0.004719	4.6%	5.516e-05	42.6%
6-6.5	0.002445	6.1%	2.768e-05	57.7%
6.5-7	0.001491	7.6%	2.136e-05	63.2%
7-7.5	0.0007159	10.5%	2.386e-05	57.7%
7.5-8	0.0003907	13.8%	1.116e-05	81.7%
8-8.5	0.0002901	15.5%	6.990e-06	100%
8.5-9	0.0001483	21.1%	3.295e-06	141.4%
9-9.5	8.105e-05	27.7%	0	–
9.5-10	3.845e-05	39.2%	2.957e-06	141.4%

difference on the bottom decay electron cross section here is 34% and it indicates a large theoretical uncertainty purely from different PYTHIA modes.

In conclusion, based on PYTHIA calculations normalized to data, we measure that the integrated $B \to e$ cross section at mid-rapidity could range from 28.1 nb to 53.8 nb depending PYTHIA simulation mode and other parameters. The difference indicates the scale of the theoretical uncertainty. Also, the $B \to e$ cross section from the data is found to be 1.03 times higher than FONLL predictions.

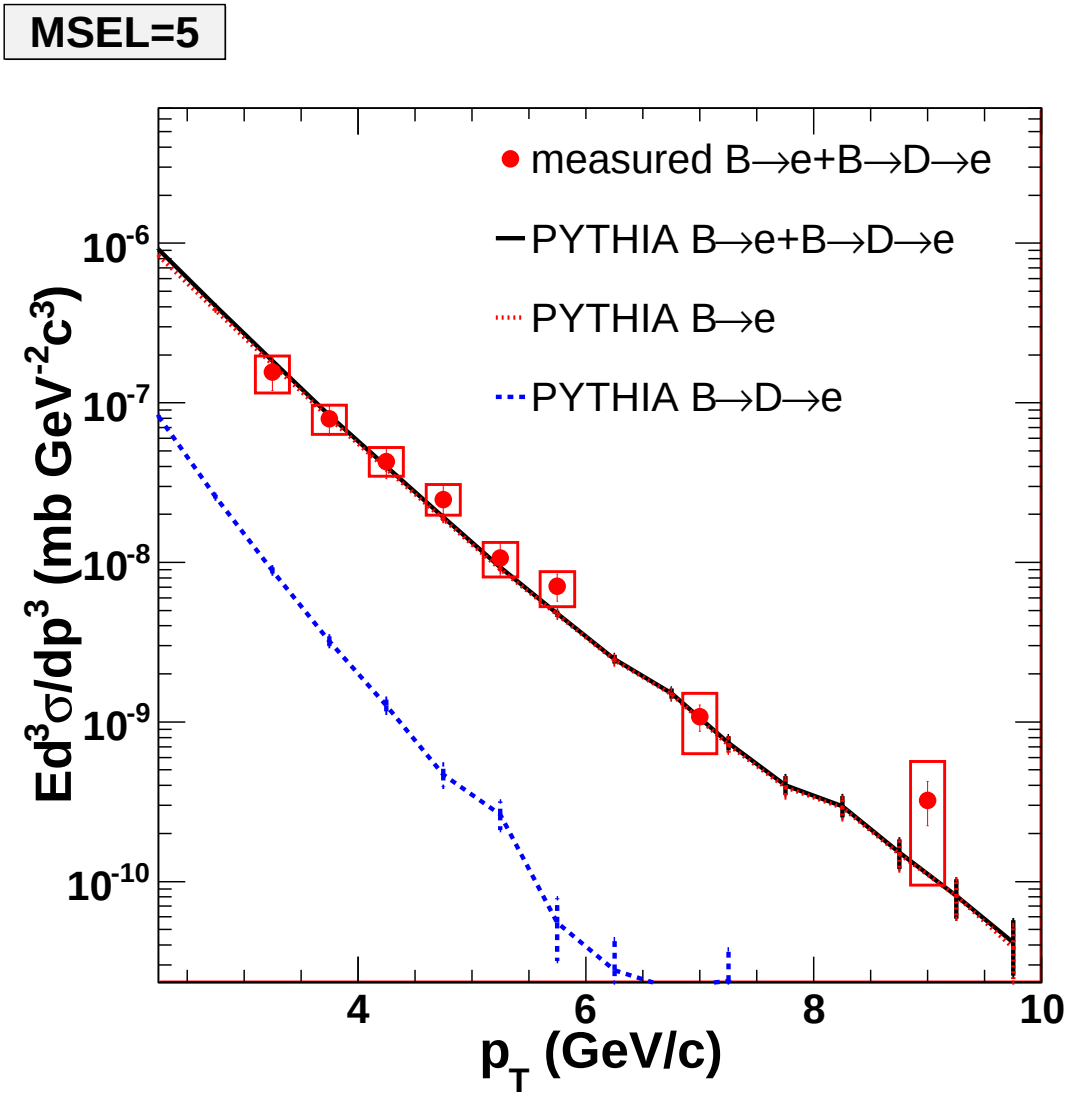

Figure 5.6: Same as Figure 5.4, but from a normalized PYTHIA calculation with the same nominal parameters except in a bottom production mode.

5.3 Bottom production cross section

To get the total bottom quark production cross section based on $B \rightarrow e$ cross section at mid-rapidity, one needs to consider the branching ratio (B.R.) of the semi-leptonic decays of all the bottom hadrons and the rapidity distribution, according to Equation 5.3.5.

$$\begin{aligned}
\sigma_{b\bar{b}} &= \frac{\sigma_{B\rightarrow e}}{B.R.} \\
&= \frac{\int \frac{d\sigma_{B\rightarrow e}}{dy_B}\, dy_B}{B.R.} \\
&= \frac{c1(\int_{-0.5}^{0.5} \frac{d\sigma_{B\rightarrow e}}{dy_B}\, dy_B)}{B.R.} \\
&= \frac{c1\, c2(\int_{-0.5}^{0.5} \frac{d\sigma_{B\rightarrow e}}{dy_e}\, dy_e)}{B.R.}
\end{aligned} \tag{5.3.5}$$

where $\int_{-0.5}^{0.5} \frac{d\sigma_{B\rightarrow e}}{dy_e}\, dy_e$ equals to $\frac{d\sigma_{B\rightarrow e}}{dy_e}\,|_{y_e=0}$. The first rapidity correction factor, $c1$, accounts for the large correction needed to extrapolate from mid-rapidity to the full rapidity range, and thus it is defined as $\frac{\int \frac{d\sigma_{B\rightarrow e}}{dy_B}\, dy_B}{\int_{-0.5}^{0.5} \frac{d\sigma_{B\rightarrow e}}{dy_B}\, dy_B}$. The second rapidity correction factor, $c2$, is a small correction to convert the electron rapidity distribution to bottom hadron rapidity distribution, both at middle rapidity. It is defined as $\frac{\int_{-0.5}^{0.5} \frac{d\sigma_{B\rightarrow e}}{dy_B}\, dy_B}{\int_{-0.5}^{0.5} \frac{d\sigma_{B\rightarrow e}}{dy_e}\, dy_e}$, where y_B is the bottom hadron rapidity, and y_e is the electron rapidity. Both $c1$ and $c2$ can be calculated in PYTHIA events.

The averaged branching ratio of the semi-leptonic decays depends on the admixture of bottom hadrons. The bottom hadron admixture has not been measured at RHIC and the PDG has a summary of measurements at LEP, Tevatron, and $Sp\bar{p}S$ [2]. In Table 5.11, we compare the admixture produced by PYTHIA with the PDG one, and they are rather consistent. We use the values from PYTHIA as the nominal values. We notice that in our PYTHIA calculation the averaged B.R. value is 10.4%, and it is very close to the lower limit of PDG value 10.5%. It

Table 5.11: The bottom hadron fractions in the admixture reported in PDG and in our nominal PYTHIA calculation, and the corresponding B.R. for semi-leptonic decays. The relative statistical errors from PYTHIA are always smaller than 1%.

Particle	Fraction in PDG	in PYTHIA	B.R. in PDG	in PYTHIA
B^0	$(40.1 \pm 1.3)\%$	39.5%	$(10.33 \pm 0.28)\%$	10.52%
B^+	$(40.1 \pm 1.3)\%$	39.7%	$(10.99 \pm 0.28)\%$	10.47%
B_s^0	(11.3 ± 1.3) %	11.6%	$(7.9 \pm 2.4)\%$	10.53%
bottom baryon	$(8.5 \pm 2.2)\%$	9.1%	$(\sim 9.3)\%$	9.24%
Average	-	-	$(10.86 \pm 0.35)\%$	10.4%

is conservative enough to use the upper limit of PDG B.R., 11.2%, as our upper limit, which is equivalent to an approximately 8% relative uncertainty, smaller than the 13% systematic uncertainty from the measured data, let alone the much larger theoretical uncertainty. The statistical uncertainty from PYTHIA is still smaller than 1%.

The admixture of the bottom baryons in our PYTHIA calculation is 77% Λ_b^0, a total of 12% Σ_b^0, Σ_b^- and Σ_b^+, a total of 11% Ξ_b^0 and Ξ_b^-, and less than 1% Ω_b^-. The dominate component, Λ_b^0 has a semi-leptonic decay B.R. = 10.5%, making the bottom baryons B.R. very close to that of bottom mesons. As a result, the final results are not sensitive to the exact fraction of bottom baryons in the admixture of bottom hadrons.

The first rapidity correction factor $c1$ is calculated as the number of bottom hadrons in all rapidity divided by that within $|y_B| < 0.5$. The bottom hadrons are inclusive, including but not limited to those decaying to electrons. The second rapidity correction factor $c2$ is calculated as the number of bottom hadrons that decay to electrons within hadron rapidity $|y_B| < 0.5$ divided by the number of electrons from bottom hadron decays within electron rapidity $|y_e| < 0.5$. We determine $c1 = 3.01, c2 = 1.15$ in the nominal minimum-bias PYTHIA calculation and $c1 = 3.07, c2 = 1.15$ in the PYTHIA calculation with MSEL=5, both with less than 1% statistical uncertainties.

Based on our PYTHIA calculations, the total bottom quark production cross

section in p+p collisions at $\sqrt{s} = 200$ GeV is measured to be $\sigma_{b\bar{b}}^{mb} = \frac{40.2nb \times 1.15 \times 3.01}{0.104} =$ 1.34 μb in the minimum-bias mode and $\sigma_{b\bar{b}}^{B-trigger} = \frac{53.8 \times 1.15 \times 3.07}{0.104} =$ 1.83 μb in the bottom triggered mode. In [59], the central FONLL prediction of total cross section of bottom production has been reported to be $1.87^{+0.99}_{-0.67}\mu b$. The measured cross section of bottom hadron decaying to electrons is 1.03 times higher than the FONLL central prediction at high p_T, and thus we multiply 1.87 μb by 1.03 and obtain $\sigma_{b\bar{b}}^{FONLL}$=1.93 μb. Finally, we note that these measurements all inherit the 12.5% statistical and 27.5% systematic uncertainties from the measured $B \rightarrow e$ cross section at high p_T.

CHAPTER 6

Conclusion and Outlook

The spectra of the non-photonic electrons in Au+Au collisions at $\sqrt{s_{\rm NN}}$ = 200 GeV have been measured in this dissertation, with a much improved precision over the previous STAR measurements [61]. The nuclear modification factors of NPE are also calculated accordingly, which approach as low as approximately $R_{AA} \sim 0.3$, confirming a significant heavy quark energy loss indicative of a strong coupling between heavy quarks and the QGP medium.

The recent understanding is that elastic collisions are likely to play an important role in the heavy quark-medium coupling interaction. Indeed, collisional energy loss models based on non-perturbative processes such as heavy flavor hadron/resonance formation inside QGP or based on improved pQCD calculations agree with our measured NPE R_{AA} values within uncertainties. However, for definitive data-model comparisons, charm and bottom decay electrons must be separated, since their energy loss are often quite different in the models.

The first STAR measurement of high p_T non-photonic electron elliptic flow, which closely reflects the elliptic flow of heavy flavor hadrons, is also presented in this dissertation. The NPE elliptic flow is not only finite but also sizable and generally higher than current model predictions. Much larger data sample are required to reduce the statistical uncertainty of the measurement. Our first attempt of the NPE elliptic flow measurement allowed us to evaluate many relevant experimental systematics and provide valuable guidance for further measurement from STAR.

In addition to elliptic flow, we initialized a study with another more differential probe, the NPE-hadron azimuthal correlation. The preliminary results indicate a broadening of the away side peak, which is likely due to heavy quark jet-medium interactions, albeit different interpretations and hidden systematic uncertainties need further investigations with better statistics. If this modification is truly a result of heavy quark jet-medium interactions, it could provide an independent way to constrain both the energy loss mechanism and the medium evolution.

In summary, the NPE from heavy quark decays can provide quantitative information about the QGP. Our results have posted serious challenges to the early dynamical models that worked well for light quark energy loss. The NPE azimuthal anisotropy and azimuthal correlation studies are emerging to be a probe for both the heavy quark-medium interactions and the dynamical evolution of the QGP medium itself. The outstanding difficulties experimentally are the limited ability to separate charm and bottom decays in heavy ion collisions, and limited data sample for more differential studies. The STAR Heavy Flavor Tracker upgrade will truly fulfill the capability of heavy flavor probes by measuring separated charm and bottom production. Heavy Quark probes are expected to quantitatively measure dynamical properties of the Quark-Gluon Plasma created in high-energy nucleus-nucleus collisions, which will deepen our understanding of the underlying fundamental theory of Quantum ChromoDynamics and the nature of Quark-hadron phase transition in the early universe.

APPENDIX A

List of Rejected Runs

A: Find outliers with Ref-Multiplicity three RMS away from the average over the entire Run 2010(Standard STAR bad runs)

11005042, 11006004, 11006005, 11006008, 11007015, 11023048, 11025034, 11025038, 11025054, 11026005, 11026008, 11026021, 11026022, 11026023, 11026025, 11026067, 11026068, 11030080, 11031061, 11035072, 11036026, 11037035, 11037037, 11037060, 11039047, 11044029, 11049023, 11051038, 11052011, 11053057, 11054059, 11054062, 11058005, 11072032, 11072044, 11072045, 11073001, 11073003, 11075048

B: No BEMC runs (Standard STAR bad runs)

11002140, 11002141, 11002142, 11002143, 11002144, 11015069, 11015071, 11016024, 11017006, 11018007, 11018008, 11019080, 11019081, 11035008, 11035009, 11038048, 11038049, 11038050, 11047065, 11047066, 11047067, 11048037, 11049001, 11049002, 11049005, 11051049, 11051051, 11051055, 11051063, 11051064, 11051068, 11054021, 11054022, 11059076, 11059077, 11061008, 11061009, 11061034, 11061037, 11061038, 11063006, 11063008, 11063011, 11063013, 11063014, 11063015, 11063016, 11063017, 11065038, 11066045, 11073049, 11075039, 11075045

C: Runs with significant shift of primary vertex position and mean track p_T (Standard STAR bad runs)

11028004, 11028005, 11028006, 11028007, 11028008, 11028009, 11028010, 11028011, 11028012, 11028013, 11028014, 11028015, 11028016, 11028017, 11028018, 11028019, 11028020, 11028021, 11028022, 11028023, 11028024, 11028025, 11028026, 11028027, 11026042

D: Runs with 4 or more bad TPC Readout boards (RDO) (Standard STAR bad runs)

11021015, 11021026, 11021027, 11021028, 11021030, 11021031, 11021032, 11004007, 11004008, 11004009, 11004010, 11004011, 11004012, 11004013, 11004014, 11004015, 11004016, 11004018, 11004020, 11004021, 11004023, 11004024, 11004025, 11004026, 11004028, 11004029, 11004030, 11004032, 11004033, 11004034, 11004035, 11004037, 11004038, 11003101, 11003102, 11041022, 11041023, 11041040, 11041041, 11042001, 11042002, 11042003, 11042004, 11042005, 11042006, 11042007, 11042008, 11042011, 11042012, 11042018, 11042019, 11042020, 11042021, 11042022, 11042023, 11042024, 11042025, 11042026, 11042027, 11042042, 11042043, 11042044, 11042045, 11042046, 11042047, 11042048, 11042049

E: Runs with too few (less than one thousand) good MiniBias events (Standard STAR bad runs)

11011019, 11030041, 11039067, 11054024, 11054066, 11057012, 11057035, 11057036, 11058050, 11058083, 11059043, 11059055, 11059060, 11059075, 11060049, 11060059, 11060076, 11061008, 11061021, 11061037, 11063007, 11063017, 11063036, 11063083, 11064003, 11064023

F:Runs with bad NPE11/MiniBias events ratio (Non-Standard STAR bad runs)

11051050,11051045,11047067,11047066,11047065,11044024,

11038050,11038049,11038048,11038047,11030045,11028004,
11025069,11019081,11019080,11019079,11018036,11018008,
11018007,11017006,11016024,11015069,11011087,11011084,
11011083,11011082,11011081,11011080,11011079,11011078,
11011077,11011053

G:Runs with different efficiencies of the cuts $|V_Z| < 30cm$ and $|V_Z^{TPC} - V_Z^{VPD}| < 3cm$ (Non-Standard STAR bad runs)
11071056,11071055,11040078,11031064,11030068,11030067,11030065,
11030025,11030009,11029087,11029086,11026010,11019001,11018003

APPENDIX B

Error propagation in elliptic flow calculations

The Standard Deviation (or "error") of a measured variable is the square root of the variance of the sample mean for this variable, *i.e.*

$$S = \frac{RMS}{\sqrt{N}} = \frac{\sqrt{\frac{\sum(x_i-\hat{\mu})^2}{N}}}{\sqrt{N}} \tag{B.0.1}$$

where root mean square (RMS)= $\sqrt{\frac{\sum(x_i-\hat{\mu})^2}{N}}$ is used.

To combine several data sets

$$S^2_{total} = \frac{\frac{\sum_\alpha[\sum_i(x_{\alpha i}-\hat{\mu}_\alpha)^2+N_\alpha\hat{\mu}^2_\alpha]}{\sum_\alpha N_\alpha} - [\frac{\sum_\alpha(N_\alpha\hat{\mu}_\alpha)}{\sum_\alpha N_\alpha}]^2}{\sum_\alpha N_\alpha} \tag{B.0.2}$$

where α means different data sets, *e.g.* different η bins or p_T bins.

We can check this with, for example, the case of two data sets, where

$$\hat{\mu} = \frac{N_1\hat{\mu}_1 + N_2\hat{\mu}_2}{N_1 + N_2}$$

and $N = N_1 + N_2$. Then,

$$
\begin{aligned}
RMS^2 = & \frac{\sum_1 (x_{1i} - \frac{N_1\hat{\mu}_1 + N_2\hat{\mu}_2}{N_1+N_2})^2 + \sum_2 (x_{2i} - \frac{N_1\hat{\mu}_1 + N_2\hat{\mu}_2}{N_1+N_2})^2}{N_1 + N_2} \\
= & \frac{\sum_1 [x_{1i} - \hat{\mu}_1 + \frac{N_2(\hat{\mu}_1 - \hat{\mu}_2)}{N_1+N_2}]^2 + \sum_2 [x_{2i} - \hat{\mu}_2 + \frac{N_1(\hat{\mu}_2 - \hat{\mu}_1)}{N_1+N_2}]^2}{N_1 + N_2} \\
= & \frac{\sum_1 \{(x_{1i} - \hat{\mu}_1)^2 + [\frac{N_2(\hat{\mu}_1 - \hat{\mu}_2)}{N_1+N_2}]^2 + (x_{1i} - \hat{\mu}_1)\frac{2N_2(\hat{\mu}_1 - \hat{\mu}_2)}{N_1+N_2}\}}{N_1 + N_2} \\
& + \frac{\sum_2 \{(x_{2i} - \hat{\mu}_2)^2 + [\frac{N_1(\hat{\mu}_2 - \hat{\mu}_1)}{N_1+N_2}]^2 + (x_{2i} - \hat{\mu}_2)\frac{2N_1(\hat{\mu}_2 - \hat{\mu}_1)}{N_1+N_2}\}}{N_1 + N_2} \\
= & \frac{[\sum_1 (x_{1i} - \hat{\mu}_1)^2 + \sum_2 (x_{2i} - \hat{\mu}_2)^2] + (N_1 N_2^2 + N_1^2 N_2)(\frac{\hat{\mu}_1 - \hat{\mu}_2}{N_1+N_2})^2}{N_1 + N_2} \\
= & \frac{[\sum_1 (x_{1i} - \hat{\mu}_1)^2 + \sum_2 (x_{2i} - \hat{\mu}_2)^2] + \frac{(N_1 N_2)(\hat{\mu}_1 - \hat{\mu}_2)^2}{N_1+N_2}}{N_1 + N_2}
\end{aligned}
\tag{B.0.3}
$$

where $\sum_1 (x_{1i} - \hat{\mu}_1) = 0$ and $\sum_2 (x_{2i} - \hat{\mu}_2) = 0$ are used. Finally,

$$
S^2 = \frac{RMS^2}{N_1 + N_2} = \frac{[\sum_1 (x_{1i} - \hat{\mu}_1)^2 + \sum_2 (x_{2i} - \hat{\mu}_2)^2] + \frac{(N_1 N_2)(\hat{\mu}_1 - \hat{\mu}_2)^2}{N_1+N_2}}{(N_1 + N_2)^2} \tag{B.0.4}
$$

At the same time, in the case of two (2) bins, the original formula becomes

$$
\begin{aligned}
S^2_{total} = & \frac{\frac{\sum_1 (x_{1i} - \hat{\mu}_1)^2 + \sum_2 (x_{2i} - \hat{\mu}_2)^2 + N_1\hat{\mu}_1^2 + N_2\hat{\mu}_2^2}{N_1+N_2} - [\frac{N_1\hat{\mu}_1 + N_2\hat{\mu}_2}{N_1+N_2}]^2}{N_1 + N_2} \\
= & \frac{\sum_1 (x_{1i} - \hat{\mu}_1)^2 + \sum_2 (x_{2i} - \hat{\mu}_2)^2}{(N_1 + N_2)^2} \\
& + \frac{(N_1\hat{\mu}_1^2 + N_2\hat{\mu}_2^2)(N_1 + N_2) - (N_1^2\hat{\mu}_1^2 + N_2^2\hat{\mu}_2^2 + 2N_1\hat{\mu}_1 N_2\hat{\mu}_2)}{(N_1 + N_2)^3} \\
= & \frac{\sum_1 (x_{1i} - \hat{\mu}_1)^2 + \sum_2 (x_{2i} - \hat{\mu}_2)^2}{(N_1 + N_2)^2} + \frac{N_1 N_2(\hat{\mu}_1 - \hat{\mu}_2)^2}{(N_1 + N_2)^3} = S^2
\end{aligned}
\tag{B.0.5}
$$

References

[1] V. W. Hughes, T. Kinoshita, "Anomalous g values of the electron and muon." *Rev. Mod. Phys.* **71**, S133 (1999).

[2] K. Nakamura et al. (Particle Data Group), *J. Phys.* **G37**, 075021 (2010).

[3] M. E. Peskin, D. V. Schroeder, "An Introduction to Quantum Field Theory." Westview Press (1995). Chapter 16 and references therein.

[4] R. K. Ellis, W. J. Stirling, B. R. Webber, "QCD and Collider Physics." Cambridge University Press (1996).

[5] S. Chekanov et al. (ZEUS Collaboration), "A ZEUS next-to-leading-order QCD analysis of data on deep inelastic scattering." *Phys. Rev.* **D67**, 012007 (2003).

[6] A. Abulencia et al. (CDF Collaboration), "Measurement of the inclusive jet cross section using the k_T algorithm in pp collisions at $\sqrt{s} = 1.96$TeV with the CDF II detector." *Phys. Rev.* **D75**, 092006 (2007).

[7] B. I. Abelev, et al. (STAR Collaboration), "Longitudinal double-spin asymmetry and cross section for inclusive jet production in polarized proton collisions at $\sqrt{s} = 200$ GeV." *Phys. Rev. Lett.* **97**, 252001 (2006).

[8] G. Baym, "RHIC: From dreams to beams in two decades." *Nucl. Phys.* **A698**, XXIII-XXXII (2002).

[9] R. Stock, "Relativistic Nucleus-Nucleus Collisions and the QCD Matter Phase Diagram." arXiv:0807.1610.

[10] F. Karsch, "Lattice QCD at high temperature and density." *Lect. Notes Phys.* **583**, 209 (2002).

[11] J. .C Collins, M. J. Perry, "Superdense Matter: Neutrons or Asymptotically Free Quarks?" *Phys. Rev. Lett.* **34**, 1353 (1975).

[12] G. F. Burgio, M. Baldo, P. K. Sahu, H.-J. Schulze, "Hadron-quark phase transition in dense matter and neutron stars." *Phys. Rev.* **C66**, 025802 (2002).

[13] Committe on the Physics of the Universe, National Research Council, "Connecting Quarks with the Cosmos: Eleven Science Questions for the New Century." (2003).

[14] J. Adams et al. (STAR Collaboration), "Experimental and Theoretical Challenges in the Search for the Quark Gluon Plasma: The STAR Collaborations Critical Assessment of the Evidence from RHIC Collisions." *Nucl. Phys.* **A757**, 102 (2005).

[15] P. Braun-Munzinger, J. Stachel, "The quest for the quark−gluon plasma." *N*ature **448**, 302 (2007).

[16] J. Letessier, J. Rafelski, "Hadrons and Quark-Gluon Plasma." Cambridge University Press (2002).

[17] A. Chodos, R. L. Jaffe, K.Johnson, C. B. Thorn,V. F. Weisskopf, "New extended model of hadrons." *Phys. Rev.* **D9**, 3471-3495 (1974).

[18] C. E. DeTar, J. F. Donoghue, "Bag Models of hadrons." *Ann. Rev. Nucl. Part. Sci.* **33**, 235 (1983).

[19] T. D. Lee, G. C. Wick, "Vacuum stability and vacuum excitation in a spin-0 field theory." *Phys. Rev.* **D9**, 2291 (1974).

[20] M. J. Tannenbaum, "Recent results in relativistic heavy ion collisions: from 'a new state of matter' to 'the perfect fluid'." *Rep. Prog. Phys.* **69**, 2005 (2006).

[21] H. H. Gutbrod, A. M. Poskanzer, H. G. Ritter, "Plastic Ball experiments." *Rep. Prog. Phys.* **52**, 1267 (1989).

[22] A. Andronic, P. Braun-Munzinger, J. Stachel, H. Stöcker, "Production of light nuclei, hypernuclei and their antiparticles in relativistic nuclear collisions." *Phys. Lett.* **B697**, 203 (2011).

[23] S. S. Adler et al (PHENIX collaboration), "Identified Charged Particle Spectra and Yields in Au+Au collisions at $\sqrt{s_{\rm NN}}$ = 200 GeV." *Phys. Rev.* **C69**, 034909 (2004).

[24] C. Nonaka, S. A. Bass, "Space-time evolution of bulk QCD matter." *Phys. Rev.* **C75**, 014902 (2007).

[25] A. M. Poskanzer, S. A. Voloshin, "Methods for analyzing anisotropic flow in relativistic nuclear collisions." *Phys. Rev.* **C58**, 1671 (1998).

[26] J. Adams et al (STAR collaboration), "Azimuthal anisotropy in Au+Au collisions at $\sqrt{s_{\rm NN}}$ = 200 GeV." *Phys. Rev.* **C72**, 014904 (2005)

[27] J. Adams et al. (STAR Collaboration), "Azimuthal anisotropy and correlations at large transverse momenta in p+p and Au+Au collisions at $\sqrt{s_{\rm NN}}$ = 200 GeV." *Phys. Rev. Lett.* **93**, 252301 (2004).

[28] S. S. Adler et al (PHENIX collaboration), "Elliptic Flow of Identified Hadrons in Au+Au Collisions at $\sqrt{s_{\rm NN}}$ = 200 GeV". *Phys. Rev. Lett.* **91**, 182301 (2003).

[29] B. Müller, J. L. Nagle, "Results from the Relativistic Heavy Ion Collider." *Ann. Rev. Nucl. Part. Sci.* **56**, 93 (2006).

[30] P. Huovinen, private communication (2004) with the authors of [26]. T_c=165MeV, T_f=130 MeV, EoS=Q.

[31] R. J. Fries, C. Nonaka, "Evaluating results from the Relativistic Heavy Ion Collider with perturbative QCD and hydrodynamics." *Prog. Part. Nucl. Phys.* **66**, 607 (2011)

[32] http://www.bnl.gov

[33] P. K. Kovtun, D. T. Son, A. O. Starinets, "Viscosity in Strongly Interacting Quantum Field Theories from Black Hole Physics." *Phys. Rev. Lett.* **94**, 111601 (2005).

[34] B. Alver et al (PHOBOS collaboration). "Event-by-event fluctuations of azimuthal particle anisotropy in Au+Au collisions at $\sqrt{s_{\rm NN}}$ = 200 GeV." *Phys. Rev. Lett.* **104**, 142301 (2010).

[35] J. Adams et al. (STAR Collaboration), "Azimuthal anisotropy at RHIC: the first and fourth harmonics." *Phys. Rev. Lett.* **92**, 062301 (2004).

[36] P. Romatschke, U. Romatschke, "Viscosity Information from Relativistic Nuclear Collisions:How Perfect is the Fluid Observed at RHIC?" *Phys. Rev. Lett.* **99**, 172301 (2007).

[37] R. Fries, V. Greco, P. Sorensen, "Coalescence Models for Hadron Formation from Quark-Gluon Plasma." *Ann. Rev. Nucl. Part. Sci.* **58**, 177 (2008).

[38] M. He, R. J. Fries, R. Rapp, "Scaling of Elliptic Flow, Recombination and Sequential Freeze-Out of Hadrons in Heavy-Ion Collisions." *Phys. Rev.* **C82**, 034907 (2010).

[39] N. Armesto, "Nuclear shadowing." *J. Phys.* **G32**, R367 (2006).

[40] J. J. Aubert et al (The European Muon Collaboration), "The ratio of the nucleon structure functions F_2^N for iron and deuterium." *Phys. Lett.* **B124**, 275 (1983).

[41] P. R. Norton, "The EMC effect." *Rep. Prog. Phys.* **66**, 1253 (2003).

[42] J. Adams et al. (STAR Collaboration), "Evidence from $d + Au$ measurements for final-state suppression of high p_T hadrons in $Au + Au$ collisions at RHIC." *Phys. Rev. Lett.* **91**, 072304 (2003).

[43] M. L. Miller, K. Reygers, S. J. Sanders, P. Steinberg, "Glauber Modeling in High-Energy Nuclear Collisions." *Ann. Rev. Nucl. Part. Sci.* **57**, 205 (2007).

[44] CMS Collaboration, "Study of high-p_T charged particle suppression in $PbPb$ compared to pp collisions at $\sqrt{s_{\rm NN}}$ =2.76 TeV." *Eur. Phys. J.* **C 72**, 1945 (2012).

[45] I. Vitev, M. Gyulassy, "High-p_T Tomography of $d + Au$ and $Au + Au$ at SPS, RHIC, and LHC." *Phys. Rev. Lett.* **89**, 252301 (2002).

[46] M. Gyulassy, P. Levai, I. Vitev, "Jet Quenching in Thin Quark-Gluon Plasmas I: Formalism." *Nucl. Phys.* **B571**, 197 (2000).

[47] C. A. Salgado, U. A. Wiedemann, "A Dynamical Scaling Law for Jet Tomography." *Phys. Rev. Lett.* **89**, 092302 (2002).
N. Armesto, A. Dainese, C. A. Salgado, U. A. Wiedemann, "Testing the Color Charge and Mass Dependence of Parton Energy Loss with Heavy-to-light Ratios at RHIC and LHC." *Phys. Rev.* **D71**, 054027 (2005).

[48] T. Renk, H. Holopainen, R. Paatelainen, K. J. Eskola, "Systematics of the charged-hadron p_T spectrum and the nuclear suppression factor in heavy-ion collisions from $\sqrt{s_{\rm NN}}$ = 200 GeV to $\sqrt{s_{\rm NN}}$ = 2.76 TeV." *Phys. Rev.* **C84**, 014906 (2011).

[49] R. Baier, Yu. L. Dokshitzer, A. H. Mueller, S. Peigné, D. Schiff, "Radiative energy loss of high energy quarks and gluons in a finite volume quark-gluon plasma." *Nucl. Phys.* **B483**, 291 (1997).

[50] A. Dainese, C. Loizides, G. Paic, "Leading-particle suppression in high energy nucleus-nucleus collisions. *Eur. Phys. J.* **C38**, 461 (2005).

[51] X. N. Wang, X. F. Guo, "Multiple Parton Scattering in Nuclei: Parton Energy Loss" *Nucl. Phys.* **A696**, 788 (2001).

[52] M. He, R. J. Fries, R. Rapp, "Heavy-Quark Diffusion and Hadronization in Quark-Gluon Plasma." arXiv:1106.6006, and references therein.

[53] L. D. Landau and I. J. Pomeranchuk, *Doklady. Akad. Nauk. S.S.S.R* **92**, 535 (1953);
A. B. Migdal, "Bremsstrahlung and Pair Production in Condensed Media at High Energies." *Phys. Rev.* **103**, 1811 (1956).

[54] N. Armesto et al, "Comparison of Jet Quenching Formalisms for a Quark-Gluon Plasma 'Brick'." arXiv:1106.1106.

[55] J. Jia (PHENIX collaboration), "Zeroing in on jet quenching: a PHENIX perspective." *Nucl. Phys.* **A855**, 92 (2011)

[56] J. Liao, E. Shuryak, "Angular Dependence of Jet Quenching Indicates Its Strong Enhancement near the QCD Phase Transition." *Phys. Rev. Lett.* **102**, 202302 (2009).

[57] Z. Lin, M. Gyulassy, "Open charm as a probe of preequilibrium dynamics in nuclear collisions?" *Phys. Rev.* **C51**, 2177 (1995).

[58] M. Cacciari, M. Greco, P. Nason, "The p_T Spectrum in Heavy-Flavour Hadroproduction." *J*HEP**9805**, 007 (1998).

[59] M. Cacciari, P. Nason, R. Vogt, "QCD Predictions for Charm and Bottom Quark Production at RHIC." *Phys. Rev. Lett.* **95**, 122001 (2005);
M. Cacciari and R. Vogt, private communications.

[60] Yu. L. Dokshitzer, D. E. Kharzeev, "Heavy-quark colorimetry of QCD matter." *Phys. Lett.* **B519**, 199 (2001).

[61] B. I. Abelev et al. (STAR Collaboration), "Erratum: Transverse Momentum and Centrality Dependence of High-pT Nonphotonic Electron Suppression in Au+Au Collisions at $\sqrt{s_{\rm NN}}$ = 200 GeV." *Phys. Rev. Lett.* **106**, 159902(E (2011).

[62] A. Adare et al. (PHENIX Collaboration) "Energy Loss and Flow of Heavy Quarks in Au+Au Collisions at $\sqrt{s_{\rm NN}}$ = 200 GeV." *Phys. Rev. Lett.* **98**, 172301 (2007).

[63] G. D. Moore, D. Teaney, "How much do heavy quarks thermalize in a heavy ion collision?" *Phys. Rev.* **C71**, 064904 (2005).

[64] M. Gyulassy, "Getting to the bottom of the heavy quark jet puzzle", *APS Physics* **2** 107 (2009).

[65] A. Buzzatti, M. Gyulassy, "Dynamical magnetic enhancement of light and heavy quark jet quenching at RHIC." *Nucl. Phys.* **A855**, 307 (2011).

[66] R. Sharma, I. Vitev, B. W. Zhang, "Light-cone wave function approach to open heavy avor dynamics in QCD matter." *Phys. Rev.* **C80**, 054902 (2009).

[67] P. B. Gossiaux, R. Bierkandt, J. Aichelin "Tomography of quark gluon plasma at energies available at the BNL Relativistic Heavy Ion Collider (RHIC) and the CERN Large Hadron Collider (LHC)." *Phys. Rev.* **C79**, 044906 (2009).

[68] J. Noronha, M. Gyulassy, G. Torrieri, "Conformal Holography of Bulk Elliptic Flow and Heavy Quark Quenching in Relativistic Heavy Ion Collisions." *Phys. Rev.* **C82**, 054903 (2010).

[69] S. S. Gubser, "Using string theory to study the quark-gluon plasma: progress and perils." *Nucl. Phys.* **A830**, 657 (2009)

[70] R.Rapp, H. V. Hees, "Heavy Quarks in the Quark-Gluon Plasma." arXiv:0903.1096 and R. C. Hwa, X. -N. Wang (Ed.), "Quark Gluon Plasma 4", World Scientific (2010).

[71] P. Gossiaux, J.Aichelin, T. Gousset, "Theory of heavy quark energy loss." arXiv:1201.4038, proceedings for ISMD 2011 Conference..

[72] M. M. Aggarwal et al. (STAR Collaboration), "Measurement of the Bottom Quark Contribution to Nonphotonic Electron Production in p+p Collisions at $\sqrt{s} = 200$ GeV." *Phys. Rev. Lett.* **105**, 202301 (2010).

[73] H. Agakishiev et al. (STAR Collaboration), "High p_T non-photonic electron production in p+p collisions at $\sqrt{s} = 200$ GeV." *Phys. Rev.* **D83**, 052006 (2011); and private communications among the authors.

[74] M. Harrison, S. Peggs, T. Roser, "The RHIC Accelerator." *Ann. Rev. Nucl. Part. Sci.* **52**, 425 (2002).

[75] S. M. Guertin, "Mid-Rapidity π^0 production in $d + Au$ collisions at $\sqrt{s} =$ 200 GeV." Ph.D. dissertation, University of California, Los Angeles (2008). And references therein.

[76] K. H. Ackermann et al. (STAR Collaboration), "STAR detector overview." *Nucl. Instr. Meth.* **A499**, 624 (2003).

[77] M. Anderson et al., "The STAR time projection chamber: a unique tool for studying high multiplicity events at RHIC." *Nucl. Instr. Meth.* **A499**, 659 (2003).

[78] W. J. Llope et al., "The TOFp/pVPD time-of-flight system for STAR." *Nucl. Instr. Meth.* **A522**, 252 (2004).

[79] M. Shao et al., "Extensive particle identification with TPC and TOF at the STAR experiment." *Nucl. Instr. Meth.* **A558**, 419 (2006).

[80] M. Beddo et al., "The STAR Barrel Electromagnetic Calorimeter." *Nucl. Instr. Meth.* **A499**, 725 (2003).

[81] C. E. Allgower et al., "The STAR endcap electromagnetic calorimeter." *Nucl. Instr. Meth.* **A499**, 740 (2003).

[82] F. Bergsma et al., "The STAR detector magnet subsystem." *Nucl. Instr. Meth.* **A499**, 633 (2003).

[83] L. Ruan et al., "Perspectives of a Midrapidity Dimuon Program at RHIC: A Novel and Compact Muon Telescope Detector." *J. Phys.* **G36**, 95001 (2009).

[84] F. S. Bieser et al., "The STAR trigger." *Nucl. Instr. Meth.* **A499**, 766 (2003).

[85] J. Abele et al., "The laser system for the STAR time projection chamber." *Nucl. Instr. Meth.* **A499**, 692 (2003).

[86] D. Beavis et al., "The STAR Heavy Flavor Tracker Technical Design Report."
http://drupal.star.bnl.gov/STAR/system/files/HFT_TDR_Final.pdf

[87] H. Masui, A. Schmah, "Centrality update in Run10 Au+Au at 200 GeV."
www.star.bnl.gov/protected/bulkcorr/hmasui/2011/Centrality_200GeV_Nov08/hmasui_centrality_Run10_AuAu_200GeV_PWGC_Nov08_2011.pdf

[88] W. Dong, "Measurement of non-photonic electron azimuthal anisotropy v_2 from Au+Au collisions at $\sqrt{s_{\rm NN}}$ = 200 GeV." Ph.D. dissertation, University of California, Los Angeles (2006).

[89] H. Bichsel, "A method to improve tracking and particle identication in TPCs and silicon detectors." *Nucl. Instr. Meth.* **A562**, 154 (2006).

[90] STAR Collaboration, "J/ψ production at high transverse momenta in p+p and Au+Au collisions at $\sqrt{s_{\rm NN}}$ = 200 GeV." in preparation. Z. Tang, private communication.

[91] A. Adare et al. (PHENIX Collaboration), "J/ψ Production versus Centrality, Transverse Momentum, andRapidity in Au+Au Collisions at $\sqrt{s_{\rm NN}}$ = 200 GeV." *Phys. Rev. Lett.* **98**, 232301 (2007).

[92] T. Sjöstrand, S. Mrenna, P. Skands, "PYTHIA 6.4 Physics and Manual." *J*HEP **0605**, 026 (2006);
http://home.thep.lu.se/∼torbjorn/pythia/pythia6409.f

[93] T. Ullrich, "Study of the contribution of J/ψ decay electrons to the NPE yield measured."
www.star.bnl.gov/protected/heavy/ullrich/jpsiee.pdf

[94] T. Sjöstrand, S. Mrenna, P. Skands, "A Brief Introduction to PYTHIA 8.1." *Comput. Phys. Commun.* **178**,852 (2008).

[95] A. Adare et al. (PHENIX Collaboration), "Heavy-quark production in p+$p$and energy loss and ow of heavy quarks in Au+Aucollisions at $\sqrt{s_{\rm NN}}$ = 200 GeV." *Phys. Rev.* **C84**, 044905 (2011).

[96] D. Kikola, M. Mustafa, "$K_{e3} \rightarrow e$ background in non-photonic electron studies in p+p 200 GeV."
http://drupal.star.bnl.gov/STAR/system/files/Npe_Ke3_Bg_March_1_2012.pdf

[97] GEANT 3.21, CERN Program Library.
http://wwwasdoc.web.cern.ch/wwwasdoc/geant_html3/geantall.html

[98] O. D. Tsai, Notes on SMD0+SAS Optimization (1998).
www.physics.ucla.edu/%7Etsai/bsmd/sassmdopt.ps.

[99] N. M. Kroll, W. Wada, "Internal Pair Production Associated with the Emission of High-Energy Gamma Rays." *Phys. Rev.* **98**, 1355 (1955).

[100] A. Adare et al. (PHENIX Collaboration), "Detailed measurement of the e+e- pair continuum in p+p and Au+Au collisions at $\sqrt{s_{\rm NN}}$ = 200 GeV and implications for direct photon production." *Phys. Rev.* **C81**, 034911 (2010).

[101] B. I. Abelev et al. (STAR Collaboration), "Transverse Momentum and Centrality Dependence of High-p_T Nonphotonic Electron Suppression in Au+Au Collisions at $\sqrt{s_{\rm NN}}$ = 200 GeV." *Phys. Rev. Lett.* **98**, 192301 (2007).

[102] A. Adare et al. (PHENIX Collaboration), "Measurement of High-p_T Single Electrons from Heavy-Flavor Decays in p+p Collisions at $\sqrt{s}$ = 200GeV." *Phys. Rev. Lett.* **97**, 252002 (2006).

[103] http://www.star.bnl.gov/protected/common/common2010/centrality/200GeV/table/table_Ncoll_vs_centrality_systematicerror.txt

[104] P. B. Gossiaux, J. Aichelin, "Towards an understanding of the RHIC single electron data." *Phys. Rev.* **C78**, 014904 (2008).

[105] J. Barrette et al. (E877 Collaboration), "Proton and pion production relative to the reaction plane in Au+Au collisions at 11A GeV/c." *Phys. Rev.* **C56**, 3254 (1997).

[106] http://root.cern.ch

[107] A. Ohlson, "Calculating Jet vn and the Event Plane in the Presence of a Jet." arXiv:1205.1172.

[108] B. H. J. Biritz, "Electron-hadron azimuthal correlation in Au+Au Collisions at $\sqrt{s_{\rm NN}}$ = 200 GeV." Ph.D. dissertation, University of California, Los Angeles (2010).

[109] P. Sorensen, "Higher flow harmonics in heavy ion collisions from STAR." *J. Phys.* **G38**, 124029 (2011).

[110] S. S. Gubser, S. S. Pufu, A. Yarom, "Sonic booms and diffusion wakes generated by a heavy quark in thermal AdS/CFT." *Phys. Rev. Lett.* **100**, 012301 (2008).

[111] S. S. Gubser, S. S. Pufu, A. Yarom, "Shock waves from heavy-quark mesons in AdS/CFT." *J*HEP**807**, 108 (2008).

[112] J. Noronha, M. Gyulassy, G. Torrieri, "Di-Jet Conical Correlations Associated with Heavy Quark Jets in antide Sitter Space/Conformal Field Theory Correspondence." *Phys. Rev. Lett.* **102**, 102301 (2009).

[113] B. I. Abelev et al. (STAR Collaboration) "Υ cross section in p+p collisions at $\sqrt{s} = 200$ GeV." *Phys. Rev.* **D82**, 012004 (2010)

[114] J. Adams et al. (STAR Collaboration), "Open charm yields in d + Au collisions at $\sqrt{s_{\rm NN}} = 200$GeV." *Phys. Rev. Lett.* **94**, 062301 (2005).

[115] http://www.phys.ufl.edu/∼rfield/cdf/tunes/py_tuneA.html